Investigating the Interaction of an Annular Air Jet with a Spray Flame Using Phase-Doppler Interferometry and Laser-Induced Fluorescence

by

Jacob A. Friedman

A thesis
presented to the University of Waterloo
in fulfilment of the
thesis requirement for the degree of
Doctor of Philosophy
in
Mechanical Engineering

Waterloo, Ontario, Canada, 1997

©Jacob A. Friedman 1997

National Library of Canada
Acquisitions and Bibliographic Services
395 Wellington Street
Ottawa ON K1A 0N4
Canada

Bibliothèque nationale du Canada
Acquisitions et services bibliographiques
395, rue Wellington
Ottawa ON K1A 0N4
Canada

Your file Votre référence

Our file Notre référence

The author has granted a non-exclusive licence allowing the National Library of Canada to reproduce, loan, distribute or sell copies of this thesis in microform, paper or electronic formats.

L'auteur a accordé une licence non exclusive permettant à la Bibliothèque nationale du Canada de reproduire, prêter, distribuer ou vendre des copies de cette thèse sous la forme de microfiche/film, de reproduction sur papier ou sur format électronique.

The author retains ownership of the copyright in this thesis. Neither the thesis nor substantial extracts from it may be printed or otherwise reproduced without the author's permission.

L'auteur conserve la propriété du droit d'auteur qui protège cette thèse. Ni la thèse ni des extraits substantiels de celle-ci ne doivent être imprimés ou autrement reproduits sans son autorisation.

0-612-30609-7

Canada

The University of Waterloo requires the signatures of all persons using or photocopying this thesis. Please sign below, and give address and date.

ABSTRACT

This thesis describes an experimental investigation of the interaction of an annular air jet with a spray flame using phase Doppler interferometry (PDI) and planar laser-induced fluorescence (PLIF). The geometry studied consisted of a standard .75-60°A pressure-swirl nozzle concentrically located in a 63.6mm x 50.4mm annular air jet. Methanol fuel was sprayed from the nozzle at a flow rate of 0.42 g/s and ignited. Measurements were made in the resulting spray flame, with annular air flow rates of 0, 2.38, 4.77, 7.15 and 9.52 *l*/s (Reynolds numbers based on bluff body diameter of 0, 6500, 13000, 19500 and 26000 respectively). Photographic images were made using laser sheet lighting to illuminate a centreline slice of the spray, and instantaneous and time-averaged planar laser-induced fluorescence images of OH fluorescence were made, showing reaction zone locations. Quantitative OH concentrations were extracted from the PLIF images. An attempt to obtain PLIF images of CH fluorescence in the spray flame was unsuccessful. Phase Doppler interferometry measurements allowed mapping of fuel droplet size and velocity distribution, as well as local volume flux. Post-processing of PDI data allowed determination of the gas-phase velocity. A method was developed to enhance the visibility of seed particles in the presence of large droplets and thus increase data rates, and was applied to the spray centreline to obtain turbulence information including local integral timescales and turbulent energy spectra. Temperature measurements were made using thermocouples in regions where droplet impingement was not significant. It was found that the annular air jet profoundly influences the spray flame, reducing the overall flame height by half, and changing the structure from a two reaction zone system to a single reaction zone system. The annular air jet tended to direct droplets toward centreline, thus providing a confinement effect.

ACKNOWLEDGMENTS

I would like to thank Metin Renksizbulut for his support and encouragement during the course of this project.

The lab space, equipment and technical support of Prof. E. Weckman and Prof. J. Hepburn is acknowledged with thanks.

Financial support from the Natural Sciences and Engineering Research Council of Canada, the Ontario Graduate Scholarship Program and the Faculty of Engineering at the University of Waterloo is gratefully acknowledged.

I would also like to thank my parents for their continued interest and encouragement.

Most of all, I would like to thank my wife and children for allowing me the opportunity to pursue this project, and for their constant interest and support.

CONTENTS

Abstract iv

Acknowledgments v

List of Figures ix

List of Tables xiv

Nomenclature xv

Chapter 1

Introduction 1

Chapter 2

Literature Review 3

2.1 Previous Work 3

2.2 Summary 7

Chapter 3

Phenomenological Discussion 10

3.1 The Annular Jet 10

3.2 The Atomizer 13

3.3 Droplet Statistics 19

3.4 Combustion 23

3.5 Combustion of Practical Sprays 26

Chapter 4

Experimental Systems 29

4.1 Phase Doppler Interferometry 29

4.1.1 Phase Doppler Interferometry Theory 30

4.1.2 Aerometrics Phase Doppler Particle Analyzer 36

4.1.3 Instrument Output 43
4.1.4 Post-Processed Results 46
4.1.5 Limitations 49
4.1.6 Increasing PDI Sensitivity to Small Particles 50
4.2 Planar Laser-Induced Fluorescence 68
4.2.1 Laser-Induced Fluorescence Theory 68
4.2.2 Camera Calibration 87
4.3 Temperature Measurements 93
4.4 Photographic Techniques 94

Chapter 5

Facility and Experimental Procedure 95
5.1 The Burner System 95
5.2 Experimental Description 98
5.3 Photographic Study 98
5.4 PLIF Measurements 98
5.5 PDI Measurements 99
5.6 Temperature Measurements 99

Chapter 6

Results and Discussion 100
6.1 Photographic Tests and Visual Observations 100
6.2 PLIF OH Images 108
6.3 PLIF CH Images 134
6.4 Phase Doppler Interferometry Results 137
6.4.1 Droplet Diameter Measurements 138
6.4.2 Volume Flux Profiles 152
6.4.3 Mean Velocity Fields 162
6.5 Temperature Measurements 176

6.6 Turbulence Measurements 186
6.7 Summary 201

Chapter 7

Experimental Uncertainties 204
7.1 Introduction 204
7.2 PDI Uncertainties 206
7.3 Turbulent Statistics Uncertainties 213
7.4 PLIF Uncertainties 216
7.5 Temperature Measurement Uncertainties 222

Chapter 8

Conclusions and Recommendations 227

Chapter 9

References 229

Appendix 1

ICCD Camera Calibration and OH Concentration Calculation 237

LIST OF FIGURES

2.1 Annular Jet Flow Features 9

3.1 Annular Jet with Spray Flow Features 12

3.2 Pressure-Swirl Atomizer 18

3.3 Comparison of Log-Normal and Rosin-Rammler Distributions 22

3.4 OH Equilibrium Concentration as a Function of Temperature for Stoichiometric Combustion of Methanol 25

3.5 Typical Spray Flame Features 28

4.1 Intersection of Two Laser Beams to Form Probe Volume 34

4.2 Phase Doppler Geometry 35

4.3 PDI System Layout 41

4.4 Receiver Geometry 42

4.5 Droplet Scattering Geometry 59

4.6 Ratio of Intensity of Scattered Refracted Light for Dyed and Undyed Droplets . 60

4.7 Ratio of First Order Refracted Intensity at 30° Collection Angle for Dyed Droplets 61

4.8 Comparison of Refracted Scattered Intensity for Dyed and Undyed Droplets . . 62

4.9 Comparison of Correction Schemes Applied to a Log-Normal Raw Distribution, and an absorptivity of $\gamma = 0.015$ /μm and $G = 35$ 63

4.10 PDI Measured Deviation from Expected Diameter with Dyed Droplets 64

4.11 Measured Scattered Intensity Versus Diameter for Undyed Droplets 65

4.12 Measured Scattered Intensity Versus Diameter for Dyed Droplets 66

4.13 Typical Droplet Diameter Histogram with Dyed Droplets and Nebulizer-seeded Airflow 67

4.14 Four Level Fluorescence Model 85

4.15 Planar Laser-Induced Fluorescence System Layout 86

4.16 ICCD Camera Response Curve 90

4.17 Nikor 105mm f/4.5 UV-Grade Lens Response 91

4.18 Laser Sheet Intensity Variation 92
4.19 Thermocouple Diagram 93
4.20 Photographic Arrangement 94
5.1 Rig Cross-Section 96
5.2 Burner System Schematic Diagram 97
6.1a Annular Air Jet Off, Long Exposure 103
6.1b Annular Air Jet Off, Short Exposure 103
6.2a Annular Air = 2.38 *l*/s, 1/8 Sec Exposure 104
6.2b Annular Air = 2.38 *l*/s, 1/60 Sec Exposure 104
6.3a Annular Air = 4.77 *l*/s, 1/8 Sec Exposure 105
6.3b Annular Air = 4.77 *l*/s, 1/60 Sec Exposure 105
6.4a Annular Air = 7.15 *l*/s, 1/8 Sec Exposure 106
6.4b Annular Air = 7.15 *l*/s, 1/60 Sec Exposure 106
6.5a Annular Air = 9.52 *l*/s, 1/8 Sec Exposure 107
6.5b Annular Air = 9.52 *l*/s, 1/60 Sec Exposure 107
6.6 Annular Air Off Composite Image 113
6.7a Annular Air Off, Single Shot Image, z = 0 to 65mm 114
6.7b z = 65 to 130mm 114
6.7c z = 130 to 195mm 114
6.8 Five Single-Shot Images in the z = 0 to 65mm Plane with Annular Air Off ... 115
6.9 Annular Air 2.38 *l*/s 100 Shot Average Composite Image 116
6.10a Air = 2.38 *l*/s Single Shot Image, z = 0 to 65mm 117
6.10b z = 65 to 130mm 117
6.10c z = 130 to 195mm 117
6.11 Five Single-Shot Images in the z = 0 to 65mm Plane, Air Flow Rate = 2.38 *l*/s 118
6.12 Annular Air 4.77 *l*/s 100 Shot Average Composite Image 119
6.13a Air = 4.77 *l*/s Single Shot Image, z = 0 to 65mm 120
6.13b z = 65 to 130mm 120
6.13c z = 130 to 195mm 120

6.14 Five Single-Shot Images in the z = 0 to 65mm Plane, Air Flow Rate = 4.77 *l*/s 121
6.15 Annular Air 7.15 *l*/s 100 Shot Average Composite Image 122
6.16a Air = 7.15 *l*/s Single Shot Image, z = 0 to 65mm 123
6.16b z = 65 to 130mm 123
6.16c z = 130 to 195mm 123
6.17 Five Single-Shot Images in the z = 0 to 65mm Plane, Air Flow Rate = 7.15 *l*/s 124
6.18 Annular Air 9.52 *l*/s 100 Shot Average Composite Image 125
6.19a Air = 9.52 *l*/s Single Shot Image, z = 0 to 65mm 126
6.19b z = 65 to 130mm 126
6.19c z = 130 to 195mm 126
6.20 Five Single-Shot Images in the z = 0 to 65mm Plane, Air Flow Rate = 9.52 *l*/s 127
6.21 Mean OH Concentration Profiles with Annular Air Off 128
6.22 Mean OH Concentration Profiles with Annular Air = 2.38 *l*/s 129
6.23 Mean OH Concentration Profiles with Annular Air = 4.77 *l*/s 130
6.24 Mean OH Concentration Profiles with Annular Air = 7.15 *l*/s 131
6.25 Mean OH Concentration Profiles with Annular Air = 9.52 *l*/s 132
6.26 Instantaneous OH Fluorescence in the z = 25mm Plane for the
Annular Air Off and Air = 9.52 *l*/s Cases 133
6.27 CH Fluorescence Image in a Bunsen Burner Flame 135
6.28 CH Fluorescence in a Spray Flame 136
6.29 Typical Droplet Diameter Distribution, Obtained at z = 25mm, r = 18mm
with an Annular Air Flow Rate of 4.77 *l*/s 141
6.30 Typical Droplet Diameter - Axial Velocity Correlation, Obtained at z = 25mm
r = 18mm with an Annular Air Flow Rate of 4.77 *l*/s 142
6.31 Typical Radial-Axial Velocity Correlation, Obtained at z = 25mm
r = 18mm with an Annular Air Flow Rate of 4.77 *l*/s 143
6.32 Variation of Arithmetic Mean Diameter with Radial Position
in the z = 10mm Plane 144
6.33 Variation of Arithmetic Mean Diameter with Radial Position

in the z = 25mm Plane 145
6.34 Variation of Arithmetic Mean Diameter with Radial Position
in the z = 40mm Plane 146
6.35 Variation of Arithmetic Mean Diameter with Radial Position
in the z = 60mm Plane 147
6.36 Variation of Arithmetic Mean Diameter with Radial Position
in the z = 80mm Plane 148
6.37 Variation of Arithmetic Mean Diameter with Radial Position
in the z = 100mm Plane 149
6.38 Variation of Arithmetic Mean Diameter with Radial Position
in the z = 140mm Plane 150
6.39 Variation of Arithmetic Mean Diameter with Radial Position
in the z = 200mm Plane 151
6.40 Variation of Volume Flux in the z = 10mm Plane 153
6.41 Variation of Volume Flux in the z = 25mm Plane 154
6.42 Variation of Volume Flux in the z = 40mm Plane 155
6.43 Variation of Volume Flux in the z = 60mm Plane 156
6.44 Variation of Volume Flux in the z = 80mm Plane 157
6.45 Variation of Volume Flux in the z = 100mm Plane 158
6.46 Variation of Volume Flux in the z = 140mm Plane 159
6.47 Variation of Volume Flux in the z = 200mm Plane 160
6.48 Integrated Volume Flux Curves for All Air Flow Rates 161
6.49 Vector Plot of Gas-phase Velocity with Annular Air Off 165
6.50 Vector Plot of Gas-phase Velocity with Annular Air = 2.38 *l*/s 166
6.51 Vector Plot of Gas-phase Velocity with Annular Air = 4.77 *l*/s 167
6.52 Vector Plot of Gas-phase Velocity with Annular Air = 7.15 *l*/s 168
6.53 Vector Plot of Gas-phase Velocity with Annular Air = 9.52 *l*/s 169
6.54 Vector Plot of Large Droplet (> 30 μm) Velocity with Annular Air Off 170
6.55 Vector Plot of Large Droplet (> 30 μm) Velocity with Annular = 2.38 *l*/s 171

6.56 Vector Plot of Large Droplet (> 30 μm) Velocity with Annular = 4.77 *l*/s 172
6.57 Vector Plot of Large Droplet (> 30 μm) Velocity with Annular = 7.15 *l*/s 173
6.58 Vector Plot of Large Droplet (> 30 μm) Velocity with Annular = 9.52 *l*/s 174
6.59 Vector Plot of Large Droplet (> 30 μm) and Gas-Phase Velocity in the z = 10mm Plane with Annular Air Flow = 7.15 *l*/s 175
6.60 Temperature Variation in the z = 25mm Plane 178
6.61 Temperature Variation in the z = 40mm Plane 179
6.62 Temperature Variation in the z = 60mm Plane 180
6.63 Temperature Variation in the z = 80mm Plane 181
6.64 Temperature Variation in the z = 100mm Plane 182
6.65 Temperature Variation in the z = 140mm Plane 183
6.66 Temperature Variation in the z = 200mm Plane 184
6.67 Centreline Temperature Development 185
6.68 Comparison of Arithmetic Mean Diameter for the Old and New Nozzles in the z = 25mm Plane with Annular Air Off 191
6.69 Comparison of Mean Axial Velocity for the Old and New Nozzles in the z = 25mm Plane with Annular Air Off 192
6.70 Centreline Velocity Development for the Burning and Non-Burning Spray Cases with an Annular Air Flow Rate of 4.77 *l*/s 193
6.71 Mean Axial Centreline Velocity Development for All Air Flow Rates Tested . 194
6.72 Centreline RMS Fluctuating Velocity Development 195
6.73 Centreline Local Turbulent Intensity 196
6.74 Centreline Integral Timescale Development 197
6.75 Shear Stress in the z = 60mm Plane 198
6.76 Turbulent Centreline Energy Spectra Development with Axial Distance from the Nozzle with an Annular Air Flow Rate of 7.15 *l*/s 199
6.77 Turbulent Energy Spectra on Centreline, 60mm Downstream of the Nozzle .. 200
7.1 Log-Normal Distribution with D_g = 20 μm, σ_g = 1.65 μm 213
7.2 Catalytic Surface Combustion on Thermocouple 226

LIST OF TABLES

2.1 Summary of Published Annular Jet Research 8

3.1 Droplet Mean Diameters Typically Used 19

4.1 PDI System Optical Parameters 37

4.2 PDI System Settings 38

4.3 Influence of Correction Scheme on Statistical Diameters for a Log-normal Raw Distribution with Droplet Absorptivity $\gamma = 0.015$ /μm and Instrument Gain $G^2 = 1000$ 58

4.4 Spectroscopic Constants for OH and CH 81

4.5 LIF Operating Parameters 84

6.1 Symmetry Test Results 137

6.2 Temporal Stability of the Flow 138

6.3 Summary of Turbulent Reynolds Numbers at Locations of Spectra Measurements 189

7.1 Effect of Droplet Rejection Bias on Mean Diameters 210

7.2 Summary of Fluorescence Measurement Uncertainties 221

7.3 Summary of Temperature Measurement Uncertainties 225

NOMENCLATURE

ROMAN SYMBOLS

a	Voigt parameter
A	Laser sheet cross-sectional area
	Fringe spacing between 1st and 3rd rings of fringe pattern
	Area viewed by collection optics
A_{00}	Spontaneous emission rate from $v' = 0$ to $v'' = 0$
A_{01}	Spontaneous emission rate from $v' = 0$ to $v'' = 1$
A_{10}	Spontaneous emission rate from $v' = 1$ to $v'' = 0$
A_{11}	Spontaneous emission rate from $v' = 1$ to $v'' = 1$
A_b	Surface area of themocouple junction
a_i	Radius of ith size class
A_i	Area of probe volume for ith size class
a_{max}	Radius of largest size class
A_{max}	Area of probe volume for largest size class
A_p	Area of laser sheet imaged by pixel
B	Bias error
b_{10}, b_{01}	Stimulated emission rate
B_{10}	Einstein coefficient for stimulated absorption
B_i	ith bias error
B_v	Rotational constant
c	Speed of light
C_b	Junction specific heat
C_D	Drag coefficient
D	Droplet diameter
	Divergence (Eq. 4.21, 4.22)

D_{10}	Arithmetic mean diameter
D_{20}	Area mean diameter
D_{30}	Volume mean diameter
D_{32}	Sauter mean diameter
dD	Width of size range
df	Fraction of droplets with diameter between (D - dD/2) and (D + dD/2)
D_g	Geometric mean diameter
D_i	Mean droplet diameter in ith size class
E	Energy
E_0	Laser pulse energy
E_i	Incident laser energy
E_{Ray}	Rayleigh scattered energy
f	Frequency
f_D	Doppler frequency
F_D	Drag force
f_J	Boltzmann fraction in rotational state J
f_m	Measured frequency
f_{shift}	Shift frequency
f_v	Boltzmann fraction in vibrational state v
F_y	Fluorescence yield
g	Absorption lineshape function
G	Square root of instrument gain
g_D	Doppler lineshape function
h	Planck's constant
h_b	Effective convection coefficient at thermocouple junction
h_L	Laser sheet height

I	Intensity
I_0	Incident intensity
I_b	Incident light intensity
I_{max}	Maximum intensity scattered by particle of size a_{max}
J	Rotational quantum number
k	Boltzmann constant
k_w	Thermocouple wire thermal conductivity
L	Length of imaged volume
	Integral length scale
L_C	Local flow characteristic length
m	Relative index of refraction
	Number of time lags (Eq. 4.16)
	Mass of molecule
m_b	Junction mass
n	Number of laser pulses
N	Total number of droplets, samples
n_0	Number density of probed molecule
n_1	Number of molecules in excited state
N_A	Number density of air molecules
$n_{c,i}$	Corrected count in ith bin
n_d	Number of sub-records
N_D	Dark charge noise of the ICCD
	Droplet number density
n_i	Number of drops, counts in ith size class
	Number density of ith species
n_m	Index of refraction of surroundings
n_p	Number of photons emitted

N_{ph}	Photon shot noise associated with signal
n_{pp}	Number of photons directed to pixel
N_R	Readout noise of the ICCD
N_T	Total signal noise
p	Scattering mode
q	Rosin-Rammler distribution parameter
Q	Fraction of total volume contained in drops of diameter larger than D
Q_0, Q_1	Quench rates
q_{cat}	Heat addition due to catalysis
Q_i	Quench rate due to ith species
$\Re$	Autocorrelation function
r	Radial co-ordinate
	Radius of thermocouple wire
r_b	Radial displacement from beam centreline
Re_R	Reynolds number based on relative velocity
r_w	Beam waist diameter ($1/e^2$)
s	Radial distance from particle centre
S	Precision error
	Detector separation
S_i	ith precision error
S_{PSF}	Uncertainty in power spectrum function
S_{RMS}	Uncertainty in RMS
St_m	Mean Stokes number
$\Im$	Integral timescale
t	Time
	Laser sheet thickness
	Student t value

T	Time period
	Temperature
	Fringe width
T_{00}, T_{01},	Filter transmittances
T_{10}, T_{11}	
T_g	Gas temperature
T_{surr}	Surroundings temperature
T_w	Thermocouple wire temperature
$\overline{U}$	Mean axial velocity
U	Axial velocity
U_C	Local flow mean velocity
u_i	Relative velocity between colliding species
U_i	Axial velocity of the ith particle
U_R	Relative velocity
u'	Axial fluctuating velocity
v	Vibrational quantum number
$\overline{uv}$	Turbulent shear stress
$\overline{V}$	Mean radial velocity
V	Radial velocity
	Downward transfer rate
	Voigt parameter
V_i	Radial velocity of the ith particle
V_Z	Z component of particle velocity
v'	Radial fluctuating velocity
We	Weber number
x	Distance from junction
	Voigt parameter

X	Rosin-Rammler mean diameter
	Discrete Fourier transform
z	Axial co-ordinate
$z_{\alpha/2}$	Standard normal variate

Greek Symbols

β_1, β_2	Scattering phase functions
γ	Absorptivity
δ	Fringe spacing
	Total measurement uncertainty
$\Delta\nu_c$	Pressure broadened linewidth
$\Delta\nu_D$	Doppler linewidth
$\Delta\nu_L$	Laser linewidth
$\Delta\Phi$	Phase difference between observers
ϵ	Emissivity
ϵ_2	Fresnel coefficient
θ	Laser intersection angle
	Scattering angle
θ'	Scattering angle
λ	Laser wavelength
	Taylor length scale
μ_g	Gas viscosity
ν	Frequency
	Viscosity
ν_0	Centre frequency
ρ_g	Gas density
ρ_p	Droplet density

σ_g	Geometric standard deviation
σ	Surface tension
	Standard deviation
	Stefan-Boltzmann constant
σ_i	Collisional cross-section of *i*th species
σ_{Ray}	Rayleigh scattering cross-section
τ	Optical angles
	Interaction timescale
τ_D	Droplet relaxation time
τ_F	Local mean flow timescale
τ'	Optical angle
ϕ	Off axis angle
ψ	Elevation angle
Ω	Solid angle of collection
ω_v	Molecular vibrational frequency

CHAPTER 1

INTRODUCTION

The combustion of liquid fuels currently provides the energy used by many stationary and most mobile powered systems, such as industrial and domestic furnaces and boilers, and automotive and aerospace engines. In all these applications, performance demands are becoming increasingly stringent. In the aerospace field, requirements for high thrust, low weight and low NO_x engines are driving ongoing research into spray combustion. Legislative requirements for automotive engines and industrial emissions demand continued improvement of fuel delivery systems and combustion control.

In virtually all cases, the liquid fuel is sprayed and mixed with an oxidizer to ensure complete combustion and sufficient energy density to efficiently power the system. Since the liquid fuel itself must be vaporized before it will burn, the fuel vaporization rate strongly influences the combustion process. Generally speaking, the smaller the fuel spray particles produced for a given fuel mass flow rate, the faster the fuel vaporization rate and hence the more intense the combustion. The flame characteristics for a given fuel depend not only on the fuel droplet size distribution, but on the spray spatial distribution and its interaction with the oxidizer flow field. These interactions include turbulent heat, mass and momentum transfer, as well as complicated chemical kinetics. Each of these phenomena is extremely complicated in its own right, and, when coupled together in a real flow situation, form a formidable challenge for the combustion researcher.

The ultimate goal in understanding the spray combustion process is to be able to control combustion conditions to meet specific design criteria, while minimizing undesirable reactions and resulting pollutant and soot formation, and maximizing combustion efficiency. The spray combustion process is too complicated to be successfully modeled at present, although models are constantly being improved as computer power and speed increase, so there is an ongoing need for experimentation. The spray flame environment is an extremely

hostile one in which to make measurements. Temperature extremes range from ambient to beyond 3000 K, and fuel droplets abound, making intrusive measurements difficult to obtain. Recent developments in non-intrusive laser-based diagnostic systems, reviewed by Chigier [1] have provided new tools to extend knowledge of the combustion process in spray flames along several fronts. Phase Doppler interferometry (PDI) allows researchers to obtain spatially resolved information on fuel droplet size and velocity at high data rates, even in hostile environments, and can be extended to track the gas-phase velocity as well, thus allowing velocities in the two-phase flow field to be resolved. Planar laser-induced fluorescence (PLIF) allows two-dimensional imaging of the OH (or other radicals) radical concentration in the spray flame, a good marker of the reaction and recombination zones. The technique also has the potential to provide an instantaneous two dimensional temperature map in a spray flame, although this has yet to be attempted.

The work reported herein applies these non-intrusive techniques to a practical spray combustion system in an attempt to demonstrate the effectiveness of this instrument combination. A technique is described to allow better discrimination of gas-phase velocity and turbulence characteristics. The resulting data set will allow correlation of reaction zone location with the two phase flow field, information that has been unavailable or unattainable until recently.

The geometry chosen for study was the bluff body stabilized flame. This configuration has the advantages of having been previously studied, particularly in non-reacting flows, and is axi-symmetric, limiting the number of data points required and lending itself to numerical simulation. This latter feature is important as experimental data is required for validation of numerical codes as they are developed.

The objective of this work was two-fold; namely to demonstrate the effectiveness of combining PDI and PLIF techniques to obtain as complete a picture of a spray flame as possible, and to use this data set to evaluate the effect of the annular air jet on the resulting spray flame with regard to temperature distribution, reaction zone location, flame shape and flame stability.

CHAPTER 2

Literature Review

2.1. Previous Work

Spray flames in general and specific diagnostic techniques such as phase Doppler interferometry have been extensively reported in the literature, and will not be discussed herein. The following discussion will be limited to investigations of annular jets and spray interactions with annular jets, as well as planar LIF imaging as applied to spray flames.

As indicated in the previous section, the axi-symmetric bluff body configuration has been quite extensively studied, particularly in non-reacting situations. The aerodynamics of the non-reacting single and double annular jet (an outer annular jet with a co-axial inner air jet) was investigated by Chigier and Beér [2] in 1964 to characterize the velocity fields, particularly within the bluff body recirculation zone where a flame would be expected to stabilize. This study involved an annular jet of 9.52cm outer diameter by 6.35cm inner diameter. Measurements were made using Pitot probes, limiting measurements to mean velocities and pressures only. The general flow features of the annular jet are illustrated in Figure 2.1. In 1971, Davies and Beér[3] reported on a study of the wake region of the free annular jet under non-reacting conditions, this time using a hot wire anemometer system to obtain turbulent velocity data. This study examined the annular jet resulting from air flow emerging from an annular passage formed by a variety of objects located coaxially within a 15.24cm diameter nozzle, producing blockage ratios ranging from 0.11 to 0.54. Turbulent intensities in excess of 50% were reported within the recirculation zone.

Subsequent studies by Durão and Whitelaw [4] and Taylor and Whitelaw [5] examined the wake region formed by an annular jet produced by a disk coaxially located at the discharge of a pipe using a laser Doppler anemometer, again under non-combusting conditions. The Durão and Whitelaw study examined the annular jet resulting from a variety

of disks coaxially located within a discharge nozzle 2.0cm in diameter. Blockage ratios ranged from 50% to 20%, and Reynolds numbers from 8600 to 22700, based on bluff body diameter. Measurements indicated that the flow in the recirculation region close to the bluff body is strongly anisotropic, with minimum turbulent inensities of 30%. Continuation of this study by Taylor and Whitelaw [5] using larger annular passages (5.03cm outer diameter with bluff bodies ranging from 2.54 to 3.56cm diameter) found similar turbulent intensities and strong anisotropic behaviour in the recirculation zone. An attempt by Pope and Whitelaw[6] to numerically model the wake region of a non-reacting annular jet using a k-ϵ model, as well as two forms of a Reynolds stress model, did not produce results in agreement with measurements, suggesting that models available at the time of the study were insufficient to model this complex, non-isotropic flow. It is therefore likely that numerical simulation of an annular air jet interacting with a liquid spray under reacting conditions will require, among other things, significant new advances in turbulence modelling.

The annular jet with a co-flowing fuel jet or spray has been studied by several researchers. Li and Tankin[7] performed a photographic investigation of reacting and non-reacting flows around a bluff body, using a propane jet coaxially located within an annular air jet. This study examined annular jets issuing from an annular passage 5.32cm outside diameter by 4.52 and 3.85cm inside diameter. The central fuel jet had diameters ranging from 6.35 to 12.7mm. A tapered nozzle configuration was also used in this work. Many features of the flow, including visible flame shape, recirculation zone length, and influence of fuel jet momentum on the recirculation zone were investigated. An analytical model for predicting the length of the recirculation zone in the pure annular flow case as well as the co-flowing, non-combusting jet case was also developed.

In 1989, Li and Tankin[8] performed a similar study, this time examining photographically the interaction of a non-reacting liquid spray with the annular jet. The geometries tested consisted of an inner bluff body 2.54cm in diameter coaxially located within outer annular passage of 3.56, 4.44 and 5.08 cm diameter, respectively. This study showed that the annular air jet greatly influences the spray pattern, widening the spray cone angle in the recirculation zone, and tending to confine droplets outside the recirculation zone to a

narrow region, a feature noteworthy in that many practical combustors require confinement to prevent droplet impingement on combustor walls.

The advent of phase Doppler interferometry introduced a powerful tool in examining liquid spray/air flows. McDonnell *et al*[9][10][11][12] performed extensive studies of non-reacting and reacting methanol spray flames, measuring droplet diameter and velocity distributions as well as temperature and hydrocarbon concentrations. Droplet size and velocity were measured using phase Doppler interferometry, and temperature using thermocouple. Hydrocarbon concentration was measured using infrared extinction/scattering (IRES), a line-of-sight measurement technique that requires deconvolution to obtain spatially resolved data. These studies were conducted using a specially built research-grade atomizer that could be operated as a pressure-swirl atomizer or an air-assisted atomizer. As well, flame stabilization could be achieved through swirl and/or bluff body stabilization.

Friedman and Renksizbulut [13] investigated the interaction of an annular air jet on a non-reacting water spray, using a single component phase Doppler interferometer system. The geometry studied consisted of an inner 2.54cm diameter cylinder mounted concentrically within an outer 3.17cm diameter nozzle, with a pressure-swirl atomizer located at the tip of the inner bluff body. Measurements included droplet diameter and velocity, as well as gas-phase velocity and liquid volume flux measurements. High turbulent intensities were noted within the recirculation zone, but data rates of small seed particles were insufficient to extract many turbulent parameters. Experiments by Saumweber *et al* [14] using the same nozzle used in this work and a dyed water spray demonstrated a technique for enhancing visibility of seed particles, and allowed extraction of turbulent energy spectra and integral scales at some locations in the flow, even in the presence of large spray droplets.

Hardalupas *et al*[15] investigated bluff-body stabilized kerosene spray flames using a confined disk as bluff body. These experiments were conducted using two different sizes of disk (4.38cm and 3.16 cm) co-axially located within a 5.08cm diameter tube. In some of the tests, a diffuser was used to help stabilize the flame. The spray nozzle used was an air-blast atomizer producing a 30° spray cone. Measurements of droplet velocity and diameter were made using a phase Doppler interferometer system. Gas phase velocities were inferred

by post-processing diameter-velocity data to examine only velocities observed for droplets below 10μm, which were shown to accurately follow the gas phase flow only in certain regions of the flame. No turbulence parameters were reported, likely due to the difficulty of obtaining sufficient counts of small particles in the presence of large droplets. Temperatures were measured using thermocouples in one geometry only (with diffuser), that resulted in the low spatial droplet densities required for successful thermocouple use. These studies, though extensive, do not present complete pictures of combusting sprays. In the case of the studies done by McDonnell *et al* [9-12], locations of reaction zones are not identified, while the study by Hardalupas *et al* [15] does not provide complete gas phase velocity profiles, reaction zone location or hydrocarbon concentration. In addition, temperature measurements are intrusively made using thermocouples, and are limited to locations where the probability of droplet impingement on the thermocouple is low.

Recently, some researchers have begun to use planar laser-induced fluorescence techniques to produce two dimensional species concentration maps in spray flames. Allen and Hanson [16] successfully imaged OH, CH and fuel vapour in a heptane/air spray flame, using an ArF excimer laser and an intensified charge-coupled device (ICCD) camera, allowing accurate determination of reaction zone location on an instantaneous and time-averaged basis. The CH images provided information on the location and structure of the reaction zone, while OH images provided information on both reaction zone location and location of hot products of combustion. The system used was an air-atomized nozzle, with n-heptane fuel, at low flow rates and with fine atomization. Allen *et al*[17] imaged OH and fuel fragments using planar LIF in a spray flame with heptane, methanol and ethanol fuels at pressures ranging from 0.1 to 1 MPa, but reported only qualitative results with regard to OH concentration, as the main thrust of this work was to examine the effects of pressure on the fluorescence signal. Goix *et al* [18] and Stepowski *et al* [19] used both phase Doppler interferometry and planar laser-induced fluorescence of OH in a methanol spray flame to provide detailed mapping of OH in the reaction zone, as well as droplet trajectory and size distributions; the only reported study found combining both these techniques to characterize spray flames. No attempt was made to map the temperature field in either study. These studies examined a rocket-style atomizer,

using a high velocity, small annular air jet to atomize a co-axial fuel jet. The fuel jet was 2mm diameter, and the annular jet was 3.4mm x 2.5mm, with jet velocities in the range of 70 m/s..

Beyond these studies, there does not appear to have been much work done in applying LIF techniques to spray flames, likely due to the complications imposed by the presence of droplets in the optical field and the unsteady nature of the flame. As well, it is only recently that spectroscopic techniques such as LIF have emerged from chemistry labs as tools for engineering studies. In addition, LIF temperature mapping techniques, which could provide valuable information when applied to spray flames, are difficult to apply in unsteady flows even with clean flames, and do not appear to have been attempted in spray flames.

2.2. Summary

There has been a considerable amount of research done on single phase, isothermal annular jets, particularly examinations of the velocity fields within the recirculation zone. These studies have included experimental approaches using Pitot tubes, laser Doppler velocimetry, hot wire probes and photographic flow visualization, and are summarized in Table 2.1. An attempt to model this high turbulent intensity flow did not produce results in agreement with experiment. There has also been some activity investigating this geometry in conjunction with reacting and non-reacting sprays, using PDI as well as photographic techniques. The presence of a spray, whether reacting or non-reacting, limits the range of experimental techniques that can be applied, since many intrusive techniques such as hot wire anemometry and Pitot probes will not give reliable results under spray conditions. PLIF has been proven as an effective investigative technique in the hostile environment of a spray flame, but has only recently begun to be applied to practical combustion systems. Only two related investigations [18-19] have been reported where both PDI and PLIF have been applied to a spray flame.

Reference	Geometry	Conditions	Measurements	Diagnostics Used
Saumweber, Friedman and Renksizbulut (1997) [14]	Pressure/swirl atomizer in annular jet	Non-reacting, non-evaporating dyed water spray	U, V, u′, v′, shear stress, integral scale, turbulent spectra	2D-PDPA
Allen, McManus, Sonnenfroh and Paul (1995) [17]	Pressure/swirl atomizer in slow annular flow	Reacting heptane, ethanol and methanol	[OH] and [hydrocarbon fragments]	PLIF (imaging only)
Stepowski, Cessou and Goix (1994) [19]	Air-atomized fuel jet in annular jet	Reacting methanol	U, V, u′, v′ D_{10}, D_{32}, Volume flux [OH]	2D-PDPA PLIF
Friedman and Renksizbulut (1994) [13]	Pressure/swirl atomizer in annular jet	Non-reacting, non-evaporating water spray	U, D_{10}, D_{32}, Volume flux	1D-PDPA
Hardalupas, Lui and Whitelaw (1994) [15]	Spray in wake of confined disk	Reacting kerosene	U, V, u′, v′ D_{10}, D_{32}, Volume flux, T	1D-PDPA Thermocouple
McDonnell, Adachi and Samuelsen (1992-1994) [9-12]	Pressure/swirl atomizer in slow annular flow	Non-reacting and reacting methanol	U, V, u′, v′, D_{10}, D_{32}, Volume flux, Vapor concentration, T	2D-PDPA Infrared extinction/scattering Thermocouple
Li and Tankin (1989) [8]	Spray in annular jet	Non-reacting, non-evaporating water spray	Gross flow features	High speed video
Li and Tankin (1987) [7]	Double annular jet	Propane inner jet in an annular air jet, reacting and non-reacting	Stagnation point location Gross flow features	Photographic (laser sheet illumination)
Allen and Hanson (1986) [16]	Spray in quiescent air	reacting heptane	[OH], [CH], [Fuel vapor] (qualitative)	Planar laser-induced fluorescence (PLIF)
Taylor and Whitelaw (1983) [5]	Wake region of confined disk	Non-reacting air jet	U, V, W, u′, v′, w′	1-D LDV
Durão and Whitelaw (1977) [4]	Wake region of an annular jet	Non-reacting air jet	U, V, W, u′, v′, w′	1-D LDV
Davies and Beér (1971) [3]	Wake region of an annular jet	Non-reacting air jet	U, V, W, u′, v′, w′	Hot wire anemometer
Chigier and Beér (1964) [2]	Double annular jet	Non-reacting air jet	U, V, W	Pitot probes

TABLE 2.1: Summary of published annular jet research

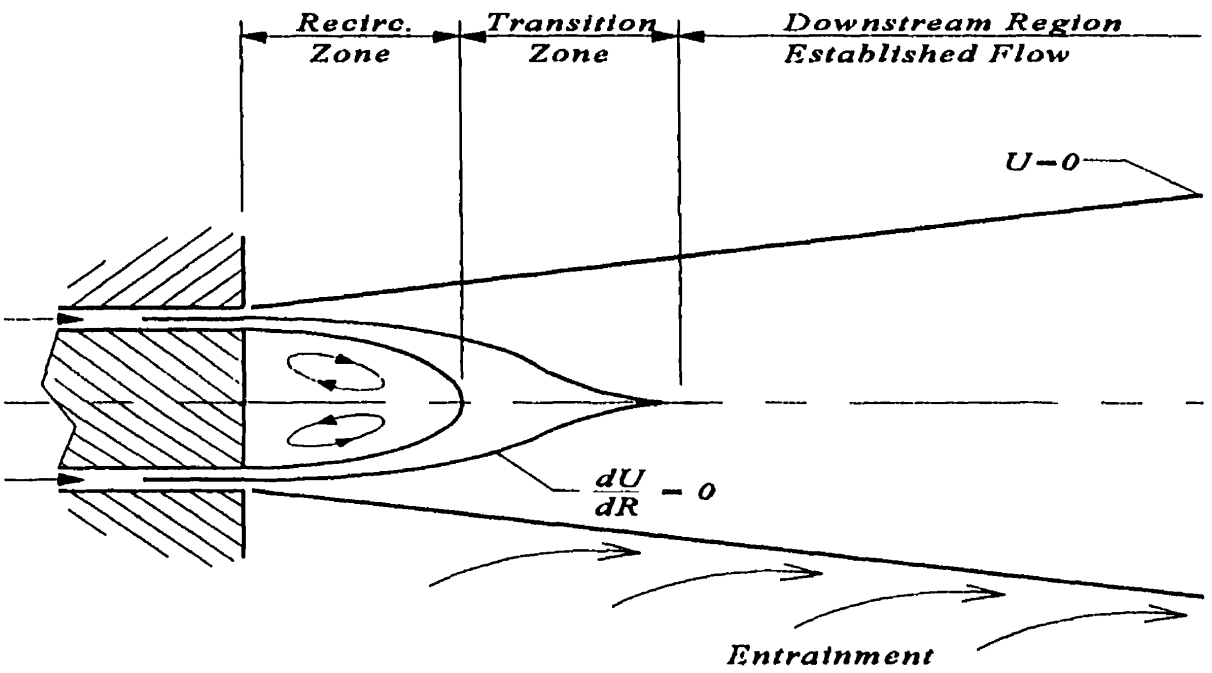


FIGURE 2.1: Annular jet flow features

CHAPTER 3

Phenomenological Discussion

3.1. The Annular Jet

Investigations of the wake region of an annular jet without any co-flow have revealed several flow features, previously shown in Figure 2.1. Humphries and Vincent [20] describe the near wake region of an annular jet as being strongly influenced by the free shear layers caused by the flow separation at the bluff body. These shear layers become turbulent a short distance downstream, and subsequent turbulent mixing entrains fluid from the region behind the bluff body. The resulting low pressure region draws the shear layers in toward the longitudinal axis of the jet, forming a "bubble" enclosing a relatively stable mean vortex ring. Turbulent intensities in this region, generally referred to as the recirculation zone, have been measured by Humphries and Vincent [20], Davies and Beér [3], Duraõ and Whitelaw [4] and others, and have been found to exceed 40% for Reynolds numbers (based on bluff body diameter and area-averaged jet velocity) in the 20,000 - 100,000 range. These turbulent intensities were measured under non-reacting conditions, and will not necessarily be comparable to a similar, but reacting, flow. Turbulent intensities are generally reported based on area averaged mean annular jet exit velocity, since the standard definition, based on local mean velocity, breaks down when the local mean velocity is zero, which does occur in the region near the end of the recirculation zone.

These studies have also shown that the flow in the recirculation zone is highly anisotropic, tending to isotropy farther downstream, beyond the recirculation zone. Mean axial velocity measurements along the centreline of the jet have shown strong negative velocities within the recirculation zone, which then rapidly increase to strong positive velocities downstream of the recirculation zone. The centreline velocity reaches a maximum approximately 2-3 bluff body diameters downstream, then slowly decays in a manner similar

to that measured in a round jet. Axial centreline mean strain rates in excess of 4000 (m/s)/m have been measured near the end of the recirculation zone. Radial mean strain rates have been reported by Friedman and Renksizbulut [13] to exceed 10000 (m/s)/m in the recirculation zone.

Most investigators define the recirculation zone length, L_{RZ} as the Z co-ordinate at which the mean axial velocity passes through zero. It has been found that the recirculation zone length is not significantly influenced by annular jet velocity, and is approximately one bluff body diameter in length, depending somewhat on the annular width.

Investigations into annular jet flows with a non-reacting co-axially located spray by Li and Tankin [8] and Friedman and Renksizbulut [13] have shown the same general features. In both these studies, the momentum ratio of the annular air jet to the liquid spray was high, so the air flow field was not strongly affected by the presence of the spray. On the other hand, the annular air jet strongly influenced the spray field by altering the spray droplet trajectories preferentially, with smaller droplets influenced more than larger, high momentum ones. The redistribution of droplets had the effect of widening the emerging spray cone angle somewhat, and entraining smaller particles back to the centreline of the flow. It was suggested that this redistribution could have a profound influence on flame characteristics if this geometry were examined under reacting conditions. Similar work by Saumweber *et al* [14] on a larger annular jet arrangement showed similar trends. Figure 3.1 illustrates the effect of the annular jet on the spray field under non-reacting conditions. Without spray, the annular air jet induces a stable mean vortex ring (dotted lines) and strong negative velocities on the flow centreline in the region close to the nozzle, defining a recirculation zone. With spray on, in the region close to the spray nozzle, the droplet momentum and number density are high, and tend to decelerate the reverse flowing air, which has the effect of displacing the vortex rings downstream (solid lines).

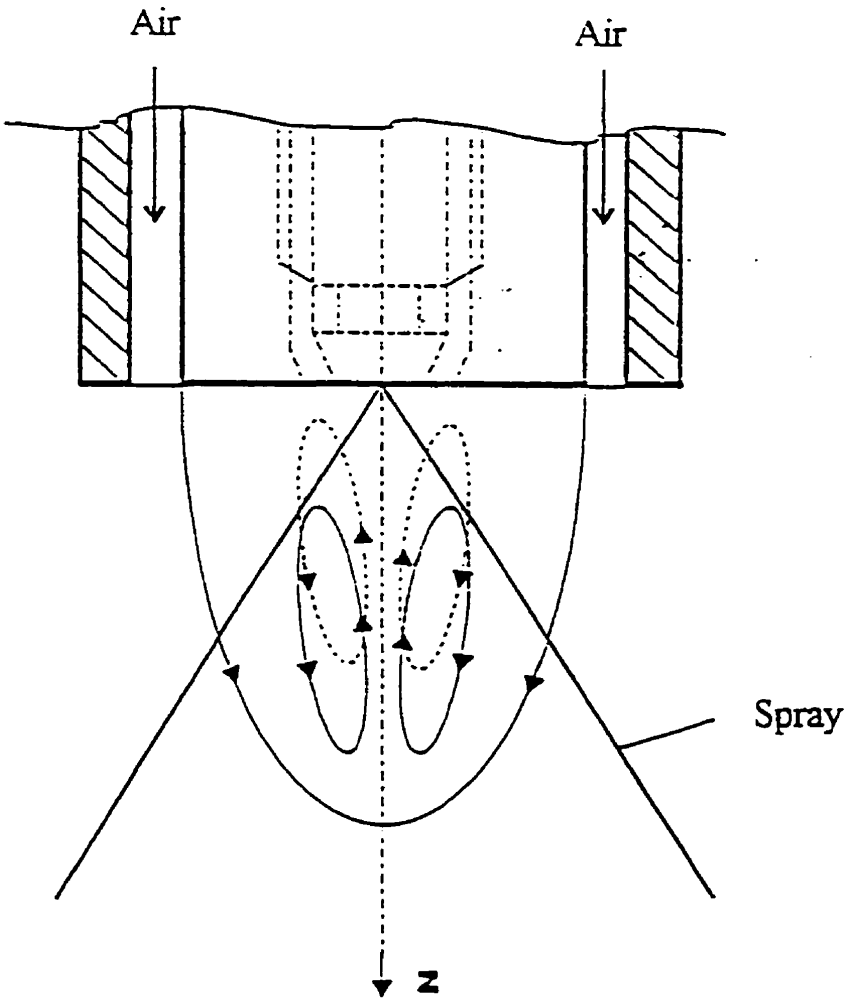


FIGURE 3.1: Annular air jet with spray flow features

3.2. The Atomizer

The atomizer used in this study is a standard pressure-swirl atomizer manufactured by Delavan, shown schematically in Figure 3.2. This type of atomizer produces a spray by forcing a swirling liquid flow through an orifice, which produces a conical sheet on discharge. This conical sheet then becomes unstable, first forming ligaments and then individual droplets of various sizes. Interactions with the surrounding air field then disperse the droplets through space, and can even enhance the atomization process through secondary droplet break-up at high Weber numbers.

A number of mechanisms are thought to be involved in the disintegration of the conical sheet into a spray [21]. The initial formation of the conical sheet is influenced mainly by its initial velocity and fluid properties. Surface tension forces tend to contract the sheet, opposing momentum and centrifugal forces associated with the liquid velocity. A low initial velocity will not allow a conical sheet to form, instead forming a hollow "tulip" shape at the orifice exit which is then drawn in by surface tension forces to form a round jet or large individual drops. As velocity increases, the conical sheet forms, expands and lengthens until a leading edge is formed, where equilibrium exists between the surface tension and inertial forces. The conical sheet subsequently disintegrates by several modes. Fraser and Eisenklam [22] identified three modes of sheet disintegration, described as rim, perforated sheet and wave sheet disintegration. Rim disintegration occurs when the leading edge of the conical sheet thickens in to a rounded rim due to surface tension forces, then breaks up in a manner similar to a free jet, as described by Lefebvre [21]. This mode of disintegration is dominant when the surface tension and viscosity of the fluid are relatively high, and tends to form large droplets. Perforated sheet disintegration occurs when holes form in the conical sheet, enclosed by rims containing the fluid that was initially contained within the hole. These holes rapidly grow, and coalesce with adjacent holes forming ligaments of irregular size that then disintegrate in to drops of varying size. Wave disintegration can occur in the absence of perforations through the propagation of wave motion in the liquid sheets. Areas of the sheet, corresponding to a half or full wavelength of the disturbance, are torn away. These areas contract due to surface tension, and disintegrate through interaction with the air to form

droplets. This process is graphically illustrated in Lefebvre [21].

Pressure-swirl atomizers generally exhibit all three modes of sheet disintegration, resulting in a fairly wide range of droplet sizes. Further interaction with the air field may or may not enhance the atomization process, depending on the fluid properties and the relative velocities of the droplets and air field. Aerodynamic interactions are characterized by the Weber number, which is the ratio of aerodynamic forces acting on the droplet to surface tension forces. As long as surface tension forces exceed the aerodynamic forces, the droplet will remain intact. The Weber number is given by:

$$We = \frac{\rho_g U_R^2 D}{\sigma} \qquad \textbf{3.1}$$

where: We = Weber number

ρ_g = Air density

U_R = Relative velocity between air and drop

D = Drop diameter

σ = Liquid surface tension in air

For free-falling drops, Hinze [23] estimated the critical Weber number, We_c, for drop breakup to be approximately 22, and for a drop suddenly exposed to a high velocity stream, $We_c \approx 13$.

Sprays also interact with the airfield in a manner that does not produce droplet breakup, but does involve momentum and mass exchange between the droplet and the gas phase. Momentum transfer is accomplished primarily via droplet aerodynamic drag, wherein force is exerted on the droplet by the fluid (or vice versa) whenever a velocity difference exists. The equation relating drag force to relative velocity is given by:

$$F_D = \frac{\pi}{8} C_D \rho_g D^2 U_R^2 \qquad \textbf{3.2}$$

where: F_D = Drag force

C_D = Drag coefficient

ρ_g = Gas density

D = Droplet diameter

U_R = Relative velocity between droplet and gas

At low rates of evaporation and Weber number, the drag coefficient, C_D, is a function of the droplet relative Reynolds number, given by:

$$Re_R = \frac{\rho_g U_R D}{\mu_g} \qquad \textbf{3.3}$$

where: Re_R = Relative Reynolds number

U_R = Relative velocity between droplet and gas

D = Droplet diameter

ρ_g = Gas density

μ_g = Gas absolute viscosity

One of the simplest droplet drag coefficient correlations, agreeing with experimental data within 2% over the range $3<Re_R<400$ is given by [27]:

$$C_D = \frac{24}{Re_R}\left(1 + \frac{Re_R^{2/3}}{6}\right) \qquad \textbf{3.4}$$

There is some expectation that turbulence influences the drag coefficient. Several investigations into the effects of turbulence on the drag coefficient are cited in reviews by Bearman and Morel [24], among others. There is no quantitative agreement between existing studies, and little data exists in the Reynolds and Weber number ranges relevant to spray combustion. Recent experiments conducted by Warnica [25] and Omielan [26] suggest some drag coefficient dependence on turbulence, but the effect does not appear to be strong.

The effect of aerodynamic drag on the velocity and trajectory of a particle is

dependent not only on the drag force, but also on the inertia of the particle. The manner in which a particle reacts to changes in flow velocity can be characterized by its relaxation time. For droplets, the relaxation time to reach 63% of its terminal velocity when subjected to a step change in relative velocity is given by [27]:

$$\tau_D = \left(\frac{4}{3} \right) \left(\frac{\rho_p}{\rho_g} \right) \left(\frac{D}{C_D U_R} \right) \qquad \textbf{3.5}$$

where: τ_D = Droplet relaxation time

ρ_g = Gas density

ρ_p = Droplet density

D = Droplet diameter

C_D = Drag coefficient

U_R = Relative velocity between droplet and gas

Typically, a water droplet in the 30 μm diameter range with an initial relative velocity of 10 m/s would have a relaxation time of around 1 ms in air. A useful measure of whether a droplet will be strongly influenced by a velocity field is to determine the local Stokes number, the ratio between the local flow timescale to the droplet timescale. The mean Stokes number is defined by:

$$St_m = \frac{\tau_F}{\tau_D} \qquad \textbf{3.6}$$

where: St_m = Mean Stokes number

τ_F = Local mean flow timescale

τ_D = Droplet relaxation time

The mean flow timescale is defined by:

$$\tau_F = \frac{L_C}{U_C} \qquad 3.7$$

where: τ_F = Local mean flow timescale

L_C = Local flow characteristic length

U_C = Local flow mean velocity

As long as the Stokes number is small, the flow will not strongly influence the droplet trajectory. Many other Stokes numbers are useful, including the turbulent Stokes number, defined as the ratio of the turbulent timescale to the droplet relaxation time. Stokes number considerations are particularly important in determining the size of seed particles required for the measurement of instantaneous flow velocity using phase Doppler interferometry.

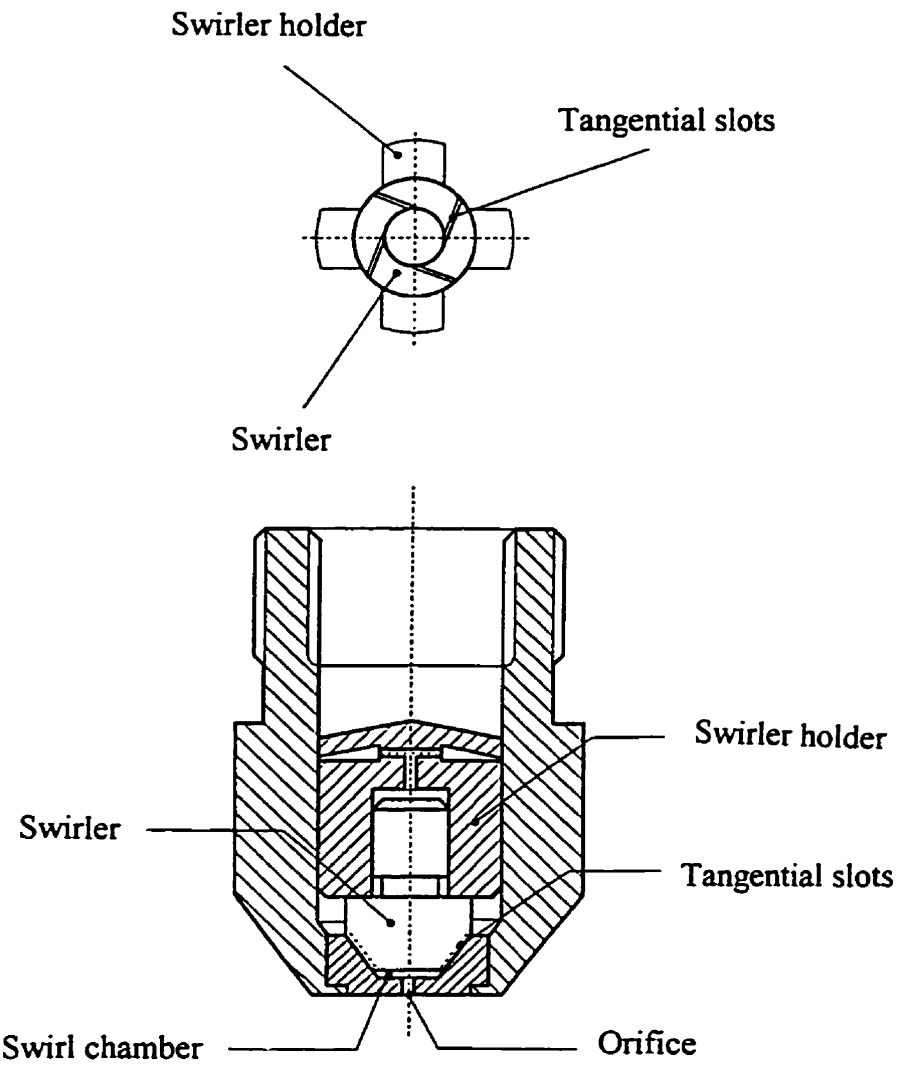


FIGURE 3.2: Pressure-swirl atomizer

3.3. Droplet Statistics

In most sprays, there is substantial variation of drop size spatially and temporally. It is therefore convenient to apply statistical analysis to sprays to characterize the mean droplet size distribution of the spray. Several mean diameters are often used, with the general form as shown below:

$$D_{pq} = \left[\frac{\sum n_i D_i^p}{\sum n_i D_i^q} \right]^{\frac{1}{(p-q)}} \qquad \textbf{3.16}$$

where: p, q = Exponents

n_i = Number of drops in size class i

D_i = Mean droplet diameter in size class i

The following table lists some of the commonly used mean diameters.

SYMBOL	p	q	NAME	APPLICATION
D_{10}	1	0	Arithmetic mean diameter	Spray comparisons
D_{20}	2	0	Area mean diameter	Surface area dependent processes
D_{30}	3	0	Volume mean diameter	Volume, mass dependent processes
D_{32}	3	2	Sauter mean diameter	Mass transfer, reactions (combustion)

TABLE 3.1: Droplet mean diameters typically used

The arithmetic mean diameter, D_{10}, is the arithmetic average drop size in a distribution, and is useful for comparing different sprays, or different regions within the same spray. However, since surface area of a drop scales with diameter squared, and volume (and mass) scale with diameter cubed, the arithmetic average drop size is often not appropriate to use when

considering processes which depend on total spray surface area, such as evaporation. For these cases, the Sauter mean diameter is often used, since it characterizes the mean drop size based on the ratio of mass (or volume) to surface area, an important ratio for reacting and evaporating processes such as combustion. When surface diffusion and evaporation control the overall reaction rate, decreasing the Sauter mean diameter will increase the reaction rate by increasing the surface area of reactant per unit mass.

Another useful tool in assessing a spray distribution is the use of distribution models. There are many distribution models available, some of which have been found to match spray distributions reasonably well. The log-normal distribution is a two parameter model, which models some sprays quite well, and is easy to manipulate mathematically. It is expressed as follows:

$$df = \frac{1}{\sqrt{2\pi}\, D \ln(\sigma_g)} \exp\left[- \frac{(\ln D - \ln D_g)^2}{2 \ln(\sigma_g)^2} \right] dD \qquad \textbf{3.17}$$

$$D_g = \exp\left[\frac{\sum_i n_i D_i}{N} \right] \qquad \textbf{3.18}$$

$$\sigma_g = \exp\left[\sqrt{\frac{\sum_i n_i (\ln D_i - \ln D_g)^2}{N-1}} \right] \qquad \textbf{3.19}$$

where: df = Fraction of droplets with diameter between (D-dD/2) and (D+dD/2)

dD = Width of size range

D = Diameter

σ_g = Geometric standard deviation

D_g = Geometric mean diameter

n_i = Number of drops in ith size class

D_i = Diameter of ith size class

N = Total number of droplets

It should be noted that the integral of df from D=0 to D→∞ is 1. The log-normal model requires only two parameters, σ_g and D_g, to completely describe the size distribution. Another two-parameter model commonly employed in describing sprays is the Rosin-Rammler distribution model, originally developed to classify pulverized coal particle size distributions. The Rosin-Rammler model is given by:

$$Q = 1 - \exp\left[-\left(\frac{D}{X}\right)^q\right] \qquad \textbf{3.20}$$

where: Q = Fraction of total volume (or mass) contained in drops of diameter larger than D

X = Rosin-Rammler mean diameter

q = Rosin-Rammler distribution parameter

The Rosin-Rammler is extremely simple mathematically, and is best suited when mass or volume information is desired. Figure 3.3 illustrates the shapes of the Rosin-Rammler and log-normal distribution models. As can be seen, the log-normal distribution has a longer large diameter tail than the Rosin-Rammler distribution, but overall, the distribution shapes are similar.

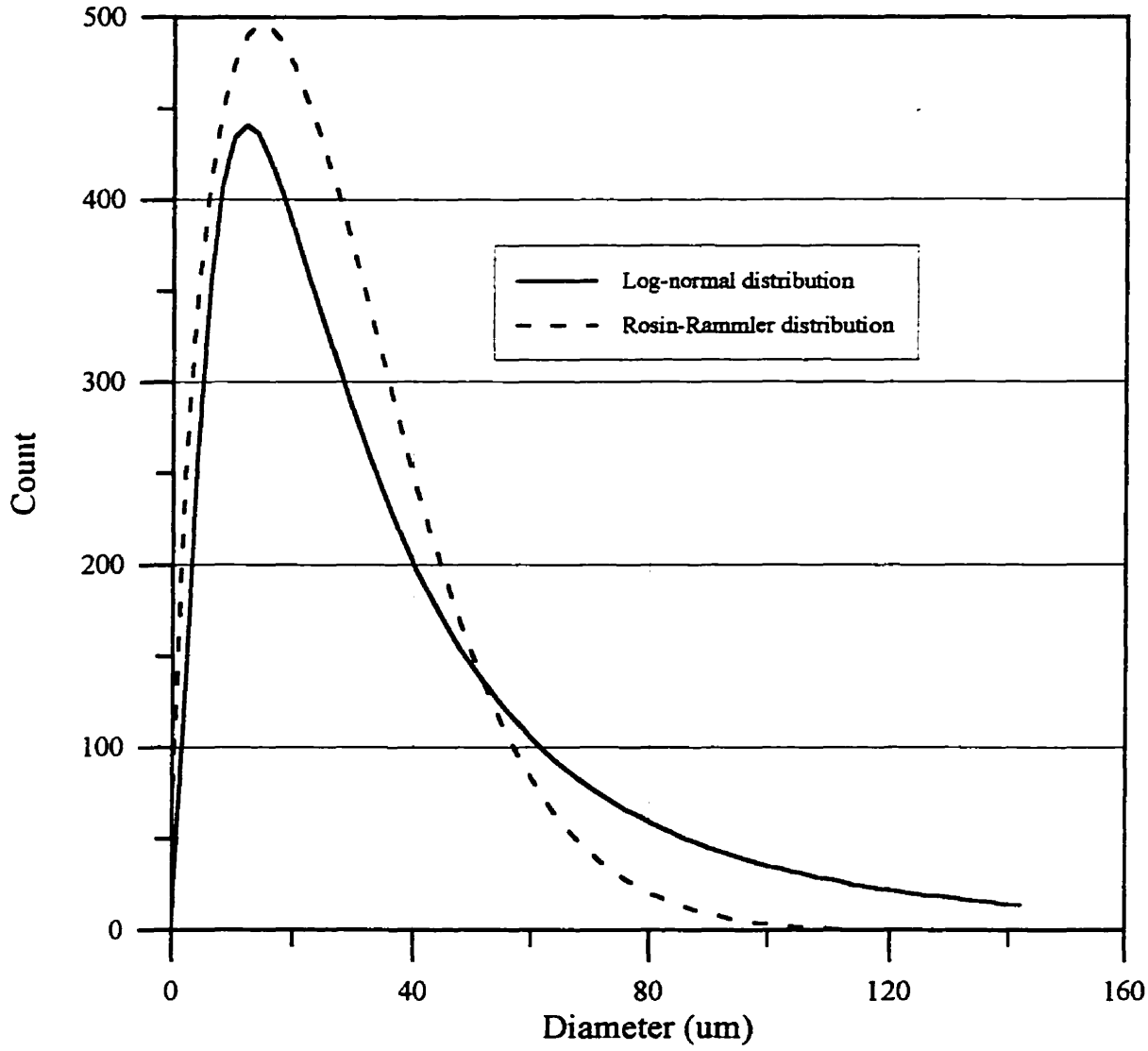


FIGURE 3.3: Comparison of log-normal (σ_g = 2.5 μm, D_g = 30 μm) and Rosin-Rammler (X = 30μm, q = 1.5) distributions

3.4. Combustion

The combustion of hydrocarbon fuels involves the rapid oxidation of the fuel to produce various combustion products, as well as heat. In this study, the fuel used was methanol, CH_3OH. The global reaction for the stoichiometric oxidation of methanol is given by:

$$CH_3OH + 1.5\,O_2 \rightarrow CO_2 + 2\,H_2O + 639.4\,kJ \qquad \textbf{3.21}$$

In actual fact, the combustion of any fuel is much more complicated. A more appropriate global reaction for methanol oxidation in air would be:

$$CH_3OH + \frac{3}{2}O_2 + 5.66\,N_2 \rightarrow a\,CO_2 + b\,CO + c\,H_2O + d\,N_2 + e\,NO + \ldots. \qquad \textbf{3.22}$$

where a, b, c etc are the stoichiometric coefficients of each species produced. The dominant species will be those expected from Equation 3.21 (CO_2 and H_2O), but pollutants and unburned hydrocarbons such as NO and CO will be produced in amounts strongly dependent on the combustion conditions. It should be noted that the oxidation process does not occur in one step as suggested by the global reaction noted above. In fact, many elementary reaction steps are involved, producing intermediate radicals such as CH and OH that propagate and/or terminate the reaction chain. Westbrook and Dryer [28] compiled a detailed chemical kinetic mechanism for the oxidation of methanol that involved 84 elementary reactions and 26 chemical species. The reaction rates of many of these elementary reactions are unknown or poorly known, hence comprehensive reaction modeling is difficult.

At high temperatures, substantial dissociation of combustion products occurs, such that the species composition of the products of combustion at flame temperatures is quite different than at the final, cooler exhaust temperature. In this study, the hydroxyl radical, OH, is detected and imaged. This radical is involved in 28 of the 84 reaction steps identified by Westbrook and Dryer [28] and thus should be present in relatively high concentration in the reaction zone. In addition, the hot products of combustion contain significant amounts of water, which can dissociate at high temperatures to form the hydroxyl radical. Thus, detection

of OH in a spray flame serves as a good marker of the reaction zone and location of hot products of combustion. Figure 3.4 shows the relative hydroxyl radical concentration versus temperature for stoichiometric combustion of methanol, as calculated using the Olikara and Borman code, supplied with [29].

As can be seen, the concentration of the OH radical increases sharply with temperature, beginning around 1600K. In a diffusion flame, with steep temperature gradients across the reaction zone, the equilibrium concentration of OH falls off sharply as the temperature drops. Therefore, although some OH persists beyond the reaction zone, it disappears rapidly, and thus serves as a good reaction zone marker. In premixed flames, or in flames in insulated or very hot environments where steep temperature gradients across the reaction zone do not occur, OH concentration serves as a good marker of product of combustion flow, but not necessarily reaction zone location.

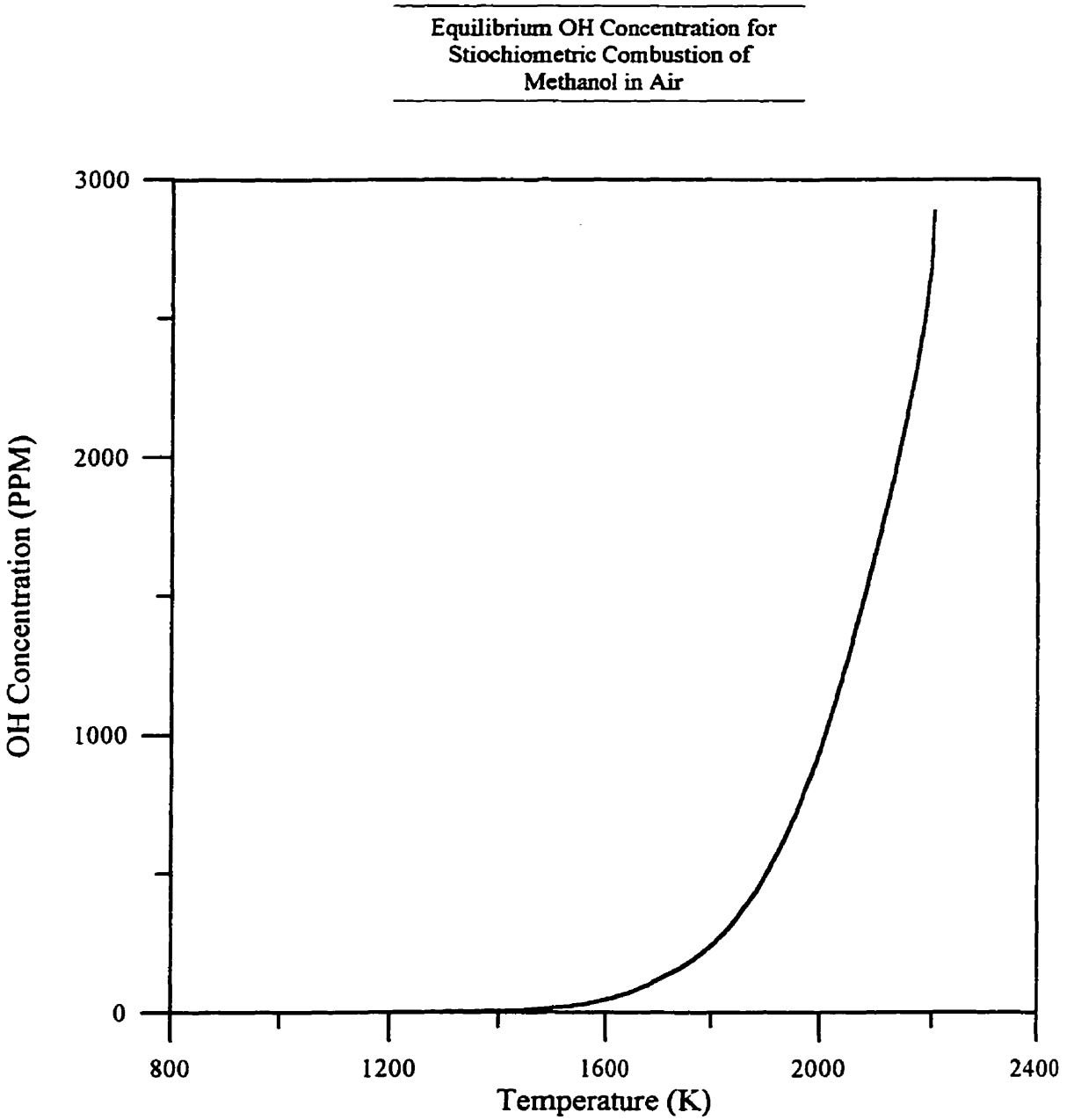


FIGURE 3.4: OH equilibrium concentration as a function of temperature for stoichiometric combustion of methanol

3.5. Combustion of Practical Sprays

The combustion of practical sprays is an extremely complicated phenomenon. The previously presented theory regarding droplet combustion was based largely on quasi-steady assumptions, and single droplet scenarios in quiescent environments. Practical spray flames generally involve the interaction of a spectrum of droplet sizes in a highly turbulent environment, which influences everything from droplet trajectory to reaction rate. In addition, quasi-steady conditions do not really exist, as droplets are constantly changing in size and temperature as they pass through turbulent eddies of hot gas. Droplets initially injected into the flow at high relative velocity are slowed due to aerodynamic forces, and are thus exposed to constantly varying Reynolds number conditions throughout their lifetimes.

In light of the complexity of real spray combustion systems, theoretical modeling is extremely difficult. Nonetheless, a considerable amount of experimental work has been done examining these flows, and certain phenomena have been identified. Chigier *et al* [30] examined the detailed structure of a bluff body stabilized kerosene spray flame, and identified several phenomenon, as shown schematically in Figure 3.5. In this configuration, a recirculation zone in the wake of the bluff body entrains small particles which quickly evaporate, producing a region rich in fuel vapour. At the zero velocity boundary between the recirculation zone and the external air flow, a primary reaction zone stabilizes just outside the spray sheath, providing hot conditions conducive to rapid fuel evaporation. The bulk of the fuel spray emerges from the recirculation zone, with the largest particle trajectories largely unaffected due to their high momentum to drag ratios. Smaller particles are deflected by the recirculating flow and external flow, and tend to follow the external flow streamlines towards the flow axis. A second, larger reaction zone is set up just downstream of the recirculation zone, with hot products of combustion convecting downstream, providing heat to vaporize the spray droplets. Oxygen from the surroundings is entrained into this region, supporting combustion. Measurements made under non-reacting conditions indicated that significant changes to the flow occur as a result of combustion. Many of the differences are due to the changes in drag forces that arise under combusting conditions due to increases in fluid dynamic viscosity and drag coefficient. No evidence was found suggesting individual droplet

combustion. Measurements of oxygen concentrations showed very low oxygen levels in the recirculation zone and in the spray core. Combustible mixtures could only occur at the spray boundaries and further downstream, where combustible mixtures could occur. Chigier [31] summarized the spray flame stabilization requirements as follows:

> *"The three prime requirements for* [spray] *flame stabilization, i.e. mixture ratios within the limits of flammability, velocities low enough to match burning velocities, and sufficient supply of heat to retain reaction, are found in the primary reaction zone outside the spray boundary. The main combustion is deferred to distances farther downstream where the spray is more dispersed, more oxygen has been entrained from the surrounding airflow, and temperature levels and mixture ratios are within the limits of flammability."*

Turbulence is an important factor in spray flames. As in gaseous diffusion flames, turbulence enhances the mixing of fuel vapour with oxidizer. It also enhances fuel evaporation and droplet dispersion. Heat removal from the reaction zone is also enhanced by turbulence, resulting in cooler mean reaction zone temperatures and more rapid cooling and dispersion of the products of combustion, although enhanced mixing due to turbulence can increase reaction rates and produce higher peak reaction zone temperatures. Lower mean reaction zone temperatures can inhibit the formation of prompt NO_x, but fast thermal quenching of the products of combustion can lead to freezing combustion intermediates such as CO. The influence of turbulence on pollutant formation is strongly dependent on the specific flow configuration of the system.

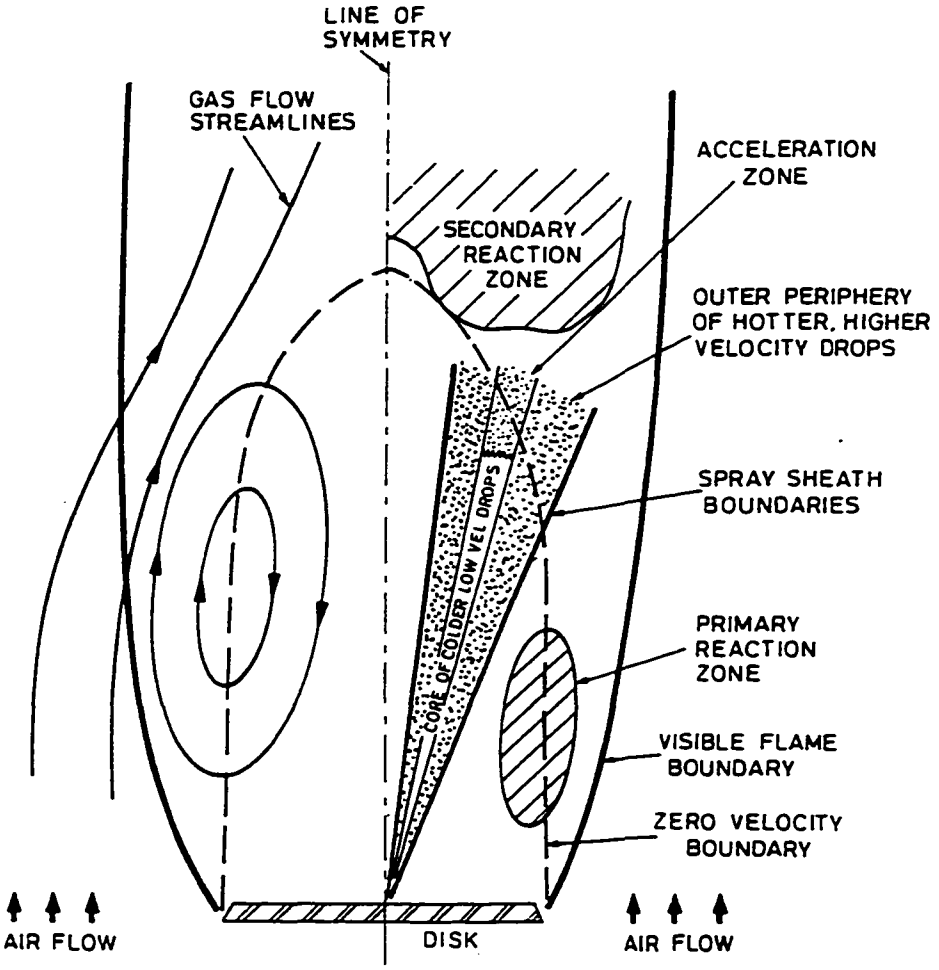


FIGURE 3.5: Typical spray flame features (from Chigier [31])

CHAPTER 4

EXPERIMENTAL SYSTEMS

4.1. PHASE DOPPLER INTERFEROMETRY

The measurement of droplet size has been an ongoing challenge in sprays research for many years. Several commercial instrument systems are available and are reviewed and compared by Dodge [32]. For many years, diffraction-based instruments such as the Malvern 2200 were the standard instrument, and are well described in the literature [33]. Instruments of this type make instantaneous line of sight measurements across a spray by analyzing the diffraction pattern generated by a laser beam traversing the spray. The data reported is generally in the form of best-fit model parameters for a user-selected model type, such as a log-normal or Rosin-Rammler distribution. The returned parameters represent the best fit of that model to the data. If the model chosen is inappropriate for that spray, however, the best fit parameters returned will still represent a poor fit, and derived parameters such as the Sauter mean diameter (D_{32}) will be inaccurate. In addition, the output of the instrument represents a line-of-sight average across the spray, and as such presents no information regarding spatial distribution of drop size and number density. This detail can be obtained through further post-processing, using deconvolution techniques such as the one described by Cormack [34] and Hammond [35].

One major difficulty in applying many of these techniques to sprays is that they depend on clearly defined boundaries, which do not exist in sprays, as the edge of a spray is not a distinct feature. Although diffraction-based instruments do suffer from these disadvantages, they are still widely used due to their relative simplicity and ease of use. In 1975 Durst and Zare [36] presented a method of obtaining spatially resolved simultaneous droplet size and velocity in sprays, which developed into the phase Doppler interferometry systems in use

today. Phase Doppler interferometry allows simultaneous measurement of droplet size and velocity at a point in a spray field, provided that the scattering droplets are spherical and larger than the incident light wavelength. Several comparisons between the two measurement systems have been made, including those by Dodge *et al* [37] and Cossali and Hardalupas [38], and have shown that the phase Doppler technique provides accurate, spatially resolved diameter information, with the additional advantage of providing velocity information. Although complete characterization of a spray is more time-consuming with the phase Doppler technique since many points must be measured, the resulting data set is generally more accurate than that obtained by deconvolution of line of sight measurements, particularly if gradients in the spray field are significant across the width of the laser beam used in diffraction measurements. It should also be noted that diffraction-based instruments such as the Malvern 2600 are difficult to use in combusting flows.

4.1.1. Phase Doppler Interferometry Theory

The Phase/Doppler Particle Analyser is an extension of the Laser Doppler Anemometer (LDA) measuring system, and is well described by Bachalo [39]. The basic theory can most easily be explained using the fringe theory and geometric optics as discussed below.

When two laser beams of the same frequency intersect at an angle, the zone of intersection, when imaged onto a detector, appears as interference fringes normal to the plane of intersection, as shown in Figure 4.1. The spacing of the fringes is related to the angle of intersection of the beams and the laser wavelength as follows:

$$\delta = \frac{\lambda}{2 \sin\left(\frac{\theta}{2}\right)} \qquad 4.1$$

where: δ = Fringe Spacing

λ = Laser Wavelength

θ = Laser Intersection Angle

A particle passing through the region of intersection, or probe volume, passes through the fringes at a rate directly proportional to its velocity component normal to the fringe plane. The frequency of fringe crossings, known as the Doppler frequency, can be measured by monitoring the intensity variation of light scattered by the particle as it passes through the probe volume, and is directly related to velocity. If the fringe plane lies in the X-Y plane, then the Z component of velocity can be found by:

$$f_D = \frac{V_Z}{\delta} \qquad \textbf{4.2}$$

where: δ = Fringe Spacing

V_Z = Z component of Particle Velocity

f_D = Doppler Frequency

One shortcoming of the above is that a particle travelling at a positive V_Z will produce an identical Doppler frequency as one travelling at an equal but negative V_Z. This limitation can be overcome by introducing a frequency shift to one of the laser beams. This causes the fringes to "move" at a frequency equal to the shift frequency, and any particle passing through the probe volume will scatter light with a frequency equal to the Doppler frequency plus the shift frequency if moving against the fringe motion, or the Doppler frequency minus the shift frequency if moving with the fringe motion. The particle velocity is then determined as follows:

$$V_Z = f_D \delta \qquad \textit{where} \qquad f_D = f_m - f_{shift} \qquad \textbf{4.3}$$

where: f_D = Doppler Frequency

V_Z = Z Component of Particle Velocity

δ = Fringe Spacing

f_m = Measured Frequency

f_{shift} = Shift Frequency

The above-described procedure allows accurate determination of particle velocities at a volume in space contained in the intersection of two laser beams. In practice, this volume is small enough that it can be considered a point in space, particularly if the observer views the probe volume through a slit or spatial filter that further limits field of view.

In phase Doppler particle analysis, a droplet's diameter is measured by analysing the phase difference between Doppler bursts as seen from two points in space, as shown in Figure 4.2, which can be shown to be directly proportional to particle diameter assuming the particle is spherical and only one scattering mode dominates at the collection angle selected. The constant of proportionality can be derived from a geometric optics analysis, as summarized by Saffman *et al* [40] for observers symmetrically placed in space, and is given by:

$$\Delta\Phi = \frac{\pi D n_m}{\lambda}(\beta_1 - \beta_2) \qquad \textbf{4.4}$$

For reflected light (p = 0):

$$\beta_1 - \beta_2 = 2\sqrt{2}\left[\left(1 + \sin\frac{\theta}{2}\sin\phi\sin\psi - \cos\frac{\theta}{2}\cos\phi\right)^{\frac{1}{2}} - \left(1 - \sin\frac{\theta}{2}\sin\phi\sin\psi - \cos\frac{\theta}{2}\cos\phi\right)^{\frac{1}{2}}\right]^{\frac{1}{2}} \qquad \textbf{4.5}$$

For first order refracted light (p = 1):

$$\beta_1 - \beta_2 = 4\left(1 + m^2 - \sqrt{2}m\left[1 + \sin\frac{\theta}{2}\sin\phi\sin\psi + \cos\frac{\theta}{2}\cos\phi \right]^{\frac{1}{2}} \right)^{\frac{1}{2}} -$$

$$4\left(1 + m^2 - \sqrt{2}m\left[1 - \sin\frac{\theta}{2}\sin\phi\sin\psi + \cos\frac{\theta}{2}\cos\phi \right]^{\frac{1}{2}} \right)^{\frac{1}{2}} \qquad \textbf{4.6}$$

where: $\Delta\Phi$ = Phase Difference Between Observers

m = Relative Index of Refraction (Droplet/Surroundings)

θ = Beam Intersection Angle

ϕ = Off Axis Angle (See Figure 4.2)

ψ = Elevation Angle (See Figure 4.2)

D = Droplet Diameter

λ = Incident light wavelength

n_m = Index of refraction of surroundings (Air = 1)

The above equations, with $p = 1$, simplify considerably on applying the small angle approximations appropriate for typical systems (ie small ψ and θ) to:

$$\Delta\Phi = \pi\frac{m}{m - 1}\sin\phi\sin\psi\left(\frac{D}{\delta}\right) \qquad \textbf{4.7}$$

where: m = Relative index of refraction

δ = Fringe spacing

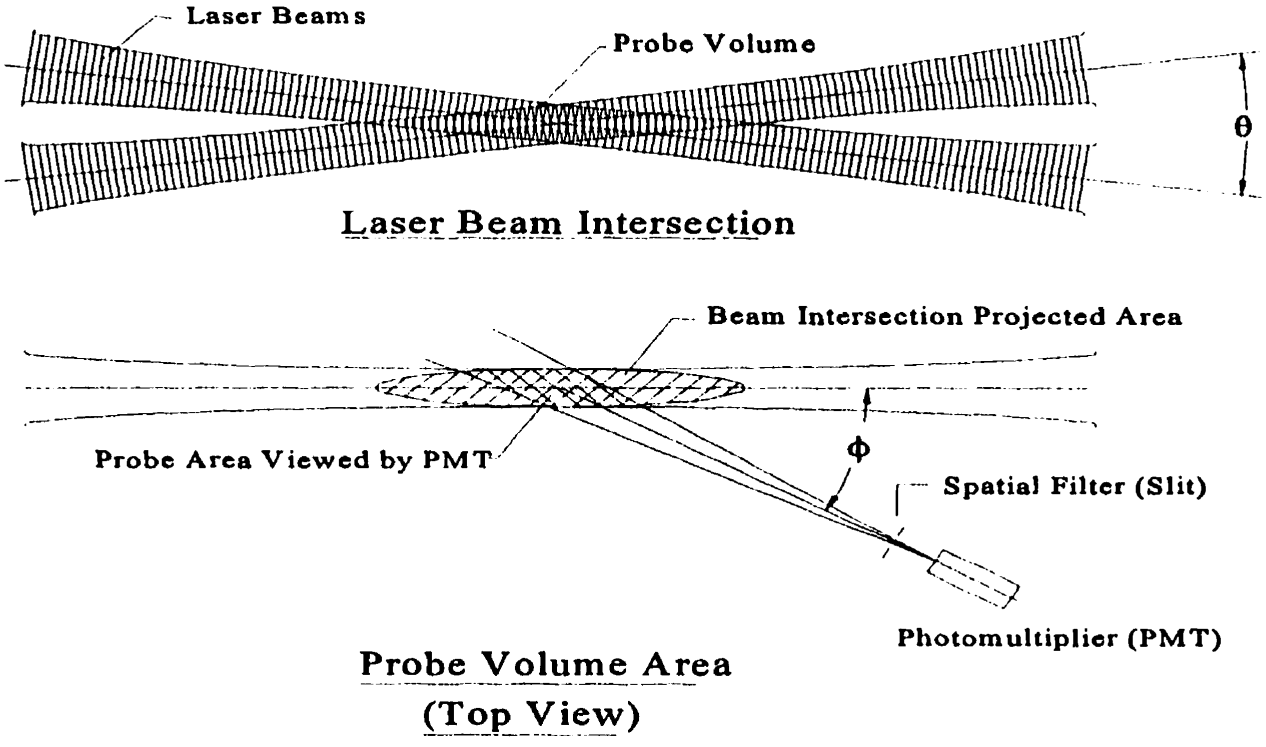


FIGURE 4.1: Intersection of two laser beams to form probe volume

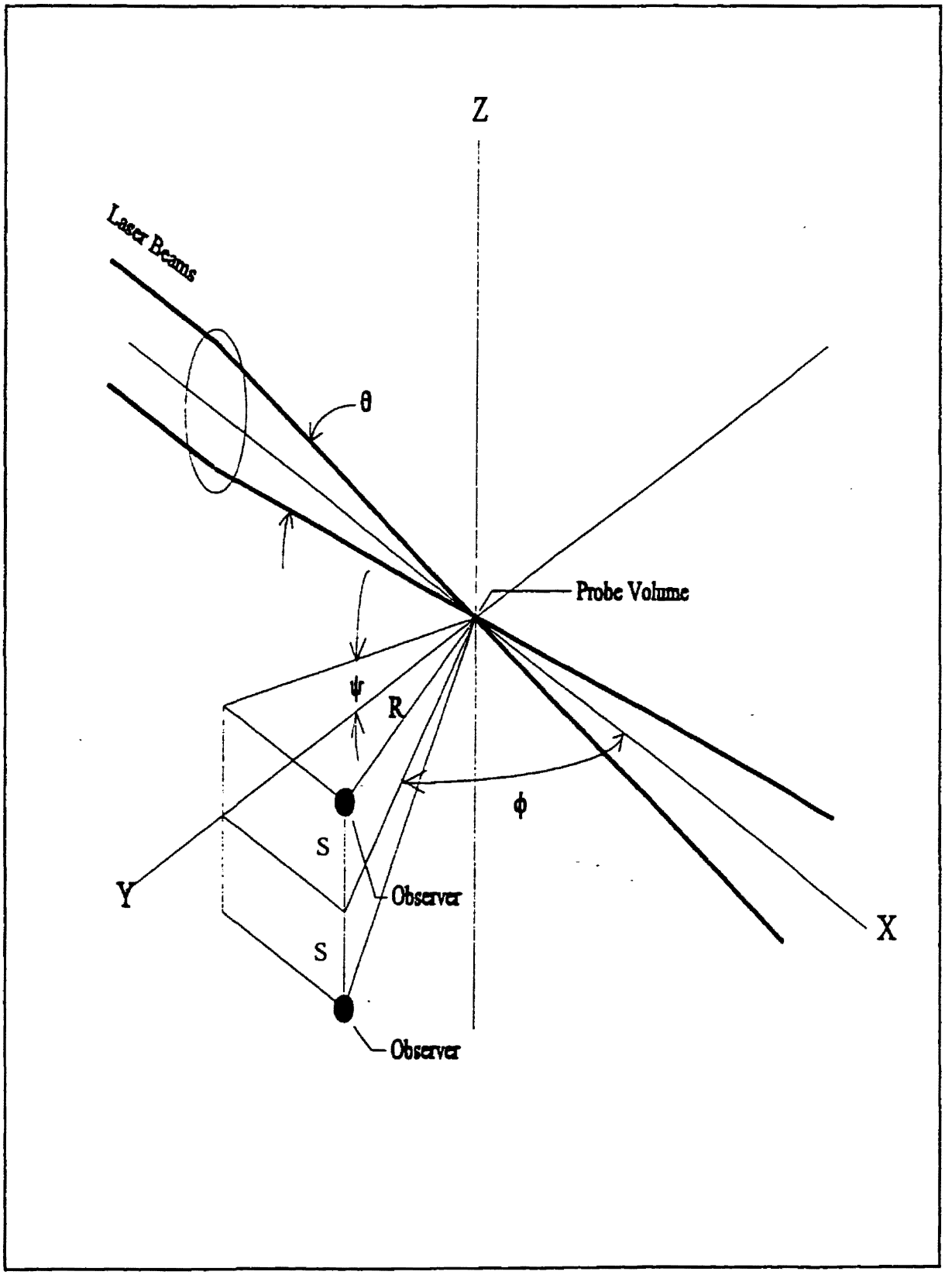


FIGURE 4.2: Phase Doppler geometry

4.1.2. Aerometrics Phase Doppler Particle Analyzer

The Aerometrics Phase Doppler Particle Analyzer used in this study is a commercially available particle sizing system based on the above-described phase Doppler method. As shown in Figure 4.3, the system consists of an argon ion laser, a beam separator and fiber optic launch module, a fiber optically coupled transmitter, a receiver fiber-optically coupled to a set of photomultipliers, a signal processor and a PC-type computer. The laser used in this experiment is a water-cooled Coherent argon-ion laser operated in multiline mode. Typical operating power used was 500-750 mW. The multiline, vertically polarized beam is steered into the beam separator module, where the beam first passes through a Bragg cell, which splits the beam into two, one of which is frequency shifted by 40 MHz. The shifted and unshifted green (515nm) and blue (488) lines are then separated, resulting in four beams, two green and two blue, with one of each colour pair frequency shifted by 40 MHz. All four beams are then launched into mode-preserving fibres and sent to the transmitter module. Coupling efficiency is approximately 30%, although 50% can be achieved for short periods.

The transmitter module consists of four fiber-optic terminators, collimating optics, a beam expanding telescope (removable), and a focussing lens. The transmitter focusses the four laser beams at a common point in space, defining the probe volume. The optical configuration used in this experiment is summarized in Table 4.1. The receiver consists of a receiving lens set, a spatial filter (slit), collimating optics, and a multimode, mutifibre cable termination. The spatially filtered image of the probe volume is expanded and projected on to the fibre optic termination plane in the receiver module, and transmitted to the photomultiplier module, where the fibres are separated in to four paths leading to four photomultipliers. The three fibre sets used for particle sizing and axial velocity are separated according to the pattern shown in Figure 4.4 to provide an "effective" spatial separation of the detectors, denoted as $S_{1\text{-}2}$ and $S_{1\text{-}3}$. A fourth fibre set, shown as the cross-hatched region in Figure 4.4, is linked to the second velocity channel photomultiplier. The photomultipliers are connected to and controlled by the Doppler Signal Analyser (DSA). The DSA determines the frequency and phase of the Doppler signals in each photodetector using fast Fourier transform techniques. The entire system is controlled by proprietary Aerometrics software

running on the PC.

LASER	
Coherent Innova 90 water-cooled argon ion laser	500-750mW
Transmitting Optics	
Beam expanding telescope ratio	2:1
Beam separation	40mm
Transmitting lens focal length	250mm
Probe volume waist ($1/e^2$)	117μm
Receiving Optics	
Receiving lens focal length	300mm
Lens diameter	72mm (f/4.2)
Spatial filter slit width	150μm
Collimating lens focal length	250mm
Magnification	0.833
Detector separation	16.32mm (A-B) 46.96mm (A-C)
Orientation	30° Off forward axis

TABLE 4.1: PDI system optical parameters used in these experiments

The system includes three photodetectors for diameter measurement, although two detectors is sufficient in theory, to provide a sphericity check by comparing phase shifts between detector pairs, as well as to extend the instrument phase range beyond 360°. There are many user-selected parameters that must be set in software, as summarized in table 4.2.

PARAMETER	DESCRIPTION	RANGE	TYP. VALUE
High Voltage	Photomultiplier voltage	188-900V	450V
Frequency Shift	Frequency shift applied to beams	40 MHz or Off	40 MHz
DC Offset	DC bias in raw signal	-75 to +75 mV	55 mV (autoset)
Mixer frequency	Frequency subtracted from observed Doppler frequency	30-45 MHz	38-42 MHz
Low Pass	Low pass filter setting applied to downmixed signal	0.5-80 MHz	2.5-10 MHz
Burst filter	Filter applied to raw signal	40 MHz B. P. 10 MHz or 50 MHz L.P.	50 MHz
Threshold	Minimum RMS trigger voltage required to trigger system	0-500 mV	5-10 mV
Envelope filter	Minimum time that threshold must be exceeded to trigger	0-3μs	1 μs
Peak Detection	Detects maximum amplitude peak of Doppler burst	On or Off	On
% After Peak	Selects % of processed signal that occurs after peak is detected (50% centres around signal peak)	0-100%	50%
# of Samples	Selects number of bits that A/D converter uses to digitize signal	64 - 512	128 or 256
Sampling Rate	Rate at which signal is sampled	78 kHz - 160 MHz	10 - 40 MHz
Min S/N Ratio	Minimum acceptable signal to noise ratio	0.01 - 9.99	0.3

TABLE 4.2: PDI system settings

In addition to the above, the user must also define the minimum and maximum velocity range, as well as the maximum diameter. As can be seen, there are many user-controlled parameters that must be set, each of which can have an effect on the measurements being made.

The photomultiplier voltage setting has a large bearing on the dynamic range of the instrument. Too low a setting results in an inability to detect small droplets, while too high a setting can result in saturation of the photomultipliers, causing signal to noise ratio problems when large droplets are present, and potentially damaging photomultiplier currents. The ideal setting depends on the type of spray distribution present. A wide droplet size and velocity distribution is the most difficult to configure the system to cover. In general, it is desirable to set the photomultiplier voltage as high as possible without saturation for about 99% of the droplets present. This can be accomplished visually by observing the saturation warning LED's on the instrument front panel, and adjusting the PM voltage until only occasional flickering occurs. In the case of wide size and velocity distributions, this set-up can still result in a very low sensitivity to small particles. This is often not a problem, since small particles carry very little of the total spray mass and can often be neglected in characterizing the spray, but in situations where the small particles serve as seed particles for tracking the gas-phase velocity, this is not a desirable situation. A method for overcoming this limitation is described in Section 4.1.6.

The frequency shift is applied to one beam of each colour to eliminate the directional ambiguity inherent in velocity measurements. The mixer frequency is the frequency that is subtracted from the raw signal frequency prior to filtration and digitization. It is chosen such that the downmixed signal frequency lies in a range that is suitable for digitization and filtration for the parameters selected. For example, if the velocity range present ranges from 0 to 10 m/s, and the fringe spacing for the optical configuration chosen is 3.2 μm, the Doppler frequency with frequency shifting on will range from 40 to 43.125 MHz. A mixer frequency setting of 38.2 MHz would result in a downmixed signal range of 1.8 to 4.925 MHz, compatible with a 5 MHz low pass filter setting. This frequency range, combined with a 40 MHz sampling rate and 256 samples would digitize 11 to 31 full cycles, sufficient for the

determination of frequency and phase[41][42].

The number of samples and sampling frequency are selected so that a reasonable number of full cycles are resolved within each Doppler burst for all velocities present. The higher the number of samples selected, the higher the resolution of phase and frequency measurement of a given burst. However, since a finite amount of memory is available, the higher the number of samples taken per Doppler burst, the fewer number of bursts that can be collected. A good compromise between number of samples per burst and number of bursts collected was found to be 128 to 256 samples, with sampling rates set to 10 - 40 MHz, depending on local flow conditions [43].

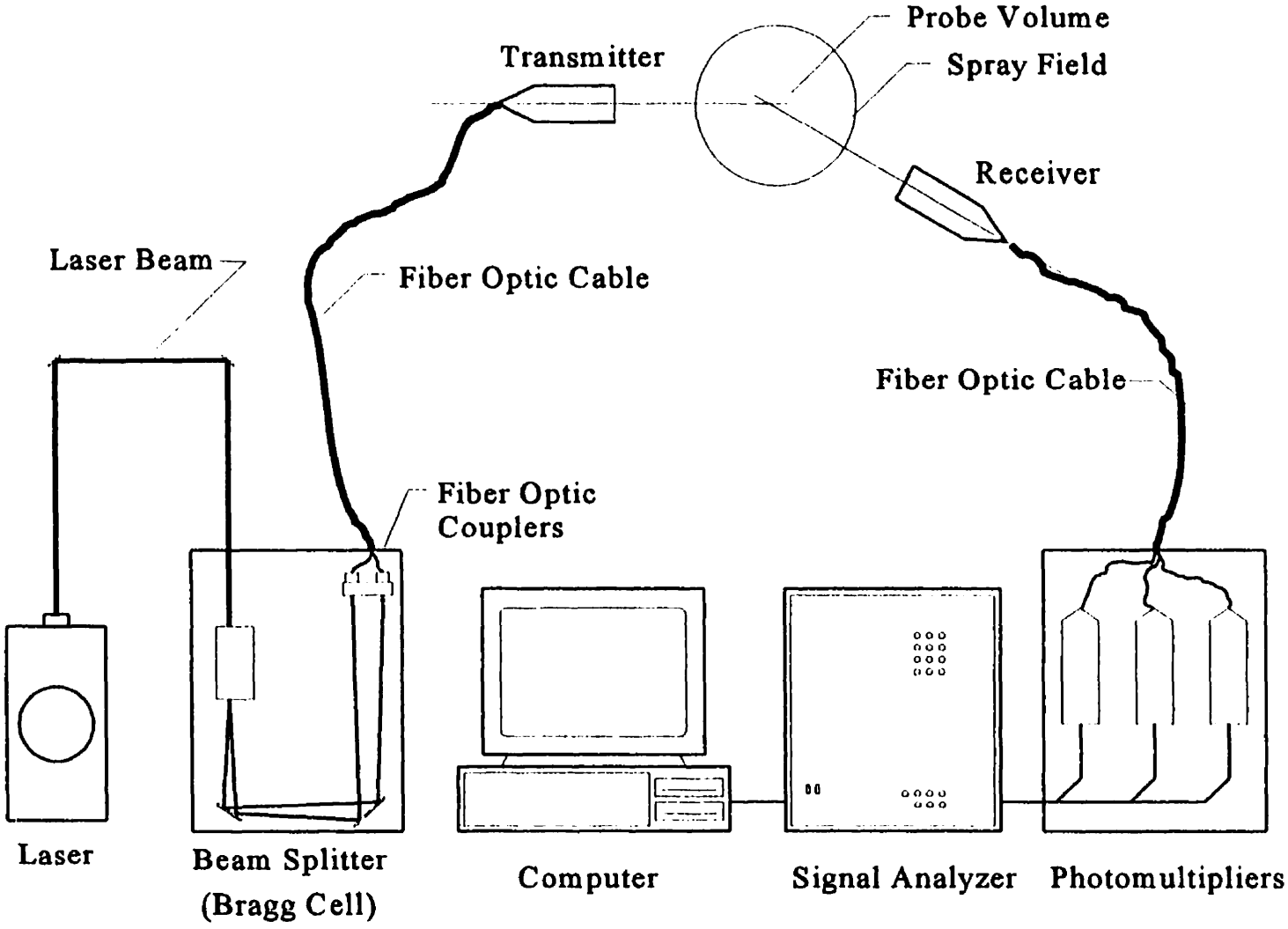
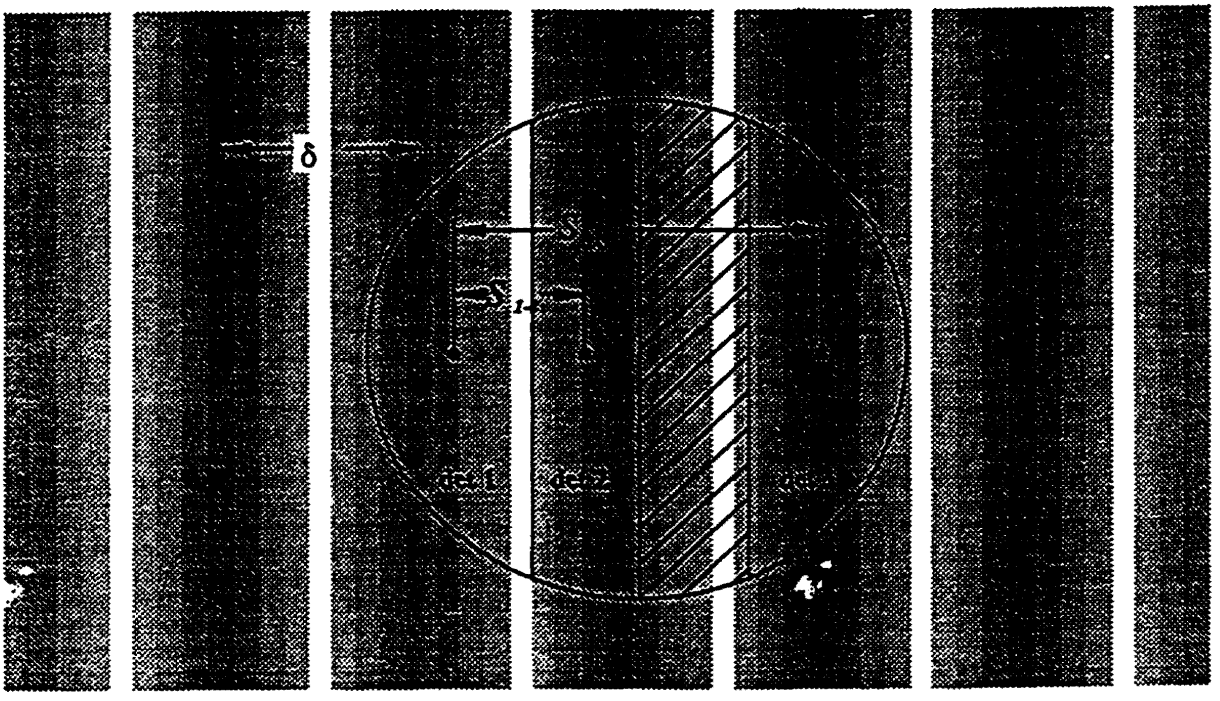


FIGURE 4.3: PDI system layout



S = Effective detector separation

FIGURE 4.4: Receiver geometry

4.1.3. Instrument Output

As discussed above, the Aerometrics Phase Doppler Particle Analyzer determines a droplet's diameter and velocity by assessing the Doppler burst frequency and phase shift resulting from a particle traversing the probe volume. Rather than report each individual particle's diameter and velocity, the instrument outputs statistical information determined from a data set of N particles, where N is a number chosen by the operator. After N particles have been validated, the system computes four statistical mean diameters (D_{10} , D_{20} , D_{30} and D_{32}), mean and RMS velocity, droplet number density and volume flux.

Droplet mean diameters and velocities are determined using a binning technique, whereby each particle measurement is placed in the appropriate diameter and velocity bin. Velocity and diameter ranges are comprised of 240 equal width bins each, where the width of each bin is determined by the instrument range configured for that variable divided by the total number of bins. The resulting diameter and velocity information is presented in tabular and histogram form by the software, with the number of counts in each bin plotted against the bin median diameter or velocity. Raw data consisting of a time tag, diameter, velocity and gate time for each individual droplet in the data set can be saved for post-processing.

Mean diameter calculations must be corrected to account for the fact that the effective probe volume size increases with particle size, hence there is a bias towards large droplets.

The probe volume is formed by the intersection of two laser beams, each of which has a Gaussian intensity profile; hence the probe volume also has a Gaussian intensity profile across its width. The effective probe volume width, which, when multiplied by the probe volume length seen through the spatial filter determines the probe volume area, is the maximum distance from the probe volume centre that a particle can pass and still produce a Doppler burst detectible by the system. Since the intensity of light scattered by a transparent or opaque particle is proportional to the square of its diameter, larger particles can pass farther from the probe volume centre than small ones and still be detected. Similarly, a faster moving particle would have to pass closer to the probe volume centre than a slower-moving one since the total number of photons scattered by a particle scales with residence time. Therefore the effective probe volume width is a function of particle size and velocity. In

addition, several instrument parameters have an influence on effective probe volume width, including laser power, photomultiplier voltage, threshold setting, envelope filter time and alignment precision. Rather than determining a theoretical probe volume width function including all of these parameters, (some of which are not monitored by the system), the instrument calculates an effective probe volume width for each size bin, using the actual data set itself as outlined below. The effective probe area is then calculated by determining the area of the parallelogram formed by projecting the probe volume width and length into the plane of velocity measurement, as shown in Figure 4.1.

The effective probe width in a particular size bin is determined by calculating the probe volume length traversed by each particle in that size class, determined by multiplying the gate time by the particle velocity. The effective width for each size class is determined by applying a proprietary algorithm that determines statistically the maximum probe volume width for each size class from the set of traverse lengths, and assumes that this maximum corresponds to the effective probe volume width for that size class [44]. The algorithm takes into account that a minimum number of fringe crossings are required to trigger the instrument, to arrive at the following expression for the probe volume width for a given bin:

$$\frac{A_i}{A_{\max}} = \sqrt{\frac{\ln\left(\frac{G a_i}{a_{\max}}\right)}{\ln(G)}} \qquad \textbf{4.8}$$

where: A_i = Area of probe volume for ith size class

A_{max} = Area of probe volume for largest size class

δ = Fringe spacing

a_i = Radius of ith size class

a_{max} = Radius of maximum size class

G = Square root of instrument gain

The value of G is determined by proprietary software included with the instrument,

which determines gain by evaluation of the product of particle transit time and velocity for all droplets measured. The maximum probe area is determined in similar fashion. By this procedure, the largest calculated probe area corresponds to the largest droplet size bin. In order to produce unbiased mean diameter calculations, the probe volume areas for each size bin are normalized by the maximum calculated probe area to produce corrected counts. The corrected count for a given size bin is computed from:

$$n_{c,i} = n_i \frac{A_{\max}}{A_i} \qquad \textbf{4.9}$$

where: $n_{c,i}$ = Corrected count in the ith bin

n_i = Actual count in the ith bin

All statistical diameter calculations that the instrument outputs are based on these corrected counts. The instrument also computes the droplet number density and the liquid volume flux. These parameters are based on the actual calculated probe areas, instead of the relative probe area used in the above. The droplet number density is determined from the following:

$$N_D = \frac{\sum_{i=0}^{239} n_{c,i}}{U\,t\,A_{\max}} \qquad \textbf{4.10}$$

where: N_D = Droplet number density

U = Droplet mean velocity

t = Total elapsed time for sample

The volume flux is calculated from:

$$Flux = \frac{\pi}{6} \frac{D_{30}^3 \sum_{0}^{239} n_{c,i}}{t\,A_{\max}} \qquad \textbf{4.11}$$

where: $Flux$ = Volume flux

D_{30} = Volume mean diameter based on corrected counts

It should be noted that the statistical diameters do not depend on an absolute calculation of effective probe area, but only on the ratio of the probe area for the bin of interest to the maximum. This ratio is relatively insensitive to the value of G. The calculated actual maximum probe area A_{max}, on the other hand, is required for volume flux and number density, and is highly sensitive to the calculated value of G, as will be discussed in Chapter 7.

4.1.4. Post-Processed Results

In order to determine parameters such as gas-phase velocity, it is necessary to post-process the raw data file to remove velocities corresponding to measurements from those particles that are too large to accurately follow the gas-phase flow. This is an iterative process since the cut-off size varies with flow conditions. Once a cut-off size has been selected, a new data file is created consisting of only velocities associated with particles less than the cut-off size, and mean and RMS velocities as well as shear stresses determined as follows:

$$\overline{U} = \frac{1}{N}\sum_{i=1}^{N} U_i \qquad \overline{V} = \frac{1}{N}\sum_{i=1}^{N} V_i \tag{4.12}$$

$$\overline{uv} = \frac{1}{N}\sum_{i=1}^{N} (U_i - \overline{U})(V_i - \overline{V}) \tag{4.13}$$

$$u = \frac{1}{N}\sqrt{\sum_{i=1}^{N} (U_i - \overline{U})^2} \qquad v = \frac{1}{N}\sqrt{\sum_{i=1}^{N} (V_i - \overline{V})^2} \tag{4.14}$$

where: U_i, V_i = Axial and radial velocities of the ith droplet

$\overline{U}$, $\overline{V}$ = Axial and radial mean velocities

u, v = Axial and radial fluctuating RMS velocities

N = Number of particles in post-processed data set

$\overline{uv}$ = Turbulent shear stress

In some cases where dyed fuel was used (see section 4.1.6) data rates of small particles were sufficiently high that further processing to obtain turbulent timescales and spectra was possible. The software in use to determine these requires data obtained at fixed time increments. Since the phase Doppler system records a particle event any time a particle passes through the probe volume, the resulting data set consists of essentially random arrival time data. After removing large particle data, the final data set consists of a random time series of velocity measurements. To convert this random time series into a fixed interval data set suitable for processing, a linear interpolation technique was employed. The random time series data set was examined to determine the mean data rate, defined as the total number of data points divided by the total elapsed time of the measurement set. The fixed interval data set was then produced at a fixed frequency approximately half the mean data rate. The processing software was set up to alert the user of excessively long time periods over which no new velocity measurements were recorded, which, on interpolation, would result in long, artificial linear variations in velocity. The resulting data set was then processed by the Mechanical Engineering Data Acquisition and Processing software [45]. The integral scales of velocity are determined from integration of the normalized autocorrelation function:

$$\Re(\tau) = \frac{1}{\overline{U^2} T} \int_0^T U(t)\, U(t+\tau)\, dt \qquad \textbf{4.15}$$

where: $\Re(\tau)$ = Normalized autocorrelation function

T = Time period of data set

$U(t)$ = U at time t

$U(t+\tau)$ = U at time $t+\tau$

The discrete form of the normalized autocorrelation function calculation is given as follows:

$$\Re(m\,\Delta\tau) = \frac{\dfrac{1}{N-m-1}\displaystyle\sum_{i=0}^{N-m-1}\left[U(i\Delta\tau)-\overline{U}\right]\left[U(i\Delta\tau+m\Delta\tau)-\overline{U}\right]}{\dfrac{1}{N-1}\displaystyle\sum_{i=0}^{N-1}\left[U(i\Delta\tau)-\overline{U}\right]^2} \qquad \textbf{4.16}$$

Where: $\Delta\tau$ = Time step between data points

N= Total number of data points

m = number of time lags up to a maximum of M (m=0,1,2,...,M)

The number of time lags considered, M, is generally chosen as the number required to reach the first zero crossing of the autocorrelation function. The autocorrelation function is usually normalized by the square of the RMS velocity, so that $\Re(0)$=1. The integral timescale is obtained by integration of the normalized autocorrelation function as follows:

$$\Im = \frac{1}{T}\int_0^T \Re(\tau)\,d\tau \qquad \textbf{4.17}$$

where: $\Im$ = Integral timescale

In regions of low intensity turbulence, Taylor's frozen flow hypothesis can be invoked, whereby integral length scales can be obtained by multiplication of local mean velocity by the integral timescale.

The turbulent energy spectrum is obtained as follows:

$$E(f) = \lim_{\Delta f\to 0}\left[\lim_{T\to\infty}\left(\frac{1}{\Delta f\,T}\int_0^T u^2(t,f,\Delta f)\,dt\right)\right] \qquad \textbf{4.18}$$

Where: $E(f)$ = Power spectral density function

Δf = Frequency range

T = Timespan of data set

f = Frequency

t = Time

The discrete form of the above, used in the processing software, is as follows [45]

$$X_{ik} = \sum_{n=0}^{N-1} u_{in} \exp\left(-i 2\pi \frac{kn}{N} \right) \qquad k = 0,1,2,\ldots,N-1 \qquad \textbf{4.19}$$

$$E(f_k) = \frac{2\Delta t^2}{n_d N \Delta t} \sum_{i=1}^{n_d} |X_{ik}|^2 \qquad k = 0,1,2,\ldots,N/2 \qquad \textbf{4.20}$$

where: X_{ik} = Discrete Fourier transform

n_d = Number of data blocks

N = Number of data points in each block

It should be noted that the variance of the power spectral density function can be quite large, even for large numbers of data points, N. This problem can be minimized by calculating the ensemble average of the spectral density functions from many smaller data blocks. While decreasing the number of data points in each block increases the variance, increasing the number of independent data blocks used to reconstruct a spectral density function decreases the variance. Generally a trial and error approach is necessary to minimize variance by altering the size and number of data blocks for a given data set.

4.1.5. Limitations

As with any measurement system, phase Doppler interferometry has its limitations.

Although the system is widely accepted for particle size and velocity measurements and seems reliable and efficient, it is important to be aware of its limitations.

One potential limitation results from the requirement that the particles being measured be spherical. In most sprays, under most conditions, this limit does not impose undue restrictions. However, in some situations where large droplets are interacting with high relative velocity or turbulent flows, droplet distortion from spherical may occur, resulting in data rejection. In these types of flows, data will be biased towards smaller particles that resist aerodynamic distortion and remain spherical.

Another limitation arises from the limited dynamic range of photomultiplier/amplifier circuitry, which have a useful range of approximately 2500:1. Since the intensity of light scattered from a droplet scales with diameter squared, the resulting dynamic range of the instrument is effectively approximately 50:1. In addition to this, since the probe volume area is related to droplet size, the effective probe volume area for small particles is much smaller than for larger particles, limiting the system's sensitivity to small seed particles. A method of overcoming this limitation is described in the next section.

A third limitation arises from the physics of light scattering by small particles. The linear phase shift/diameter relationship predicted by geometric optics as used in PDI begins to break down as the particle size approaches the incident light wavelength. Since the argon ion laser wavelength is around 0.5 μm, this represents the approximate lower diameter limit of applicability for the phase Doppler method.

4.1.6. Increasing PDI Sensitivity to Small Particles

As discussed above, it can be difficult to configure the PDI system to efficiently detect small seed particles when large particles are present due to the limited dynamic range of the photomultipliers, and due to the Gaussian nature of the probe volume, resulting in a very small effective probe volume size for small particles relative to large ones. It is often desirable to determine the gas-phase velocity in a multi-phase flow. In order to do this, velocity data is obtained from all particles passing through the probe volume. The data set is then filtered to retain only data corresponding to small particles which accurately track the gas-phase flow.

In most situations with a typical spray containing droplets up to 100μm in diameter, it is difficult to detect large quantities of small particles. In order to obtain sufficient small particle counts to calculate statistically reliable gas-phase mean and RMS velocity, extremely large raw data sets are required, and data rates of small particles are insufficient to resolve even the largest turbulent features. A method to reduce this problem has been developed by Friedman and Renksizbulut [46] using dyed droplets to attenuate the intensity of light scattered from large droplets, allowing the photomultiplier gain to be set higher, thus enhancing the visibility of small seed particles.

A particle scatters lights by reflection, first and higher order refraction as shown in Figure 4.5. The equation relating the scattered intensity to incident light intensity at a given point in space is given by [47]:

$$\frac{I}{I_b} = D\left(\frac{a\,\epsilon_2}{s}\right)^2 \qquad \textbf{4.21}$$

where: I = Scattered intensity at a point in space

I_b = Incident light intensity

D = Divergence (see below)

a = Particle radius

ϵ_2 = Coefficient

s = Radial distance from particle centre

The divergence term, D, is given by:

$$D = \frac{\sin\tau\,\cos\tau}{\sin\theta\;|\,d\theta'/d\tau|} \qquad \textbf{4.22}$$

$$\frac{d\theta'}{d\tau} = 2 - 2p\,\frac{\tan\tau}{\tan\tau'} \qquad \textbf{4.23}$$

$$\theta' = 2\,(\tau - p\,\tau') = 2\,\pi - \theta \qquad \textbf{4.24}$$

where: p = Scattering mode (0 = reflection, 1 = 1st order refraction...)

θ, θ', τ, τ' = Optical angles (see Figure 4.5)

From Snell's law:

$$\cos\tau' = \frac{1}{m}\cos\tau \qquad \textbf{4.25}$$

where: m = Relative index of refraction of scatterer

The coefficient ϵ_2 is obtained from the Fresnel coefficient r_2 as follows:

$$\epsilon_2 = r_2 \;for\; p = 0\,;\, \epsilon_2 = \left(1 - r_2^2\right)\left(-r_2\right)^{p-1} for\; p > 0 \qquad \textbf{4.26}$$

$$r_2 = \frac{m\sin\tau - \sin\tau'}{m\sin\tau + \sin\tau'} \qquad \textbf{4.27}$$

The above equations are valid for transparent spheres larger than the incident light wavelength. Partially absorbing (dyed) droplets obey Beer's law for attenuation of intensity

due to absorption, hence it is possible to modify Equation 4.21 to account for absorption of light by the droplet:

$$\frac{I}{I_0} = D\left(\frac{a \epsilon_2}{s} \right)^2 \exp(-2 p \gamma a \sin \tau') \qquad \textbf{4.28}$$

where: γ = Droplet absorptivity

In this equation, the term $\{-2p\gamma a\sin\tau'\}$ represents the optical path length through the droplet. Figure 4.6 shows the relative scattered intensity received by a detector located at 30° from the forward axis, assuming a relative index of refraction of 1.333 (water) and an absorption coefficient γ of 0.015 /μm, for first order refracted light. As can be seen, the relative attenuation significantly increases with increasing droplet size.

It is important to consider the relative intensity of refracted light to reflected light at a point in space, since the PDI system operates assuming one scattering mode is dominant. At the 30° collection angle typically employed, with water as the scattering medium, the intensity of refracted light scattered by a transparent particle is approximately 44 times that of reflected light, hence there is no significant interference from reflection. When the droplet is partially absorbing, refracted light will be attenuated but reflected light will not, hence interference from reflected light can become a problem. Figure 4.7 shows the ratio of refracted to reflected light intensity versus particle diameter for a partially absorbing (γ = 0.015 /μm) droplet. As can be seen, for droplet diameters greater than about 150μm, the intensities of refracted and reflected light are of the same order, and interference can be expected.

Figure 4.8 presents estimates of the scattered light intensity for a dyed and undyed droplet. As can be seen, the first order scattered intensity for a transparent droplet increases monotonically with diameter, while the intensity curve for the absorbing droplet exhibits a maximum near 150μm. The droplet size producing the maximum first order scattered intensity can be found by differentiation of Equation 4.28 and is given by:

$$a_{max} = \frac{1}{p\,\gamma\,\sin\tau'} \qquad \textbf{4.29}$$

The intensity of light scattered by a particle of size a_{max} is given by:

$$\frac{I_{max}}{I_b} = D\left(\frac{\epsilon_2}{s\,e\,p\,\gamma\,\sin\tau'}\right)^2 \qquad \textbf{4.30}$$

where: I_{max} = Maximum intensity scattered by particle of size a_{max}

e = Natural log base (2.7183...)

It is possible to select an absorption coefficient γ such that the maximum light intensity scattered by droplets divided by the lower detection limit of the instrument for the droplet size required falls within the range of the photomultipliers being used, thus allowing detection of all droplets larger than the lower detectability limit without overloading the photomultipliers. Of course, other optical and processing constraints, including interference from reflected light impose practical limits on the size range that can be realistically be achieved. For example, consider a typical photomultiplier range of 2500:1 and a receiver located at 30°. Selecting an absorption coefficient of 0.0185 /μm would result in no droplets scattering sufficient light to saturate the photomultipliers if the photomultiplier gain is set to detect 1 μm particles, although for very large droplets reflected light would begin to interfere with the signal and cause erroneous results. Location of the collection optics at the 73.7° Brewster angle, where reflection vanishes, would eliminate this interference, although the refracted signal intensity is also lower at this collection location.

Phase Doppler droplet diameter measurements require correction to eliminate biases induced by the variation of effective probe volume size with droplet diameter. Current instrumentation uses a correction algorithm that assumes non-absorbing droplets. Since absorbing droplets effectively reduce the probe volume area for large droplets relative to non-absorbing ones, a correction scheme that accounts for droplet absorption is required.

Consider a probe volume with a Gaussian intensity distribution:

$$\frac{I_b}{I_0} = \exp\left[\frac{-2r_b^2}{r_w^2}\right] \qquad \textbf{4.31}$$

where: I_0 = Centerline laser beam intensity

I_b = Beam intensity

r_b = Radial displacement from beam centreline

r_w = Beam waist diameter ($1/e^2$)

Substitution of the above into Equation 4.28 yields:

$$\frac{I}{I_0} = \left(\frac{a\epsilon_2}{s}\right)^2 D \exp\left[-2pa\gamma \sin\tau' - \frac{2r_b^2}{r_w^2}\right] \qquad \textbf{4.32}$$

A general expression for the maximum scattered light intensity for a particle of size a_{max} passing through the centre of the probe volume (assuming the particle size is small compared to r_w) can be obtained from Equation 4.32 as:

$$\frac{I_{max}}{I_0} = \left(\frac{a_{max}\epsilon_2}{s}\right)^2 D \exp\left(-2pa\gamma a_{max} \sin\tau'\right) \qquad \textbf{4.33}$$

For a given photodetector with a dynamic range of G^2, the minimum detectible intensity is I_{max}/G^2. Hence, using Equations 4.29 and 4.33 a general equation for the effective probe volume radius r_b for a given particle of radius a is:

$$\frac{r_b}{r_w} = \sqrt{\ln\left(\frac{Ga}{a_{max}}\right) + (p\gamma \sin\tau')(a_{max} - a)} \qquad \textbf{4.34}$$

It follows from Equation 4.34 that:

$$\frac{r_b}{r_{b,\max}} = \sqrt{\frac{\ln\left(\frac{Ga}{a_{\max}}\right) + (p\gamma\sin\tau')(a_{\max} - a)}{\ln(G)}} \qquad 4.35$$

To correct a measured distribution for probe volume bias error, it is necessary to divide the number of counts in each size class by the ratio $r_b/r_{b,max}$ for that size class as given by the above equation. For non-absorbing droplets ($\gamma = 0$), a_{max} corresponds to the largest drop size in the measurement set, and the above reduces to the standard algorithm typically used. The Aerometrics system determines the value of G^2 by evaluating minimum and maximum probe volume traverse lengths for different size classes using a proprietary algorithm. In order to extract the value of G calculated by the software from a data set, it is necessary to examine the ratio of uncorrected count to corrected count in any size class that has large numbers of counts to obtain $r_b/r_{b,max}$ then use Equation 4.35 with $\gamma = 0$ to determine G.

Figure 4.9 and Table 4.3 present results from the application of the standard correction scheme and the absorptivity-corrected scheme to a raw data set consisting of a log-normal distribution of droplets having an absorptivity of 0.015/μm with a geometric mean diameter D_g of 30μm and a geometric standard deviation σ_g of 1.75 μm. A value of $G^2 = 1000$ was assumed. As can be seen from Table 4.3, use of the correction scheme for non-absorbing droplets under these conditions results in an underestimation of the arithmetic mean diameter by 1.2 μm (3.6%).

Verification experiments with absorbing droplets were performed using a vibrating orifice droplet generator [48] and a standard pressure-swirl atomizer to confirm the above theoretical predictions. The working fluid was water, doped with Acid Red #1 dye (azophloxine). This dye has quite a high absorptivity in the 488-515 nm range at low concentrations ($\gamma \approx 0.015/\mu$m at 3 *g/l* concentration), and is quite inexpensive. Tests with a dye used in dye laser applications, Rhodamine 590, showed that this dye achieved the same absorptivity as Acid Red #1 at a concentration of just 1 *g/l*, but it is very expensive. Many

other dyes are available, and may perform better and/or more economically. Figure 4.10 shows the deviation of measured diameter from expected diameter as diameter increases, showing the effect of signal contamination by reflected light as refracted light is dampened out. As can be seen, the error associated with this phenomenon increases rapidly beyond 200μm, hence care must be used in applying this method to coarse sprays. Figure 4.11 shows the measured mean intensity scattered from spray droplets versus measured diameter for undyed droplets. It should be noted that, at the time these measurements were made, our instrument could only be configured with a maximum of a 50:1 diameter range, so two measurement sets were made, one for a range of particles of 2 to 100 μm diameter, and a second for those 100 to 300 μm in diameter, with all other parameters remaining fixed. Since these measurements were made at different times, and since laser power and alignment drift somewhat with time, a small kink is evident in the data set at 100 μm. As can be seen, the data follows the expected trend, with the best fit equation shown on the figure. Figure 4.12 shows a similar data set using a dyed spray which follows the expected trend well. A best fit equation, using the second order coefficient obtained from Figure 4.11, is displayed in the figure. At large diameters, the measured intensity is higher than the predicted value since the predicted value does not include any contribution to intensity due to reflected light, which becomes significant at these larger diameters. Finally, Figure 4.13 shows a histogram of a dyed spray seeded with nebulizer particles with an arithmetic mean diameter on the order of 2 μm. The large peak at small diameters represents detection of the seed particles even in the presence of droplets in excess of 120 μm in diameter. Photomultiplier voltage was set in each case to a level which resulted in minimal saturation (saturation LED's flicker only occasionally). In both cases, dying the spray vastly increases the visibility of seed particles in the presence of large droplets.

In summary, dying the sprayed fluid with a small quantity of an appropriate dye attenuates the intensity of scattered refracted light from large particles to a sufficient degree that photomultiplier gain can be set to a level high enough to obtain efficient detectibility of seed particles, even when large particles are present, without saturating the photomultipliers. Errors due to reflection effects can occur with larger particles, but this problem can be

avoided with judicious selection of optical configuration and dye concentration.

Statistical Diameter	Corrected Value-Absorptivity Compensated (μm)	Corrected Value-Standard Correction (μm)
D_{10}	33.1	31.9
D_{20}	38.5	37.0
D_{30}	44.3	42.5
D_{32}	58.6	56.1

Table 4.3: Influence of correction scheme on statistical diameters for a log-normal (D_g=30μm, σ_g=1.75μm) raw distribution with droplet absorptivity γ=0.015/μm and instrument gain G^2 = 1000.

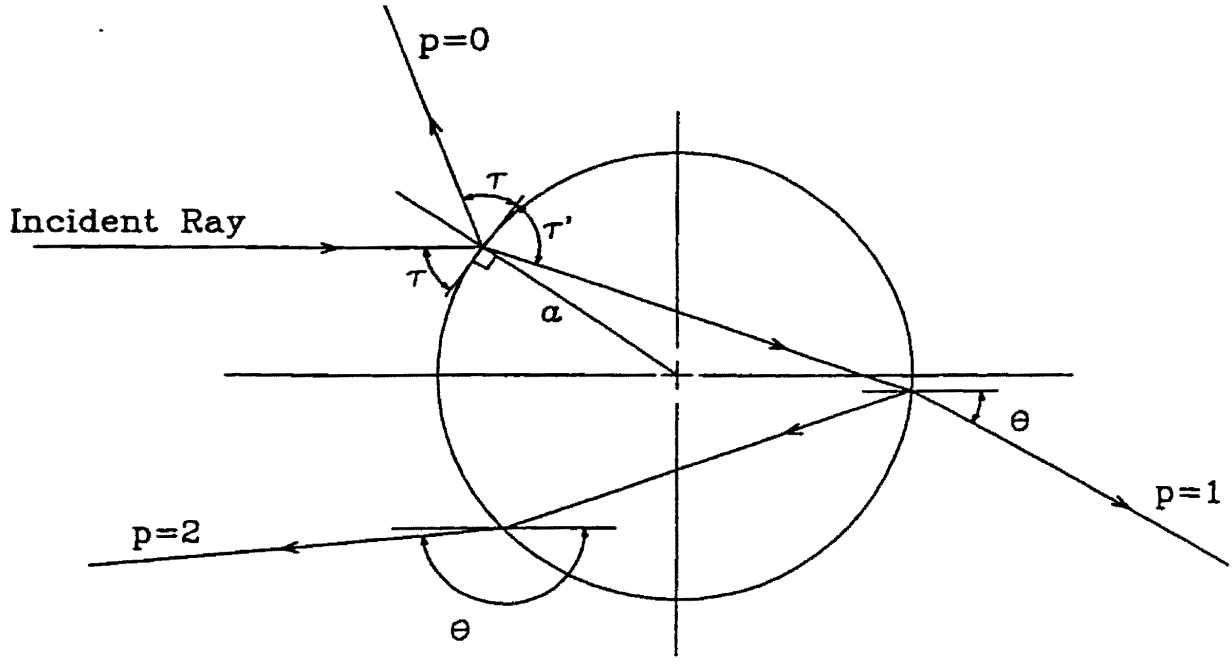


FIGURE 4.5: Droplet scattering geometry

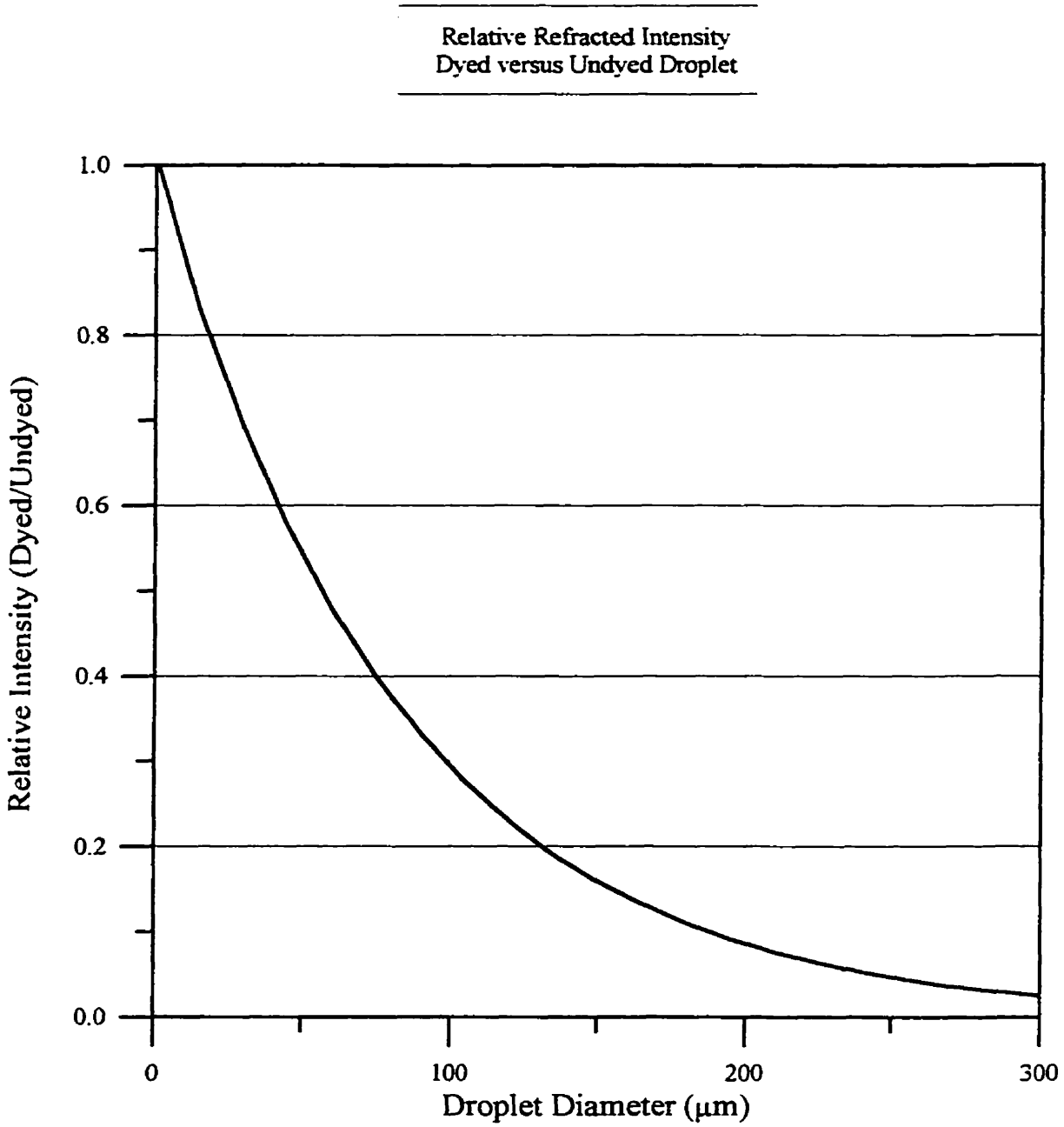


FIGURE 4.6: Ratio of intensity of scattered refracted light for dyed (γ =0.015 /μm) and undyed droplets

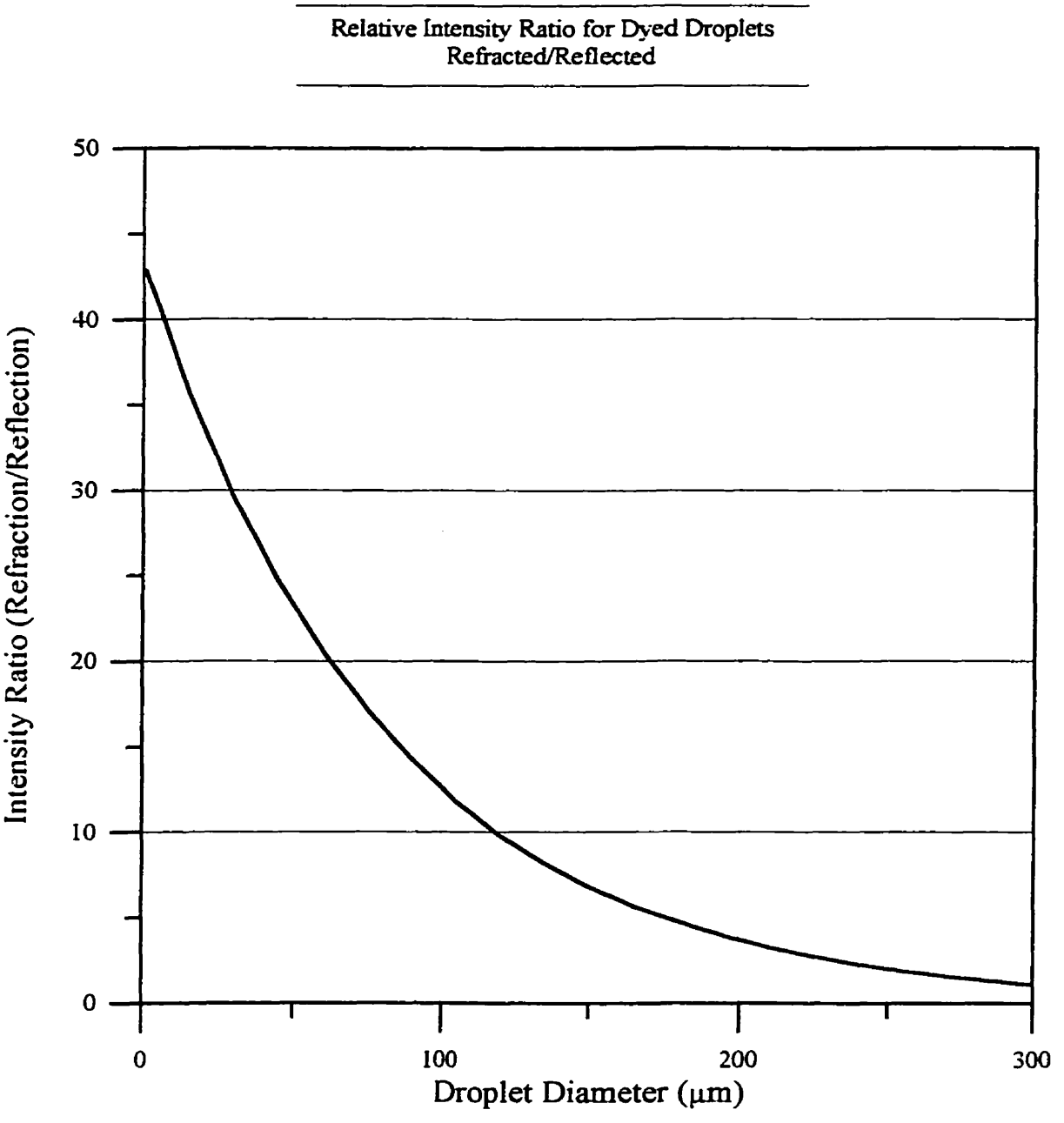


FIGURE 4.7: Ratio of first order refracted intensity to reflected intensity at 30° collection angle for dyed ($\gamma = 0.015$ /μm) droplets

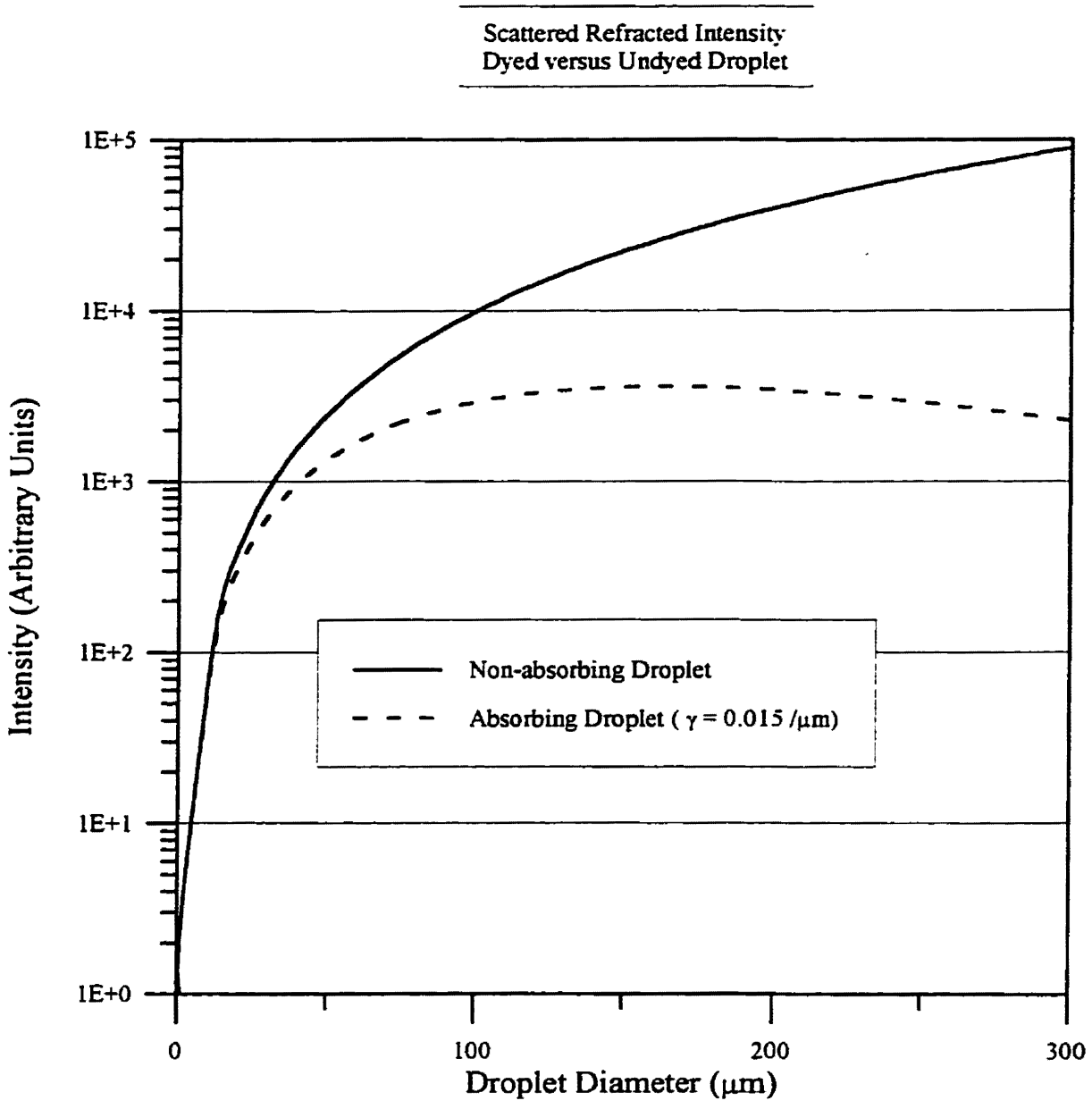


FIGURE 4.8: Comparison of refracted scattered intensity for dyed ($\gamma = 0.015/\mu m$) and undyed droplets

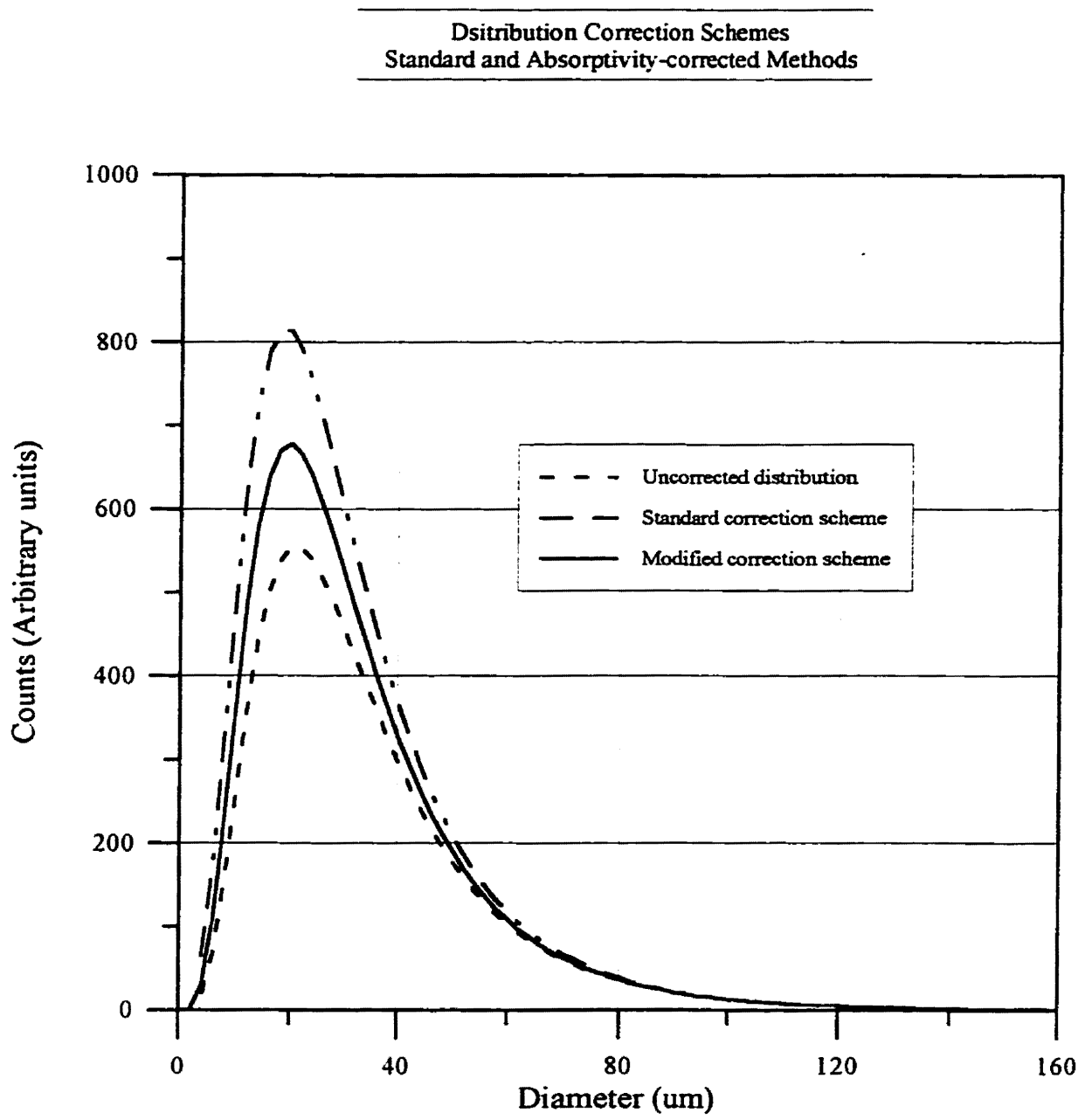


FIGURE 4.9: Comparison of correction schemes applied to a log-normal (D_g = 30 μm, σ_g = 1.75 μm) raw distribution, and an absorptivity of γ = 0.015 /μm and G = 35

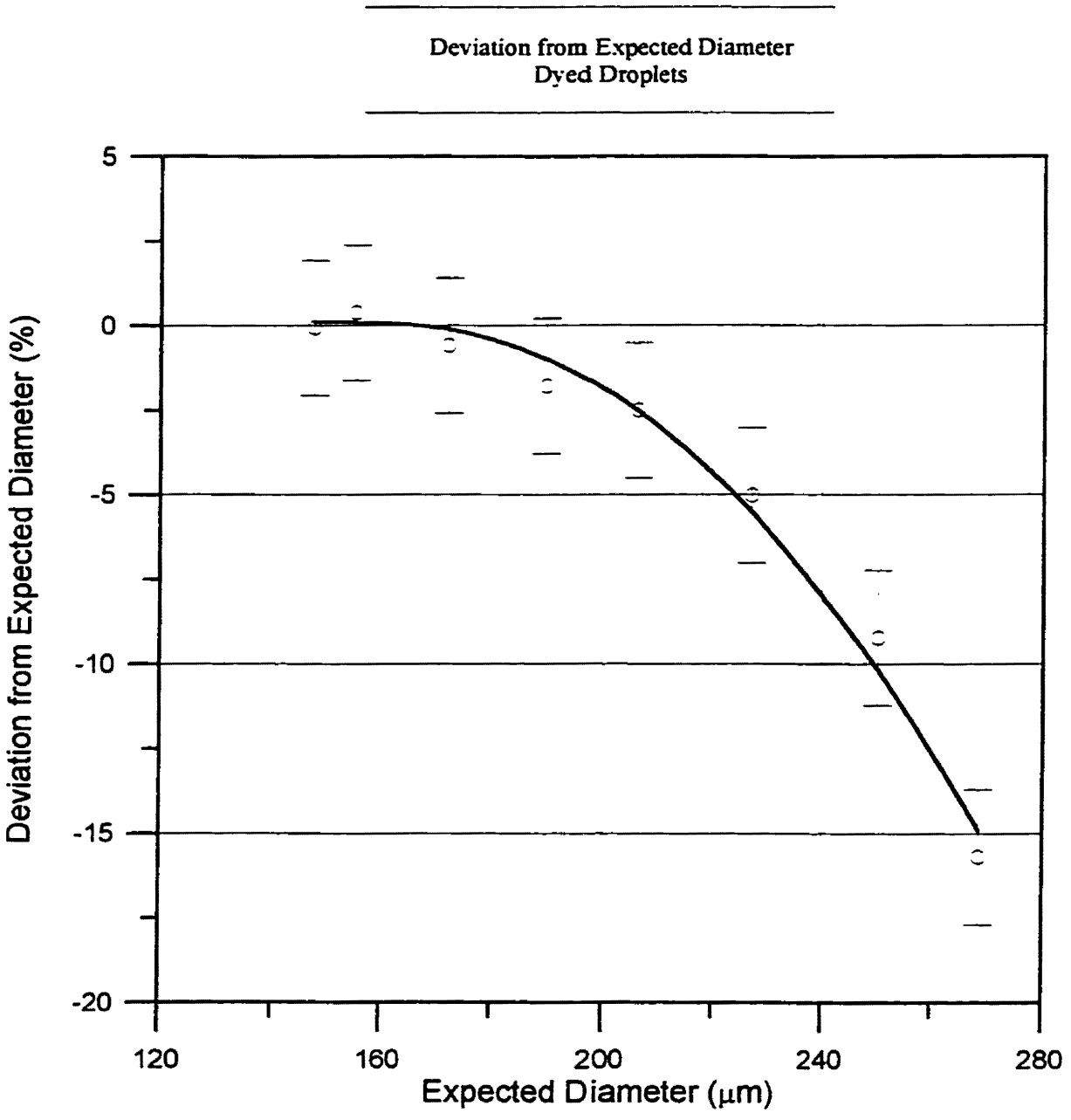


FIGURE 4.10: PDI measured deviation from expected diameter with dyed droplets ($\gamma = 0.015$ /μm)

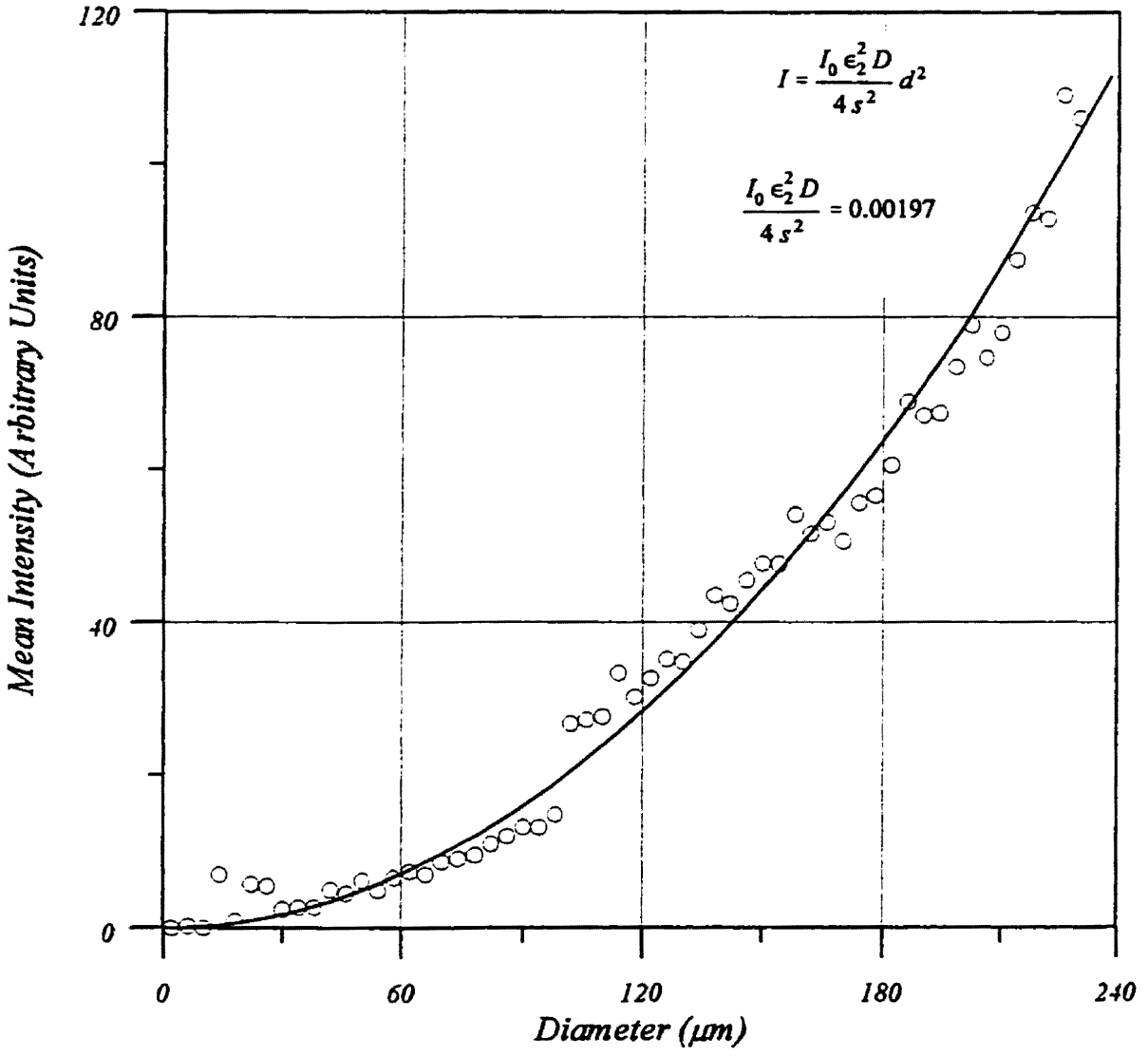


FIGURE 4.11: Measured scattered intensity versus diameter for undyed droplets

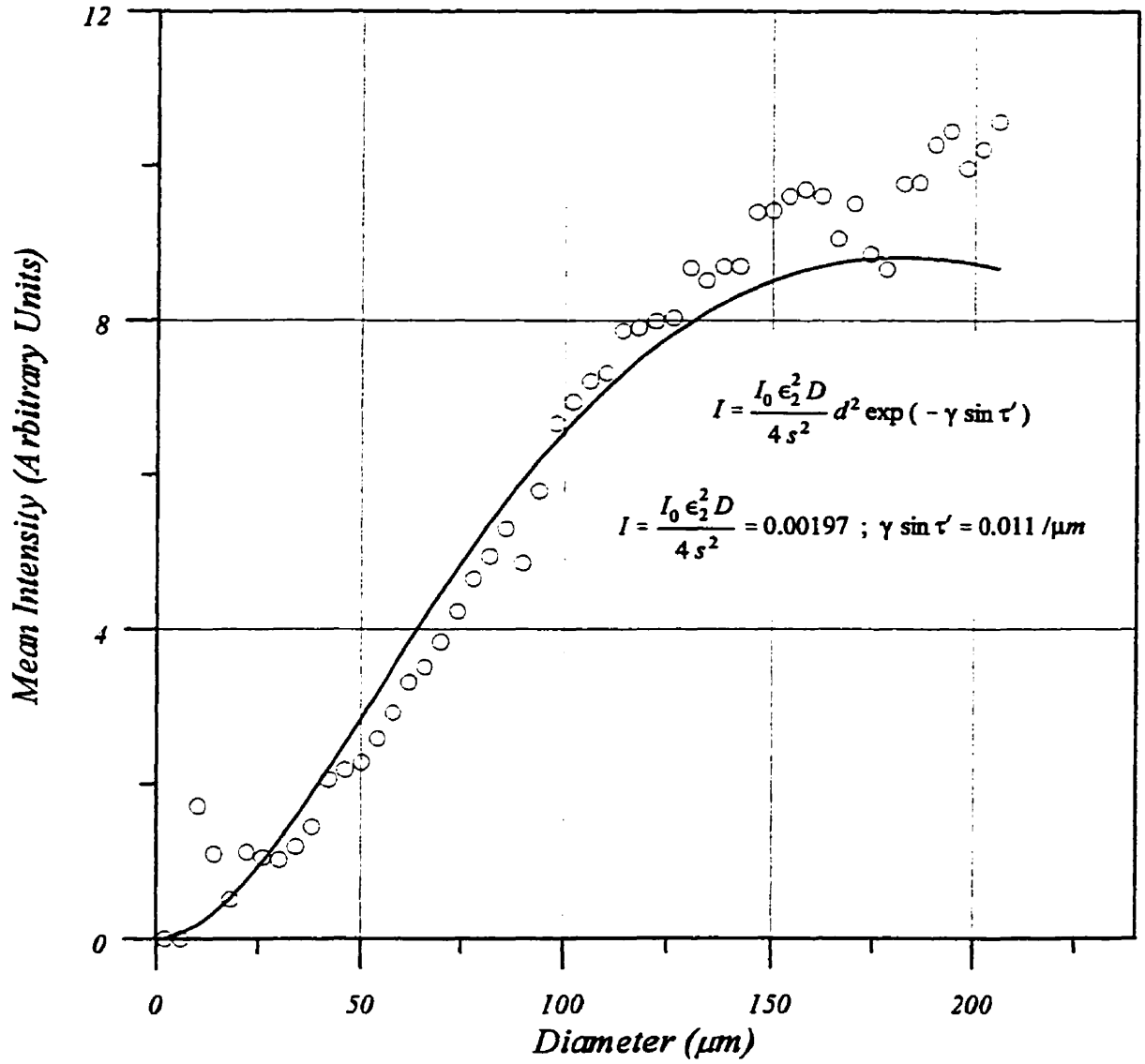


FIGURE 4.12: Measured scattered intensity versus diameter for dyed droplets ($\gamma = 0.015$ /μm)

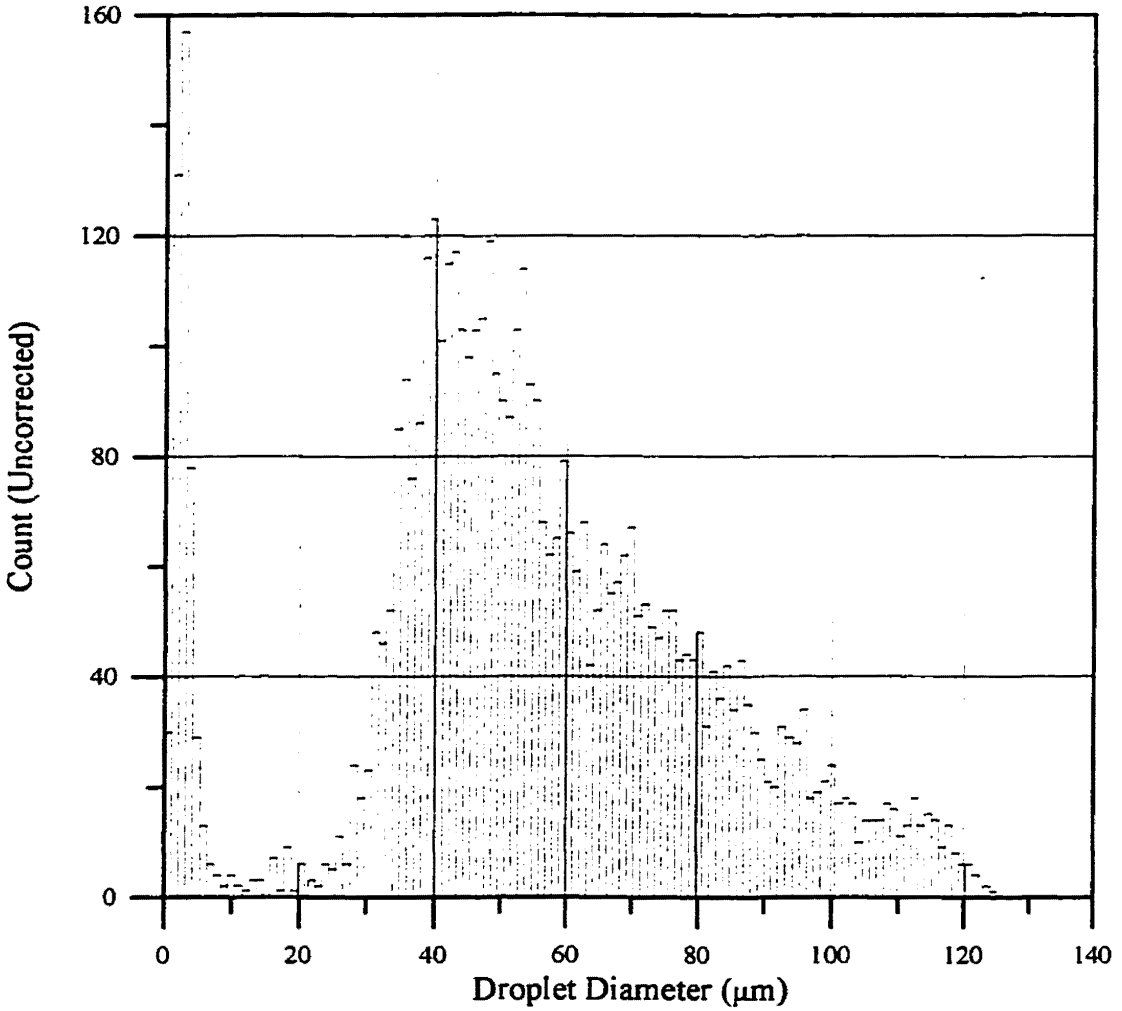


FIGURE 4.13: Typical droplet diameter histogram with dyed droplet ($\gamma = 0.015$ /μm) and nebulizer-seeded airflow

4.2. Planar Laser-Induced Fluorescence

Planar laser-induced fluorescence is a technique that allows two-dimensional imaging of species. In flames, the technique is typically used to image combustion radicals such as the hydroxyl (OH) and methylidyne (CH) radicals, although other species can be imaged as well. The two dimensional fluorescence image can be processed to determine the spatial distribution of species concentration. The method has even been used to produce instantaneous two-dimensional maps of temperature distribution when applied to flows seeded with known concentrations of NO[49]. The typical system uses a pulsed laser beam spread into a sheet and transmitted through the flame being studied, to excite the species being probed. Resulting fluorescence emission is collected at 90° using a sensitive ICCD camera. The resulting image can be used "as is" to provide an instantaneaous "picture" of the reaction zone location, or it can be further processed to obtain quantitative information regarding species concentration.

Excellent review articles summarizing the theory and implementation of spectroscopic techniques in combustion diagnostics have been written by Kohse-Hoinghaus [50] and Daily [51], and are good sources of background information regarding PLIF.

4.2.1. Laser-Induced Fluorescence Theory

Light can interact with molecules in a gas in a number of ways. Elastic (Rayleigh) scattering occurs when there is no net energy exchange between the photon and molecule, and no associated wavelength shift after interaction. Most scattered light whose energy does not correspond exactly to the difference between quantum energy levels in the molecule will be scattered in this manner. It is possible, however, for an interaction to occur wherein the incident light will be frequency shifted an amount corresponding to any quantum energy level difference, an interaction known as Raman scattering. If the Raman scattered light is of lower frequency (lower energy) than the incident radiation, it is termed Stokes shifted, and conversely, if it is of higher frequency, it is termed anti-Stokes shifted. The incident radiation does not need to be any particular wavelength for either Stokes or anti-Stokes Raman scattering to occur, as Raman scattering is not a resonant process. If the frequency of the

incident light exactly matches a quantum energy level difference of the molecule (with certain other constraints), the molecule can absorb the photon and increase its energy to a higher, excited state. The excited molecule can then relax to a lower energy level by emitting a photon with a frequency equal to the molecule's energy change. If the molecule returns to its original state, the emitted photon will have a frequency equal to the original incident radiation, and is termed resonant fluorescence. If it returns to some other lower energy state, the emitted photon will have a frequency that differs from the incident radiation. If the incident radiation is laser light, the process is called laser-induced fluorescence (LIF). Both Raman scattering and LIF have been successfully employed as spectroscopic techniques. The LIF signal, however, is several to many orders of magnitude stronger and thus is easier to acquire.

Planar laser-induced fluorescence (PLIF) allows some radical species in flames, such as OH and CH, to be imaged in a two dimensional plane at extremely high temporal resolution. The method involves exciting the species to be imaged using a sheet of laser light tuned to an excitation frequency, and observing the resulting spontaneous fluorescence at an allowed fluorescence wavelength or wavelengths. The method relies on the quantum nature of molecules, whereby only discrete energy levels are possible for a given atomic or molecular system. Contributions to internal energy of a bimolecular species are made from electronic, vibrational and rotational energy states. Changes in internal energy can only be made in quantum steps for each energy mode, with only certain quantum transitions possible. The electronic state is usually designated by letter, with the lowest energy state, (ground state) designated X, the first excited state A, the second, B etc. The vibrational state is designated by the vibrational quantum number v, which can assume any integer value from 0 up. The rotational state is designated by the rotational quantum number J.

A molecule can change its energy state by a number of mechanisms. Collisions with neighbouring molecules can result in energy redistribution, as can interactions with photons (either absorption or emission). A photon whose energy exactly matches an allowed energy difference between quantum states of a molecule can be absorbed, and if it is, that molecule rises to an energy state corresponding to the base energy plus the additional energy of the photon absorbed. The probability of this occurring is given by the Einstein coefficient for

absorption B_{nm} multiplied by the energy density of the stimulating radiation at the transition frequency, where the subscripts n and m correspond to the initial and final quantum states respectively. A photon whose energy does not match a specific allowed energy transition of a molecule is usually scattered elastically, with no energy exchange with that molecule, although there exists a small probability that a non-elastic interaction can occur. This type of non-elastic interaction can cause certain allowed transitions within a molecule and result in the emission of a photon with an energy equal to the incident photon energy plus the change in energy of the molecule, either positive or negative. This process is known as Raman scattering, as mentioned above. Although the intensity of Raman-scattered light is low, this phenomenon has been extensively exploited in clean flame diagnostics, allowing determination of major species concentration and temperature at high spatial resolution [52].

A molecule in a high (excited) energy state can relax to a lower state by several processes. It can lose energy to neighbouring molecules through collision, or it can lose energy by emitting a photon of energy equal to the molecule's energy transition. The emission of a photon can be stimulated by the presence of another photon of the same energy, a process called stimulated emission, or it can be emitted spontaneously, a process called spontaneous emission. For a molecule in an excited state (designated state m), the rate of photon emission by stimulated emission is given by the Einstein coefficient for stimulated emission, B_{mn}, multiplied by the energy density of the stimulating radiation at the transition frequency, where n represents the relaxed state. Similarly, the rate of relaxation of molecules in an excited state through spontaneous emission of a photon is given by the Einstein coefficient for spontaneous emission, A_{mn}. The probability of relaxation through collisional processes is given by the collisional quenching rate coefficient, Q_{mn}. The collisional quench rate is related to the spatial distribution, molecular size and energy level of species in the region where the excited molecule resides, and can be quite complicated to determine. The Einstein coefficients, however, are generally well known for major species.

The number of molecules pumped up to an excited state in a given volume of space by incident radiation is proportional to the number density of the species involved, the fraction that are in the appropriate quantum state for absorption, the Einstein coefficient for stimulated

absorption of the molecule and the nature of the stimulating radiation. When a population of ground state molecules is first exposed to incident radiation, the excited upper state begins to be populated as molecules are excited. At the same time, excited state molecules relax through various mechanisms, depopulating the upper state. After a period of time, the excitation and de-excitation rates balance, and a steady state is reached. The time required to reach steady state is a function of the laser spectral irradiance and any deactivating processes such as quenching. For the conditions encountered in this work, steady state is reached in approximately 1ns [52], much shorter than the laser pulse duration, so a steady state analysis is used in the following development. For fluorescence from a finite volume containing a probed species irradiated by a laser sheet of thickness t and height h_L, the number of molecules in the excited state can be determined by [52]:

$$n_1 = \left(\frac{B_{10}}{c} \right) \left[\frac{1}{h_L t} \int_0^\infty E(\nu)\, g(\nu)\, d\nu \right] (f_v f_J n_0)(A t) \qquad \textbf{4.36}$$

where: n_1 = Number of molecules in the excited state

B_{10} = Einstein coefficient for stimulated absorption

c = Speed of light

h_L = Laser sheet height

t = Laser sheet thickness

$E(\nu)$ = Laser energy lineshape function

$g(\nu)$ = Absorption lineshape

f_v = Boltzmann fraction in absorbing vibrational state

f_J = Boltzmann fraction in absorbing rotational state

n_0 = Number density of molecule being probed

A = Area viewed by collection optics

The first term in parenthesis represents the Einstein coefficient for stimulated absorption. The second term is the overlap integral between the laser energy density spectral lineshape and the

molecular absorption lineshape, which represents the amount of laser energy that can potentially be absorbed by molecules in the absorbing quantum states. The third term represents the number density of molecules in the ground state that are in the appropriate quantum state for absorption, and the final term is the volume being probed. It should be noted that the laser sheet thickness, appearing in the second and fourth terms, cancels out, and hence detailed knowledge of laser sheet thickness is not necessary in this portion of the calculation.

The number of fluorescence photons emitted isotropically by the excited molecules can be obtained by multiplying the number of molecules in the excited state by the fluorescence yield, which represents the fraction of excited state molecules that relax by spontaneous emission of a photon:

$$n_p = n_1 \cdot F_y = \left(\frac{B_{10}}{c} \right) \left[\frac{1}{h_L t} \int_0^{\infty} E(\nu)\, g(\nu)\, d\nu \right] (f_v f_J n_0)(A\, t)\, F_y \qquad \textbf{4.37}$$

where: n_p = Number of photons emitted

F_y = Fluorescence yield

A model for the fluorescence yield appropriate to the excitation/detection scheme employed in this work for OH fluorescence is a four level model that allows for several paths of de-excitation of excited state molecules, as shown schematically in Figure 4.14. In this model, OH is excited from the ground state, $v''=0$ level to the first electronic excited state at $v'=1$. Molecules in this state can relax by spontaneous emission of a photon, quenching, or downward vibrational transfer to the $v'=0$ level. In addition, molecules in this state can emit a photon by stimulated emission caused by the excitation radiation. Photons emitted by stimulated emission are emitted in phase with and in the same direction as the stimulating radiation, and are not collected as part of a fluorescence detection scheme. Molecules in the $v'=0$ excited state can relax either by spontaneous emission of a photon or by quenching. Upward vibrational transfer is neglected in this model as upward transfer rates are generally

very small compared to downward rates. This model does not discriminate between rotational levels, and does not include any rotational redistribution, as the collection scheme is assumed to be broad band, detecting all photons arising from the electronic/vibrational transitions shown, regardless of rotational state. The fluorescence yield based on this model is given by:

$$F_y = \frac{A_{11} + A_{10} + V\left(\frac{A_{01}}{Q_0} + \frac{A_{00}}{Q_0}\right)}{Q_1 + b_{01} + A_{11} + A_{10} + V} \qquad \textbf{4.38}$$

where: A_{11}, A_{10} = Spontaneous emission rates from v'=1 to v"=1 and 0 respectively

A_{01}, A_{00} = Spontaneous emission rates from v'=0 to v"=1 and 0 respectively

V = Downward transfer rate

Q_0 = Quench rate from v'=0

Q_1 = Quench rate from v'=1

b_{01} = Stimulated emission rate

The stimulated emission (or absorption) rate is determined from the Einstein coefficient for stimulated absorption multiplied by the laser spectral fluence as follows:

$$b_{10} = b_{01} = \left(\frac{B_{10}}{c}\right)\left[\frac{1}{h_L t}\int_0^{\infty} E(\nu)\, g(\nu)\, d\nu\right] \qquad \textbf{4.39}$$

Therefore, determination of the fluorescence yield requires a detailed knowledge of the laser sheet dimensions as well as temporal characteristics of the laser pulse; details that are often difficult to determine. In addition, since the laser lineshape integral appears in the denominator of the fluorescence yield calculation, when substituted in to Equation 4.38, it is apparent that fluorescence is a non-linear function of laser energy. However, examination of terms in the denominator of the fluorescence yield equation suggests that, if laser energy is sufficiently low, such that b_{01} is small in comparison with the other terms, it may be neglected and fluorescence becomes linear with laser power. In fact, in Equation 4.38, the b_{01} term should

be multiplied by the fraction of upper state molecules that are in the appropriate rotational state for interaction with the stimulating radiation. Since rotational redistributions do occur, though not considered in the above calculation, the effect of this term is substantially reduced.

In atmospheric pressure flames, it is well known that quench rates and vibrational energy transfer rates are much faster than spontaneous emission rates, and hence the spontaneous emission terms in the denominator may be ignored. Invoking these assumptions, the fluorescence yield reduces to:

$$F_y = \frac{A_{11} + A_{10} + V\left(\frac{A_{01}}{Q_0} + \frac{A_{00}}{Q_0}\right)}{Q_1 + V} \qquad \textbf{4.40}$$

Since determination of the b_{10} term is difficult, experimental verification of the theoretical linear relation between fluorescence yield and laser power was performed in this work. It was found that fluorescence intensity varied linearly with laser power up to the maximum available power of 3 mJ in a 70mm high sheet when tested with a steady bunsen burner flame. It should be noted that the maximum laser pulse energy was approximately 6 mJ/pulse, but losses due to the uncoated optics, as well as spatial filtering required to produce a reasonably uniform sheet, reduced the laser energy in the sheet by at least 50%.

The four level model involves fluorescence from four distinct transitions; $A^2\Sigma$-$X^2\Pi$ (1,1), (1,0), (0,1) and (0,0) at 314, 283, 343 and 308nm respectively. An optical collection system including an interference filter to discriminate fluorescence from Mie scattering, used in this work, requires modification of the fluorescence yield equation to account for the filter transmission at the different wavelengths involved. The modified fluorescence yield is given by:

$$F_y = \frac{T_{11}A_{11} + T_{10}A_{10} + V\left(T_{01}\frac{A_{01}}{Q_0} + T_{00}\frac{A_{00}}{Q_0}\right)}{Q_1 + V} \qquad \textbf{4.41}$$

where: T_{11}, T_{10}, T_{01}, T_{00} = Filter transmission at the transition wavelength

In this work, the interference filter used had a 10nm bandpass, centred at 314nm. The transmission factors for this filter were [53]:

$T_{11} = 0.17$

$T_{00} = 0.11$

$T_{10} = T_{01} = 0$

Hence, the fluorescence yield reduces to [54]:

$$F_y = \frac{T_{11} A_{11} + V T_{00} \dfrac{A_{00}}{Q_0}}{Q_1 + V} \qquad \textbf{4.42}$$

The number of photons emitted that are collected by a lens located at a point in space, by a region that images onto one pixel of the ICCD, can be determined from the above equations as follows:

$$n_{pp} = \left(\frac{B_{10}}{c} \right) \left[\frac{1}{h_L} \int_0^{\infty} E(\nu)\, g(\nu)\, d\nu \right] (f_v f_J n_0)(A_p)(F_y) \left(\frac{\Omega}{4\pi} \right) \qquad \textbf{4.43}$$

where: Ω = Solid angle of collection

A_p = Area of laser sheet imaged by a pixel

n_{pp} = Number of photons directed to pixel

The number of photons directed to the pixel in question do not necessarily arrive at the pixel, due to inefficiencies in the optics. However, the method used to calibrate the system, described later in Section 4.2.2, calibrates over these optical losses, and hence they do not need to be considered explicitly.

The fraction of probed molecules in the appropriate quantum states for absorption can be determined from the following expressions [52]:

$$f_v(T) = \exp\left(- \frac{v h c \omega_e}{k T} \right) \left[1 - \exp\left(- \frac{h c \omega_e}{k T} \right) \right] \qquad \textbf{4.44}$$

$$f_J(T) = \frac{h c B_v}{k T} (2J + 1) \exp\left(- \frac{B_v h c J(J + 1)}{k T} \right) \qquad \textbf{4.45}$$

where: v = Vibrational quantum number

J = Rotational quantum number

h = Planck's constant

c = Speed of light

ω_e = Molecular vibrational energy constant

B_v = Rotational constant

k = Boltzmann constant

T = Temperature

The laser fluence overlap integral term can be evaluated by considering the laser spectral lineshape and the molecular absorption lineshape. The laser lineshape is assumed to be Gaussian, and can be modelled as follows [52]:

$$E(\nu) = \frac{2 E_0}{\sqrt{\pi}\, \Delta \nu_L} \exp\left(- \frac{4 (\nu - \nu_0)^2}{\Delta \nu_L^2} \right) \qquad \textbf{4.46}$$

where: $E(\nu)$ = Laser spectral lineshape function

E_0 = Laser pulse energy

$\Delta \nu_L$ = Laser linewidth (FWHM)

ν = Frequency

ν_0 = Centre frequency

The molecular absorption lineshape may be dominated by Doppler broadening, associated with the distribution of velocities of the molecules present, or pressure broadening, associated with molecular interactions during photon absorption and/or emission, or a combination of the two. The Doppler lineshape is generally modelled as follows [52]:

$$g_D(\nu) = \frac{c}{\nu_0}\sqrt{\frac{m}{2\pi k T}}\exp\left[-4\ln 2\,\frac{(\nu-\nu_0)^2}{\Delta\nu_D^2}\right] \qquad \textbf{4.47}$$

$$\Delta\nu_D = \frac{2\nu_0}{c}\sqrt{\frac{2\ln 2\,k T}{m}} \qquad \textbf{4.48}$$

where:
$g_D(\nu)$ = Doppler lineshape function
c = Speed of light
ν_0 = Center frequency of transition
m = Mass of molecule
k = Boltzmann constant
T = Temperature
ν = Frequency
$\Delta\nu_D$ = Doppler line width at half height

It should be noted that the integral of $g_D(\nu)$ over all frequencies is 1.

The pressure broadened lineshape is modelled as a Lorentzian distribution as follows [52]:

$$g_c(\nu) = \frac{\Delta\nu_c}{2\pi}\,\frac{1}{(\nu-\nu_0)^2 + (\Delta\nu_c/2)^2} \qquad \textbf{4.49}$$

where: $g_c(\nu)$ = Pressure broadened lineshape function

$$\Delta\nu_c = \frac{1}{\pi\,\tau} \qquad \textbf{4.50}$$

$\Delta\nu_c$ = Pressure broadened linewidth

τ = Timescale of interactions

When both pressure and Doppler broadening are significant, a Voigt profile is generally used to model the resulting lineshape as follows [52]:

$$g(\nu) = 2\sqrt{\frac{\ln 2}{\pi}}\,\frac{V(a,x)}{\Delta\nu_D} \qquad \textbf{4.51}$$

$$V(a,x) = \frac{a}{\pi}\int_{-\infty}^{\infty}\frac{e^{-y^2}}{a^2 + (x-y)^2}\,dy \qquad \textbf{4.52}$$

$$a = \sqrt{\ln 2}\,\frac{\Delta\nu_c}{\Delta\nu_D} \qquad \textbf{4.53}$$

$$x = 2\sqrt{\ln 2}\,\frac{(\nu - \nu_0)}{\Delta\nu_D} \qquad \textbf{4.54}$$

Generally, the overlap integral must be evaluated numerically. In this work, the overlap integral $\int E(\nu)g(\nu)d\nu$ varied from 0.83 $E_o/\Delta\nu_L$ to 0.69 $E_o/\Delta\nu_L$ over the temperature range of 1000 - 2000K, with a value of 0.75 $E_o/\Delta\nu$ at 1500K. The variation with temperature is due to the Doppler linewidth, which increases with temperature.

The Einstein coefficients A and B are generally known for the major combustion species, as are the other constants appearing in the above equations. These are summarised for the $X^2\Pi$ - $A^2\Sigma$ (1, 0) transition for OH and the $X^2\Pi$ - $A^2\Delta$ (0, 0) transition for CH in Table 4.4.

The quench rate Q, however, is more difficult to obtain and requires a detailed knowledge of all species present in the region of interest, their number density (dependent on temperature), their collisional cross-section and velocity (also temperature dependent). Generally, experimental values are used. Garland and Crosley[55] reviewed quenching data for OH, NH and CH and concluded that "...OH quenching can be estimated to within 30-50% in many cases, but only to within a factor of three for NH and CH". In practice, the uncertainties associated with predictions of quenching rates have restricted planar measurements of species concentration in unsteady flows to qualitative imaging, or, at best, semi-quantitative measurements where a qualitative concentration field is calibrated by independent measurement or calculation of concentration at a point. One approach to quenching, given by Eckbreth [52], is to calculate the quenching rate from all collisionally active species present, using:

$$Q_i = \sum_i n_i \sigma_i u_i \qquad \textbf{4.55}$$

where: n_i = number density of ith deactivating species

σ_i = collisional cross-sectional area

u_i = relative velocity between colliding species

This method, however, requires a knowledge of species present, their temperature (as $u_t \propto T^{1.2}$) and their concentration, knowledge generally not available. More typically, experimentally-obtained values for the quenching rate are used, albeit with quite a high degree of uncertainty. Quench rates for OH in various types of atmospheric pressure flames have been reported by Garland and Crosley [55] and Tsujishita and Hirano [56], among others, and this data has been used in this work.

The total number density of the species being probed can be determined from Equation 4.43. As can be seen from Equations 4.47 and 4.48, the population fractions are a function of temperature as well as rotational and vibrational quantum numbers, and it would seem that knowledge of temperature is required to obtain concentration. However, by differentiating Equation 4.45 with respect to temperature and setting the derivative equal to zero, the rotational level J which minimizes sensitivity of ground state population to temperature can be determined [52]. For OH, selecting J = 5.5 or 6.5 limits the sensitivity to temperature to within 10% over the range of temperatures typically seen in hydrocarbon/air flames (1000 - 2300K).

From the above, and knowing the photon flux on a given pixel, the local number density of a particular species can be determined. Conversely, if the local number density is known, the local temperature can be deduced. In practice, it is possible to select molecular transitions whose initial state population does not vary much over the temperature range present in the field of interest, thus allowing reasonably accurate measurements of local number densities even when the local temperature is not known to any degree of precision.

The method of imaging OH used in this work involves excitation of the $Q_1(6)$ rotational transition (1,0) band of the $A^2\Sigma$-$X^2\Pi$ at 283 nm[57], and observing the resulting fluorescence from the (1,1) and (0,0) bands at 306-320 nm. Excitation of the (1,0) band and observation of the (1,1) and (0,0) fluorescence allows sufficient spectral distance between the excitation and fluorescence frequencies such that Mie scattered light can be effectively filtered out. Fluorescence intensity is usually sufficient to allow single shot imaging of OH. Some interference due to elastic scattering from large methanol droplets was observed, but this was not a problem in the present study as this interference had the appearance of isolated,

spherical points, and were clearly discernable from OH, which appeared in continuous structures.

CH was imaged by exciting one of the R-branch absorption lines of the $A^2\Delta$-$X^2\Pi$ (0,0) transition near 426 nm, and observing fluorescence from the Q-branch transitions as well as some of the adjacent, collisionally-populated transitions near 431.5 nm following the method used by Allen *et al* [58]. Fluorescence intensities from CH are much lower than from OH, but are still detectible with single laser shots in some cases, as will be discussed later. Table 4.5 summarizes the excitation/detection schemes employed in this work.

Constant	**OH** ($A^2\Sigma$ - $X^2\Pi$ (1, 0))	**CH** ($A^2\Delta$ - $X^2\Pi$ (0, 0))
A_{00} A_{10} A_{11}	1.4×10^6 sec^{-1} (0,0) [59] 5.11×10^5 sec^{-1} (1,0) [59] 8.38×10^5 sec^{-1} (1,1) [59]	1.8×10^6 sec^{-1} [52]
Q_0, Q_1	5.6×10^8 sec^{-1} (Q_0 and Q_1-see Equation 4.49) [55] [56]	3×10^9 sec^{-1} [55]
B_{10}	1.9×10^{24} $cm^3 J^{-1} s^{-2}$ [59][60]	8.7×10^{24} $cm^3 J^{-1} s^{-2}$ [52] [60]
B_v	18.513 cm^{-1} $^2\Pi(v'' = 0)$ 16.126 cm^{-1} $^2\Sigma(v'' = 1)$ [57]	14.192 cm^{-1} $^2\Pi(v'' = 0)$ [61] 14.579 cm^{-1} $^2\Delta(v'' = 0)$ [61]
ω_v	3569.59 cm^{-1} $^2\Pi$ [57] 2792.92 cm^{-1} $^2\Sigma$ [57]	2860.75 cm^{-1} $^2\Pi$ [61] 2933.57 cm^{-1} $^2\Delta$ [61]

Table 4.4: Spectroscopic constants for OH and CH

The equipment available for implementing the planar laser-induced fluorescence study consists of a Lumonics HY750 Nd:YAG pump laser with harmonic generator, capable of 1064, 532 and 355 nm operation. In Q-switched mode, the laser pulse duration is approximately 10 ns, and maximum pulse frequency is 20 Hz. Power output has been measured at 532 nm to be approximately 180 mJ per pulse at 10 Hz.. The Nd:YAG laser is coupled with a Lumonics HyperDye 300 pumped dye laser, capable of producing tunable laser

output over a wide range of frequencies, depending on the dye used. Conversion efficiency can approach 30%, depending on the frequency chosen and dye used. The output from the dye laser can be frequency doubled using a Lumonics HyperTrack 1000 second harmonic generator, with a maximum conversion efficiency of approximately 10%, depending on the wavelength and crystal used. Hence, the maximum theoretical UV output, assuming the UV frequency desired matches the peak operating wavelength of both the doubling crystal and dye, is approximately 6 mJ/pulse, adequate pulse energy for planar imaging of LIF signals. The bandwidth of the UV output is approximately $0.25cm^{-1}$.

The output beam from the laser system is passed through two cylindrical and one spherical quartz lens, to produce a laser sheet approximately 70mm high and 0.75mm thick at the sheet waist. The beam was passed first through a 12mm focal length cylindrical lens, then through a 300mm focal length cylindrical lens placed approximately 300mm downstream of the first lens. The output of this lens was then directed through a 1000mm focal length spherical lens to minimize the laser sheet thickness at the focal plane, where the flame being probed was located. Variation of the distances between lenses allowed variation of the laser sheet height, while maintaining minimum sheet divergence. Including optical losses (all optics are uncoated) and after spatial filtering to minimize the intensity variation across the laser sheet, the resultant maximum illumination intensity is approximately 5 mJ/cm^2, or 5×10^5 W/cm^2 at 10 ns pulse duration. Maximum spectral irradiance is approximately 2.5×10^6 $W/cm^2\text{-}cm^{-1}$. See Figure 4.15 for a general arrangement of the system.

The optical imaging system consists of a Princeton Instruments intensified, UV-extended ICCD camera, with a 576 x 384 pixel array, sensitive down to light wavelengths of approximately 180 nm. A 105mm UV-grade macro imaging lens is presently installed. The ICCD array is thermo-electrically cooled, to minimize dark charge buildup. The ICCD can be gated for exposures as short as 20 ns, within 12ns of receiving a TTL trigger signal, thus allowing for close synchronization with the laser pulse. The camera is coupled with a controller and computer, to allow on-line image display and acquisition. One shortcoming of the ICCD system is that 2 to 3 seconds are required to read off an image from the CCD chip, and an additional 1 or 2 seconds is required to store the image to the computer disk, thus limiting the

image acquisition speed. The image can be stored with an intensity resolution of 16 bits/pixel, with intensity being linearly proportional to bit count to within 1% over the upper 95% of the intensity range. There is a slight, reproducible non-linearity in the lower 5% of the range [62]. The camera is sensitive enough to detect single photoelectrons, (although S/N considerations make single photon detection somewhat suspect) and quantum efficiency at 300nm is approximately 15-20%.

The software operating the camera controls the electronic shutter, which can be set for exposure times as short as 5 ms. When operated in gate mode, the gate pulse generator triggers the image intensifier, while the software controls the shutter. When the laser is operated at 10 Hz, a typical set-up sets the shutter at 0.1 sec, and the gate pulse generator receives a TTL signal from the laser which gates the intensifier in synchronization with the laser pulse. The pulse width was generally set for approx. 40 ns, wide enough to ensure capture of the entire laser burst, but short enough that flame emission interference is insignificant.

The software also includes some image processing features, including background subtraction, which subtracts a background image (typically an exposure made with the lens cap in place) from the fluorescence image, eliminating the base bias signal from the image. This can be done on-line or in post-processing, but on-line background subtraction slows down acquisition considerably and was not used.

PROCESS	OH	CH
Excitation	$A^2\Sigma$-$X^2\Pi$ (1,0) transition at 283 nm	$A^2\Delta$-$X^2\Pi$ (0,0) transition at 426 nm
Detection	$A^2\Sigma$-$X^2\Pi$ (1,1), (0,0) transitions at 306-320 nm (10 nm filter bandwidth)	$A^2\Delta$-$X^2\Pi$ (0,0) transition at 431.5 nm (1nm filter bandwidth)
Expected pulse energy (10 ns duration)	6 mJ/pulse	15 mJ/pulse
Laser sheet dimensions	70mm x .75mm	
Imaging system	Princeton Instruments UV-extended ICCD camera, 576 x 384 pixels	
Collection lens	Nikor 105mm f/4.5	

Table 4.5: LIF Operating parameters

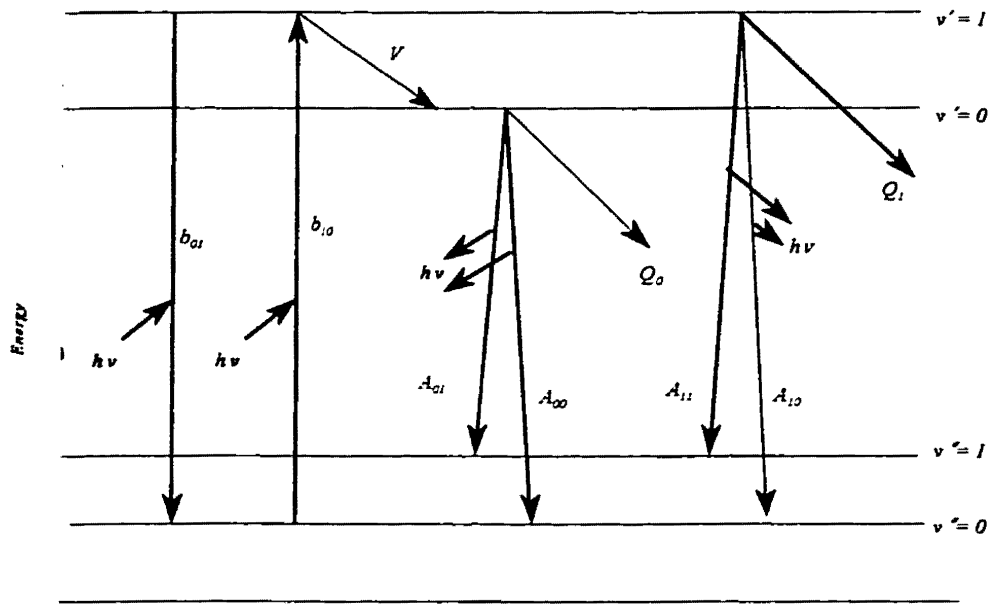


FIGURE 4.14: Four level fluorescence model

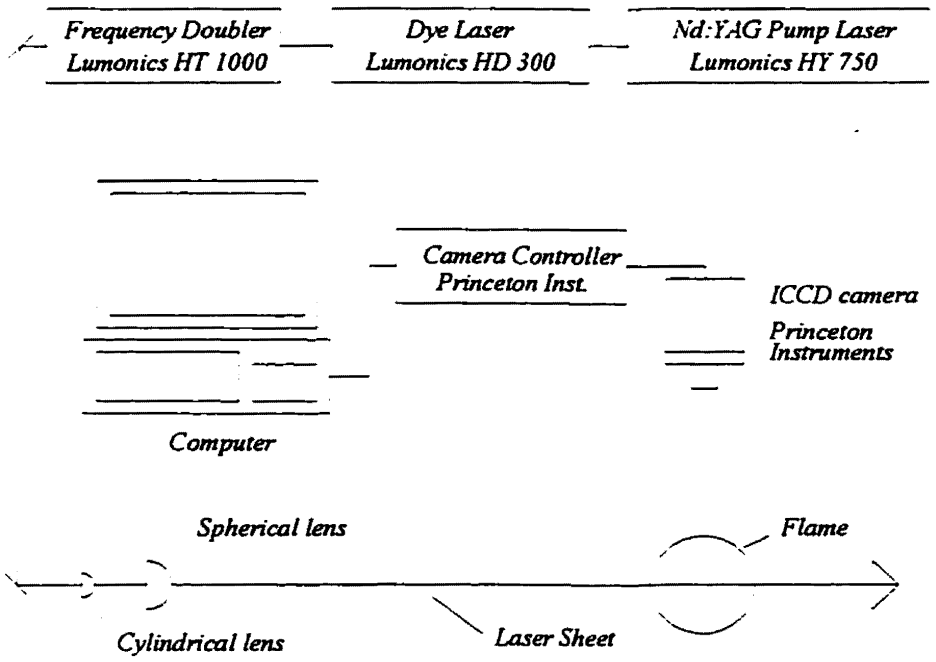


FIGURE 4.15: Planar laser-induced fluorescence system layout

4.2.2. Camera Calibration

The imaged fluorescence is given by Equation 4.43 in terms of N_{PP}, or number of photons per pixel. The output of the camera is a scaled intensity per pixel 16 bit number. In order to extract the number of photons incident on the pixel from this intensity number, a camera calibration is necessary which takes into account optical efficiency, ICCD quantum efficiency, and instrument gain. A calibration method based on Rayleigh scattering [63] was used to correlate reported intensity with number of photons per pixel. The method takes advantage of the fact that the Rayleigh scattering cross section for air is well known [64] and is 8.44 x 10^{-27} cm^2/sr at 315 nm for vertically polarized light. The Rayleigh scattered power from a given volume of air is:

$$E_{Ray} = \left(n \frac{E_i}{A} \right) (N_A \sigma_{Ray} \Omega)(A L) \qquad \textbf{4.56}$$

where: E_{Ray} = Rayleigh scattered energy

E_i = Incident laser energy

n = Number of laser pulses during exposure

N_A = Number density of air molecules

σ_{Ray} = Rayleigh scattering cross-section

Ω = Collection solid angle

L = Length of imaged volume

A = Laser sheet cross-sectional area

The first term in parenthesis is the incident energy per unit area, and the second term is the Rayleigh scattering rate per unit volume. The third term is the volume being imaged. It should be noted that the cross-sectional area of the laser beam, A, cancels out of the first and third terms, and hence knowledge of the laser beam dimensions is not required.

The incident energy arising from viewing a length L of laser beam at right angles in space can be converted to a photon count by dividing by $h\nu$, Planck's constant times

frequency. The number of photons arriving at the lens can then be determined as shown below. It should be noted that the incident pulse energy is the time averaged power divided by the number of pulses per second.

$$n_{pp} = \left(n \frac{E_i}{h \nu} \right) \left(N_A \sigma_{Ray} \Omega \right) L \qquad 4.57$$

where: n_{pp} = Number of photons arriving at lens

If L is selected to correspond to the imaged laser beam length on one pixel, then all photons arising from the volume in space defined by this laser beam length arriving at the lens will be destined for a column of pixels imaging this beam segment. If the intensity counts of the pixels in the column of pixels are summed up, a calibration factor corresponding to intensity count per photon incident at the lens can be obtained. This calibration factor can then be used to obtain n_{pp} required in the fluorescence calculation from an intensity count for a pixel. A sample calibration calculation is presented in Appendix 1.

This calibration method, if performed at the fluorescence wavelength of interest, has the advantage of eliminating the need to evaluate lens and ICCD quantum efficiencies explicitly, as it relates the ICCD pixel intensity count to a photon count incident at the camera lens. In addition, calibration based on the sum of pixel intensities for a pixel length of laser beam eliminates the need to know the intensity distribution across the laser beam.

In practise, the Rayleigh signal is quite weak, and is easily contaminated by Mie scattering from dust and particulate. In order to obtain clean signal, a horizontal laser beam was imaged and intensity readings from vertical columns of pixels summed. Any pixels receiving photons scattered by particulate would result in a high intensity, with a low limit set by pure Rayleigh scattering. The data set consisting of 576 pixel columns was examined and the low limit determined and used for calibration purposes. The result of this calibration was a correlation between intensity count and number of photons per pixel at a particular lens aperture setting and ICCD gain setting. To adjust for aperture and gain variations, intensity counts were monitored using a steady light source as gain and aperture varied, resulting in the

calibration curves shown in Figures 4.16 and 4.17.

Since the laser sheet intensity is not uniform, it is necessary to adjust the fluorescence calculation to account for local conditions in the sheet. Figure 4.18 presents the normalized (by mean sheet energy) laser sheet intensity variation. As can be seen, variations are on the order of 10% across the sheet width.

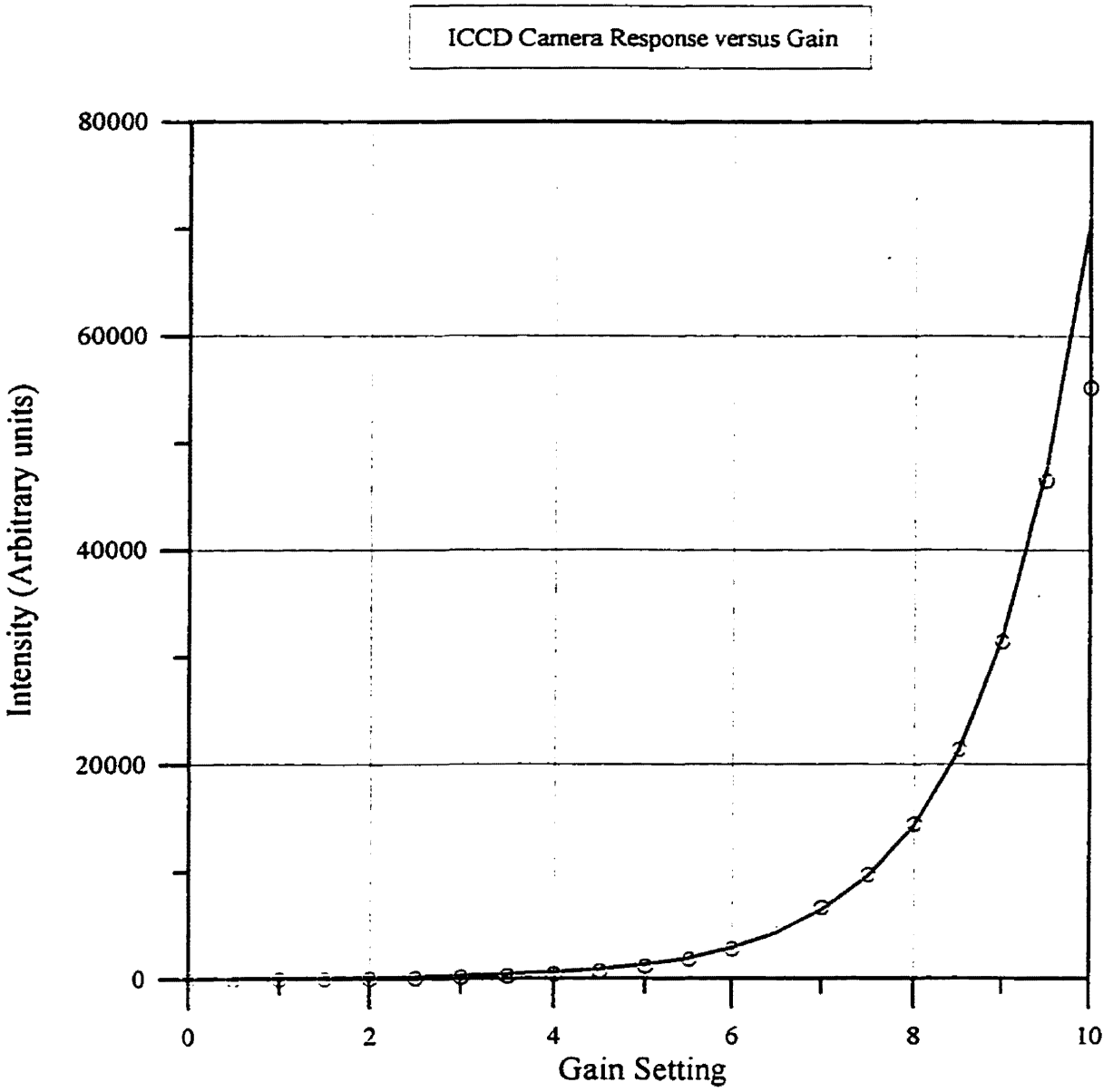


FIGURE 4.16: ICCD camera response curve

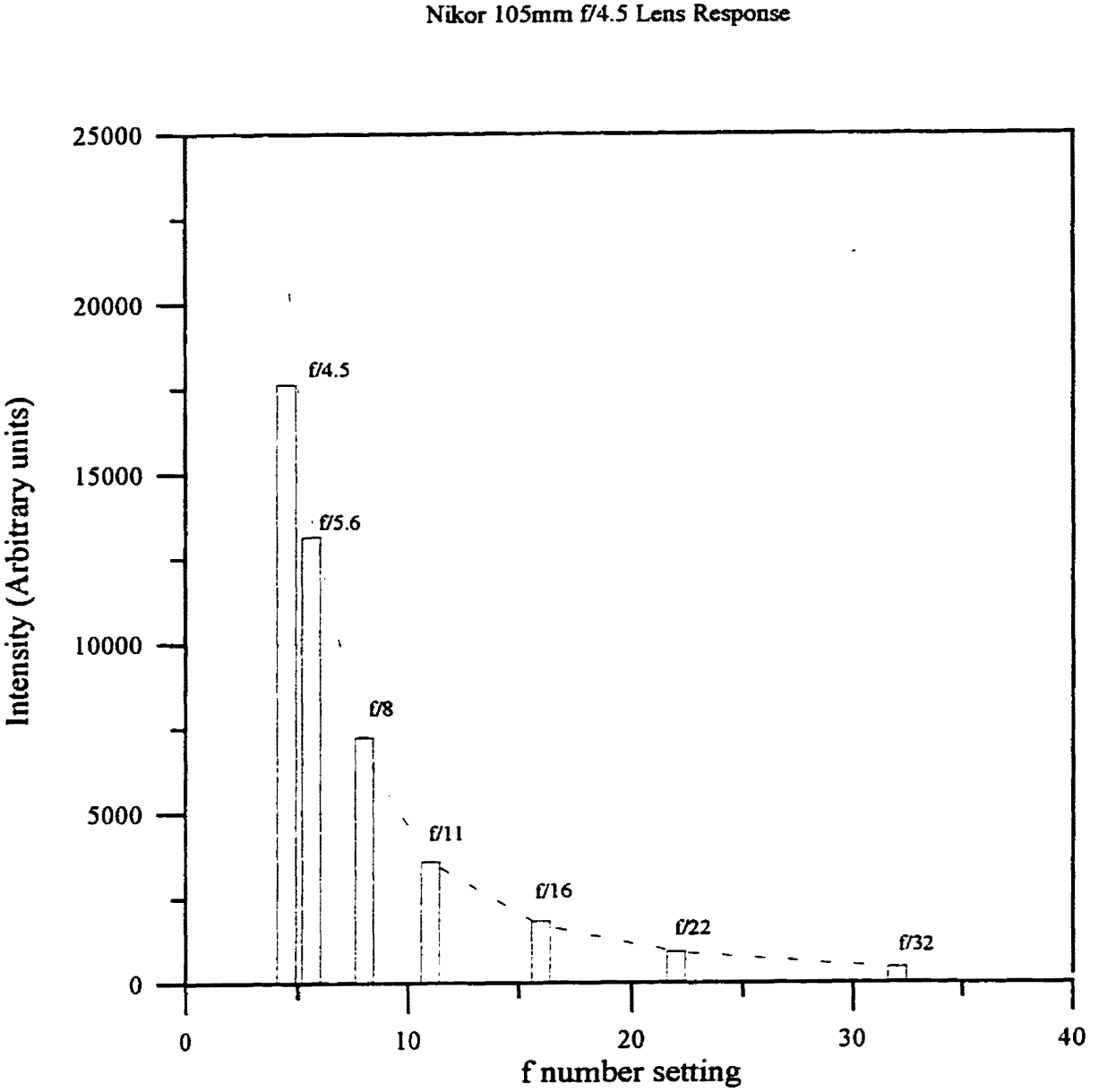


FIGURE 4.17: Nikor 105mm f/4.5 UV grade lens response

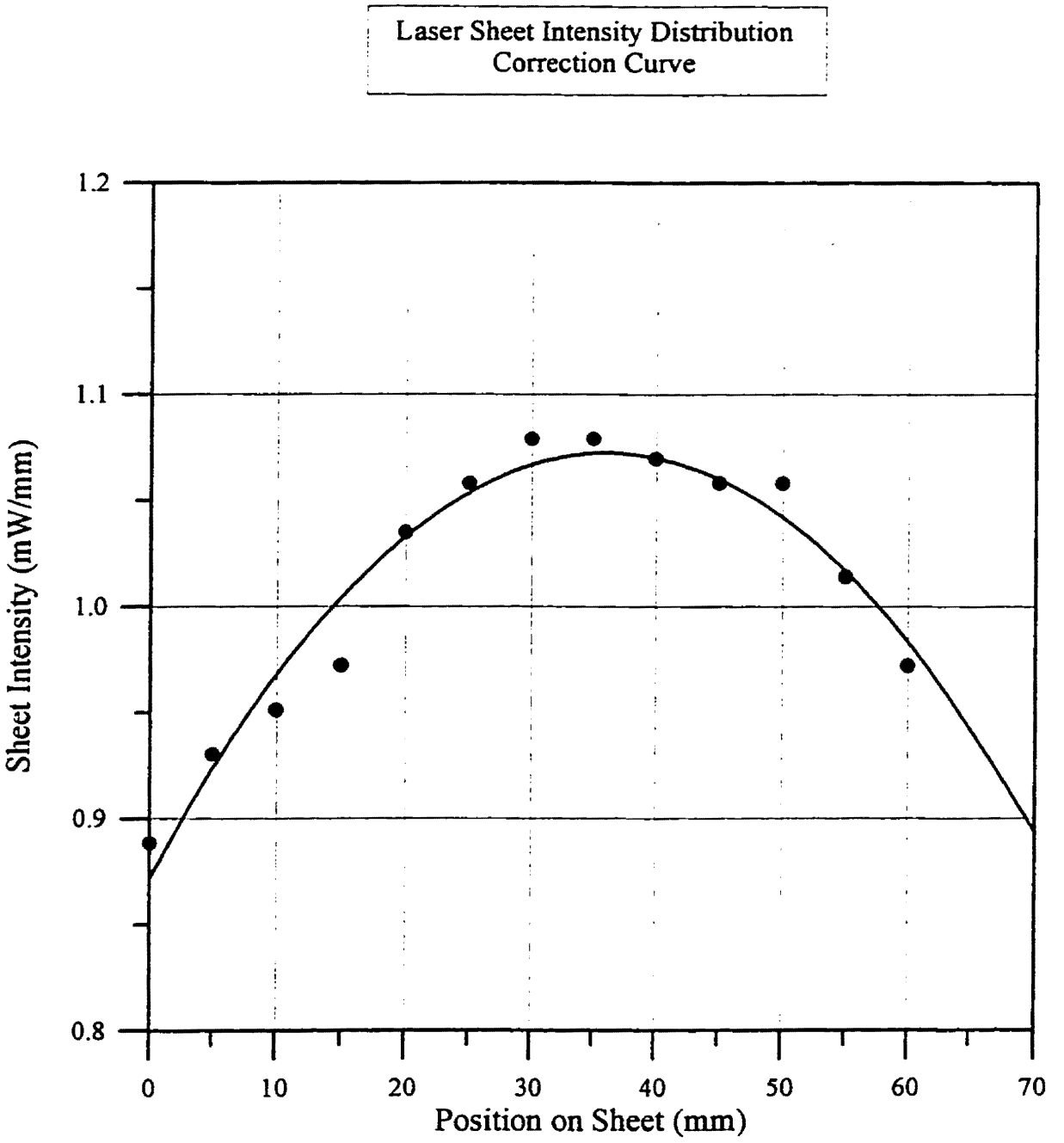


FIGURE 4.18: Laser sheet intensity variation

4.3. TEMPERATURE MEASUREMENTS

Temperature measurements were made using a 75 μm type S (Pt/Pt-10%Rh) thermocouple, as shown in Figure 4.19. The thermocouple was connected to a custom-made 400x amplifier, which was coupled to a DOSTEK 1400A LV interface which provides a 12 bit analog to digital conversion. Sampling rate and sample size were controlled through software [45]. Generally, the system was set to collect data and calculate mean temperature from a 2048 sample data set, sampled at 250 Hz, on the same order as most of the PDPA measurement sets. The reported mean temperatures were not compensated for radiation or conduction losses/gains, for reasons that will be discussed in Chapter 7.

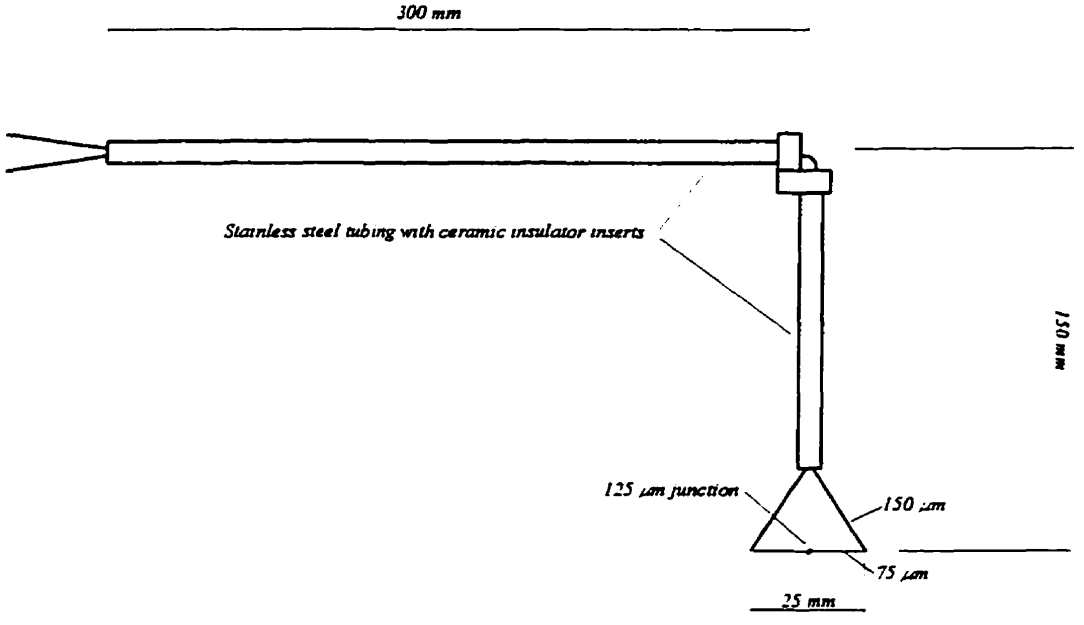


FIGURE 4.19: Thermocouple diagram

4.4. PHOTOGRAPHIC TECHNIQUES

Photographic images of the spray flame were made using laser sheet illumination, as shown in Figure 4.20. An argon-ion laser, operated in multiline mode at approximately 400 mW power was spread into a sheet using a cylindrical glass rod, and photographs made at 90° using a Pentax 35mm camera and a Pentax 50mm f/1.4 lens. ISO 400 colour film was used at exposure times ranging from 1/8 to 1/60 second, and a Vivitar 80B (blue) filter was used to enhance the visibility of laser-illuminated spray droplets against the red flame. A flat black background was used to maximize contrast.

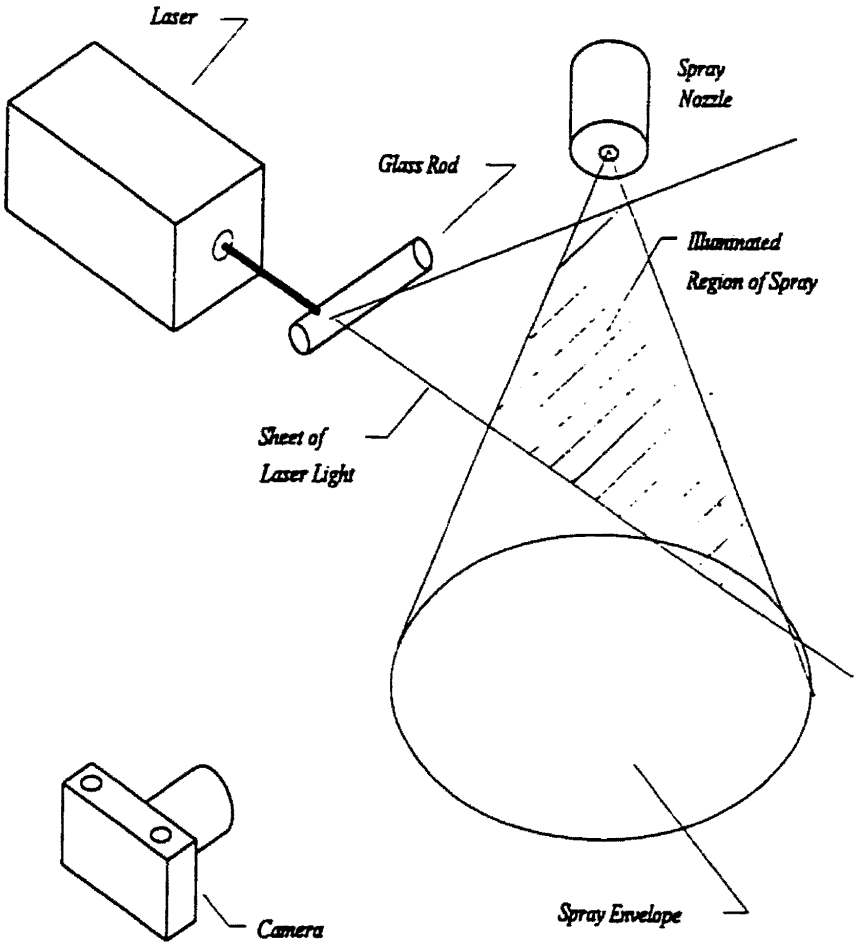


FIGURE 4.20: Photographic arrangement

CHAPTER 5

FACILITY AND EXPERIMENTAL PROCEDURE

5.1. The Burner System

The burner studied in this work consists of a hollow central brass cylinder fitted with a standard Delavan .75-60°A pressure-swirl atomizer nozzle at the exit end. These nozzle designations refer to a 60° total spray cone angle with a nominal fuel flow rate of 0.75 US gallons /hour of No. 2 heating oil at 100 PSIG (689 kPa) pressure drop. The nozzle end is also fitted with a stainless steel bluff body that fits flush with the atomizer tip. This assembly is mounted concentrically within an air shroud consisting of a conical diffuser section, followed by a straight honeycomb and a conical contraction section. The end of the contraction section is fitted with a straight stainless steel tube which surrounds the inner bluff body and ends flush with it, forming an annular passage of 64mm OD by 50mm ID. A cross section of the entire assembly is shown in Figure 5.1. Air is supplied to the burner by a turbo-blower, through a calibrated rotameter. Fuel is supplied to the atomizer through the inner brass cylinder from a pressurized holding tank, and metered through a calibrated rotameter. The entire burner assembly is mounted in the vertically up-firing position on a manual x-y-z traversing system to allow measurements to be made in three dimensions.

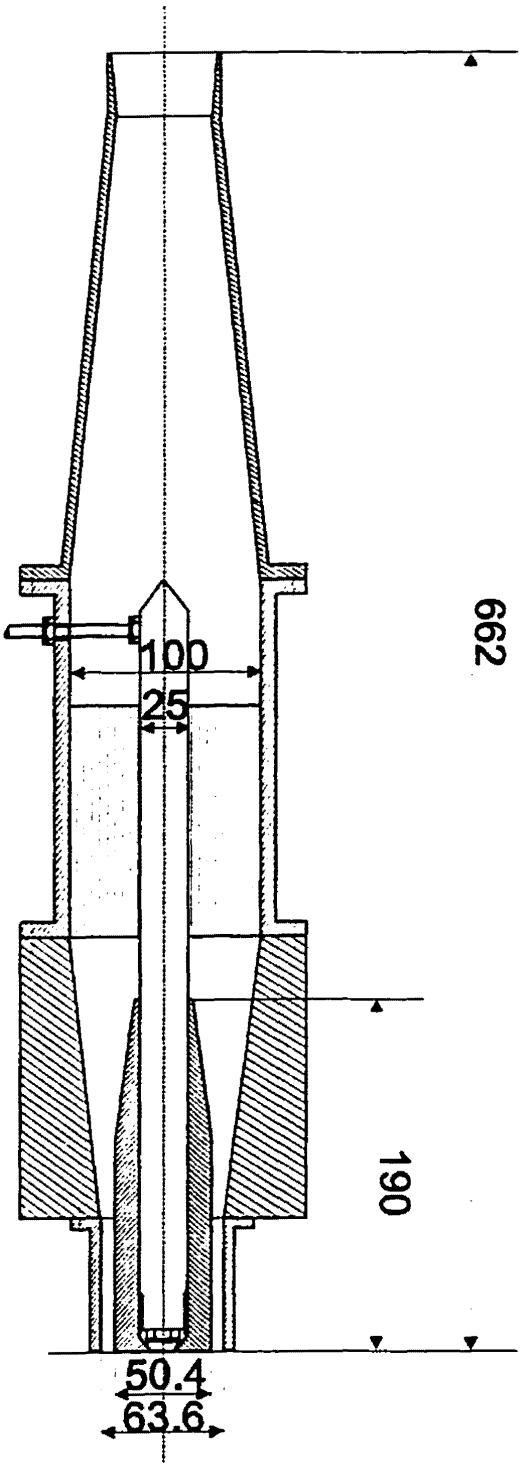


FIGURE 5.1: Rig cross-section
(all dimensions in mm)

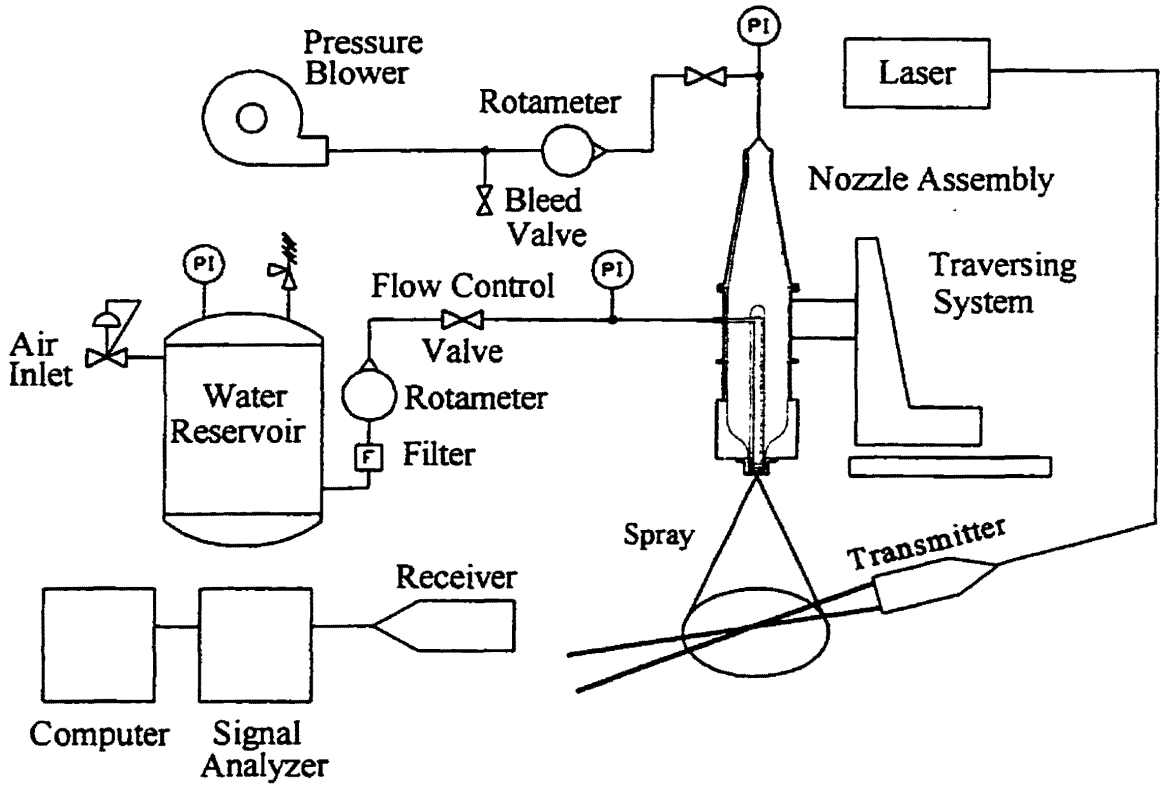


FIGURE 5.2: Burner system schematic diagram

5.2. Experiment Description

The experiments reported herein examined the burner configuration described above using industrial grade methanol at constant flow rate under five different annular air jet flow rates; 0, 2.8, 5.6, 8.4 and 11.2 g/sec, corresponding to volume flow rates of 0, 2.38, 4.77, 7.15 and 9.52 *l*/s. Reynolds numbers, based on annulus inner diameter, were 0, 6500, 13000, 19500 and 26000. The methanol flow rate was fixed at 0.42 g/s at a nozzle pressure of 620 kPa, corresponding to equivalence ratios of ∞, 1, 0.5, 0.33 and 0.25 based on annular air flow rate. The burner was firing in room air without enclosure at all times. Measurements were made using PDI, PLIF, thermocouples, and 35mm photography.

5.3. Photographic Study

Photographic images of the flame were taken under all operating conditions described above. Laser sheet lighting across the flame was used to highlight the fuel spray while maintaining good visibility of the flame envelope itself. Two sets of exposure times were used, 1/60 sec and 1/8 sec. Images made at 1/60 second were the shortest exposures that could be made while still producing good images with ISO 400 film and an f/1.4 lens, and froze some features of the flames. Images made at 1/8 second were exposed for a sufficient time that the resulting images were essentially time averaged.

5.4. PLIF Measurements

PLIF images were taken at each operating condition through the centreline plane. The field of view imaged was 100mm wide by 65mm high for all images. Images were acquired at the nozzle discharge, 65mm downstream, and 130mm downstream, covering a total of 195mm from the nozzle exit. At each location, five instantaneous and one 100-shot average images were made.

5.5. PDI Measurements

PDI point measurements were made in 8 planes downstream of the nozzle; z = 10, 25, 40, 60, 80, 100, 140 and 200mm. In each plane, data was taken along one diameter, with spacing between measurement points commensurate with the gradients present. At each measurement point, 10000 valid samples were taken (or 200 seconds of sampling, whichever came first). Each sample included particle diameter and axial and radial velocity. Derived statistics from the sample set included four different mean diameters (D_{10}, D_{20}, D_{30} and D_{32}), mean and RMS velocities, volume flux and droplet number density. In addition, several tests were made using methanol fuel dyed with Acid Red #1 in order to enhance the visibility of small droplets for subsequent determination of gas-phase velocity, as discussed in section 4.1.6.

5.6. Temperature Measurements

Temperature measurements were made in the same planes and for the same operating conditions as the PDI measurements to allow direct comparison on a point by point basis. Measurements were terminated at those locations where obvious thermocouple wetting by fuel spray was observed.

CHAPTER 6

RESULTS AND DISCUSSION

6.1. Photographic Tests and Visual Observations

Figure 6.1a and b present images of the spray flame with annular air off and a methanol flow rate of 0.42 g/s. A laser sheet illuminated the spray in a plane containing the nozzle axis, normal to the camera. Figure 6a presents a photograph taken at 1/8 second exposure. As can be seen from this figure, the flame appears to be stabilized approximately 12mm above the burner nozzle. This stabilization point is quite steady, and is quite symmetric about the nozzle axis. An inner reacting core is visible inside the flame, approximately 23mm in diameter, with little change in width downstream. This inner core was observed to be quite steady in the region within approximately 150mm of the nozzle, with transition to turbulence occurring approximately 100 mm downstream. An outer reacting region anchored at the same location as the inner zone was observed, which initially spread outward at an angle approximating the spray cone angle for a distance of approximately 50mm downstream of the nozzle. Beyond this distance, the flame sheath maintained a diameter of approximately 65mm for another 100mm or so, before becoming wavy and turbulent. Considerable amounts of fuel spray are observed outside the flame sheath, which would contribute to low combustion efficiency, although some fuel would undoubtedly be re-entrained into the flame further downstream.

Figure 6-1b is an image of the same flame, but taken with a 1/60 second exposure time. The outer boundary of the inner core appears quite smooth, suggesting laminar flow in this region. Some unsteadiness is apparent inside this core, although the details are indistinct. Some surface waviness of the outer flame shroud is also evident in this image. It is interesting to note the steadiness of flame stabilization point, despite the dense spray present in this region. The overall flame height under these operating conditions is approximately 55 cm. It should be noted that the steadiness of the flame under these conditions is strongly influenced by local

ambient conditions. Any slight draft or room air movements cause a noticeable response in the flame, as would be expected in a buoyancy-driven diffusion flame.

Figures 6.2a and b present a similar pair of photographs for the annular air flow rate of 2.38*l/s*. It would appear from the long exposure photograph (1/8 sec), Figure 6.2a, that the annular air jet has displaced the outer flame shroud downstream. The outer flame shroud observed under these conditions was highly unsteady and intermittent, as is apparent in the short exposure (1/60 sec) photograph in Figure 6.2b. An inner flame core is still apparent, although its base diameter has increased to approximately 28mm. The flame stabilization point has moved closer to the nozzle, to within about 5 or 6 mm, compared to the no annular air jet case. It is evident that a considerable amount of fuel spray emerges from the inner flame shroud, but appears to be almost entirely consumed in the flame lobes apparent in the outer flame shroud in Figure 6.2a. However, this flame region is quite intermittent, as seen in Figure 6.2b, and some fuel does escape unburned. Overall, the outer flame sheath is quite turbulent, with large scale eddy structures apparent in Figure 6.2b. The overall flame height under these operating conditions is approximately 50 cm.

When the annular air flow rate is increased to 4.77*l/s*, the flame structure changes considerably, as seen in Figures 6.3a and 6.3b. There is no longer a distinct inner core and an outer flame sheath. Only a single reaction zone is evident. It is interesting to note that flame is evident between the spray cone and the bluff body surface, with flame impingement apparent. The entire spray cone must pass through a flame before emerging into the surrounding flow. The reaction zone in the region near the nozzle has a tulip shape, with a secondary reacting flow apparent between the main tulip-shaped zone near the outer edge of the bluff body. The spray cone appears to be deflected downstream somewhat upon emerging from the reaction zone, though not to a great degree. Further downstream, the flame is quite turbulent, although the structures appear to be smaller, though more energetic, than the 2.38 *l/s* annular air flow case. There still appears to be a considerable amount of fuel spray that emerges from the flame, although some is likely to be entrained further downstream. Under this operating condition, the bluff body gets quite hot due to the direct flame impingement on it, and as a result, the fuel exiting the nozzle is quite hot. This effect causes a noticeable change

in the flame structure between initial light-up, when the bluff body is still cold, and steady state conditions, which are much steadier than the cold case. No such effect is noted under any of the other operating conditions tested. Overall flame height under these operating conditions is approximately 35 cm.

Figures 6.4a and b and 6.5a and b present the flame resulting with an annular air flow rate of 7.15 and 9.52 *l/s* respectively. The flames appear quite similar in configuration in both these cases, stabilizing just above the bluff body, and forming a tapered reaction zone that cuts through the emerging spray cone. The spray cone emerging through the reaction zone appears to curve back towards the flame, indicating re-entrainment of unburnt fuel is occurring. The short exposure images, Figures 6.4b and 6.5b, show a considerable amount of turbulence downstream of the nozzle, but appear quite steady in the region near the nozzle, with only small scale features apparent. The overall flame length for these cases is approximately 28 and 24cm respectively, approximately half the air off case.

It would seem from these images that the annular air jet completely changes the structure of the flame, compared to the air off case. The laminar, two reaction zone structure apparent in Figures 6.1a and b is replaced by a single reaction zone flame, with varying degrees of turbulence. Overall flame length is reduced with increasing annular air, and re-entrainment of unburned fuel appears to be enhanced. The annular air jet also seems to serve as a shield, reducing the effect of ambient air movement on the flame.

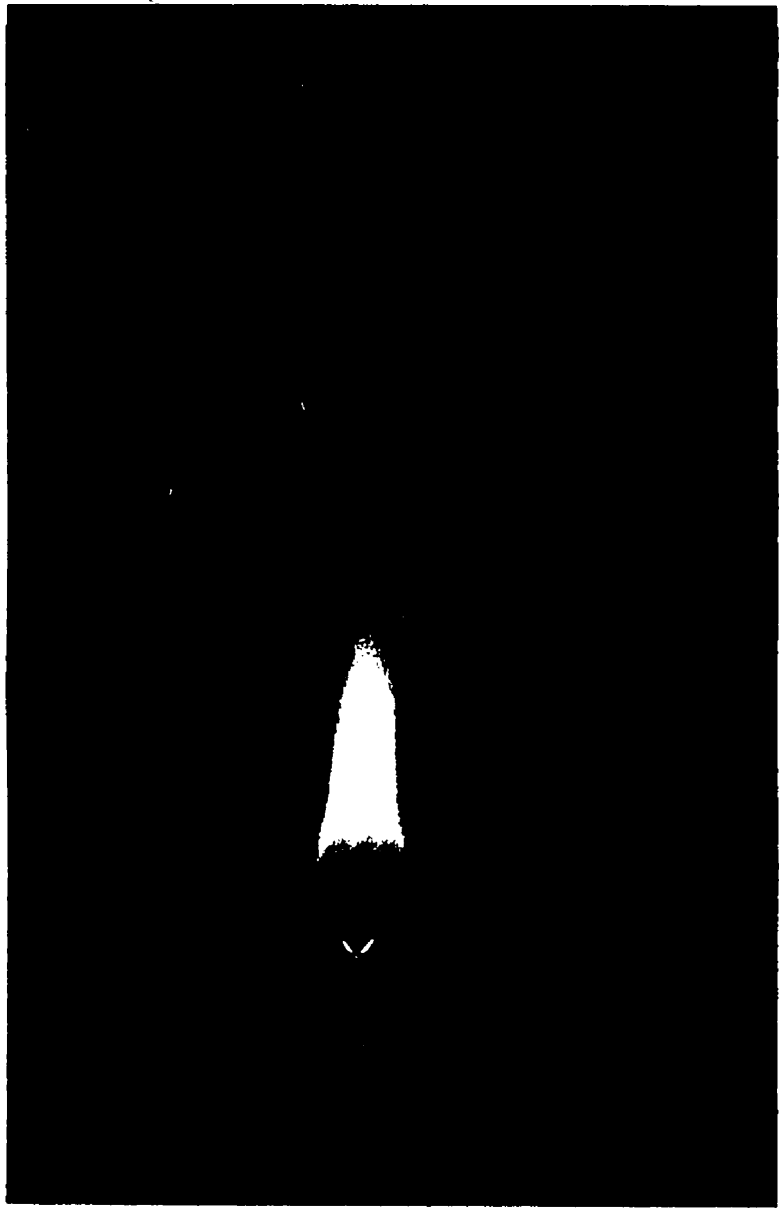


FIGURE 6.1a: Annular air jet off, long exposure (1/8 sec)

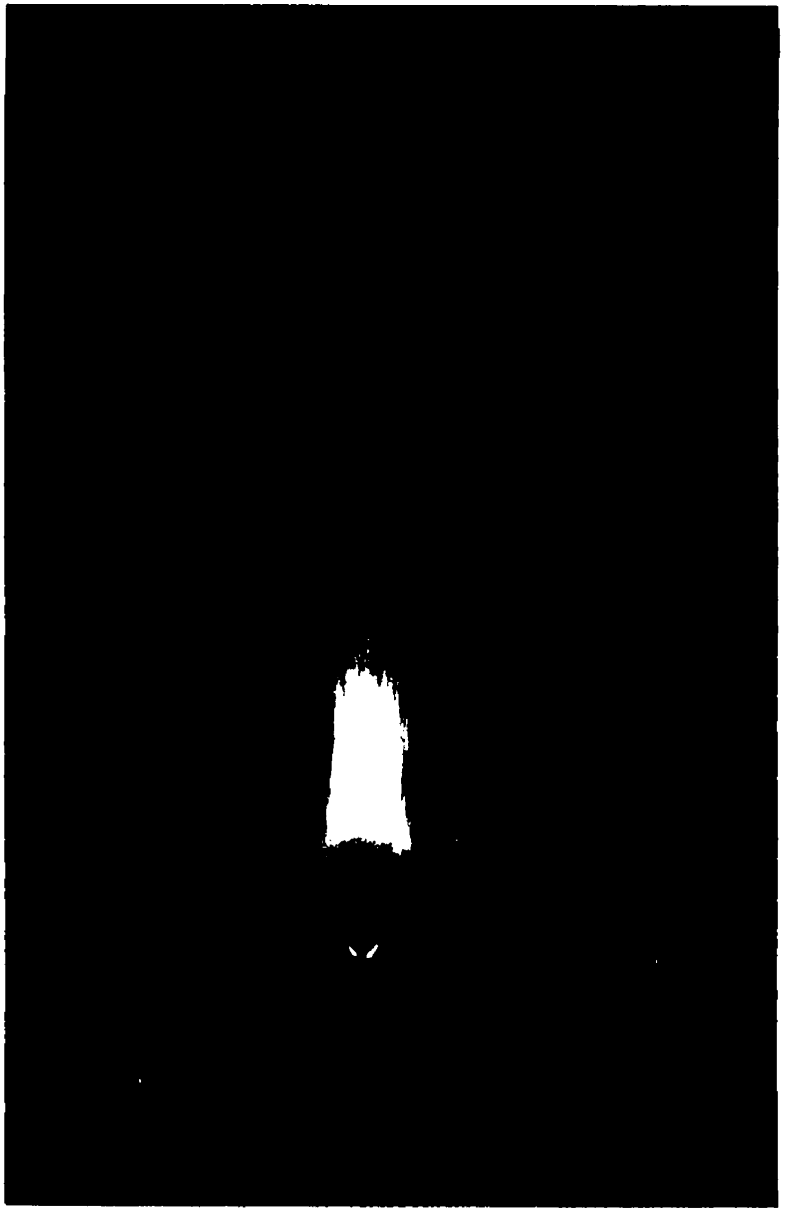


FIGURE 6.1b: Annular air jet off, 1/60 sec exposure time

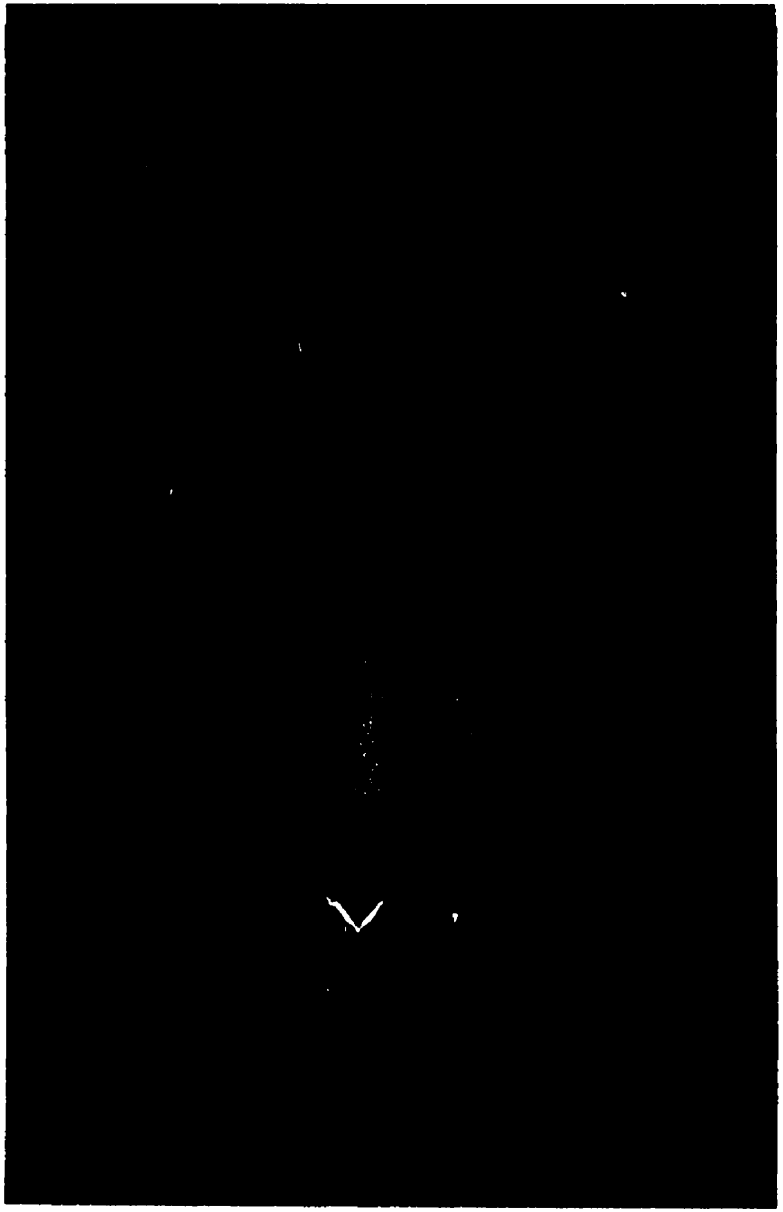


FIGURE 6.2a: Annular air =2.38*l/s* 1/8 sec exposure

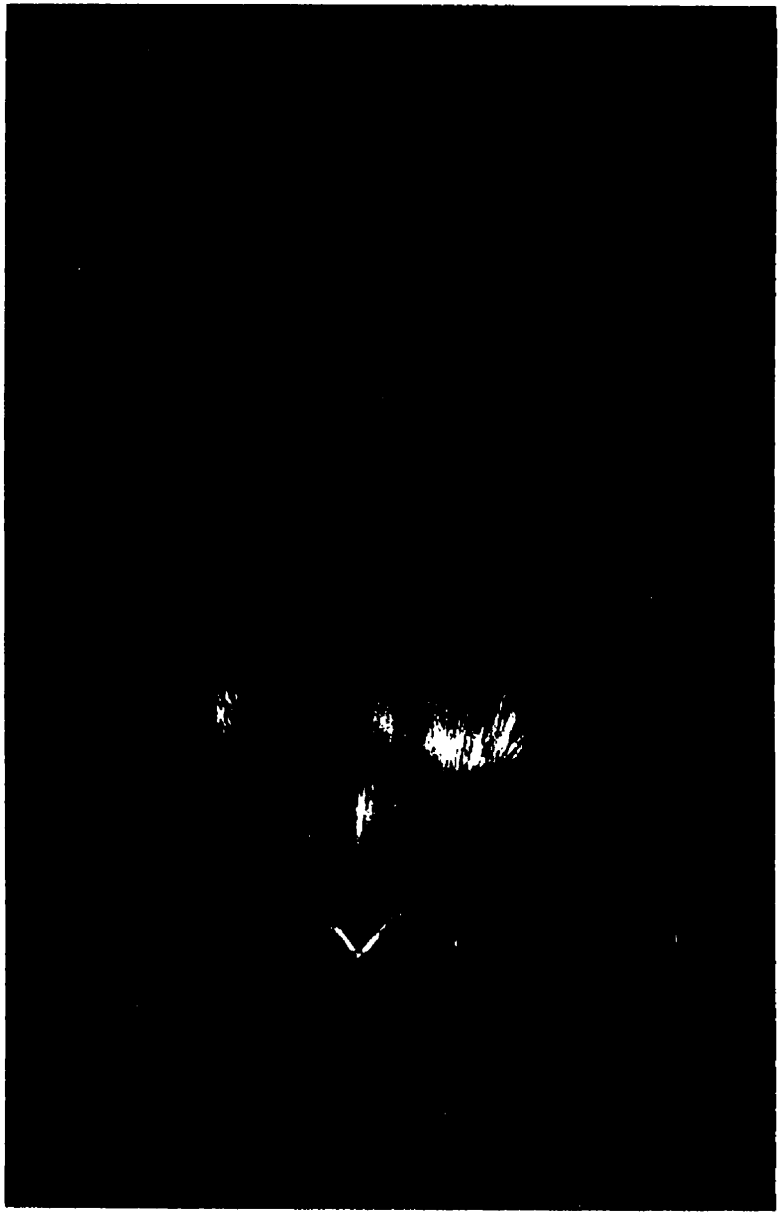


FIGURE 6.2b: Annular air=2.38*l/s* 1/60 sec exposure time

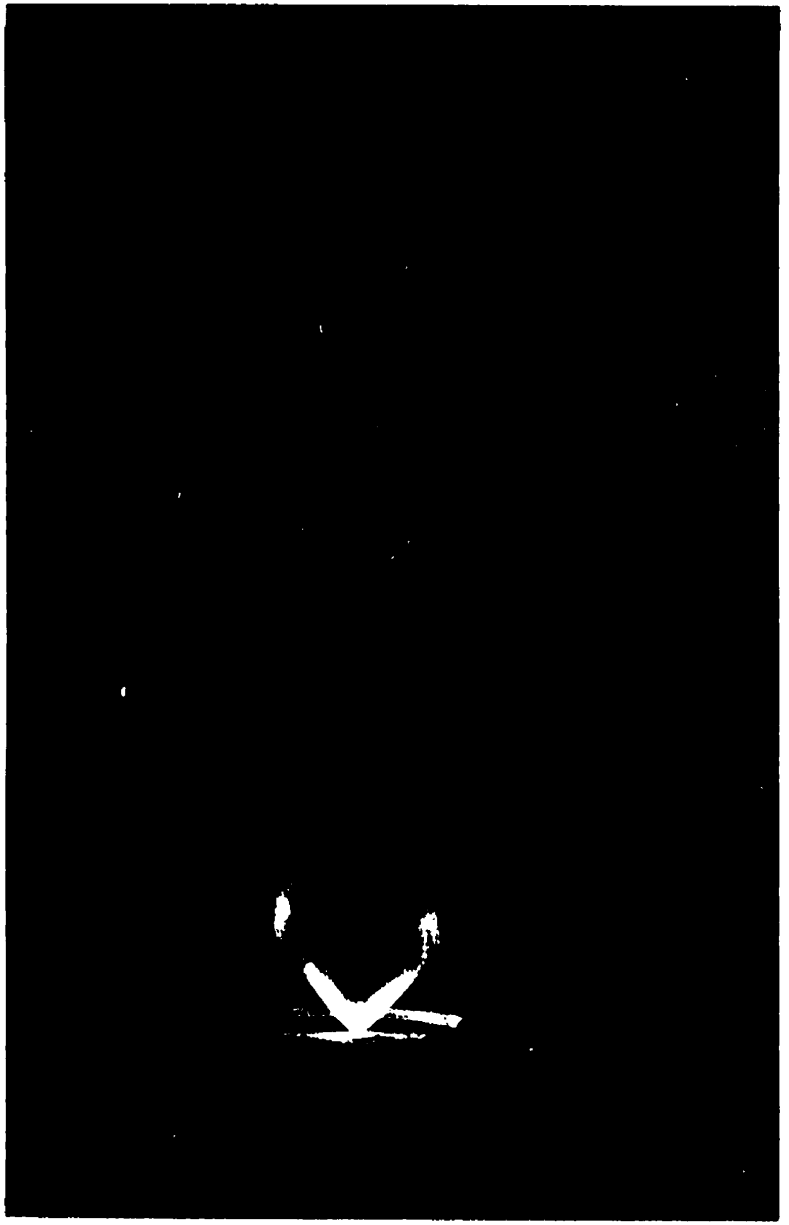


FIGURE 6.3a: Annular air = 4.77*l/s*, 1/8 sec exposure

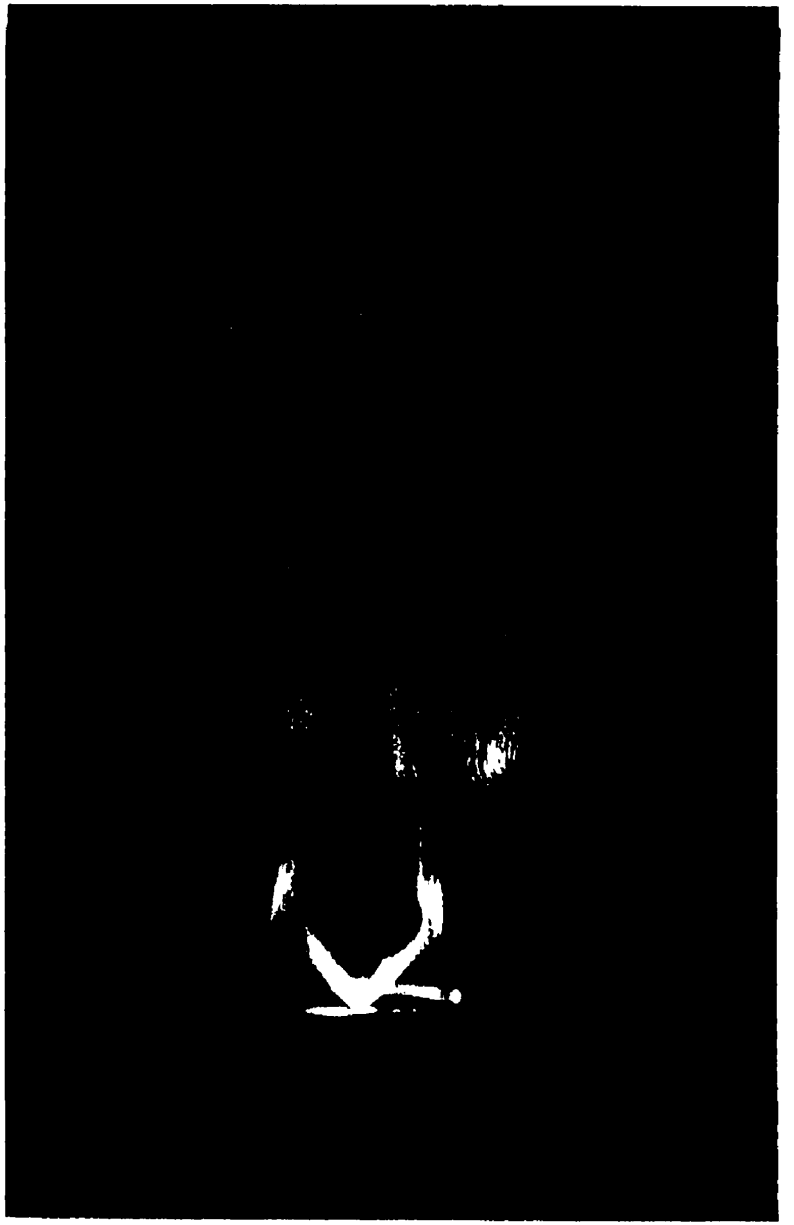


FIGURE 6.3b: Annular air = 4.77 *l/s*, 1/60 sec exposure

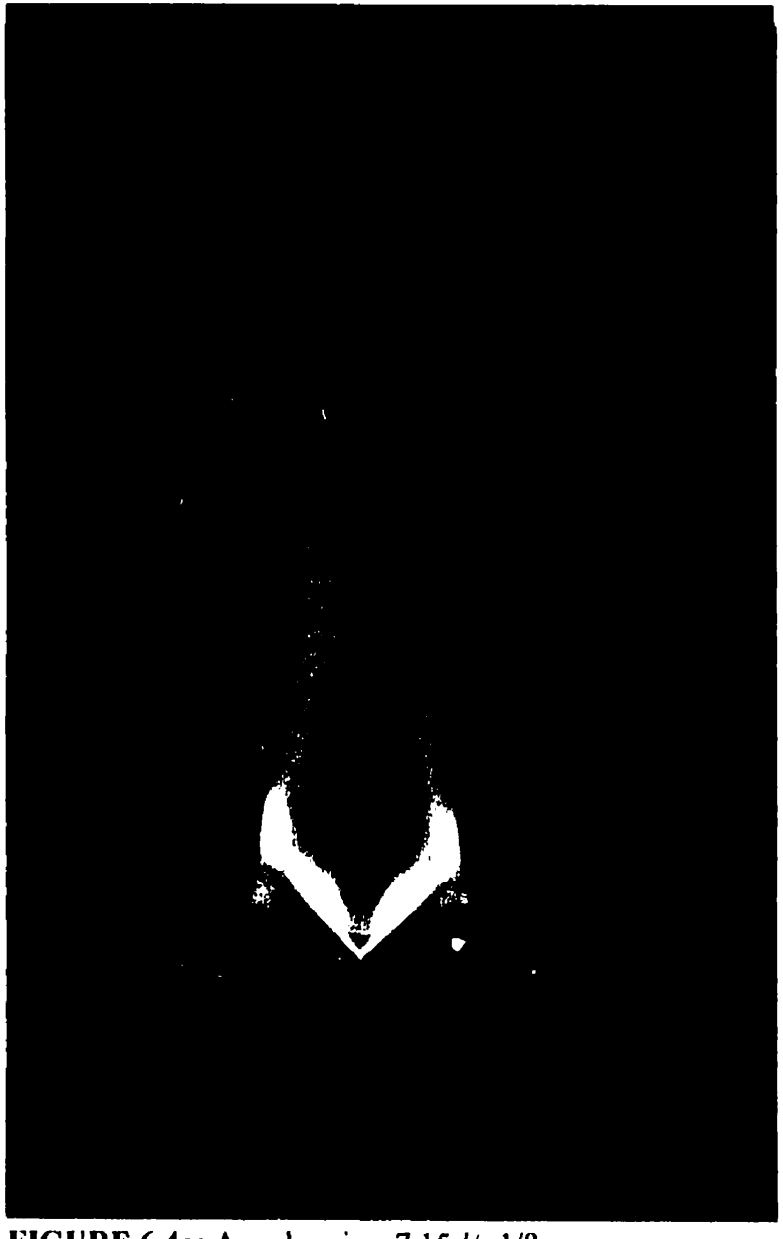


FIGURE 6.4a: Annular air = 7.15 *l/s* 1/8 sec exposure

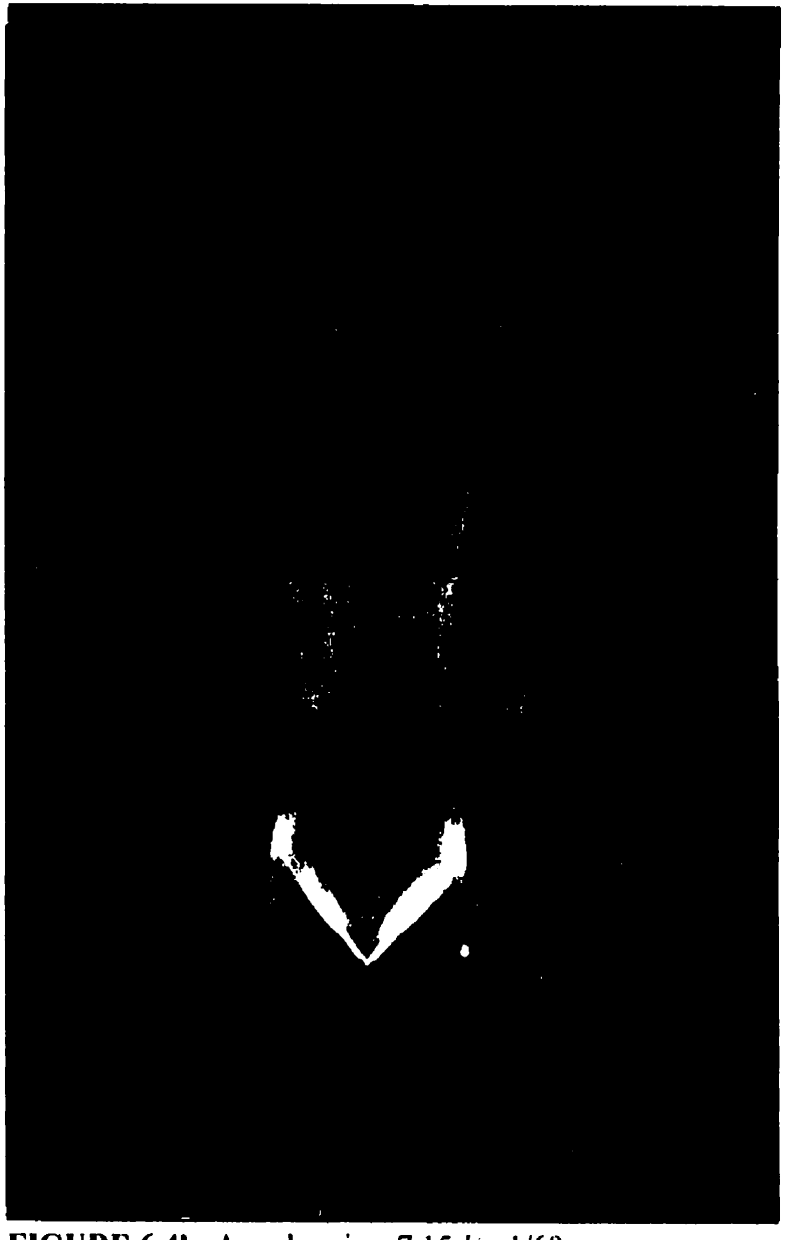


FIGURE 6.4b: Annular air = 7.15 *l/s*, 1/60 sec exposure

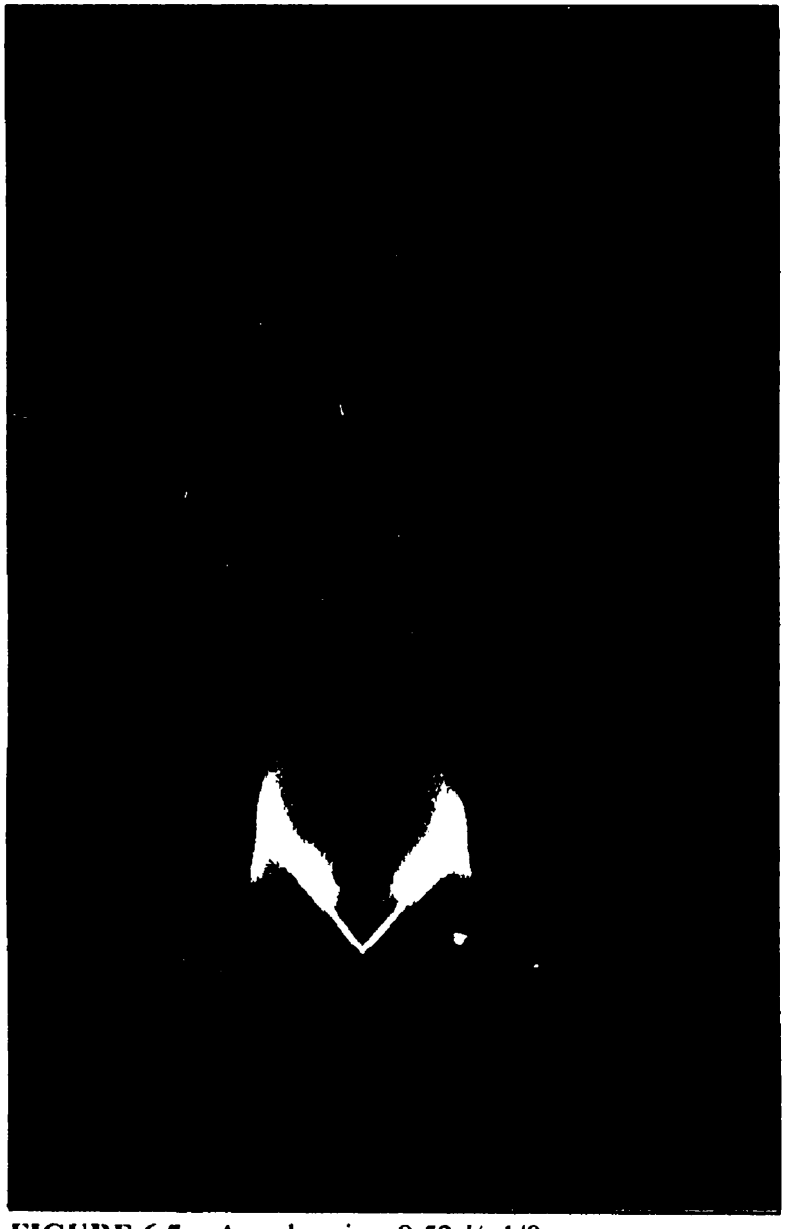


FIGURE 6.5a: Annular air = 9.52 *l/s* 1/8 sec exposure

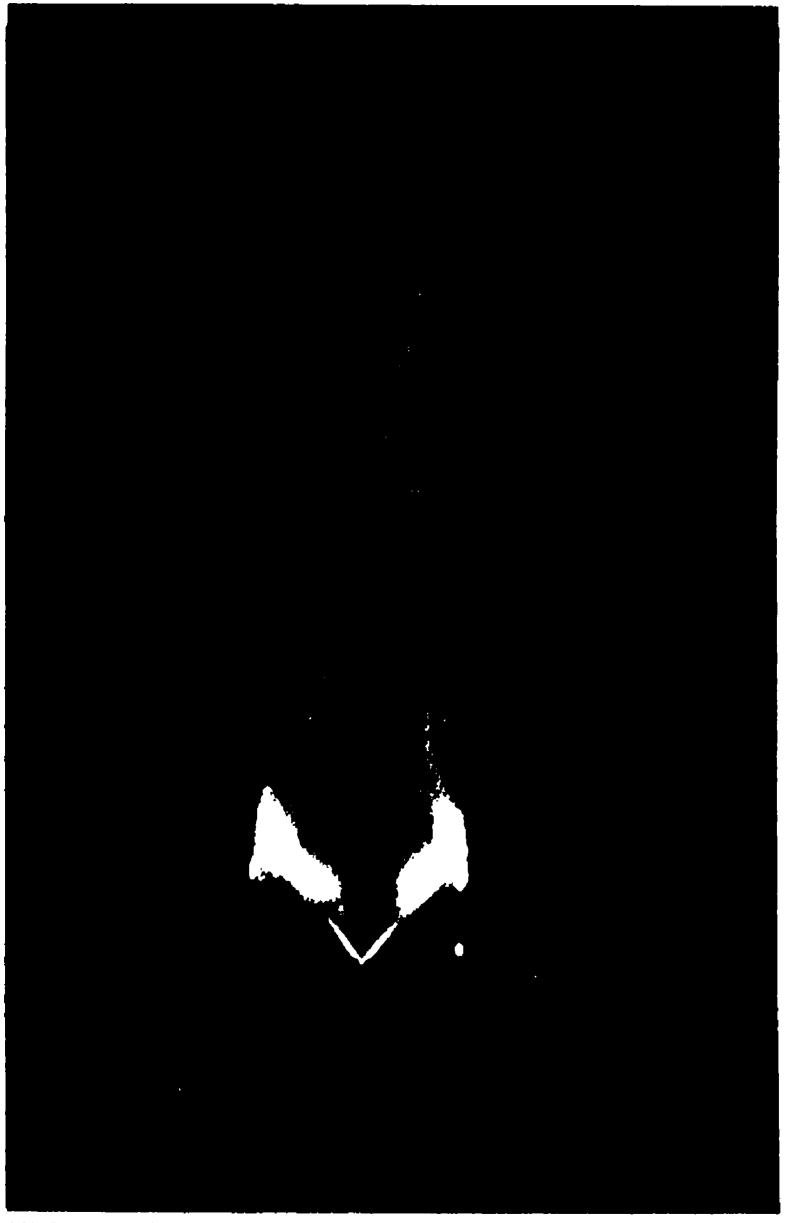


FIGURE 6.5b: Annular air = 9.52 *l/s*, 1/60 sec exposure

6.2. PLIF OH Images

Figure 6.6 shows a composite image obtained by stacking time averaged OH fluorescence images obtained in three planes. The total imaged height is 195mm. Each time-averaged image was produced by imaging the fluorescence produced by 100 laser shots onto a single exposure. The areas of highest intensity correspond to regions of high OH fluorescence, and thus high OH concentration, and mark the mean location of the reaction zones quite clearly. The structure of the flame is seen to consist of an inner and outer reaction zone, as suggested in the photographic images. The outer reaction zone appears to begin approximately 12mm above the spray nozzle. Interestingly, the inner reaction zone does not appear to begin until further downstream, approximately 24mm upstream of the nozzle, with a much less distinct anchor point than the outer zone. The emerging spray cone is seen close to the nozzle, and is visible due to strong elastic scattering of the laser light, some of which passes through the interference filter. There has also been some suggestion that the dense spray region is partially visible due to Raman scattering from the liquid methanol [19], although it is expected that the partial transmittance of the interference filter at the excitation wavelength, approximately 10^{-4}, makes elastic scattering the dominant interference mode.

Comparison of the time averaged OH image to the instantaneous images presented in Figure 6.7a, b and c shows that the outer reaction zone is essentially laminar, with only a slowly varying structure, while the inner reaction zone is quite turbulent, with a wavy structure consisting of fairly small scale structures on the order of a few millimeters. It can also be clearly seen in the instantaneous image that the inner and outer reaction zones are anchored at the same point approximately 12mm above the spray nozzle, contrary to the impression given by the time-averaged image. The first few centimeters of the inner reaction zone do not produce strong fluorescence, and the turbulent nature of this region produce quite a diffuse image in the time-averaged shot. It is interesting to note that there appears to be a closed inner region within the inner reaction zone that produces no OH fluorescence, suggesting the presence of an inner air and/or fuel vapour core extending to approximately 100mm downstream of the nozzle. Immediately beyond this inner core, across a distinct boundary, are hot products of combustion producing considerable OH fluorescence. It would appear by the

nature of the reaction zone and interface wrinkling that the turbulent length scales in this region are increasing with increasing distance from the nozzle, and may even be relaminarizing beyond the approximately 100mm. Figure 6.8, showing five single shot images in the z = 0 to 65mm plane, shows the steady nature of the outer reaction zone, and shows some discontinuities in the inner region. There is obvious attenuation of the laser beam across the flame, amounting to approximately 15% reduction. This attenuation is only apparent in the annular air off case, and is due to the laser traversing four reaction zones with high OH concentrations and resultant high absorption.

Images made with an annular air flow rate of 2.38 *l/s* show a similar structure to the photographs of the previous section. In effect, the outer reaction zone is extinguished and the inner core widens substantially. The time-averaged image, Figure 6.9, shows the flame anchored just outside the spray cone, only 3 or 4mm above the spray nozzle. The reaction zone spreads out horizontally first before turning upward to form a slowly widening flame tube approximately 22mm in initial diameter, spreading at a rate of approximately 1mm/cm with downstream distance. The flame appears quite steady. Visually, the flame has some intermittent features that appear outside the main flame tube, with periodic combustion taking place. There is little evidence of this in the time-averaged OH image, but the single shot image presented in Figure 6.10a seems to show a region of high OH concentration outside of and separate from the main reaction zone. No distinct reaction zone is seen in this image, so these are likely hot products of combustion resulting from earlier combustion that have not yet been quenched. The single shot image shows clearly a laminar reaction zone for the first 35mm or so, with very little small scale structure evident further downstream, though large scale perturbations are evident. It is possible that the unattached structures visible in Figure 6.10a are related to the large scale "kinks" seen in the main reaction zone just below, a possibility made more likely by the hot gas structure seen in Figure 6.10b, which is clearly connected to the main reaction zone close to a flame front disturbance. The relationship between the outer structures and the main reaction zone is evident from Figure 6.11, which shows five different single shot OH images, with laminar reaction zones only disturbed when the outer structures are present.

Increasing the annular air flow rate to 4.77 *l/s* shortens the flame considerably, and leads to a tulip-shaped flame structure that encloses the emerging spray for approximately 21mm downstream, before the spray cone crosses the reaction zone into the surrounding air stream. Figure 6.12 clearly shows hot products of combustion between the emerging spray cone and the bluff body surface. The region appears diffuse, suggesting a fair degree of unsteadiness in this region. In contrast, the reaction zone just downstream appears highly stationary for the first 25mm or so, until it rapidly appears more diffuse. Figure 6.13a, a single shot image of OH fluorescence in the region near the nozzle, supports this observation. The first part of the tulip-shaped reaction zone appears smooth, resembling the time-averaged structure, while further downstream distortion of the reaction zone is evident. In Figure 6.13b, a single shot image in a plane 65mm downstream of the nozzle, the turbulent nature of the flame is even more evident, with both large scale and smaller scale distortion apparent. In figure 6.13a, there is some evidence of instantaneous symmetry, but this is no longer the case further downstream, as seen in Figure 6.13 b and c. Figure 6.14 presents five different single shot images in the z = 0 to 65mm plane.

Figure 6.15 presents a composite time-averaged image of OH fluorescence with an annular air flow rate of 7.15*l/s*. As can be seen, the flame has lifted off the bluff body surface by about 4mm, and has a base diameter equal to the bluff body diameter, suggesting that the reaction zone has stabilized in a region of strong shear along the inner surface of the annular jet. The reaction zone in the vicinity of the emerging spray cone appears quite steady, as evidenced by the strong, thin appearance of the OH fluorescence, and as seen in the five single shot images of Figure 6.17. Approximately 45mm downstream of the nozzle, the structure appears much more diffuse, suggesting high degrees of turbulence in this region. This interpretation is supported by the instantaneous images presented in Figures 6.16a, b and c, which show a symmetrical, smooth reaction zone in the vicinity of the spray nozzle, with a transition to turbulent structure approximately 40mm downstream of the nozzle. As in the previous case, turbulence appears to increase further downstream, and instantaneous symmetry is lost. The reaction zone appears to be continuous for the 195mm imaged.

In Figure 6.18, the annular air flow rate is 9.52 *l/s*, resulting in a flame of similar

structure to the previous case. In this case, however, the anchor point has moved downstream, to approximately 11mm downstream of the nozzle. The laminar-like region appears to extend somewhat further downstream as well, as evidenced by the single shot image presented in Figure 6.19a and Figure 6.20. However, the turbulence appears more intense further downstream, as shown in Figure 6.19b, where considerable amounts of large and small scale structures are evident. There is little evidence of instantaneous symmetry, and isolated structures are apparent, as well as filaments that appear to be tearing off from the main reaction zone. It is noted that the reaction zone no longer appears continuous in the z = 130-195mm plane, as seen in 6.19c.

Figures 6.21 - 6.25 present mean OH concentrations and temperatures versus radial position in three planes for each air flow rate tested. In general, the temperature peaks corresponded to the peak OH concentration location, although careful examination of steady regions near the nozzle (for example, Figure 6.24, z = 25mm plane) shows that the temperature peaks consistently occur just inside the OH concentration peak, which occurs on the fuel lean side of the reaction zone, a phenomenon reported in other studies [65][66]. In general, temperature trends and OH concentration trends follow each other, although temperature alone is not a good indicator of high OH concentration, as seen in Figure 6.22 in the z = 100mm plane, where centreline temperatures are in excess of 1300K , while the OH centreline concentration is essentially zero, indicating essentially no chemical activity.

Figure 6.26 presents a typical single shot OH fluorescence trace in the z = 25mm plane, for the air off and air = 9.52 *l*/s cases, obtained with the camera gain set to 8.5, and the lens to f/4.5. Although the two flow conditions are very different, the peak OH fluorescence intensity is almost identical in both cases, corresponding to peak OH concentrations of approximately 2.2×10^{16} /cm^3 , or 5480 PPM assuming 1800K local temperature. The fact that the peak concentrations are similar is not surprising considering that a diffusion flame occurs in a region where fuel and air diffuse into the reaction zone in stoichiometric proportions, and hence conditions in the reaction zone are similar, regardless of flow conditions. The peak OH concentration falls off rapidly on either side of the reaction zone, and essentially falls to zero within a millimeter of the peak. It would appear that the region of high OH concentration is

somewhat narrower in the air = 9.52 *l*/s case, consistent with faster heat and species diffusion due to the more turbulent local conditions. The peak measured OH concentration of 5480 PPM is several times the equilibrium concentration expected from stoichiometric combustion of methanol. This super-equilibrium condition within the reaction zone has been observed and studied in other flames [67][68][69], and the peak value of 5480 PPM corresponds well to the measurements and computations in these works.

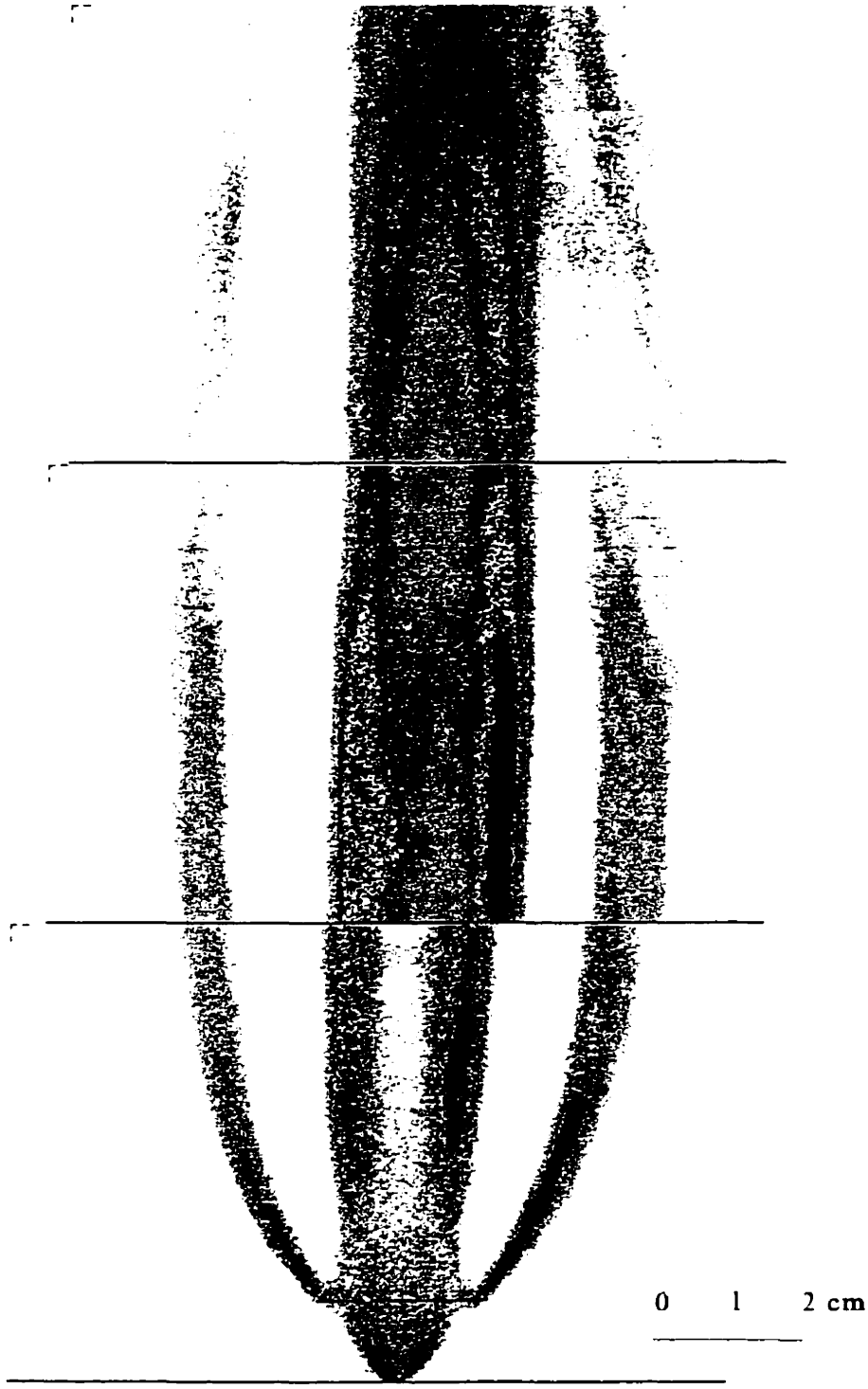


FIGURE 6.6: Annular air off 100 shot average composite image

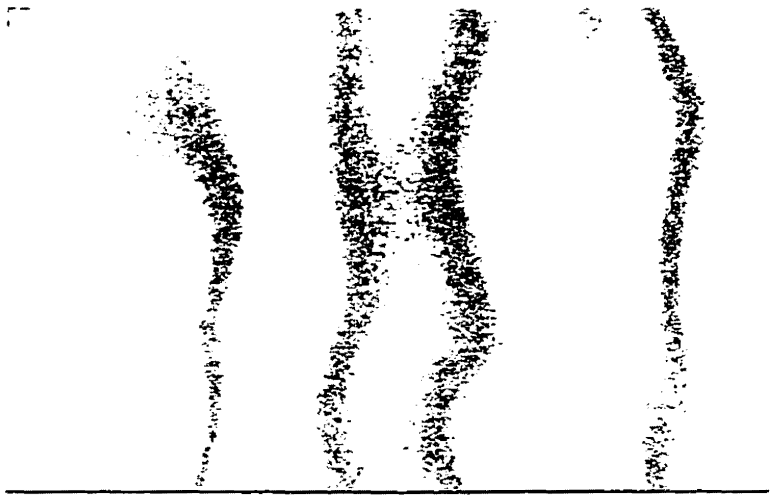


FIGURE 6.7c: z = 130 to 195mm

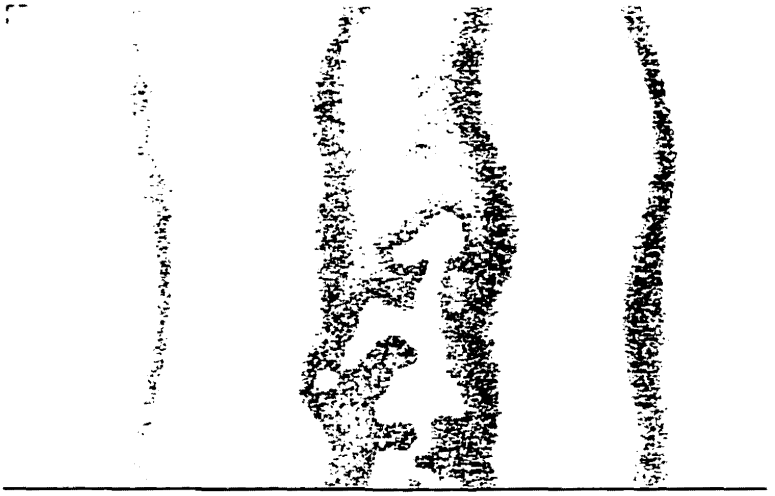


FIGURE 6.7b: z = 65 to 130mm

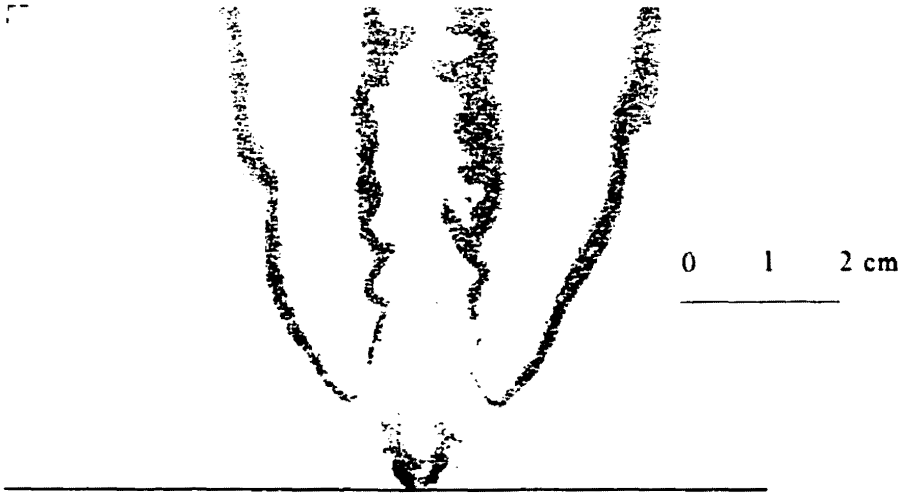


FIGURE 6.7a: Annular air off, single shot image, z = 0 to 65mm

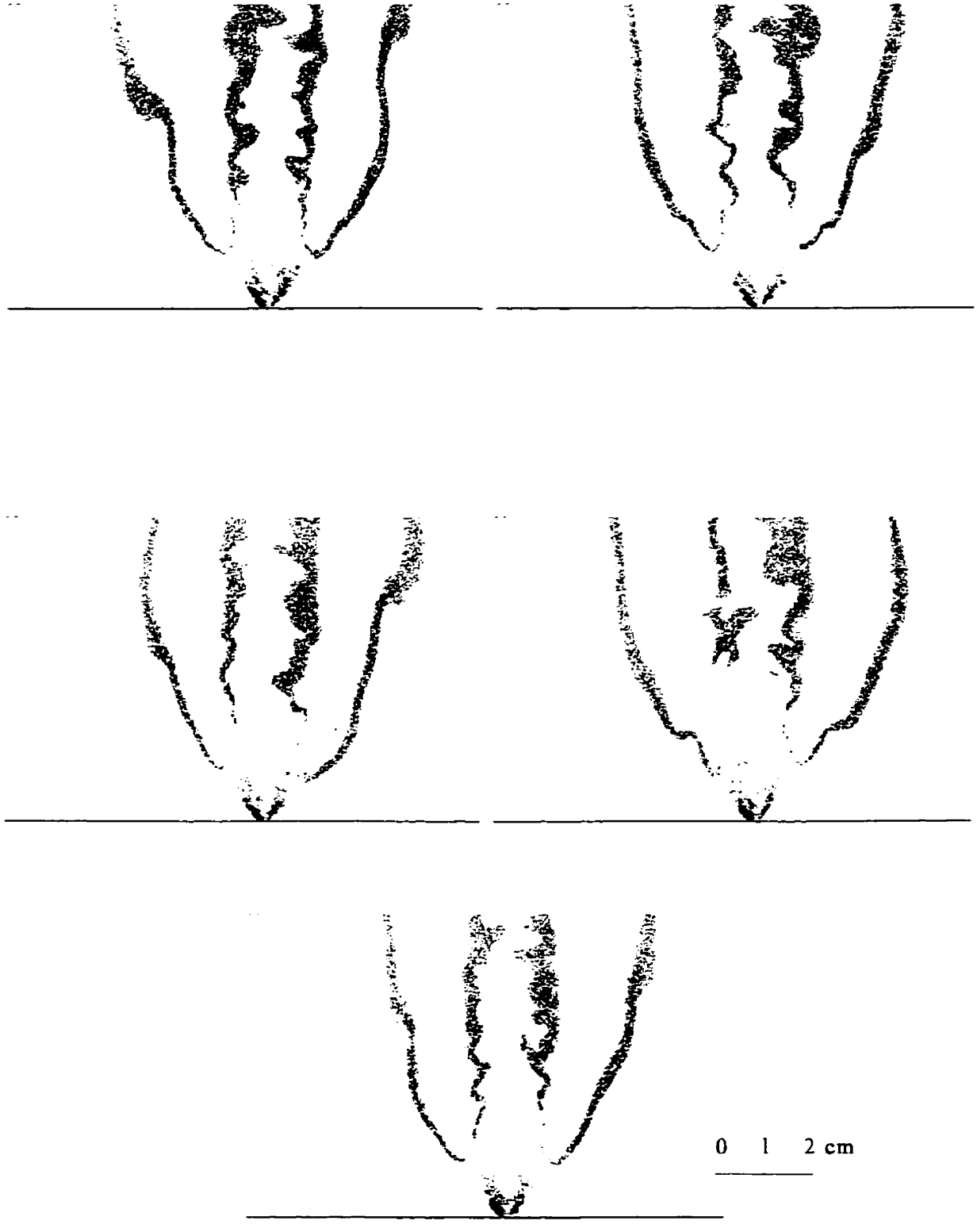


FIGURE 6.8: Five single shot images in the z = 0 to 65mm plane with annular air off

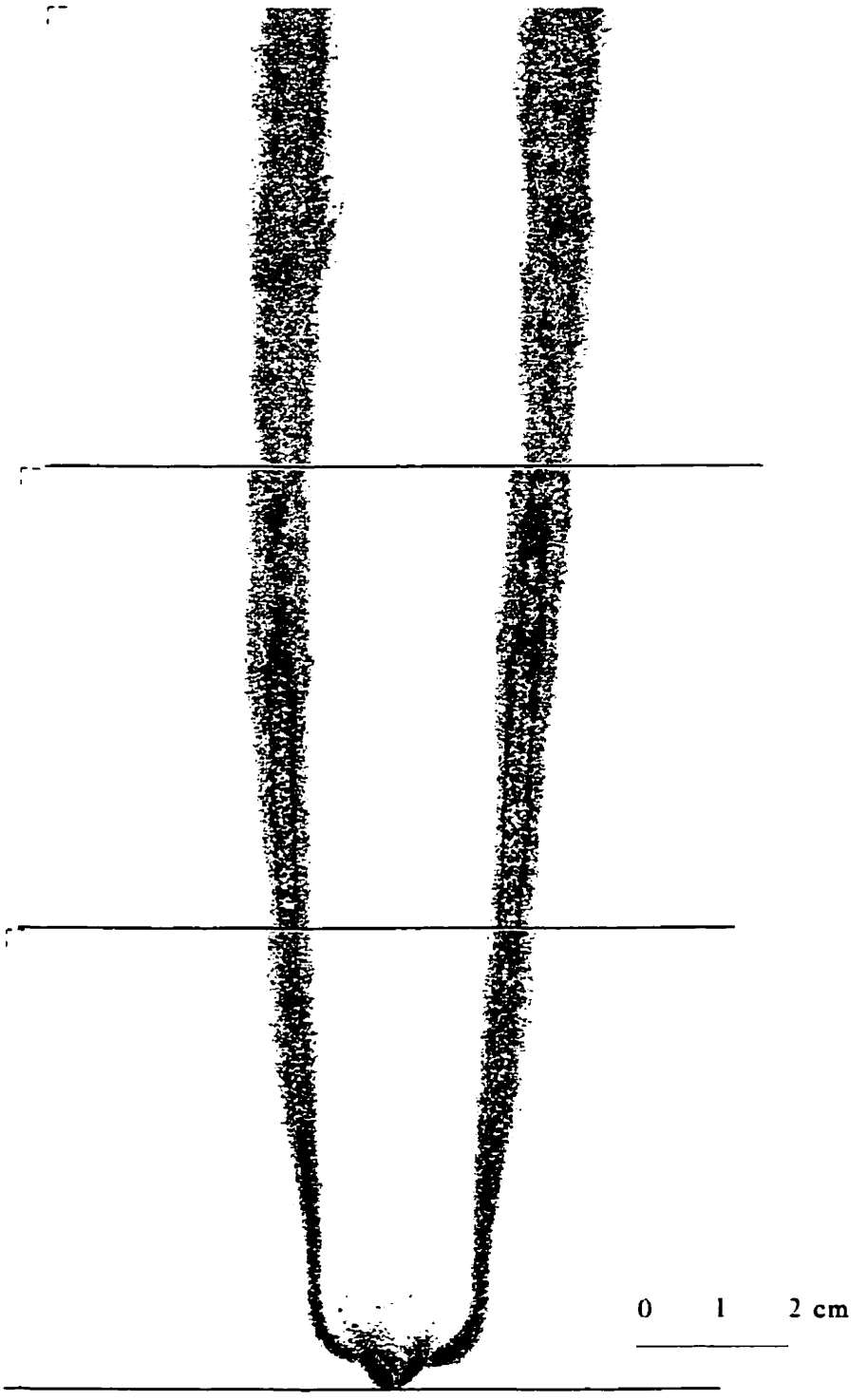


FIGURE 6.9: Annular air = 2.38*l/s*, 100 shot average composite image

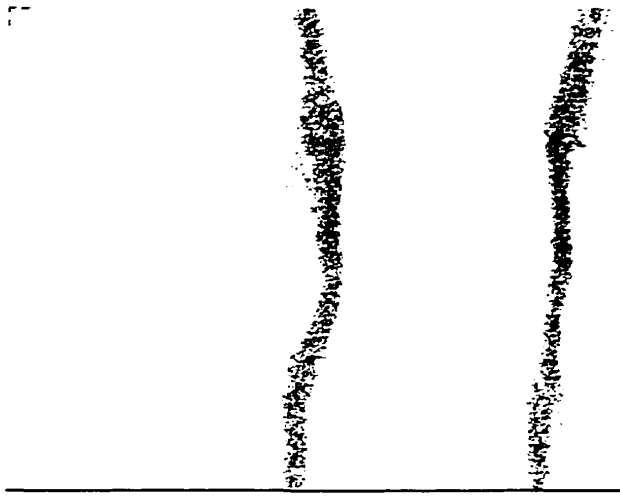


FIGURE 6.10c: z = 130 - 195mm

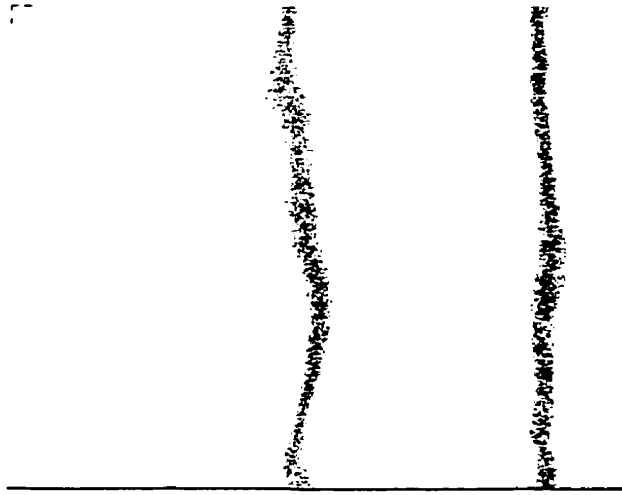


FIGURE 6.10b: z = 65 - 130mm

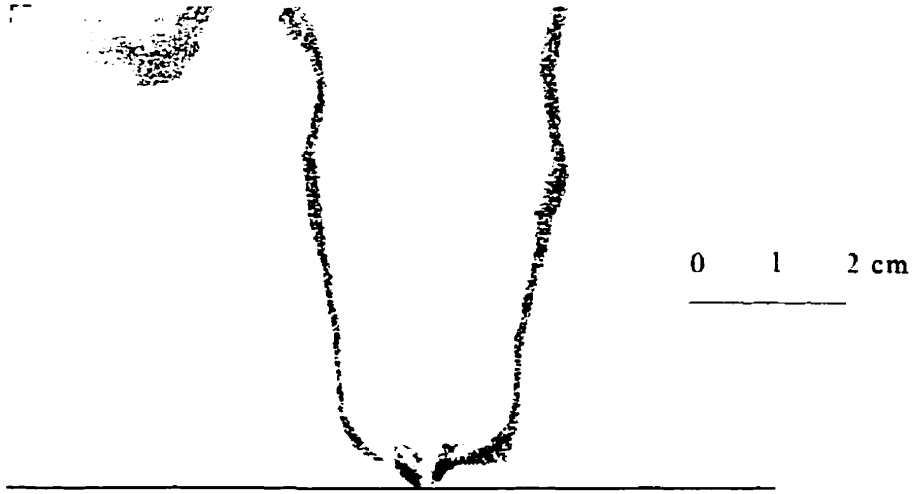


FIGURE 6.10a: Air = 2.38*l/s* single shot image, z = 0 - 65mm

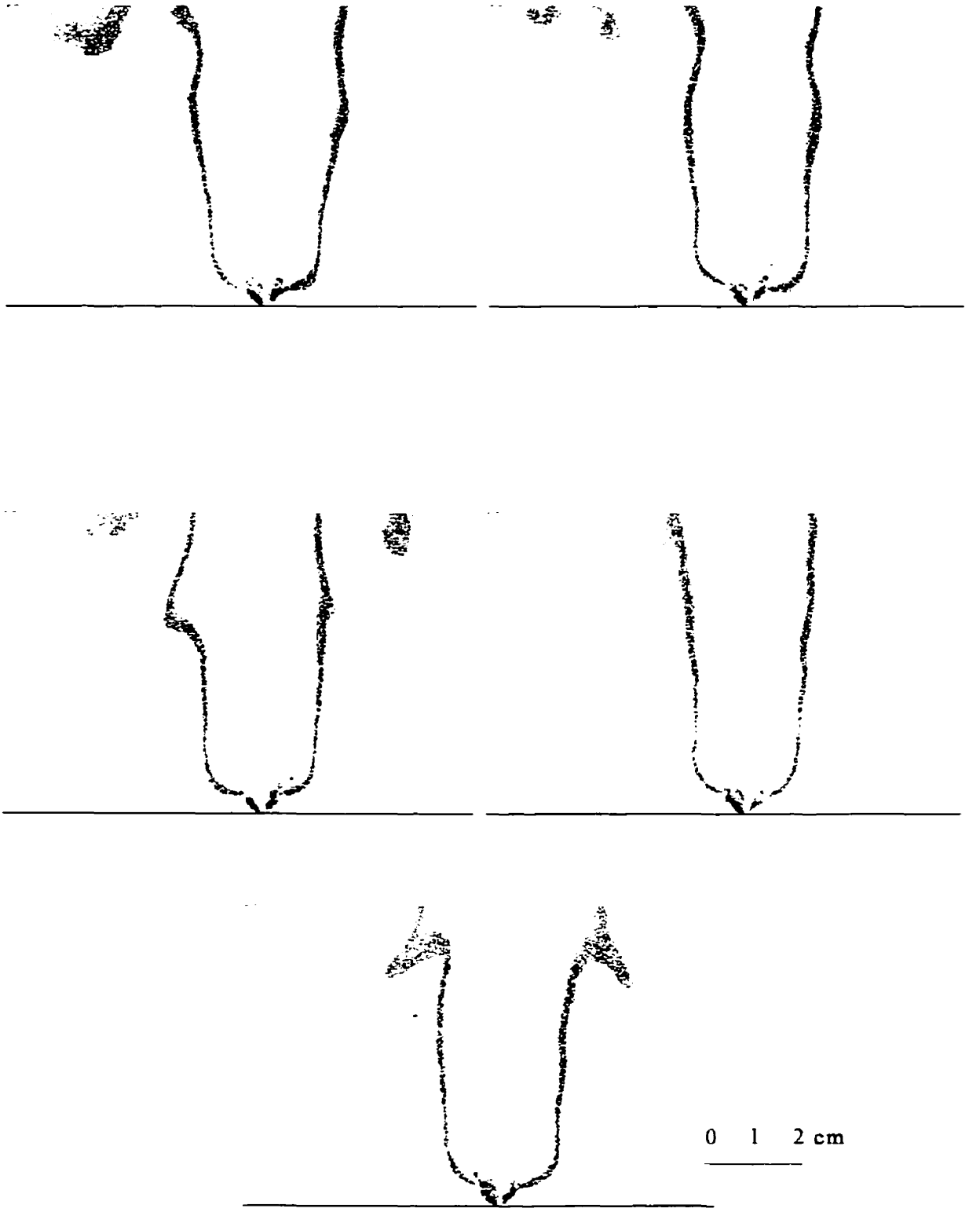


FIGURE 6.11: Five single shot images in the $z = 0$ to 65mm plane, air flow rate = 2.38*l/s*

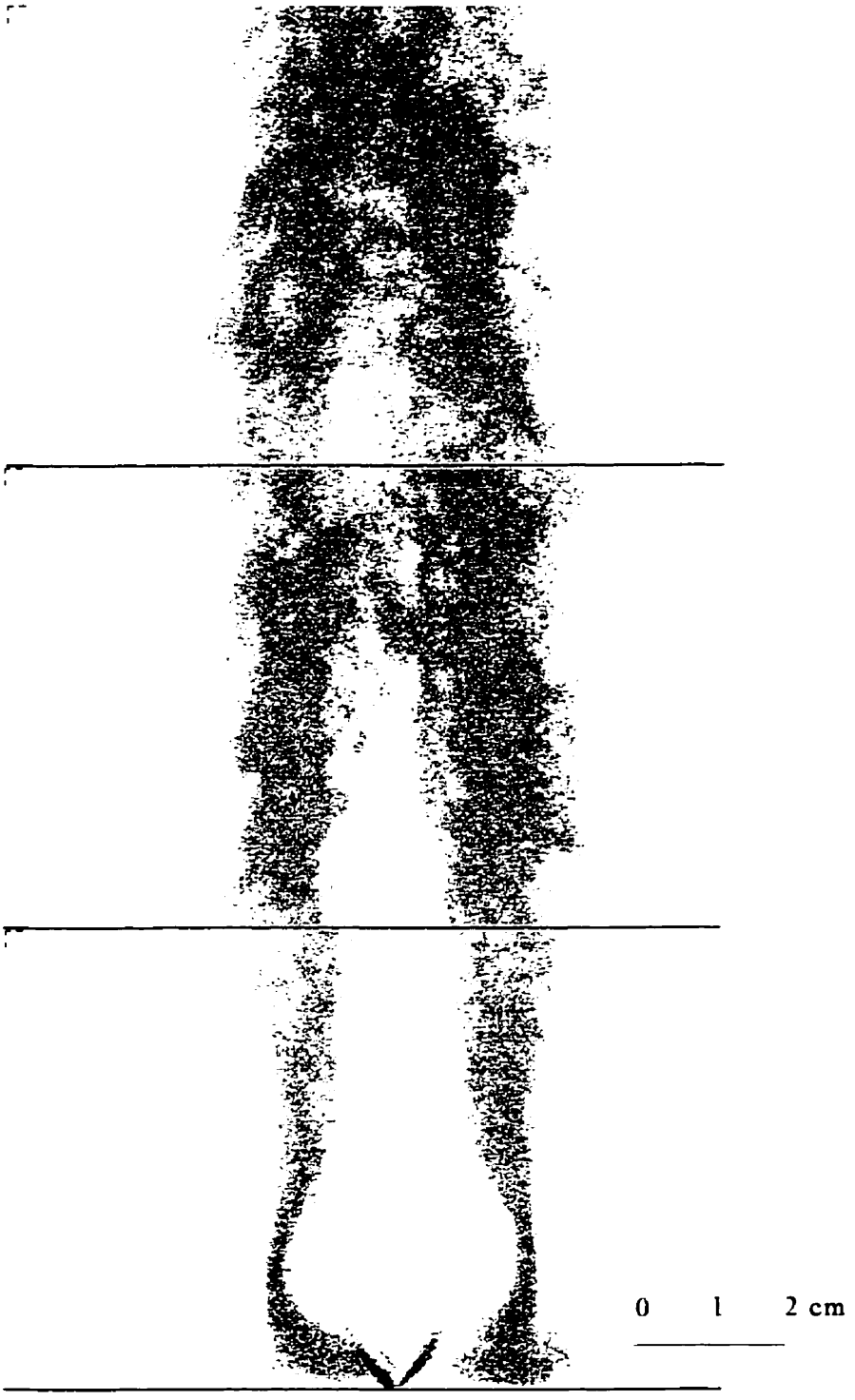


FIGURE 6.12: 100 shot average composite image, annular air = 4.77*l/s*

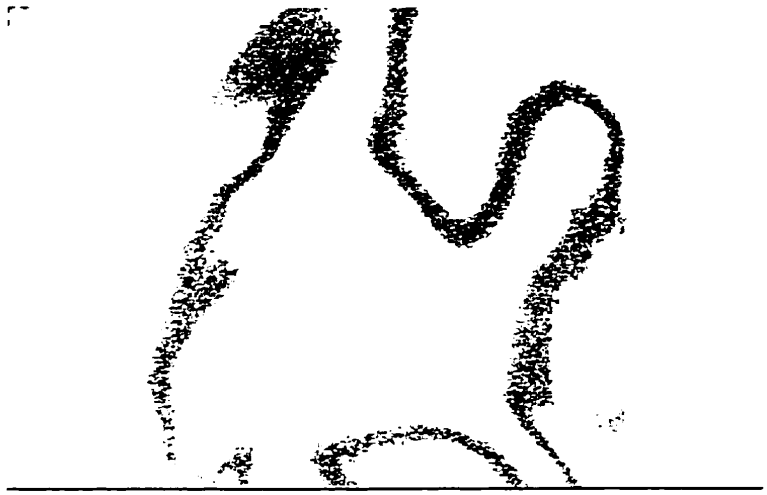


FIGURE 6.13c: Single shot image z = 130 - 195mm



FIGURE 6.13b: Single shot image z = 65 - 130mm

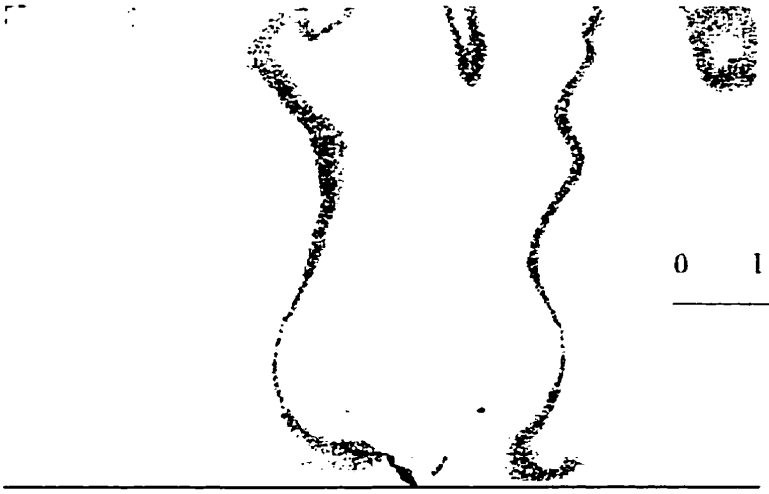


FIGURE 6.13a: Single shot image z = 0 - 65mm, air = 4.77*l/s*

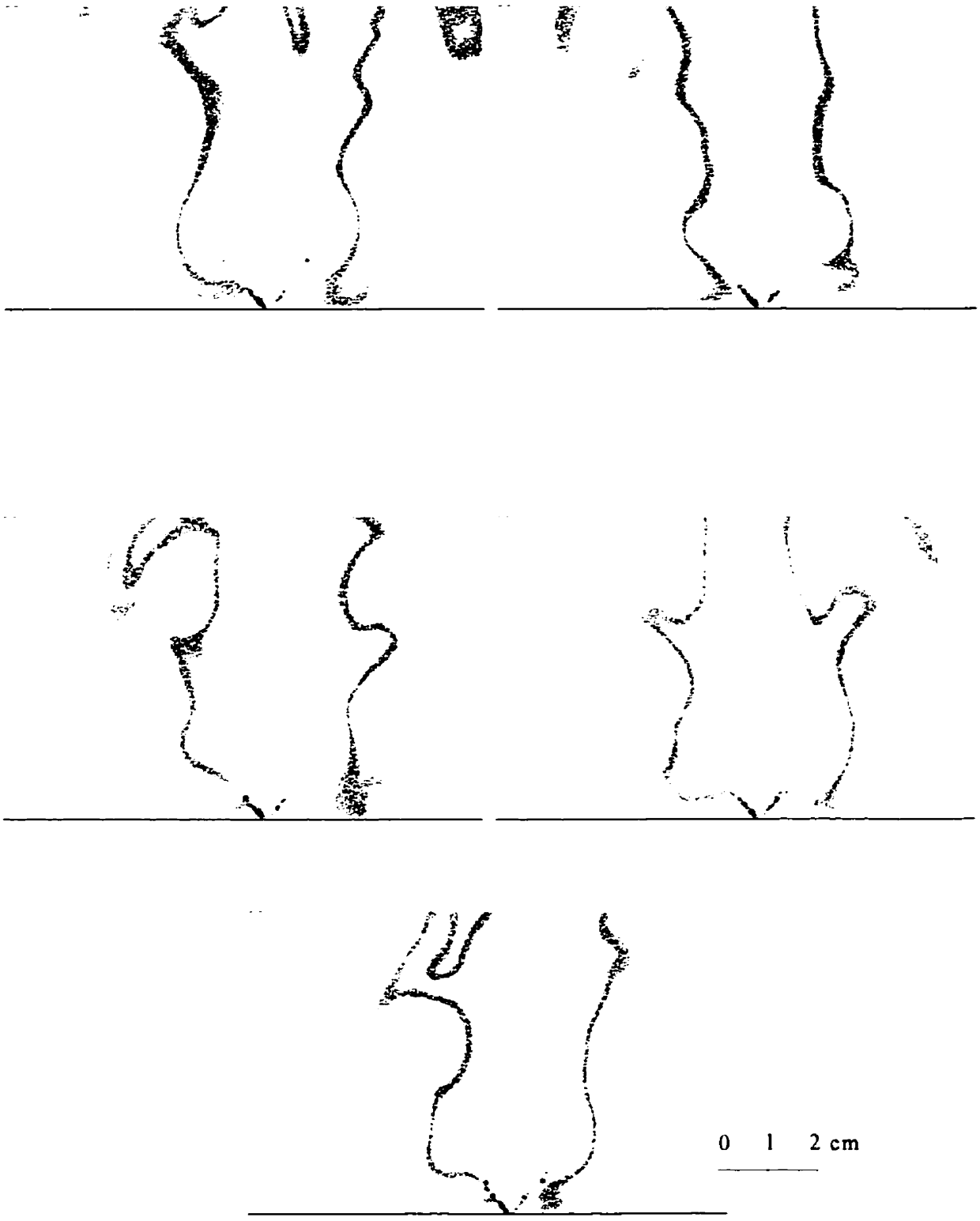


FIGURE 6.14: Five single shot images in the $z = 0$ to 65mm plane, air flow rate = 4.77ℓ/s

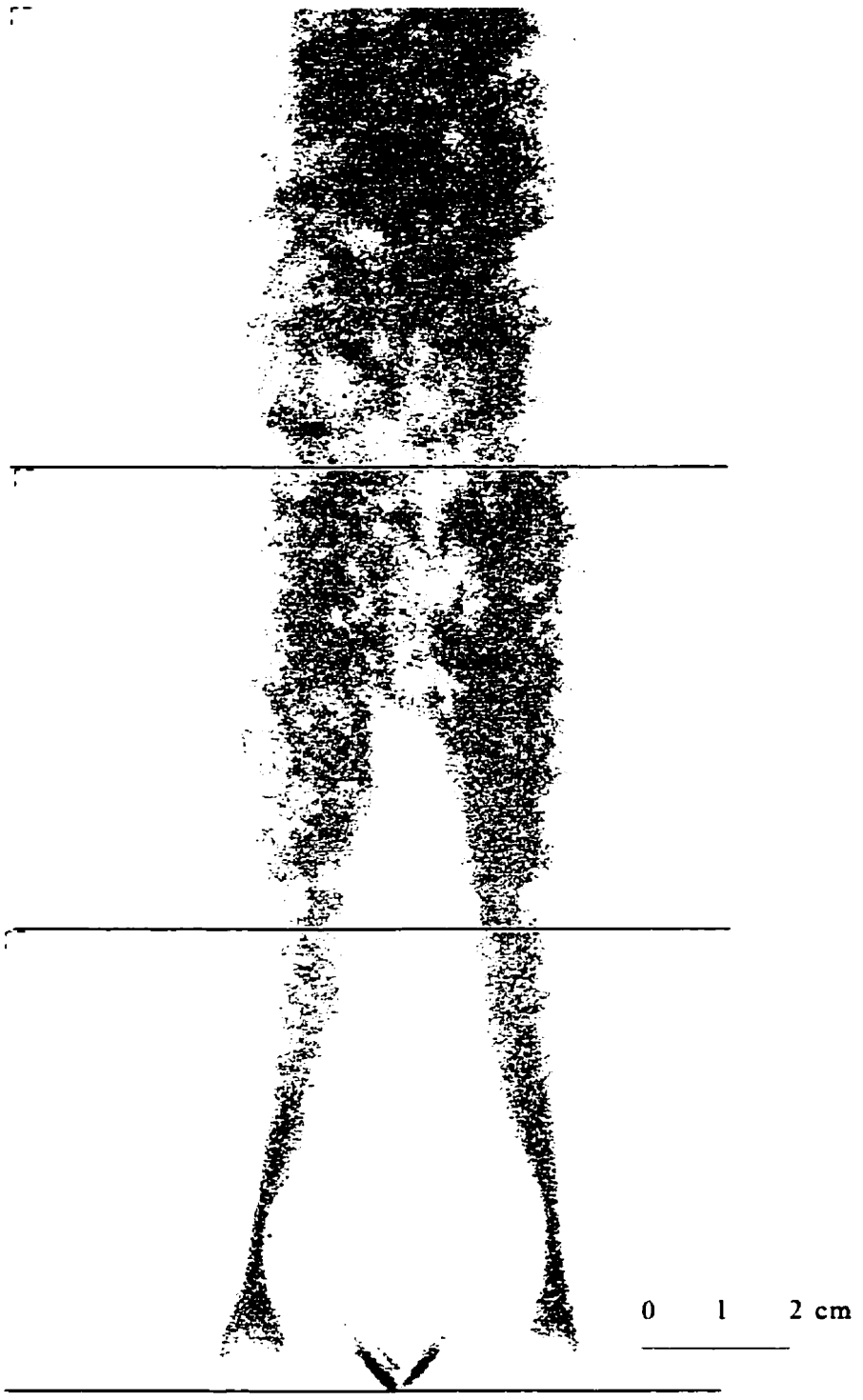


FIGURE 6.15: 100 shot average composite image, air = 7.15 *l*/s



FIGURE 6.16c: Single shot image, z = 130 - 195mm



FIGURE 6.16b: Single shot image, z = 65 - 130mm

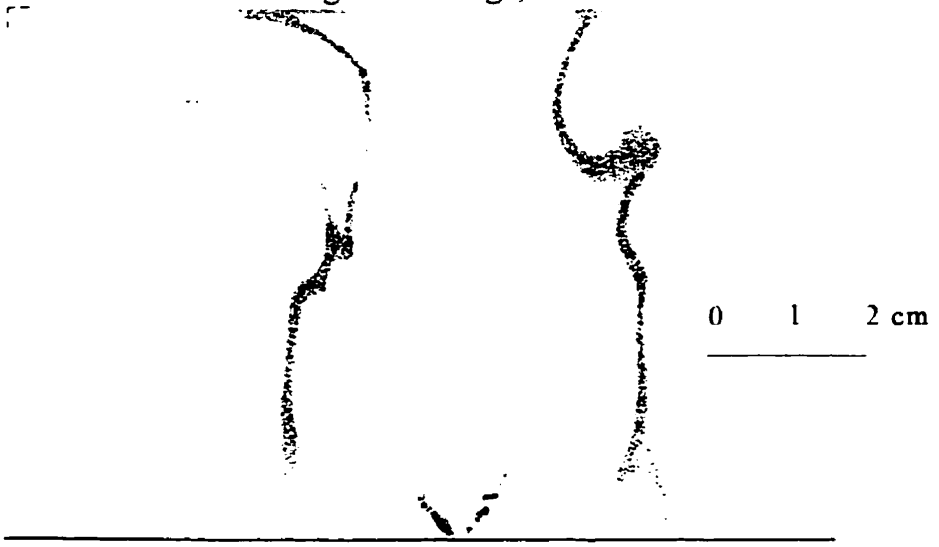


FIGURE 6.16a: Single shot image, z = 0 - 65mm, air = 7.15*l/s*

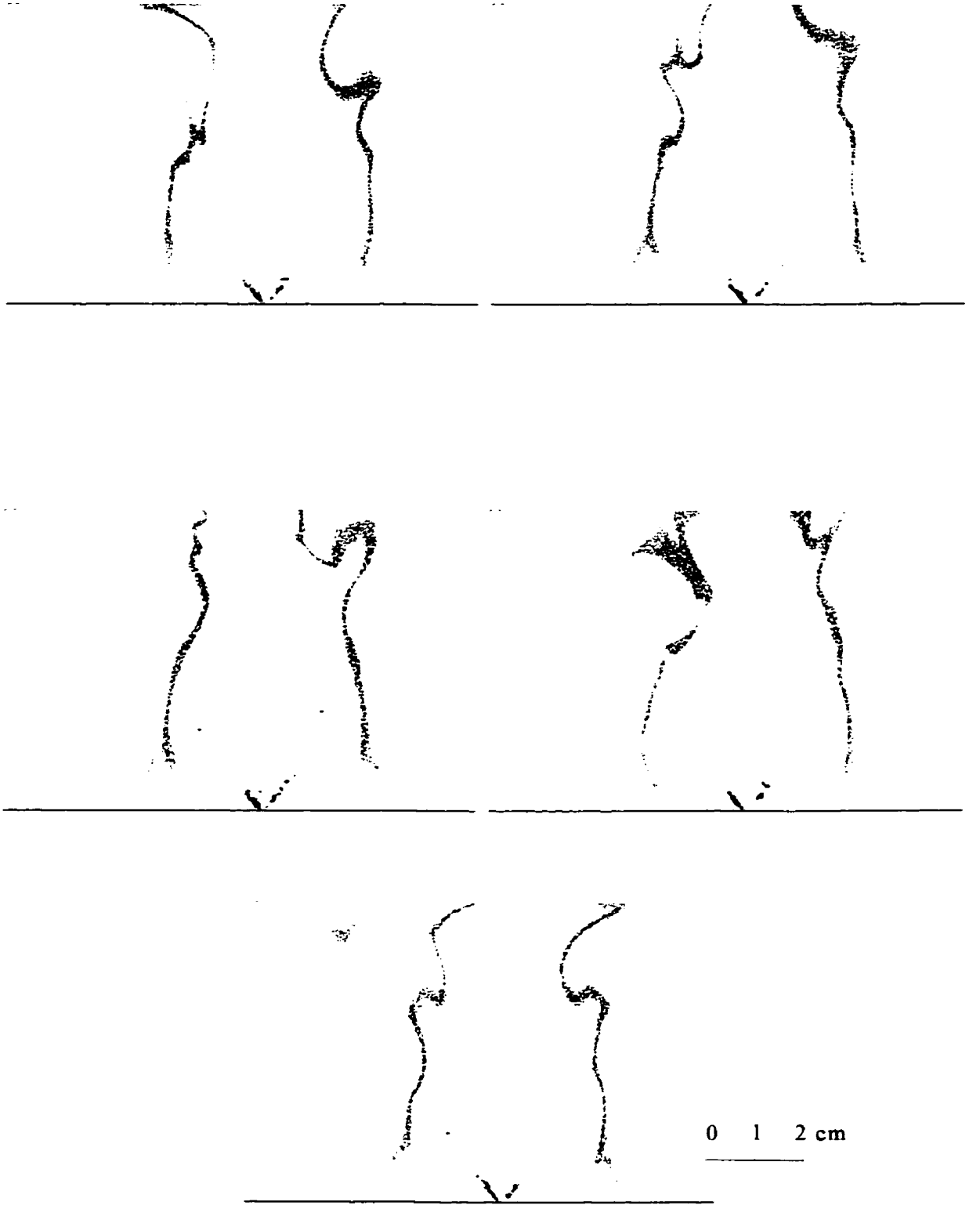


FIGURE 6.17: Five single shot images in the z = 0 to 65mm plane, air = 7.15*l/s*

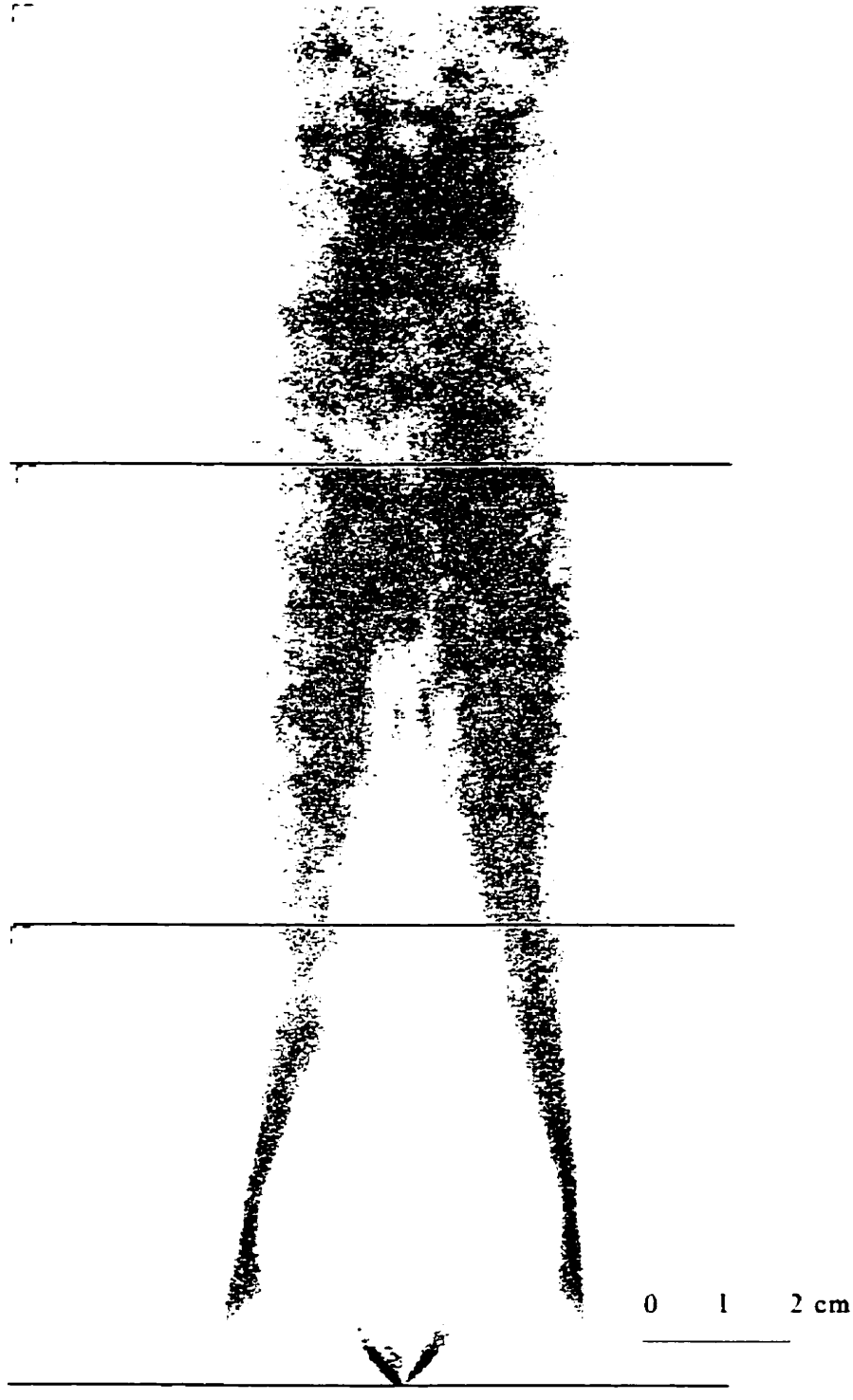


FIGURE 6.18: 100 shot average composite image, air = 9.52*l/s*



FIGURE 6.19c: Single shot image, z = 130 - 195mm



FIGURE 6.19b: Single shot image, z = 65 - 130mm

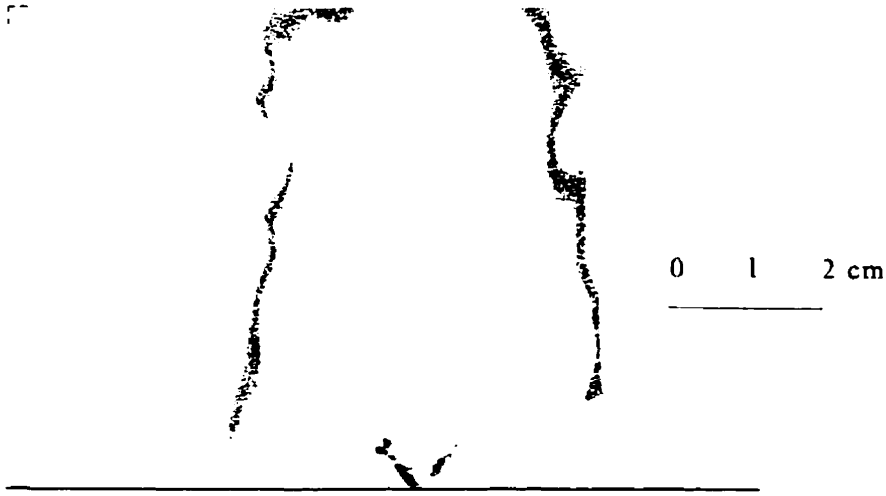


FIGURE 6.19a: Single shot image, z = 0 - 65mm, air = 9.77 *s*

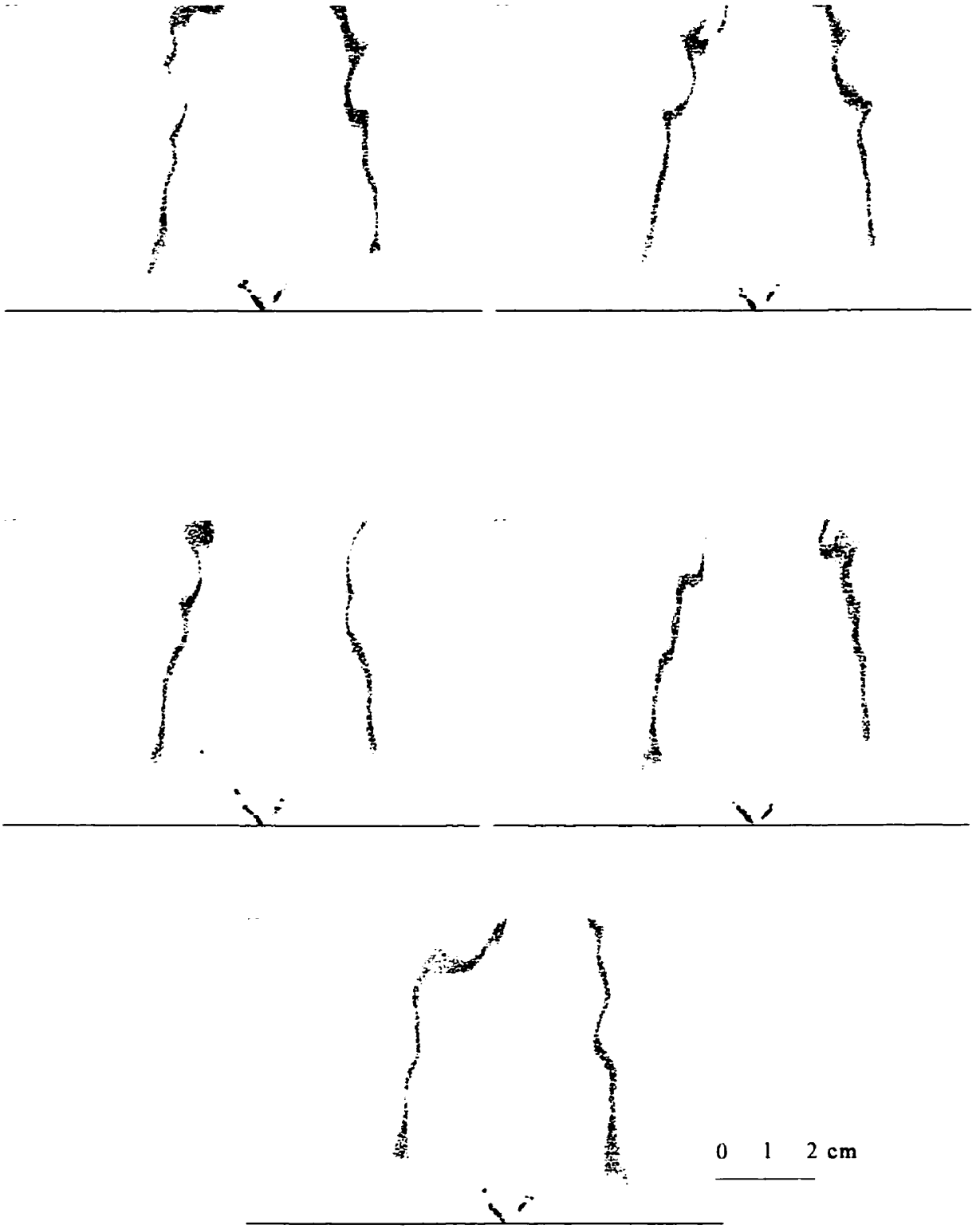


FIGURE 6.20: Five single shot images in the z = 0 to 65mm plane, air = 9.52 *l/s*

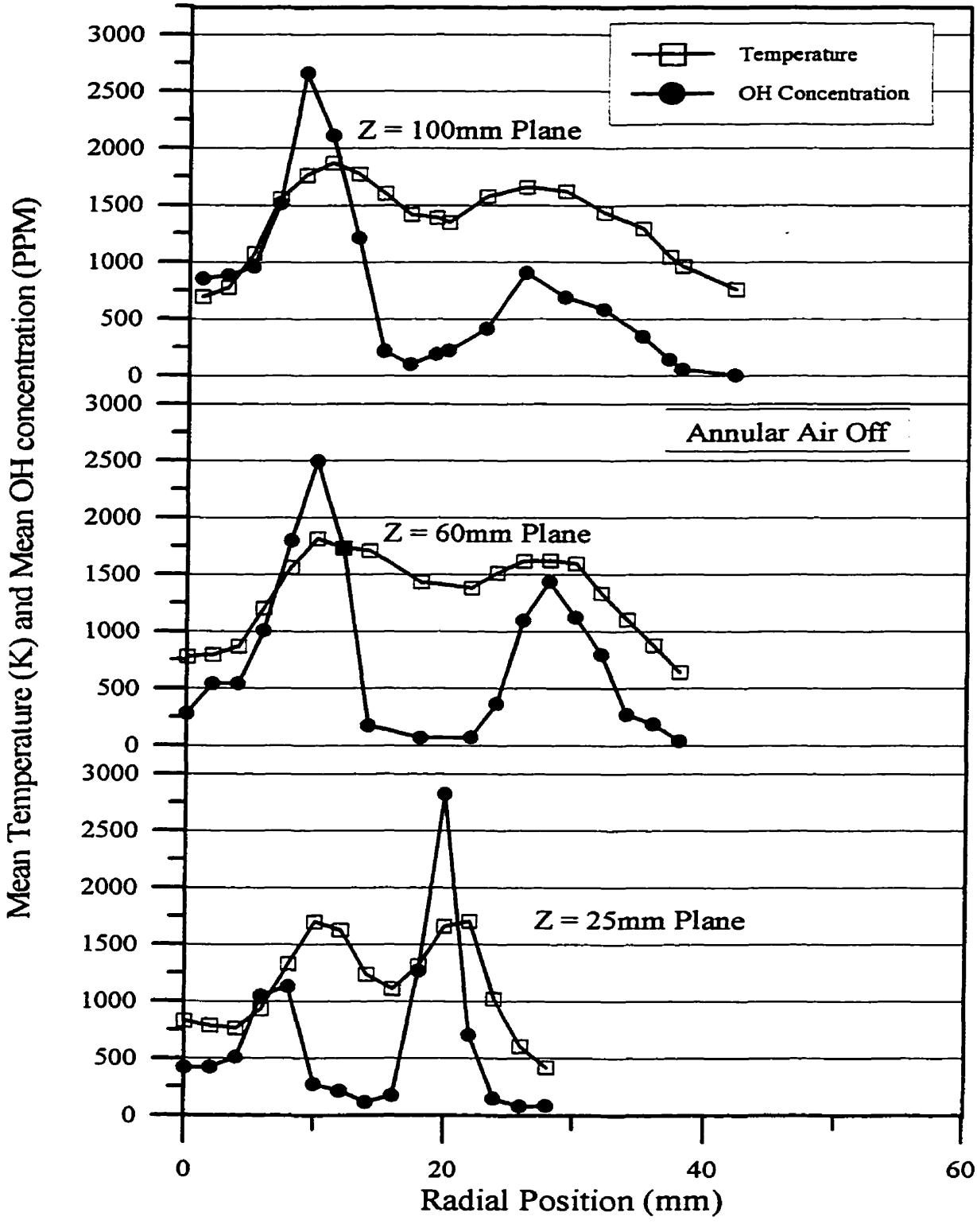


FIGURE 6.21: Mean OH concentration profiles with annular air off

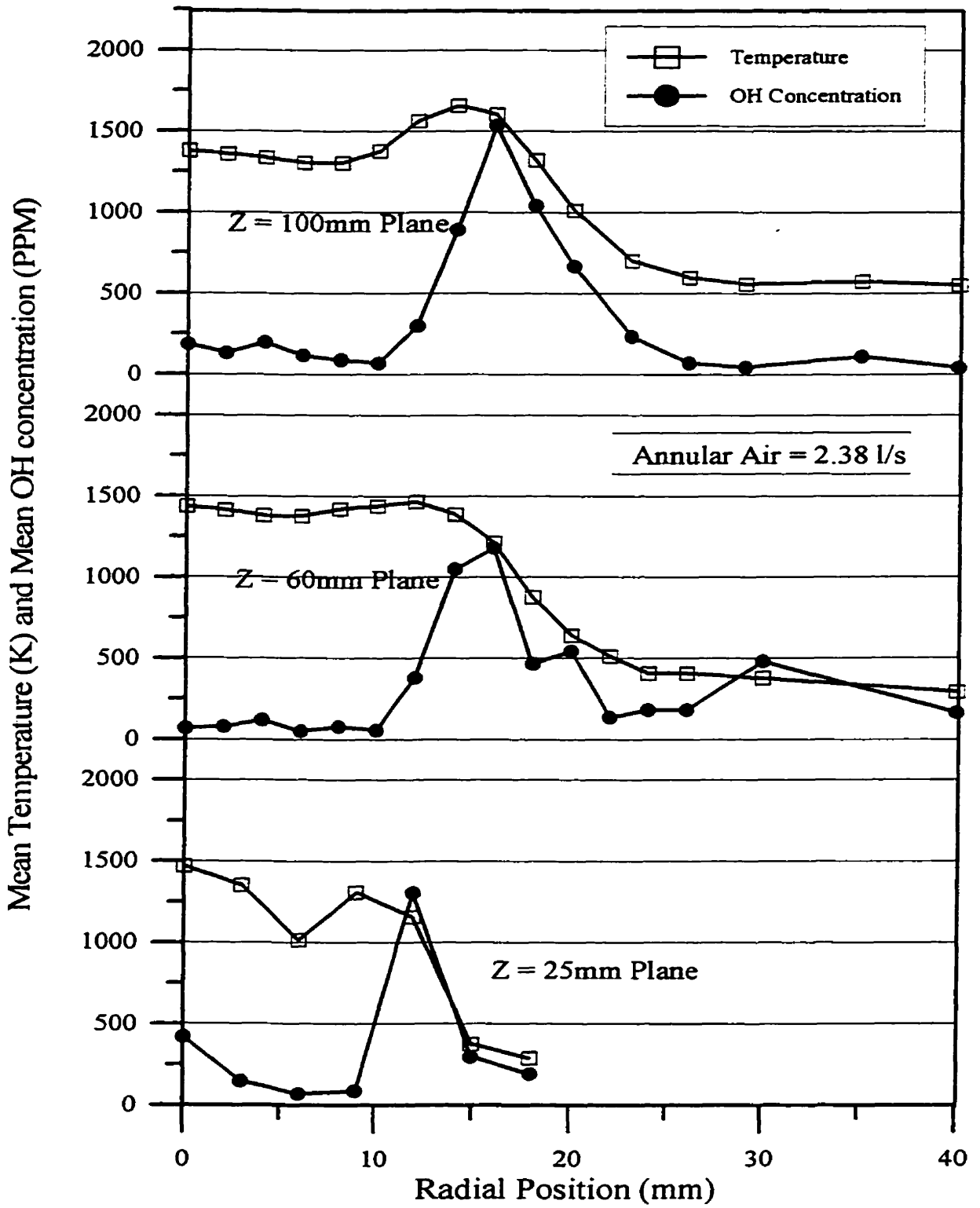


FIGURE 6.22: Mean OH concentration profiles with annular air = 2.38 *l*/s

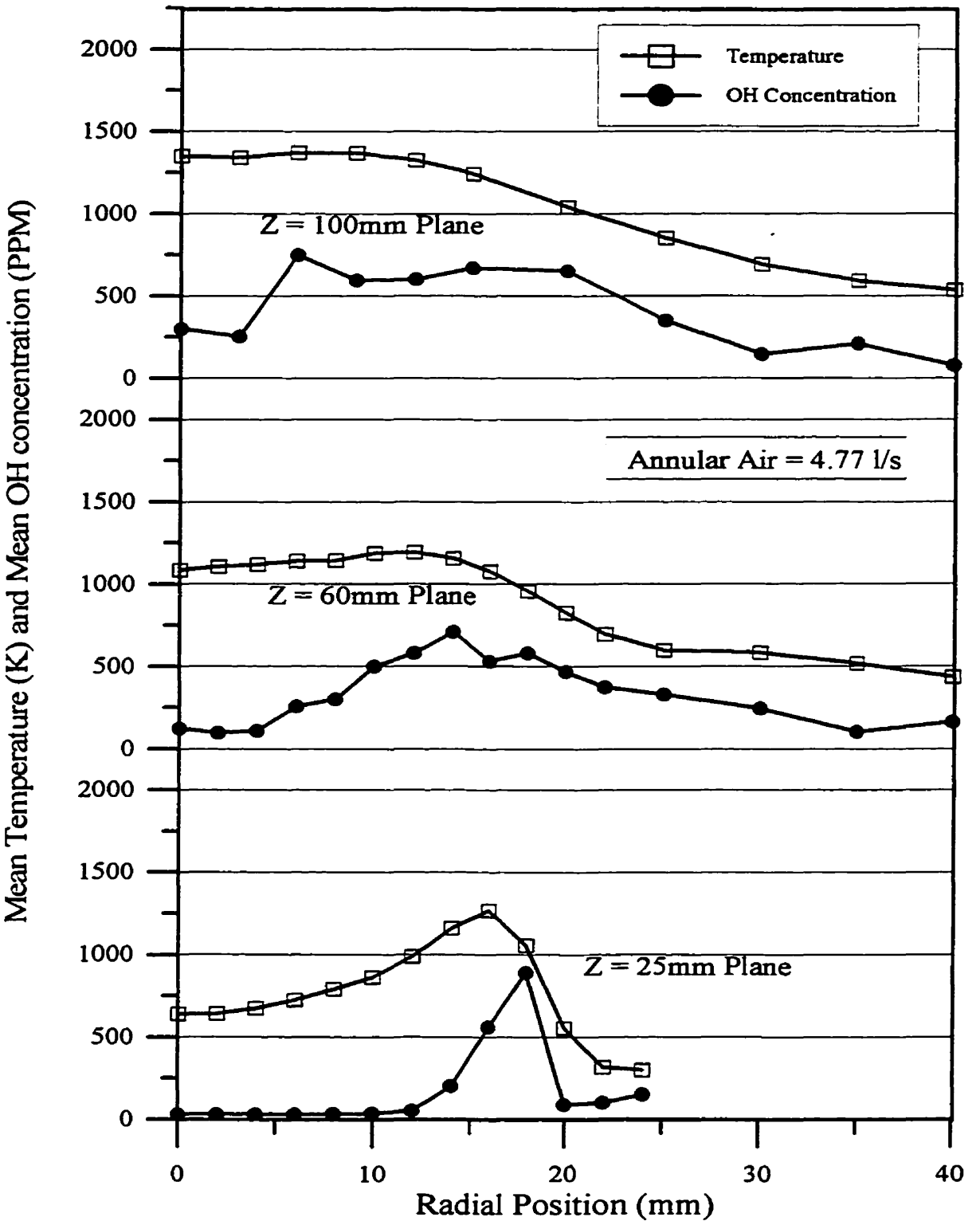


FIGURE 6.23: Mean OH concentration profiles with annular air = 4.77 *l*/s

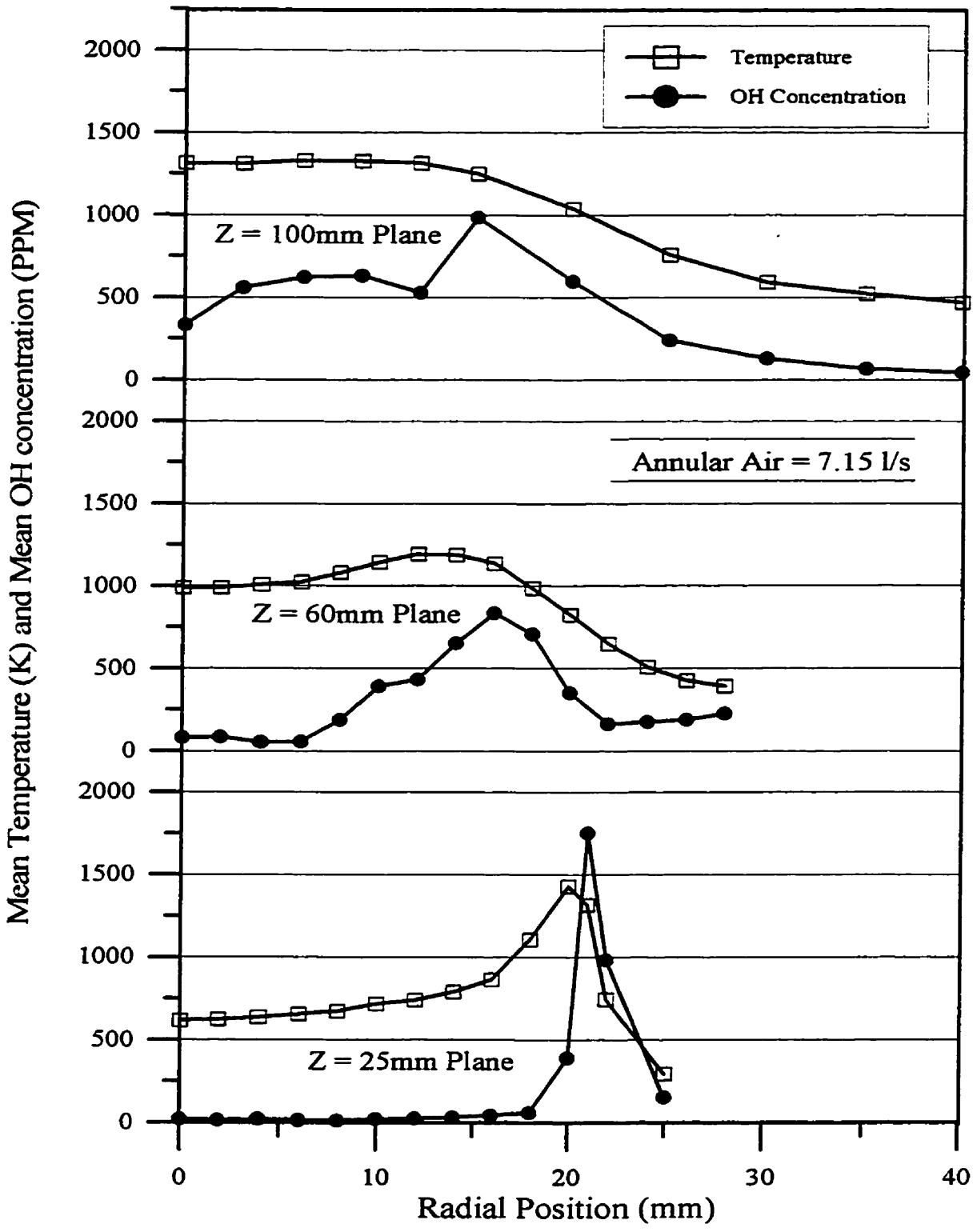


FIGURE 6.24: Mean OH concentration profiles with annular air = 7.15 *l*/s

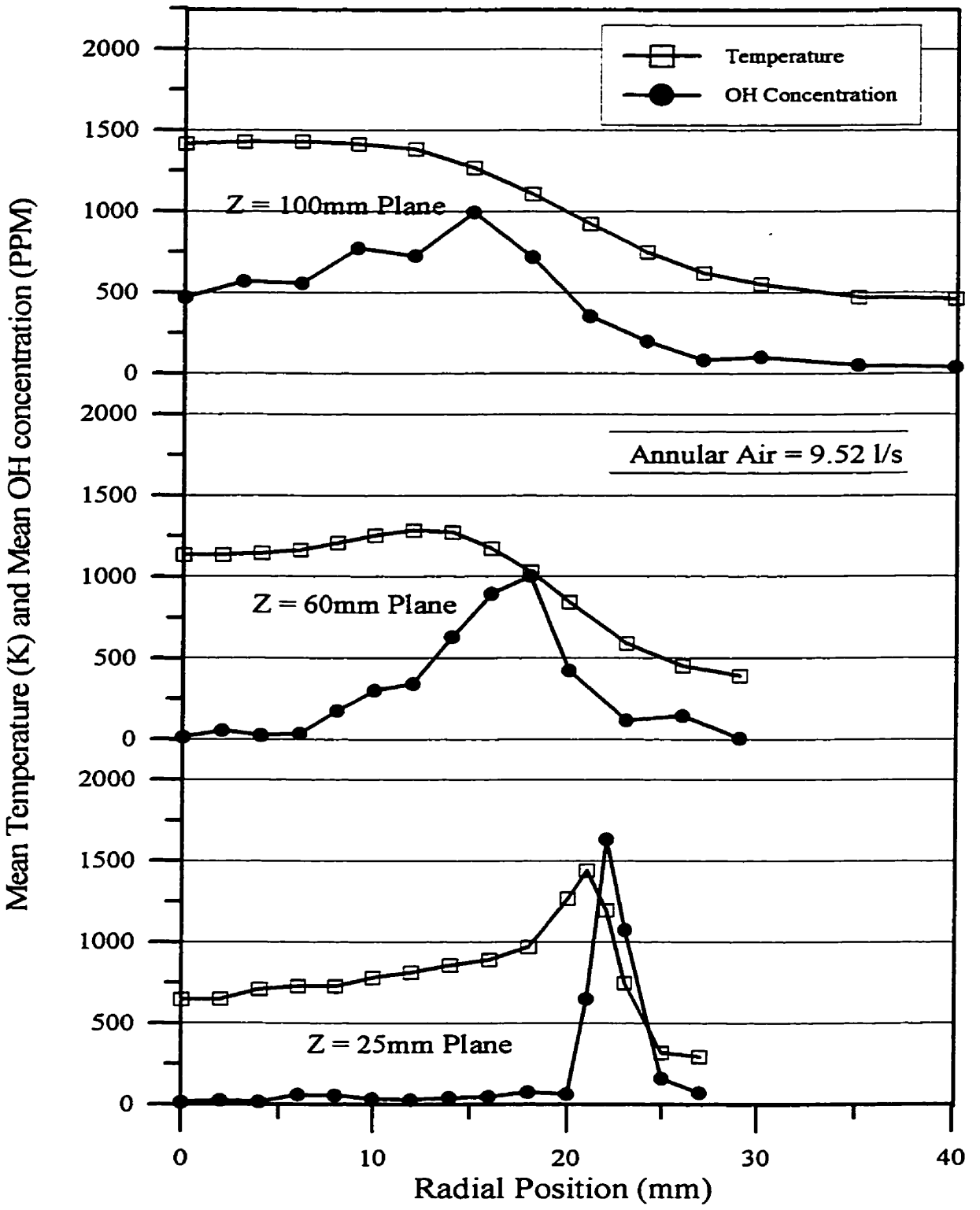


FIGURE 6.25: Mean OH concentration profiles with annular air = 9.52 *l*/s

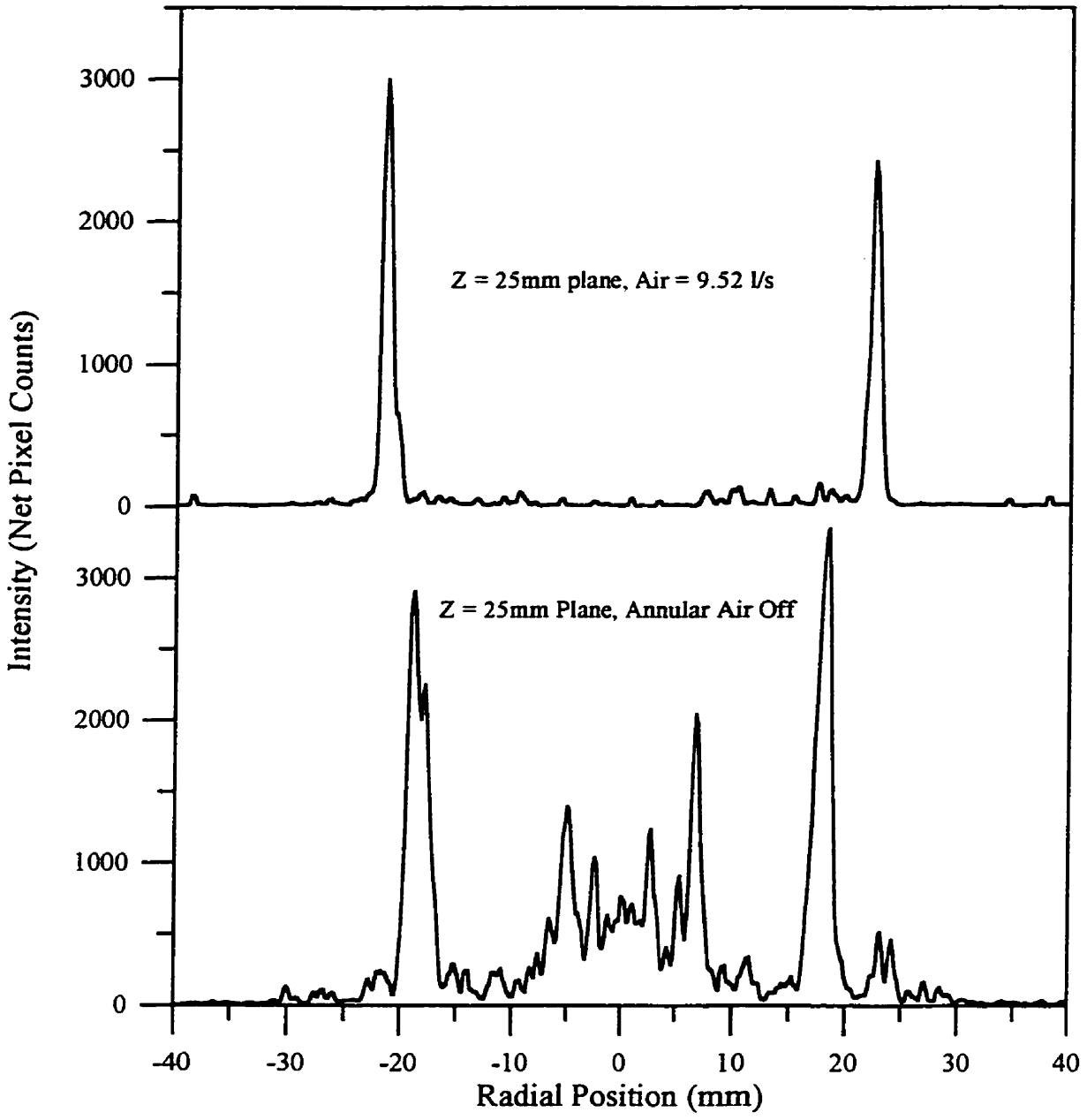


FIGURE 6.26: Instantaneous OH fluorescence in the z = 25mm plane for the annular air off and air = 9.52 *l*/s cases.

6.3 PLIF CH Images

An attempt was made to image CH in the spray flame, using a 1 nm band pass filter centred at 431.5nm, with excitation of the R_{1e} (J=7.5) and R_{1e} (J = 9.5) transitions at 425.7nm. The field of view was set to 35mm high x 52mm wide, and laser power was approximately 10 mJ/pulse, with a linewidth of 0.25 cm^{-1}.

Figure 6.27 shows an image of CH fluorescence in a bunsen burner natural gas flame. As can be seen, the signal to noise ratio is much lower than those seen for the previous OH fluorescence images, even in a clean environment such as the natural gas premixed flame shown here.

Figure 6.28 shows an attempted image of CH in a spray flame, in the plane 40 to 75mm downstream of the nozzle. Faint CH fluorescence is visible on the right hand side of the image, but the signal to noise ratio is too low in this flame to produce useful results. Noise appears in these images as random spots due to small variations in pixel intensity counts. Images are presented by scaling pixel intensity count to colour, with the range of scaling proportional to the range of pixel intensity counts in the image. If the signal intensity is of the same order as the pixel to pixel variations, then the signal image is lost as in Figure 6.28. There are several reasons for the low signal levels obtained. There is considerably less CH present in the flame than OH (three orders of magnitude in a methane-air diffusion flame [69]), and fluorescence intensity scales with number density. In addition, with the detection scheme used for CH, only a small portion of the resulting fluorescence is passed by the 1 nm bandpass filter. All these factors combined result in very low signal levels in the bunsen burner flame, and signals buried in noise from elastic scattering from droplets in the spray flame.

This excitation scheme for CH fluorescence was used successfully by Allen *et al* [58] in a spray flame, but several factors in that work allowed more success than achieved here. The primary factor that enabled production of usable images was the use of an air blast atomizer at low flow rates to produce a very fine, low density spray. The combination of low spatial density and small mean droplet size minimized interference due to elastic scattering from particles, thus allowing the fluorescence signal to be discriminated.

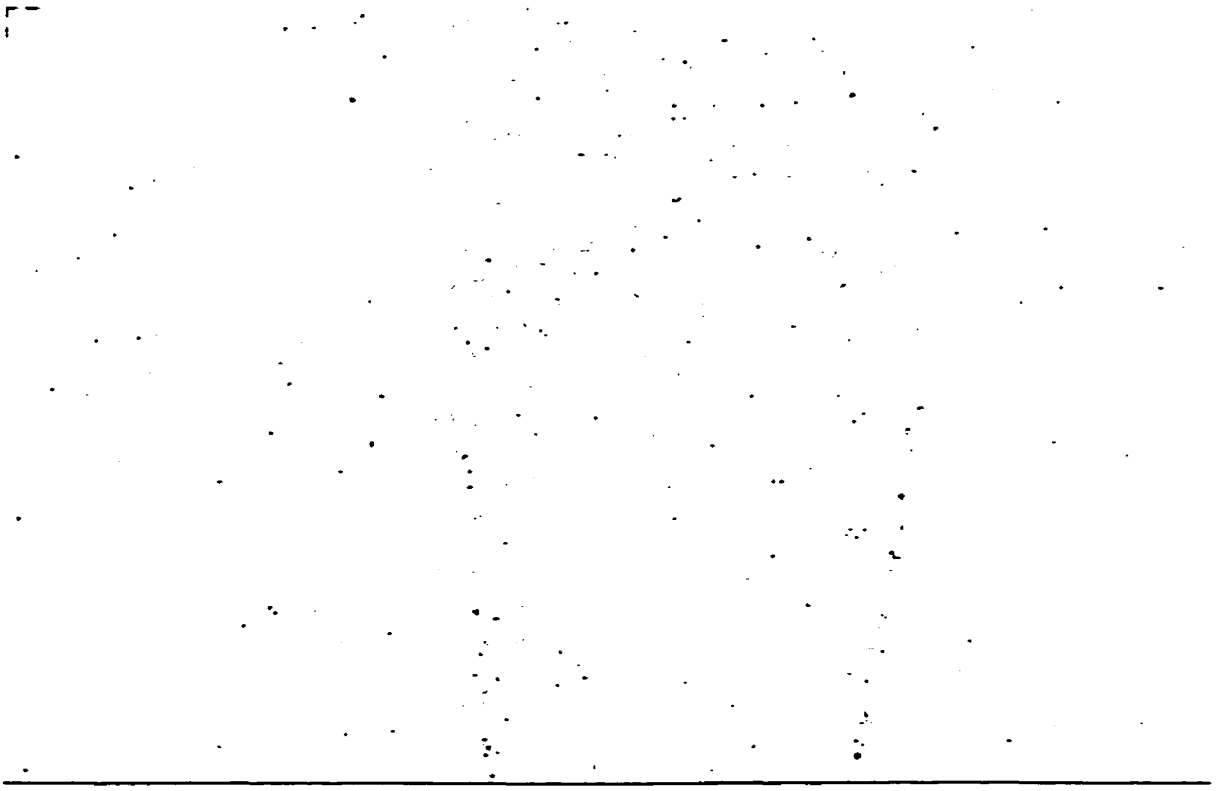


FIGURE 6.27: CH fluorescence image in a bunsen burner flame (using interference filter)

FIGURE 6.28: CH fluorescence in a spray flame

6.4. Phase Doppler Interferometry Results

Phase Doppler measurements were made across a diameter of the spray, in planes lying 15, 40, 60, 80, 100, 140 and 200mm from the nozzle exit. Each measurement set in a plane included up to 10,000 measurements of droplet size and velocity at closely spaced points along the diameter. In addition, measurements were made on centreline to obtain the centreline development of the spray. Some measurement sets were made using dyed methanol to enhance the visibility of small particles in order to extract gas-phase velocity, as discussed in Section 4.1.6. Air and fuel flow rates were as described in the previous section.

Prior to obtaining detailed measurements in the flame, the symmetry of the flow field was assessed using the phase Doppler interferometer. The photographs and PLIF images presented in the previous section indicated that there was good overall symmetry, although in many cases instantaneous symmetry was lost. In order to quantify the symmetry, an assessment was made in the region 40mm downstream of the nozzle. Measurements were made at a fixed radial distance from the flow axis, at eight different equally spaced circumferential positions. The following table summarizes the results of this test.

MEASURED QUANTITY	MEAN VALUE	STANDARD DEVIATION
Arithmetic mean diameter	26.2μm	5.7%
Sauter mean diameter	29.4μm	8.8%
Axial velocity	7.03 m/s	3.9%
RMS velocity	0.19 m/s	13.6%
Volume flux	.0015 cm^3/cm^2-s	34%

TABLE 6.1: Symmetry test results

As can be seen, diameter and velocity variations are quite small, while measured flux variations are large. The variation in measured volume flux is likely associated with the instrument itself rather than with the flow field, as will be discussed further in the next chapter. The temporal

stability of the flow was tested by taking PDI measurements at a fixed point every fifteen minutes over the course of four hours. As can be seen from Table 6.2, the flow is extremely stable. As stated above, the high degree of variability in the flux measurements are likely the result of instrument characteristics, and not a feature of the flow itself.

Measured Quantity	Mean Value	Standard Deviation
Arithmetic mean diameter	27.7μm	0.45%
Sauter mean diameter	33.3μm	0.79%
Axial mean velocity	7.299 m/s	0.37%
RMS velocity	1.593 m/s	3.7%
Volume flux	.0089 cm^3/cm^2-s	33%

TABLE 6.2: Temporal stability of the flow

6.4.1. Droplet Diameter Measurements

Figure 6.29 presents a typical droplet diameter histogram, obtained with an annular air flow rate of 4.77 *l*/s at a radial location of 18mm, 25mm downstream of the nozzle. The arithmetic mean diameter at this location is 21.4μm, and the Sauter mean diameter is 29.8μm. Figure 6.30 presents a typical droplet diameter-axial velocity correlation for the same conditions as above. As can be seen, in the droplet size range between 10 and 50μm, where the bulk of the droplet population resides, the correlation is nearly linear, as small particles are influenced by the gas-phase flow field while larger particles, with more momentum, are less strongly influenced. Below 10μm, the particle velocity appears to stabilize as droplets in this size range accurately follow the gas phase flow. Below approximately 5μm and above approximately 50μm, the correlation is quite noisy due to the low droplet counts in these size ranges. Figure 6.31 presents a typical radial-axial velocity correlation plot for the same conditions as above. The correlation is nearly linear over most of the range, with some noise at the extreme ends due to low particle counts in these velocity classes. The degree of correlation in Figures 6.30 and 6.31 is quite high, despite the wide size and velocity ranges

present. However, when it is considered that all the droplets arose from the disintegration of a liquid sheet emerging from the nozzle at fixed velocity, and hence all droplets would likely have similar initial velocity spectra at formation, the degree of correlation is not surprising. It should be noted that the points on the graph represent average velocities for all droplets in each size bin, as opposed to individual droplet size/velocity data.

Figure 6.32 presents the radial distribution of arithmetic mean diameter in a plane 10mm downstream of the nozzle. In this region very close to the nozzle, the annular air flow has little effect on the droplet size over the bulk of the spray, but out towards the edges beyond 10mm radial position, there appears to be a considerable reduction in mean droplet size. Comparison with Figure 6.40, (the volume flux distribution in this plane) shows that there is little volume flux in this region, and that the volume flux in this region is not significantly affected by the annual air flow. The reduction in arithmetic mean diameter, which appears to be proportional to the annular air flow rate, suggests that small droplets may be recirculating, thus skewing the mean diameter towards small particles. This view is reinforced by examining the velocity vector plot fields in Figures 6.52-6.53, which distinctly show recirculating flow in the z = 10mm plane, with the recirculation intensity increasing with annular air flow rate. There have been suggestions that the high relative velocities between the large droplets and the air flow field could result in aerodynamic break-up of large droplets, thus contributing to the reduction of arithmetic mean diameter in some regions. However, as seen in Figure 6.59, depicting the velocity vector field for the gas-phase flow and large (>30μm) droplets, the maximum mean relative velocity appears to be near 25m/s for the air = 7.15l/s case, resulting in a Weber number of around 2, too low to cause aerodynamic breakup, although distortion of the larger droplets is likely to occur.

Figures 6.33 to 6.39 present the variation of arithmetic mean diameter with radial position and annular air flow rate in the z = 25, 40, 60, 80, 100, 140 and 200mm planes. As can be seen, in all these planes, in contrast to the z = 10mm plane, D_{10} increases monotonically with radial distance from the spray axis, with exception of a few cases at the periphery of the spray, where few samples were taken, resulting in questionable mean diameters. The diameter of droplets at the "edge" of the spray in the z = 25mm plane, Figure 6.33, ranged from 35 to

44μm, appearing to increase with decreasing annular air flow rate. As distance from the nozzle increased, the difference appeared to diminish, until by the z = 60mm plane, the mean diameters are virtually identical. An obvious exception to the trend is the air = 4.77*l/s* case, which appears to show a sudden drop-off in mean diameter at the edge of the spray. This air flow case also displays quite a different profile of mean droplet diameter distribution in the z = 25mm plane, having a much steeper droplet diameter increase with distance from the spray axis. A likely explanation for this departure from the other air flow rate trends is that, in this case, there is direct flame impingement on the bluff body, which heats it up to approximately 150°C. The emerging methanol spray is very hot (likely above its atmospheric boiling point) and therefore behaves somewhat differently than a cold emerging spray. Beyond z = 100mm, the smallest droplets have mainly vaporized, resulting in higher arithmetic mean diameters near the centreline. Even farther downstream, only the largest droplets are left, but these have reduced in size considerably due to evaporation, so the maximum mean diameter at the spray edge has fallen. In the z = 200mm plane, very little spray remains, and what is left is relatively small. Very little symmetry is evident in this region, but no large variations are present.

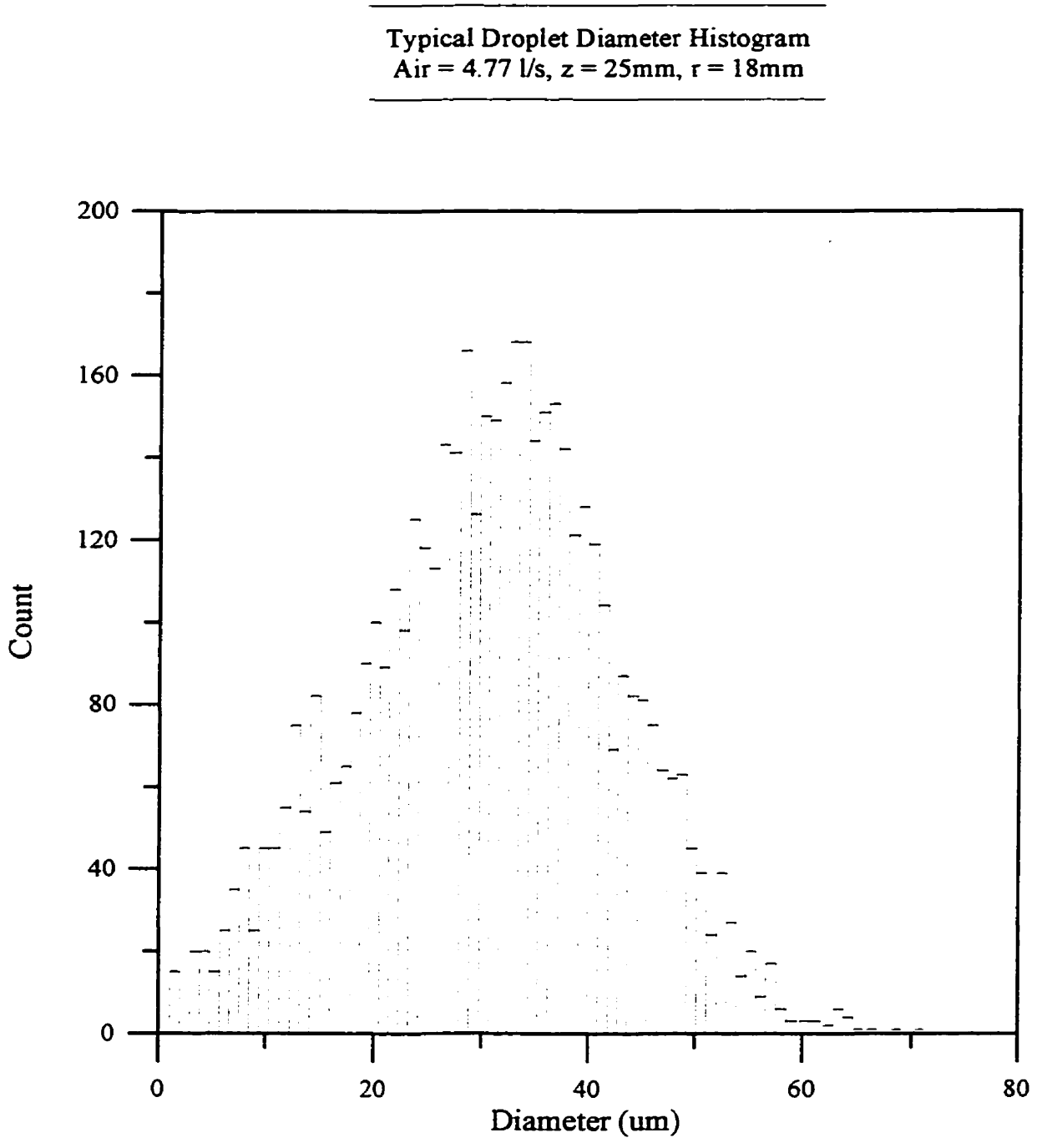


FIGURE 6.29: Typical droplet diameter distribution, obtained at z = 25mm, r = 18mm with an annular air flow rate of 4.77 *l*/s

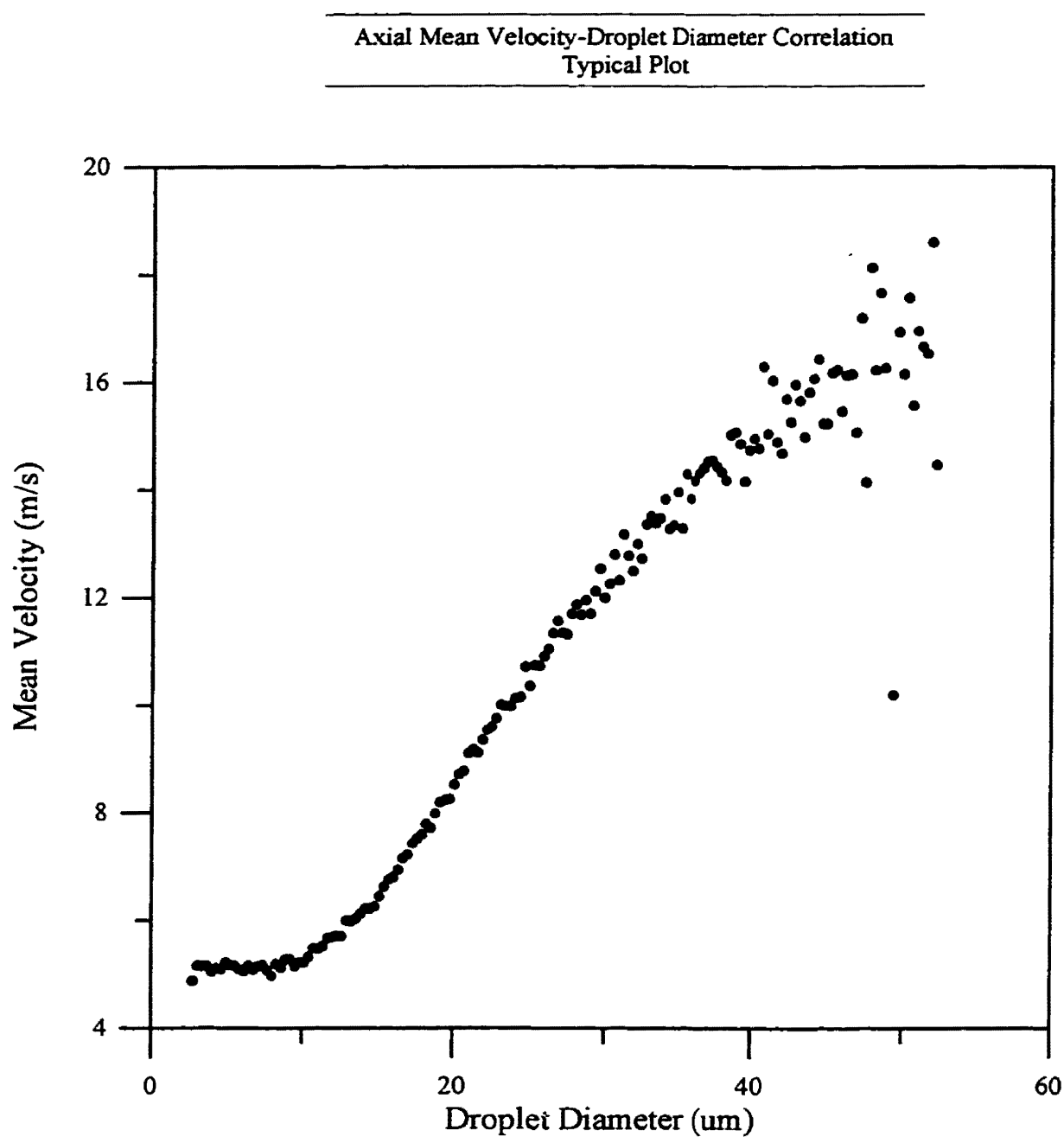


FIGURE 6.30: Typical droplet diameter-axial velocity correlation, obtained at z = 25mm, r = 18mm with an annular air flow rate of 4.77 *l*/s

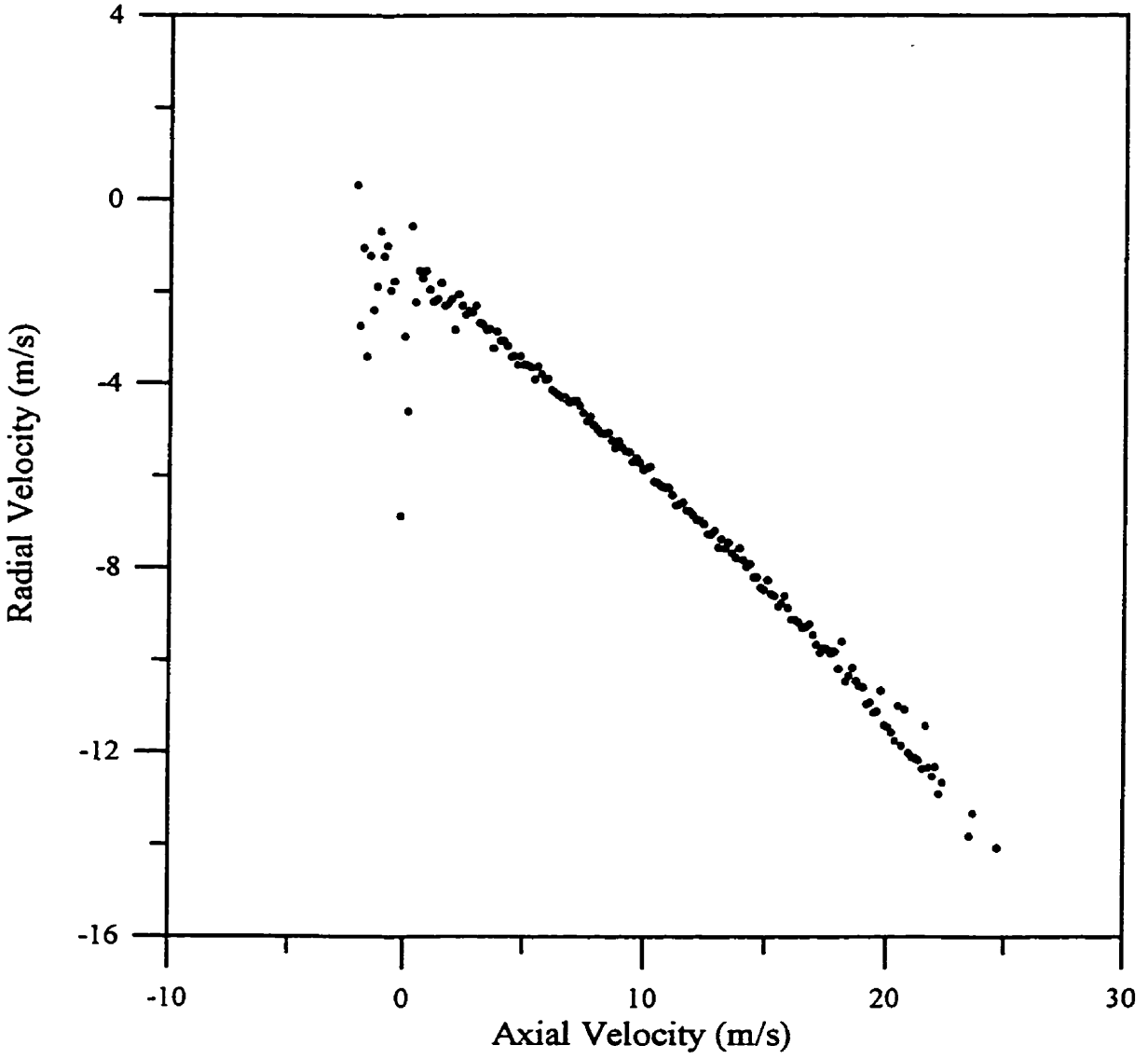


FIGURE 6.31: Typical radial-axial velocity correlation, obtained at z = 25mm, r = 18mm with an annular air flow rate of 4.77 *l*/s

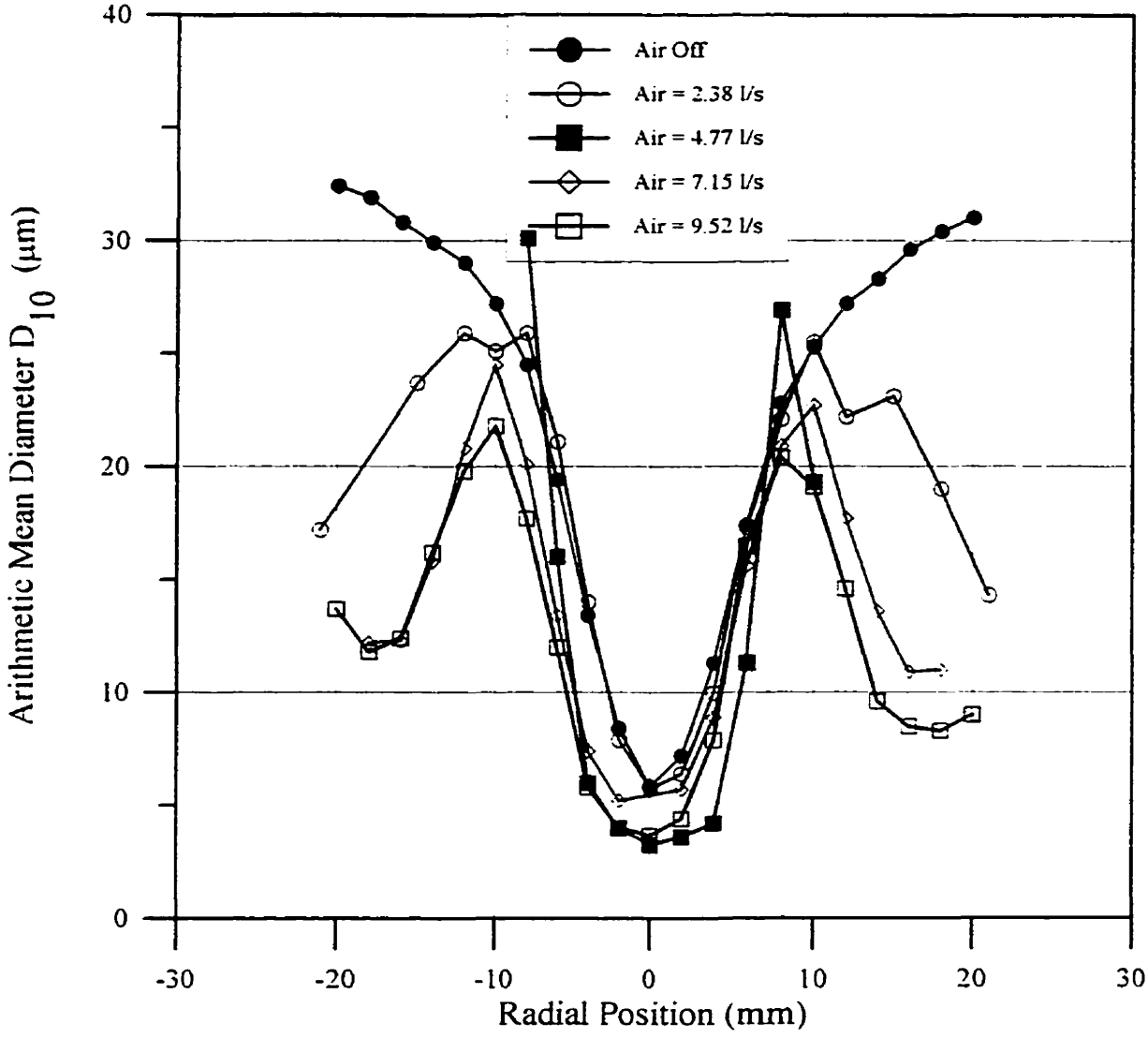


FIGURE 6.32: Variation of arithmetic mean diameter with radial position in the z = 10mm plane

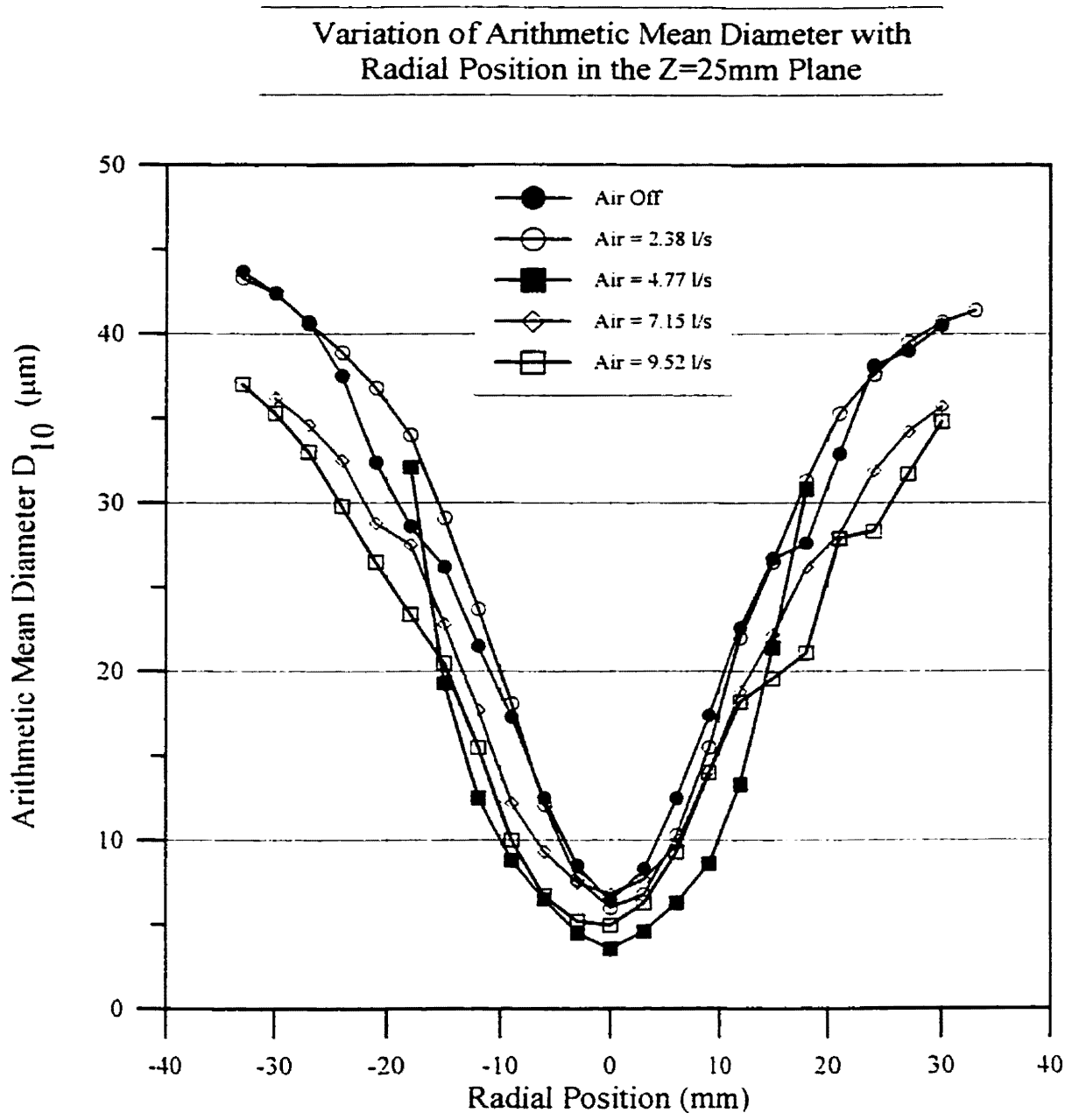


FIGURE 6.33: Variation of arithmetic mean diameter in the z = 25mm plane

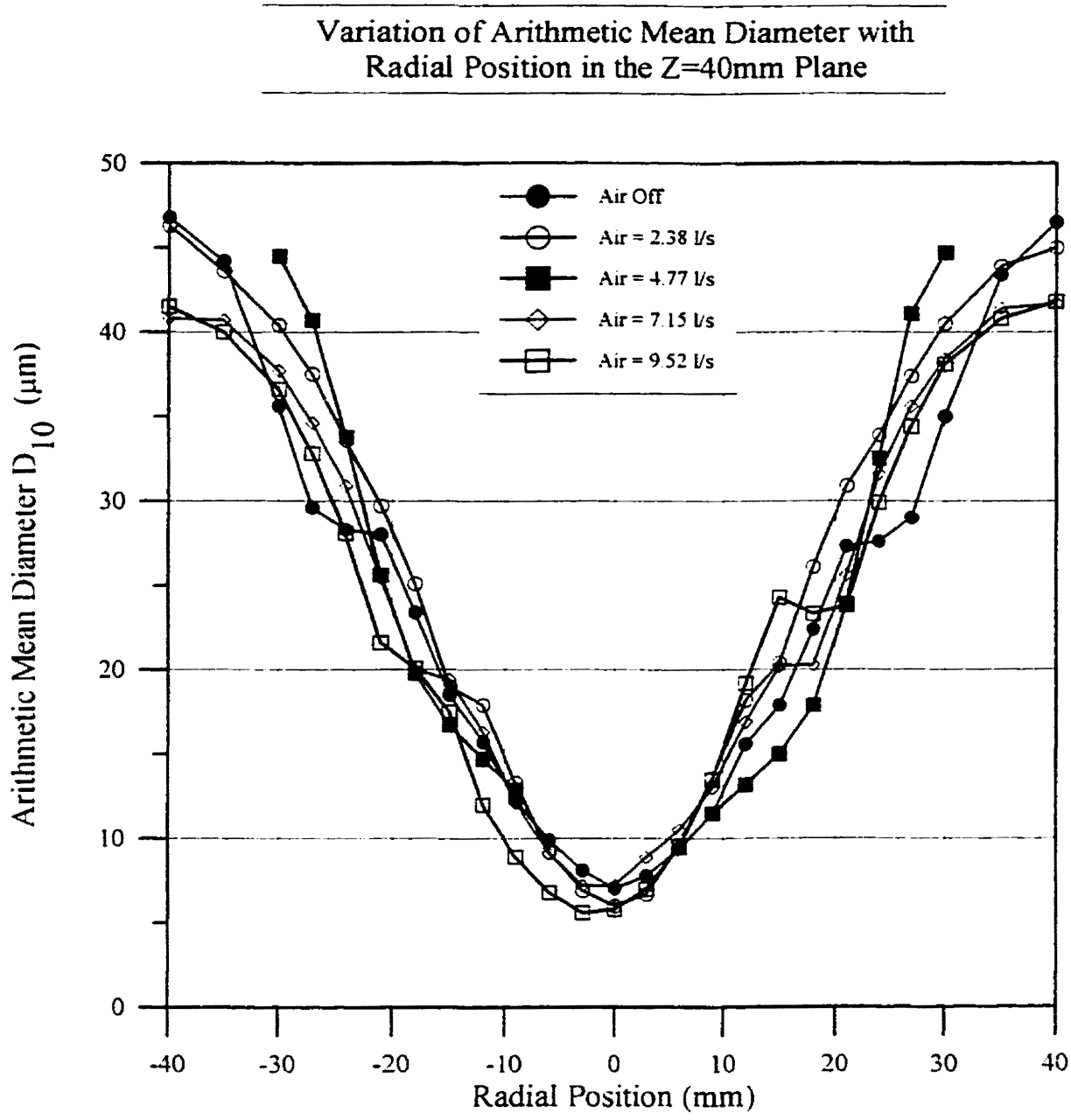


FIGURE 6.34: Variation of arithmetic mean diameter in the z = 40mm plane

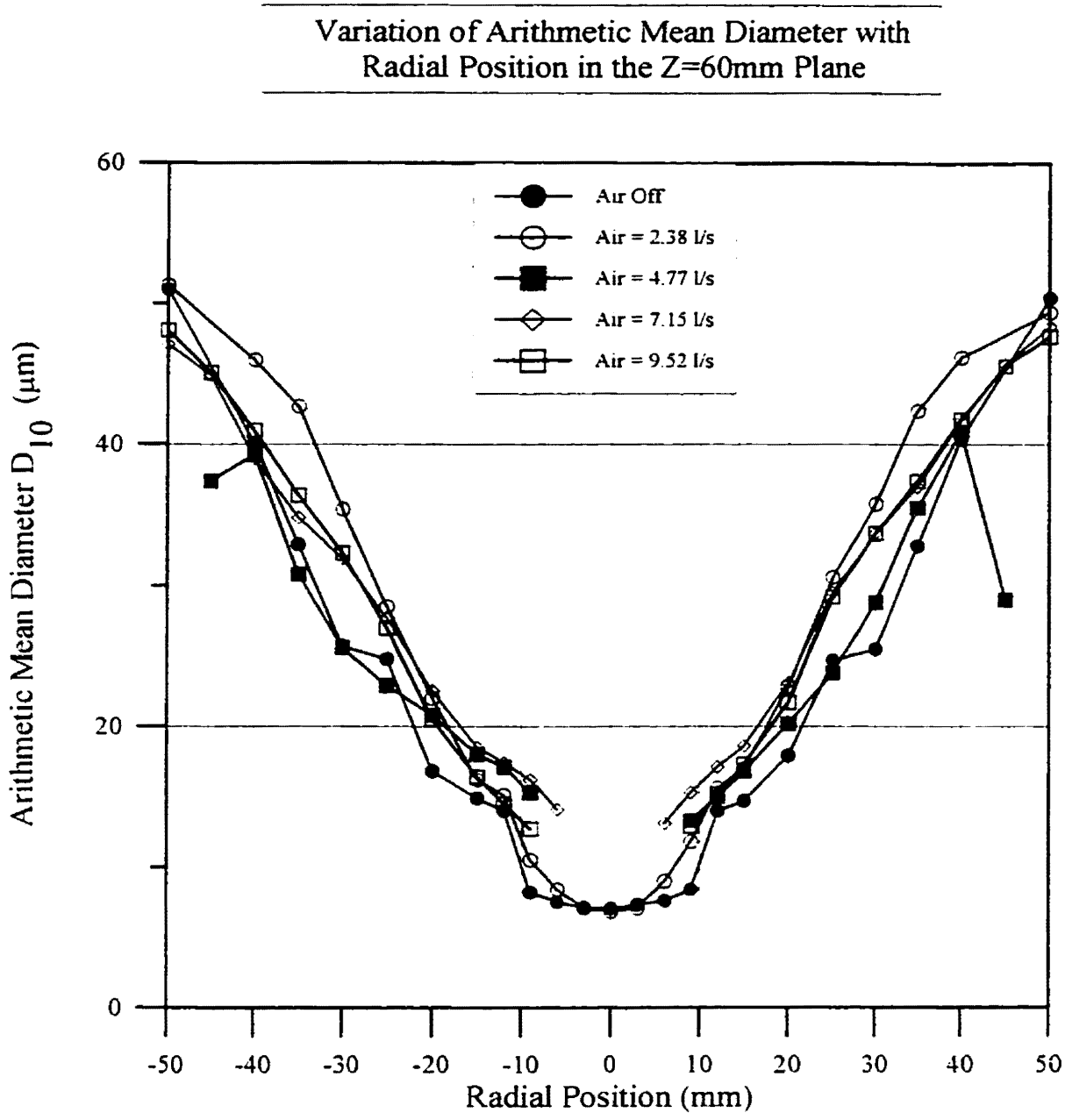


FIGURE 6.35: Variation of arithmetic mean diameter in the z = 60mm plane

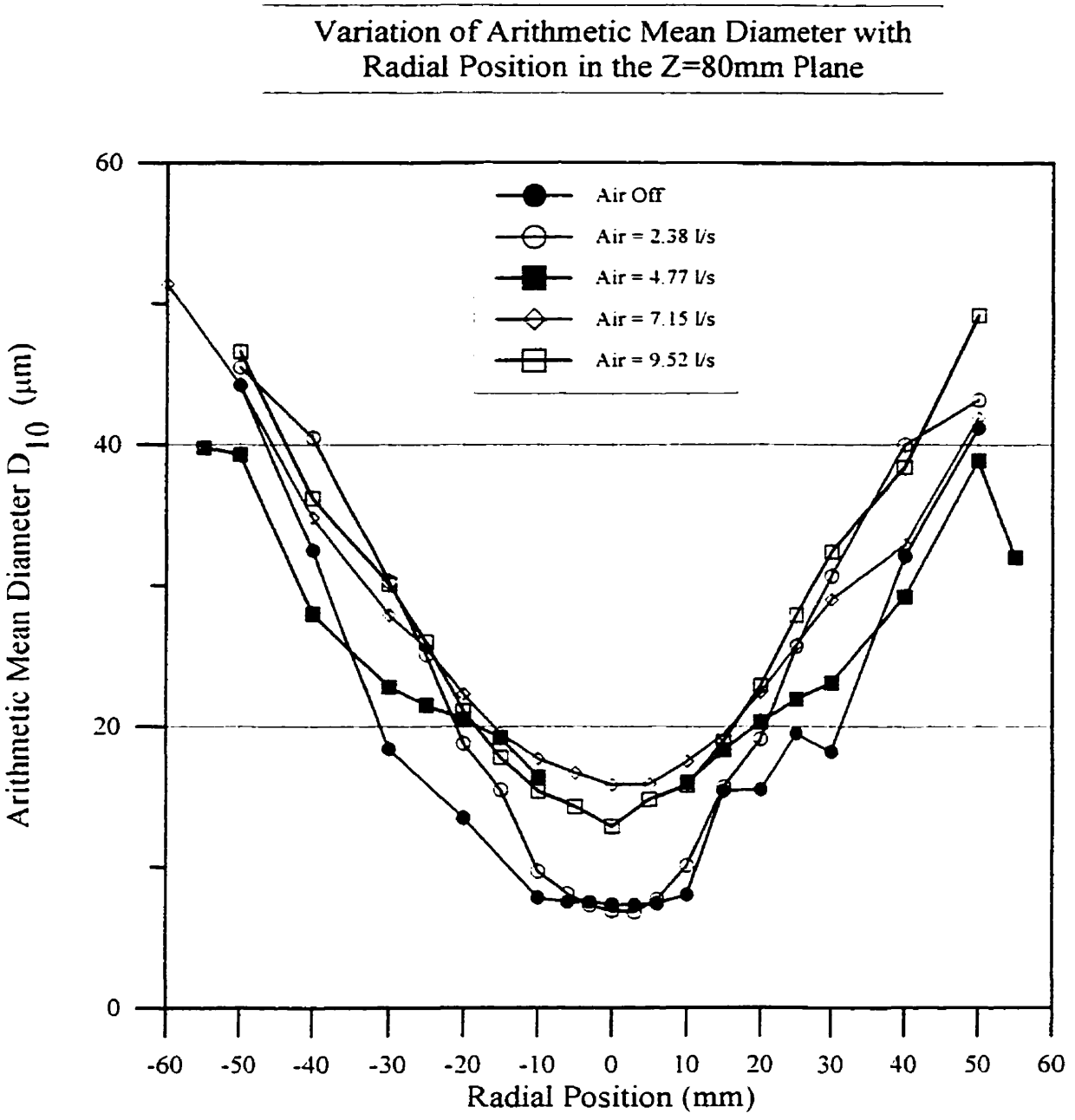


FIGURE 6.36: Variation of arithmetic mean diameter in the z = 80mm plane

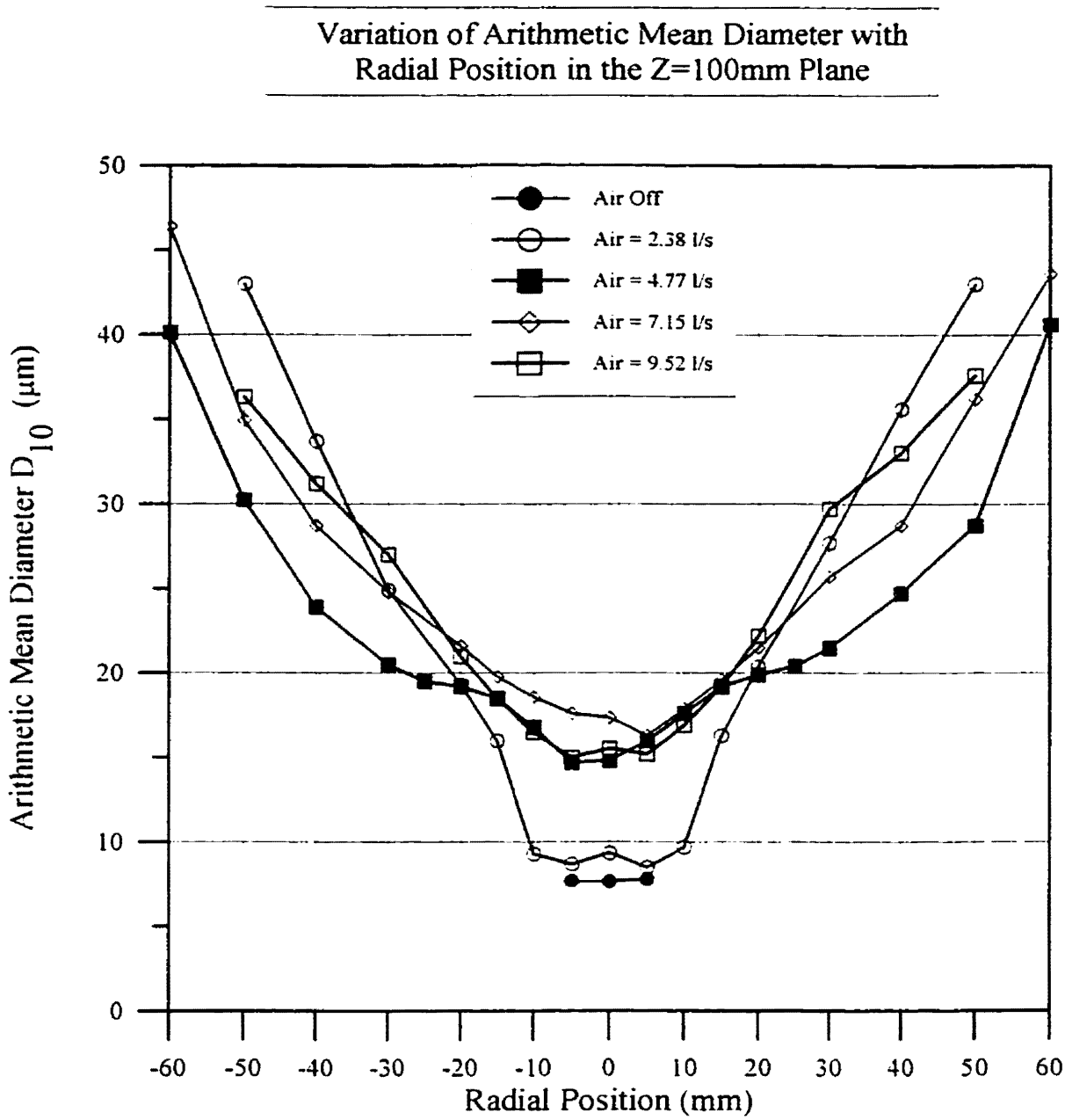


FIGURE 6.37: Variation of arithmetic mean diameter in the z = 100mm plane

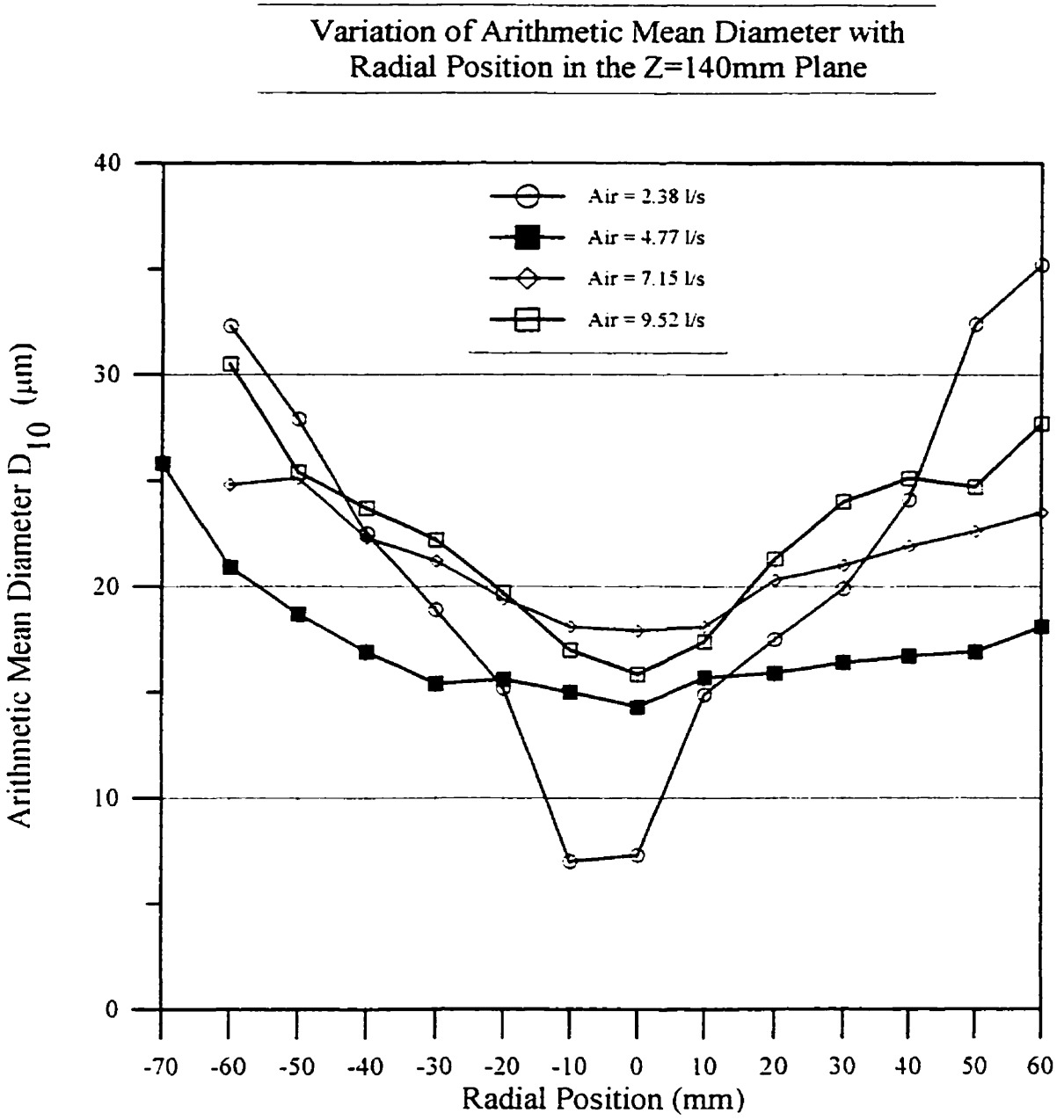


FIGURE 6.38: Variation of arithmetic mean diameter in the z = 140mm plane

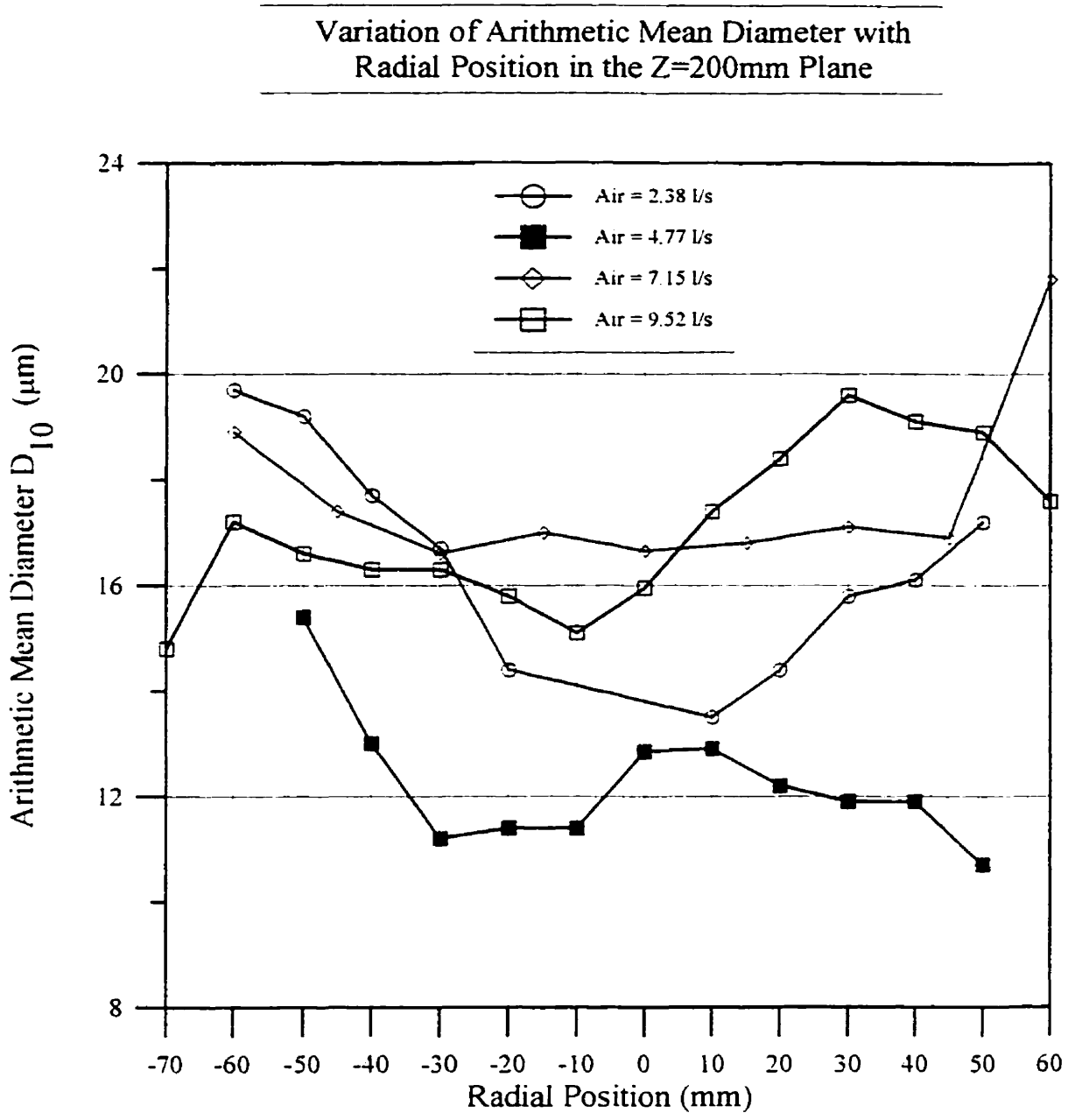


FIGURE 6.39: Variation of arithmetic mean diameter in the z = 200mm plane

6.4.2. Volume Flux Profiles

Figures 6.40 to 6.47 present the radial distribution of volume flux for all air flow rates tested in the z = 10 to 200mm planes. As can be seen in the z =10 and 25mm planes, Figures 6.40 and 6.41, the location of the volume flux peaks are not strongly affected by the annular air jet, unlike the non-burning case where increasing annular air flow leads to a widening of the spray cone [13]. The centreline volume flux diminishes with increasing annular air flow, essentially falling to zero for annular air flow rates of 4.77 *l*/s and higher. These trends are still apparent in the z = 40mm plane. For the no and low annular air flow rate cases, there appears to be a volume flux peak on centreline, as well as at approximately ±20mm radial position. In the z = 60 and 80mm planes, this centreline peak is of similar magnitude to the peak fluxes in the higher air flow rate cases. In the z = 100mm and further planes, the location of the volume flux peaks is essentially the same for all annular air flow rates, but the peak values measured in the z = 100mm plane are only approximately 1/20 of those measured in the z = 25mm plane. Integration of the volume flux curves in several planes, presented in Figure 6.48, gives an indication of the evaporation rate of the spray. Although it appears that the air off case results in the fastest and most complete vapourization of the spray, this is likely due to the low entrainment velocity which allows droplets that escape the flame envelope to settle back down due to gravity, and thus escape detection in the planes farther downstream.

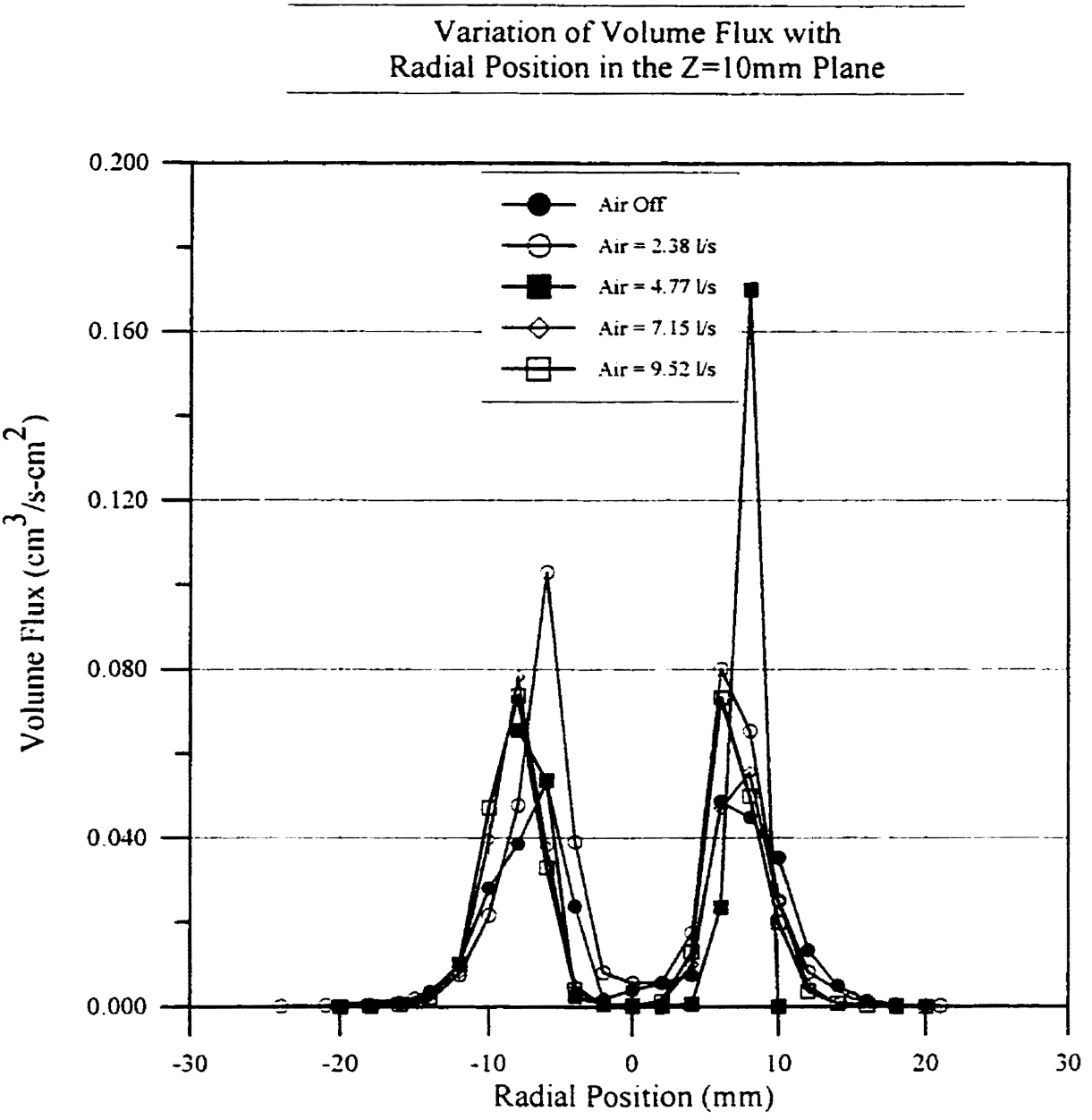


FIGURE 6.40: Variation of volume flux in the z = 10mm plane

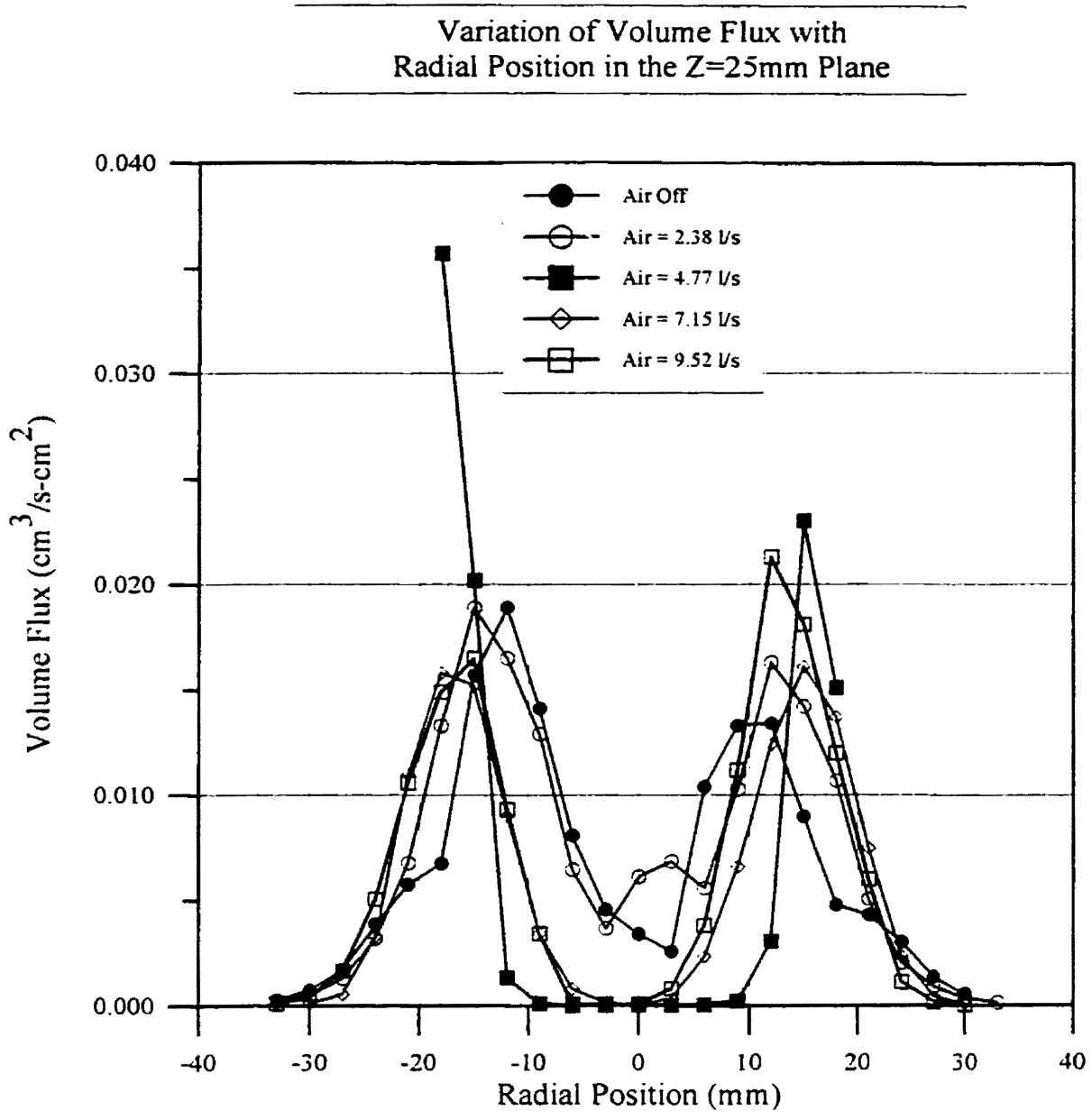


FIGURE 6.41: Variation of volume flux in the z = 25mm plane

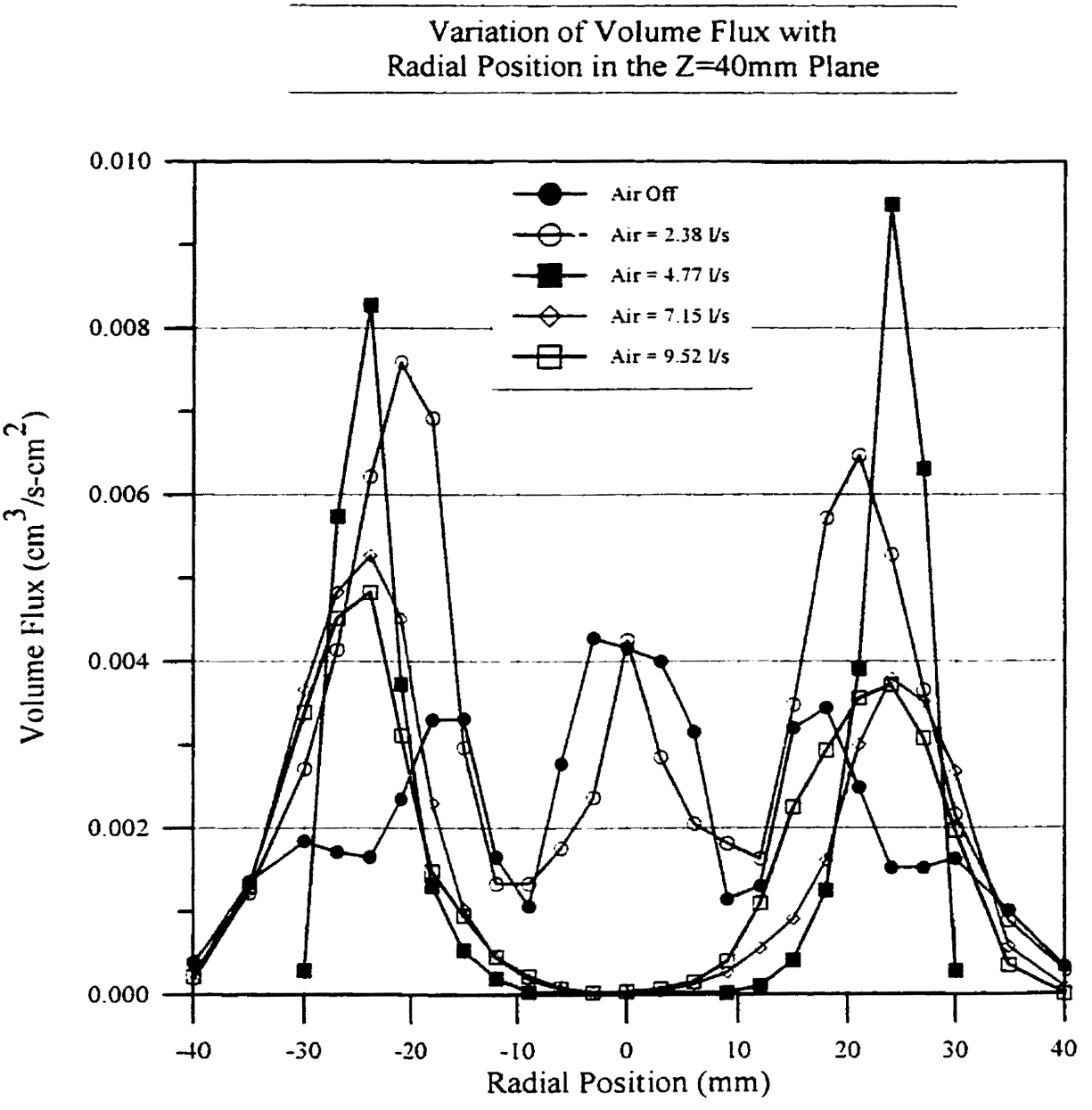


FIGURE 6.42: Variation of volume flux in the z = 40mm plane

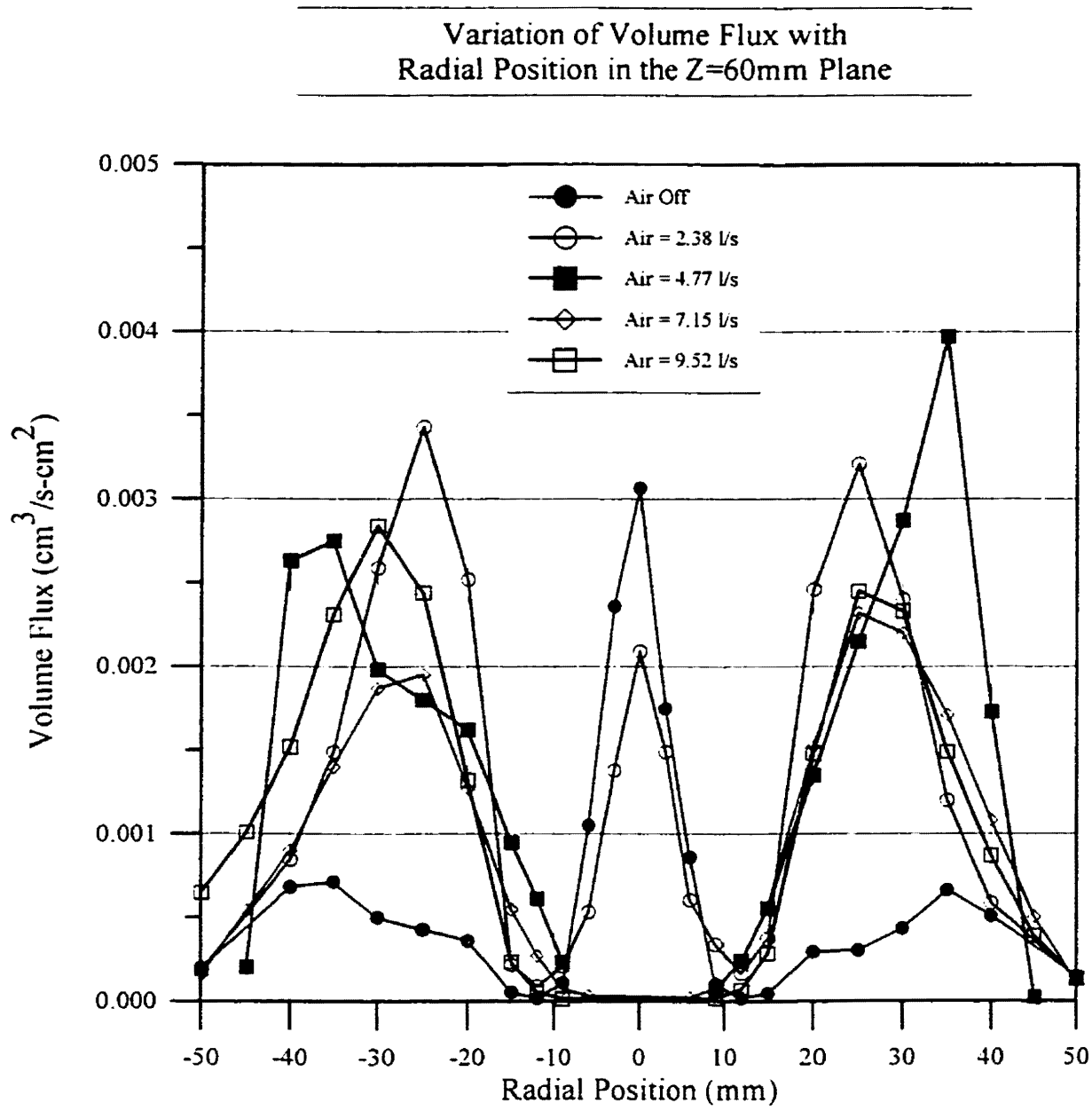


FIGURE 6.43: Variation of volume flux in the z = 60mm plane

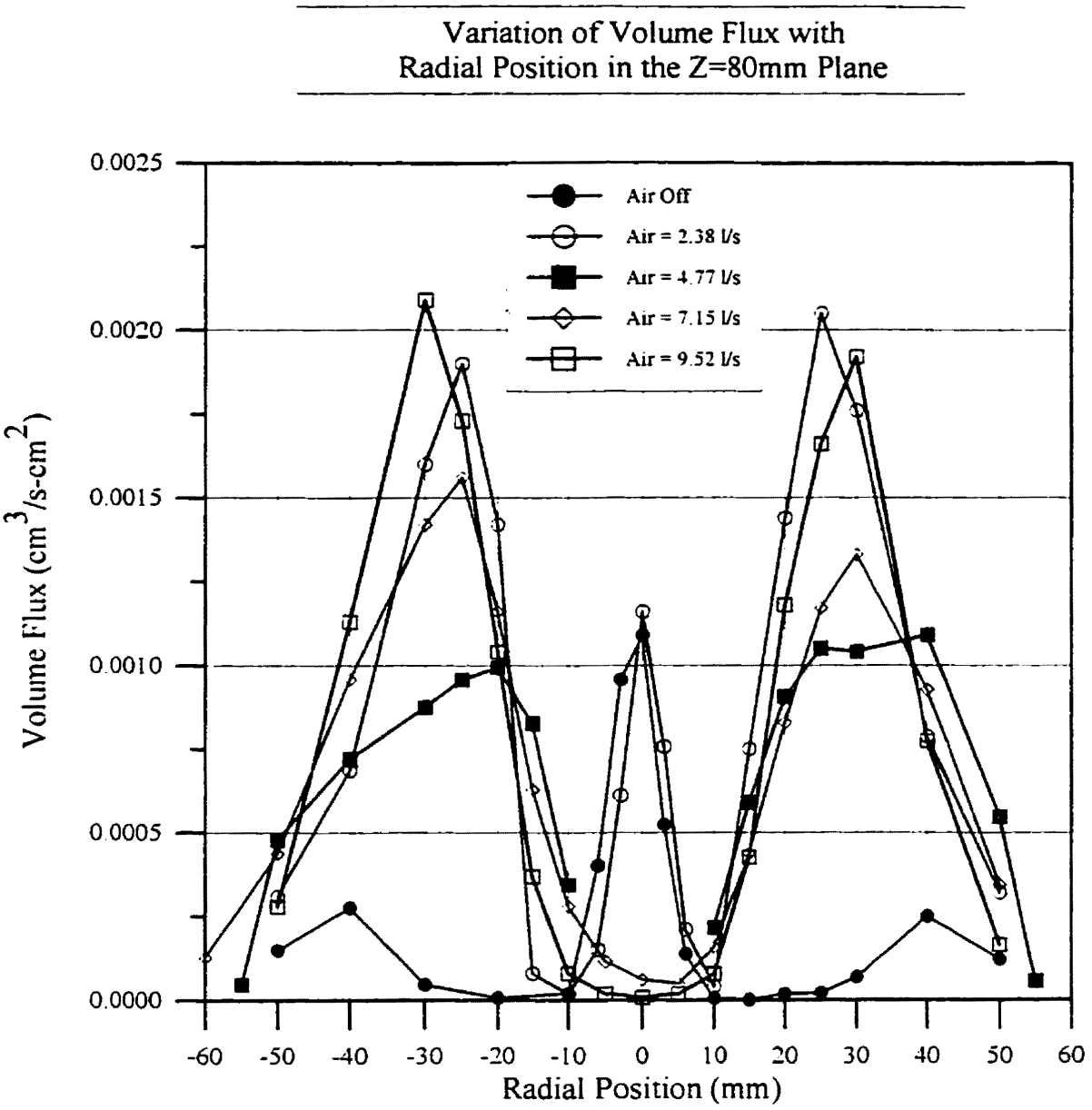


FIGURE 6.44: Variation of volume flux in the z = 80mm plane

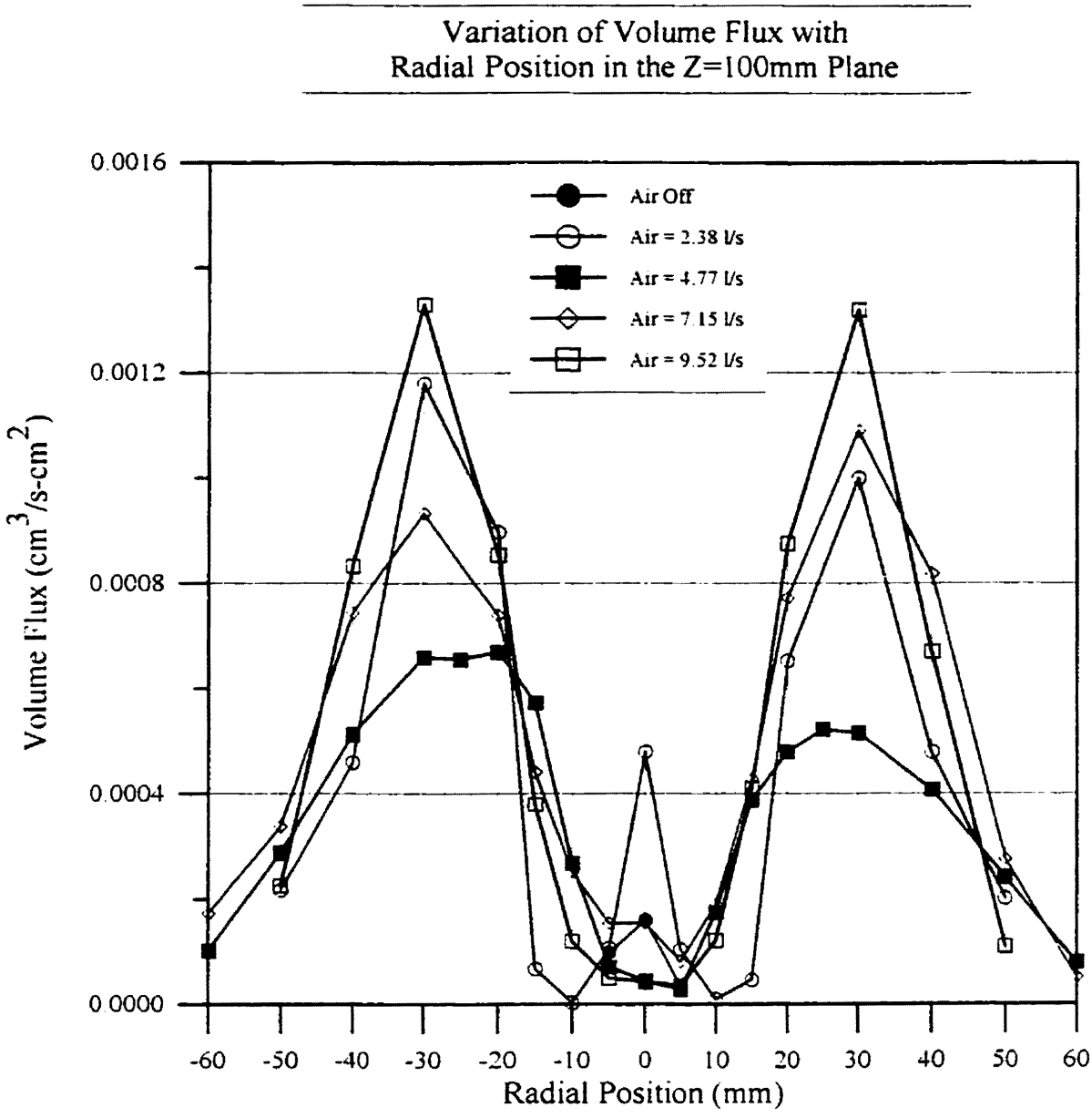


FIGURE 6.45: Variation of volume flux in the z = 100mm plane

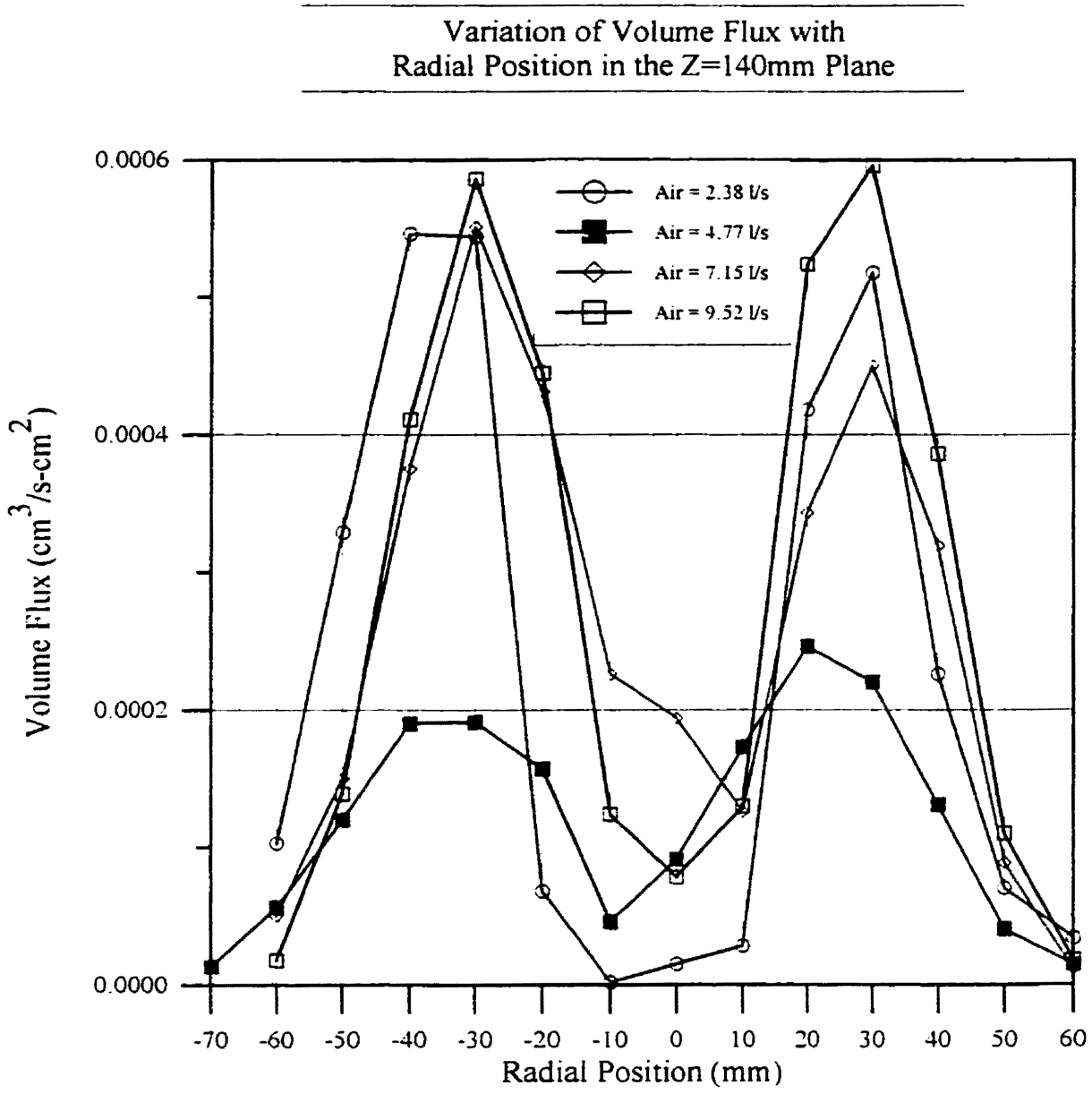


FIGURE 6.46: Variation of volume flux in the z = 140mm plane

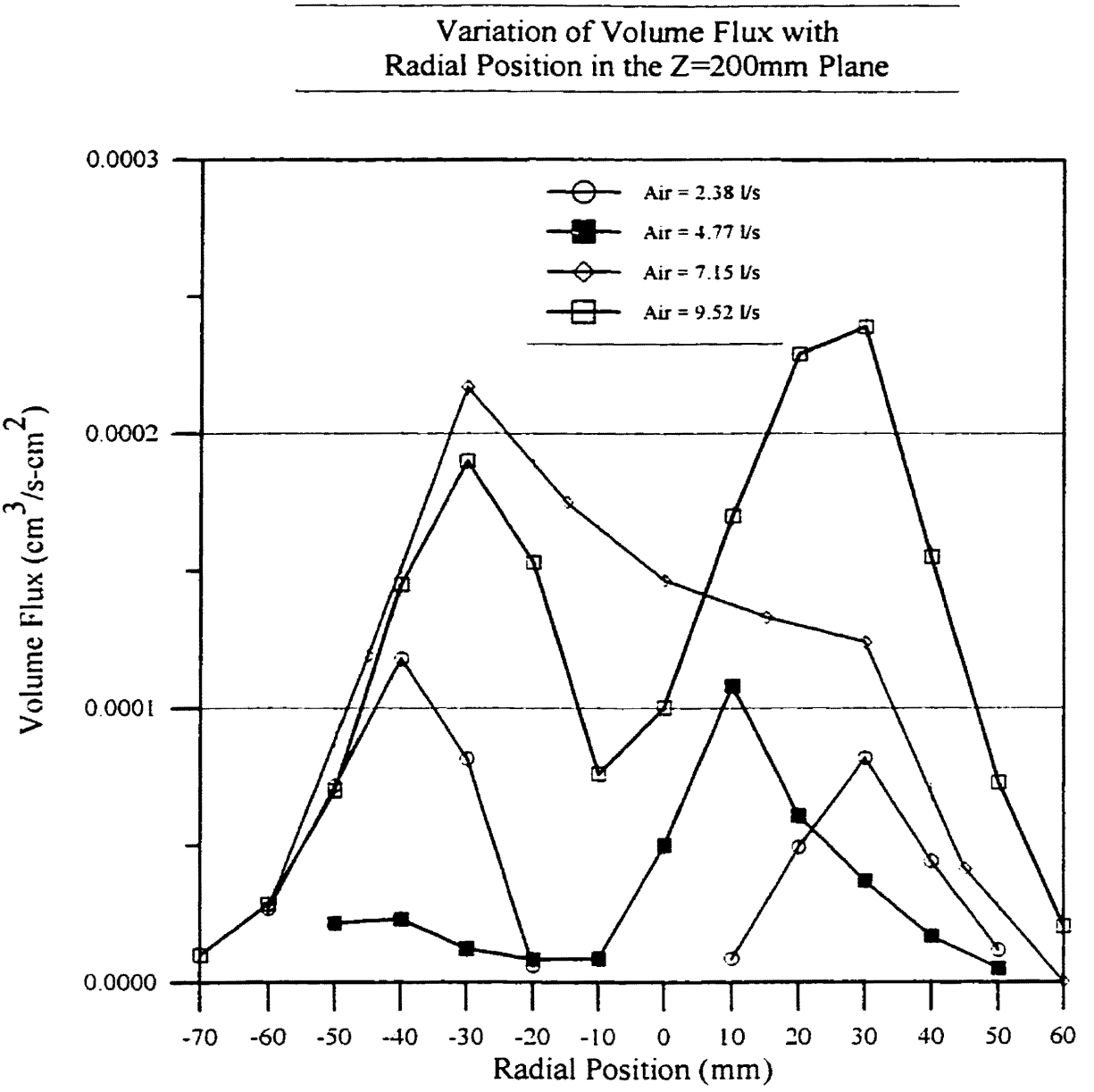


FIGURE 6.47: Variation of volume flux in the z = 200mm plane

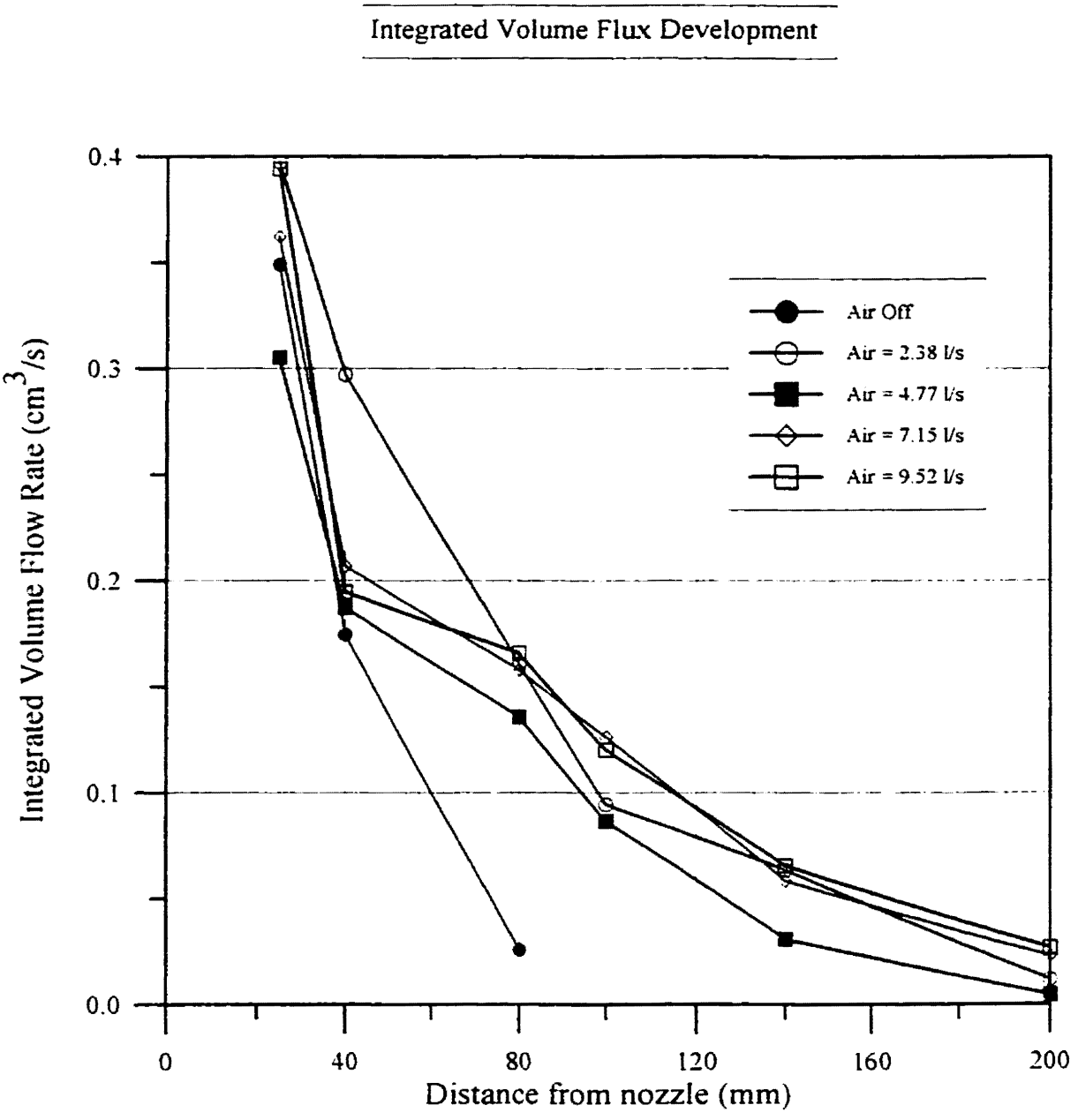


FIGURE 6.48: Integrated volume flux curves for all air flow rates

6.4.3. Mean Velocity Fields

Gas-phase mean velocity was obtained from raw data sets by filtering the data to generate a file consisting of only small droplet data. The cut-off diameter was typically 5 μm, resulting in a turbulent Stokes number of approximately 40 in a region with an integral time scale of 2 ms and initial relative velocity of 10 m/s. Figure 6.30 presents a diameter-velocity correlation plot, obtained in the z = 25mm plane, approximately 18mm off centreline in a region containing a wide spectrum of droplet sizes under highly turbulent conditions. As can be seen, there appears to be a clear cut-off in measured velocity for diameters near 10 μm, below which there is essentially no change in droplet velocity, suggesting that droplets in this size range are accurately following the gas-phase flow.

Figures 6.49 to 6.53 present the gas-phase velocity vector fields for all annular air flow rates tested, obtained by filtering the raw data set to eliminate velocity data from all particles larger than 5-10 μm, depending upon location. Figure 6.49, showing the velocity vector plot with annular air off, shows a smoothly developing velocity field, with peak velocities occurring on centreline, with a magnitude of approximately 5 m/s. The inner reaction zone, with a nearly constant diameter of 16mm, is located in a region of relatively high velocity in each plane, ranging from 2.5 to 4 m/s. The outer reaction zone, by contrast, is located in regions of relatively low velocity, below 1 m/s. In all cases, the velocity vectors are nearly parallel to the reaction zone. There are no regions of large velocity gradients present, and no evidence of recirculating flow. When the annular air flow rate is set to 2.38 *l/s*, the peak centreline velocity in the z = 25mm plane increases to nearly 9 m/s, though farther downstream in the z = 100mm plane, it has diminished to around 4.5 m/s, essentially the same as the air-off case. The reaction zone width is somewhat wider than the inner reaction zone noted in the air-off case, ranging from 22mm diameter in the z = 25mm plane to 33mm in the z = 100 plane, widening linearly with increasing distance from the nozzle. There is some evidence in the z = 10mm plane of recirculating flow outside the reaction zone. In the far downstream z = 100mm plane, there is no evidence of any re-entrainment into the flame, as all velocity vectors outside the mean location of the reaction zone are directed away from the flame front. The velocity field changes quite a bit when the annular air flow rate is increased to 4.77 *l/s*. In this case, there is a

"channeling" effect evident inside the reaction zone, where the gas flow is noted to be directed towards the centreline. Outside the reaction zone, the velocity vectors are directed away from centreline at all locations measured. The centreline velocity in the z = 100mm plane is around 3.75 m/s, less than that measured at the lower annular air flow rate of 2.38 *l/s*. Increasing the annular air flow rate further to 7.15 *l/s* reveals clear evidence of recirculating flow within the reaction zone in the z = 10 and 25mm planes, with negative axial gas-phase velocity apparent at the flame front. Interestingly, in the z = 25mm plane, it appears that the axial velocity is negative on the inner side of the reaction zone, and positive on the outside, suggesting strong shear across the flame front. The channeling effect noted in the 4.77 *l/s* air flow case is even more evident at the higher air flow rate. As before, there is no evidence of any re-entrainment occurring.

Figures 6.54 - 6.58 present velocity vector plots of large (>30μm) droplet trajectories for all air flow rates tested. As can be seen in Figure 6.54, with no annular air flow, the trajectories are essentially ballistic with an origin at the nozzle. The cone formed by the peak flux trajectories encloses an angle of approximately 55°, very close to the expected 60° from this type of nozzle. With 2.38*l/s* annular air flow rate, the droplet velocity field no longer appears ballistic. The initial cone defined by the peak flux velocity vectors remained unaffected at 55°, but narrowed considerably beyond z = 40mm. In the z = 100mm plane, there was some evidence that the droplet trajectories within the reaction zone tended towards the centreline, producing a focussing effect that would concentrate fuel flow to the centre. With an annular air flow rate of 4.77 *l/s*, this effect is even more pronounced. It is interesting to note that there is no evidence of re-entrainment of droplets that are outside the reaction zone. When the annular air flow rate is increased to 7.15 and 9.53 *l/s*, the focussing effect is very pronounced. There is still no evidence of large droplet re-entrainment, and no evidence of large droplet recirculation. The initial cone angle, defined by the location of the volume flux peak, has widened noticeably to approximately 65° in the 9.53 *l/s* annular air flow rate case. Beyond 60mm, there is no further widening of the peak flux location.

Figure 6.59 presents a vector plot of large droplet velocity superimposed on a vector plot of gas-phase velocity in the z = 25mm plane at an annular air flow rate of 7.15 *l*/s. In this

region, relative velocities between droplets and the gas-phase flow can be in excess of 25m/s. However, the Weber number for a 50μm methanol droplet subjected to this relative velocity is less than 2, so droplet break-up does not occur, although droplet distortion, resulting in non-spherical droplets, is likely. This distortion would result in PDI data rejection due to non-sphericity, and contributes to low data validation rates in this region.

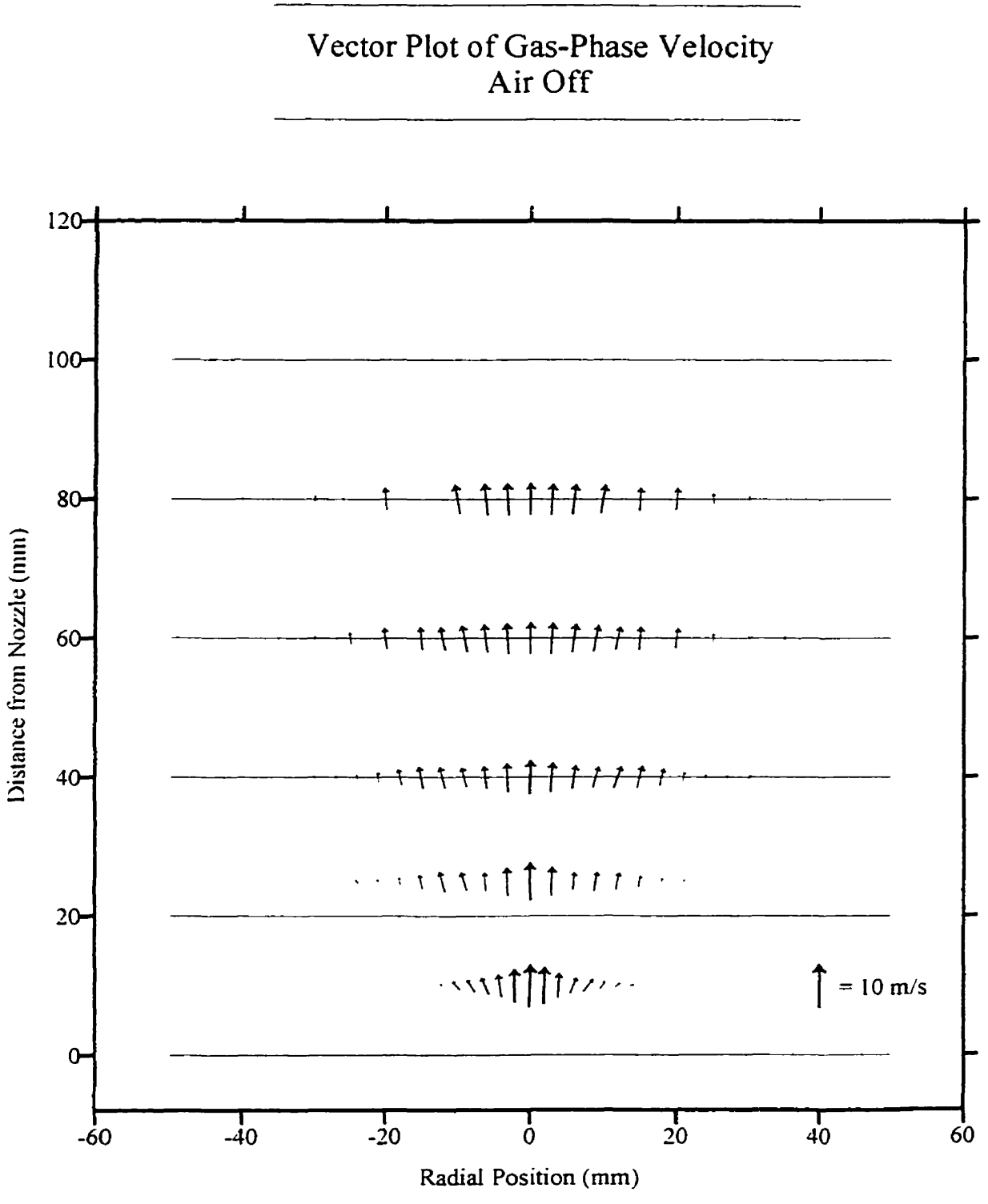


FIGURE 6.49: Vector plot of gas-phase velocity with annular air off

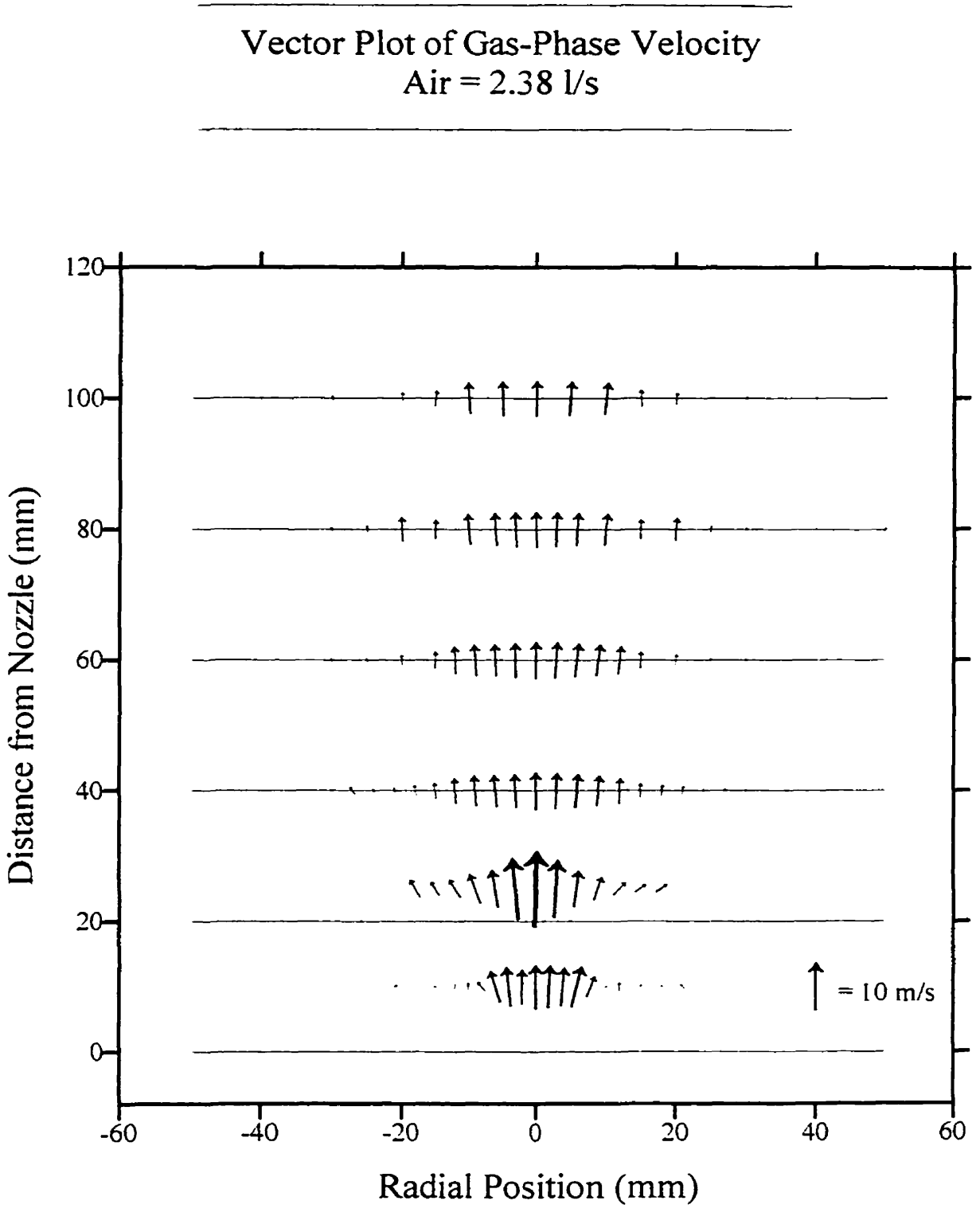


FIGURE 6.50: Vector plot of gas-phase velocity with annular air = 2.38 *l*/s

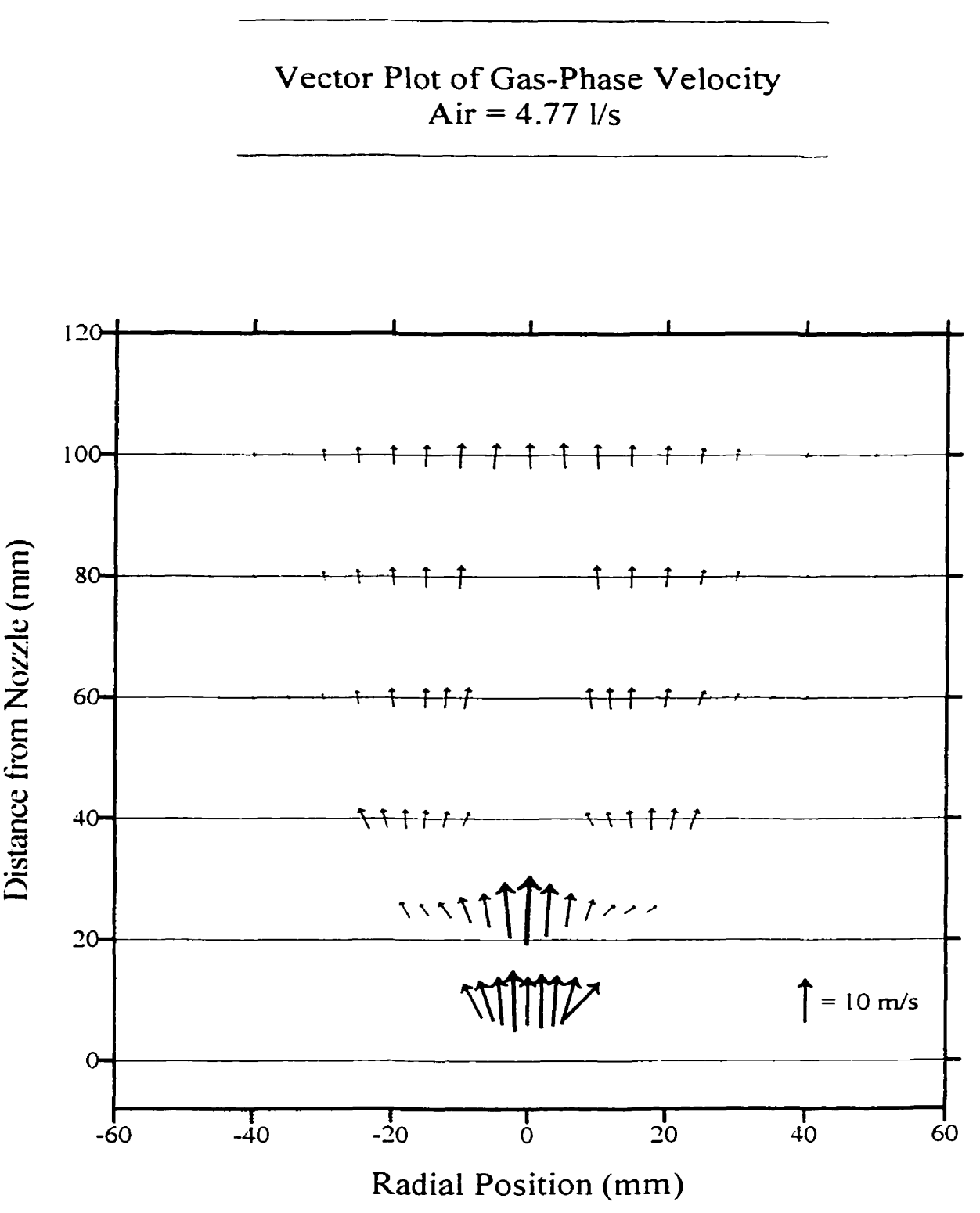


FIGURE 6.51: Vector plot of gas-phase velocity with annular air = 4.77 *l*/s

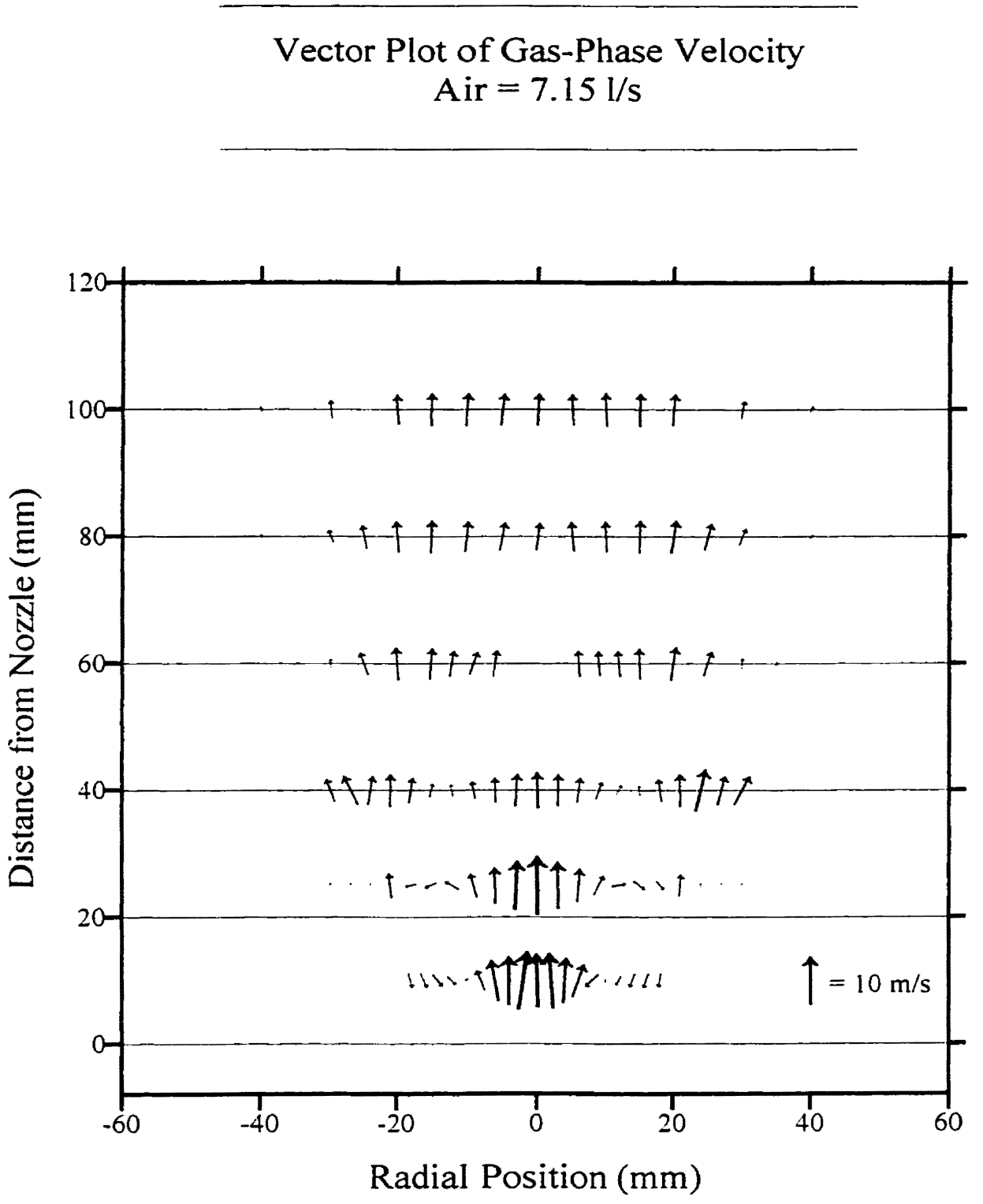


FIGURE 6.52: Vector plot of gas-phase velocity with annular air = 7.15 *l*/s

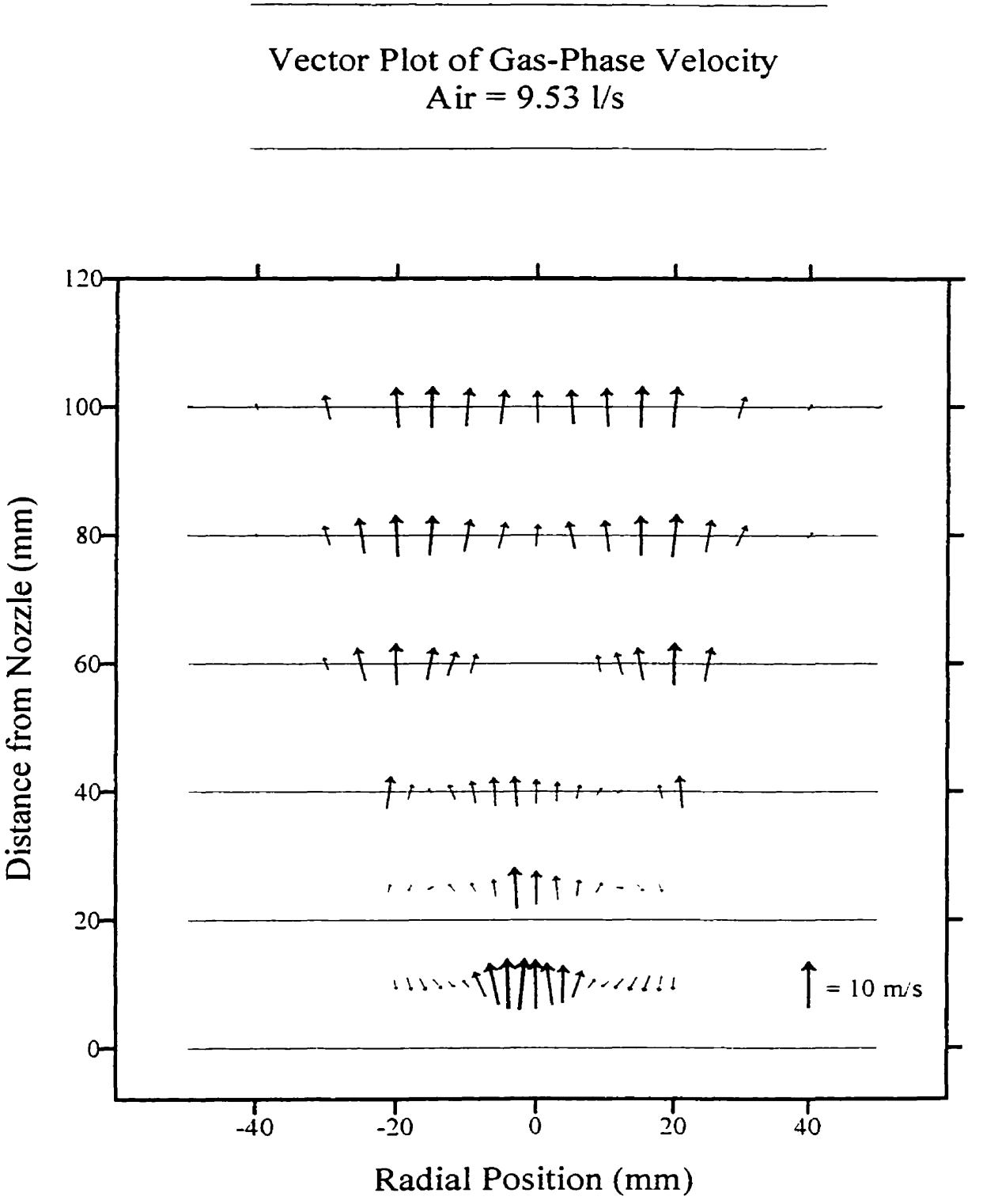


FIGURE 6.53: Vector plot of gas-phase velocity with annular air = 9.53 *l*/s

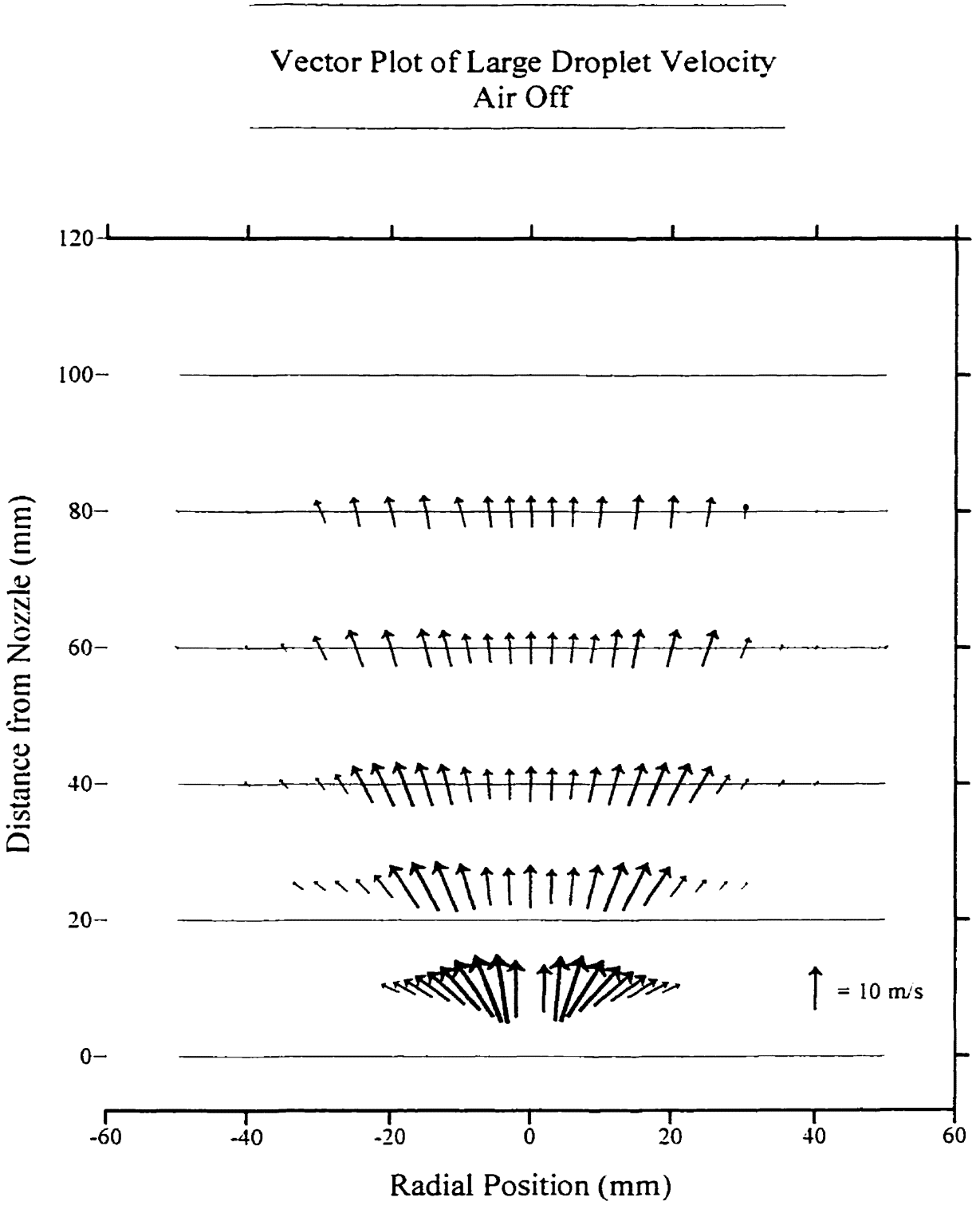


FIGURE 6.54: Vector plot of large droplet (>30μm) velocity with annular air off

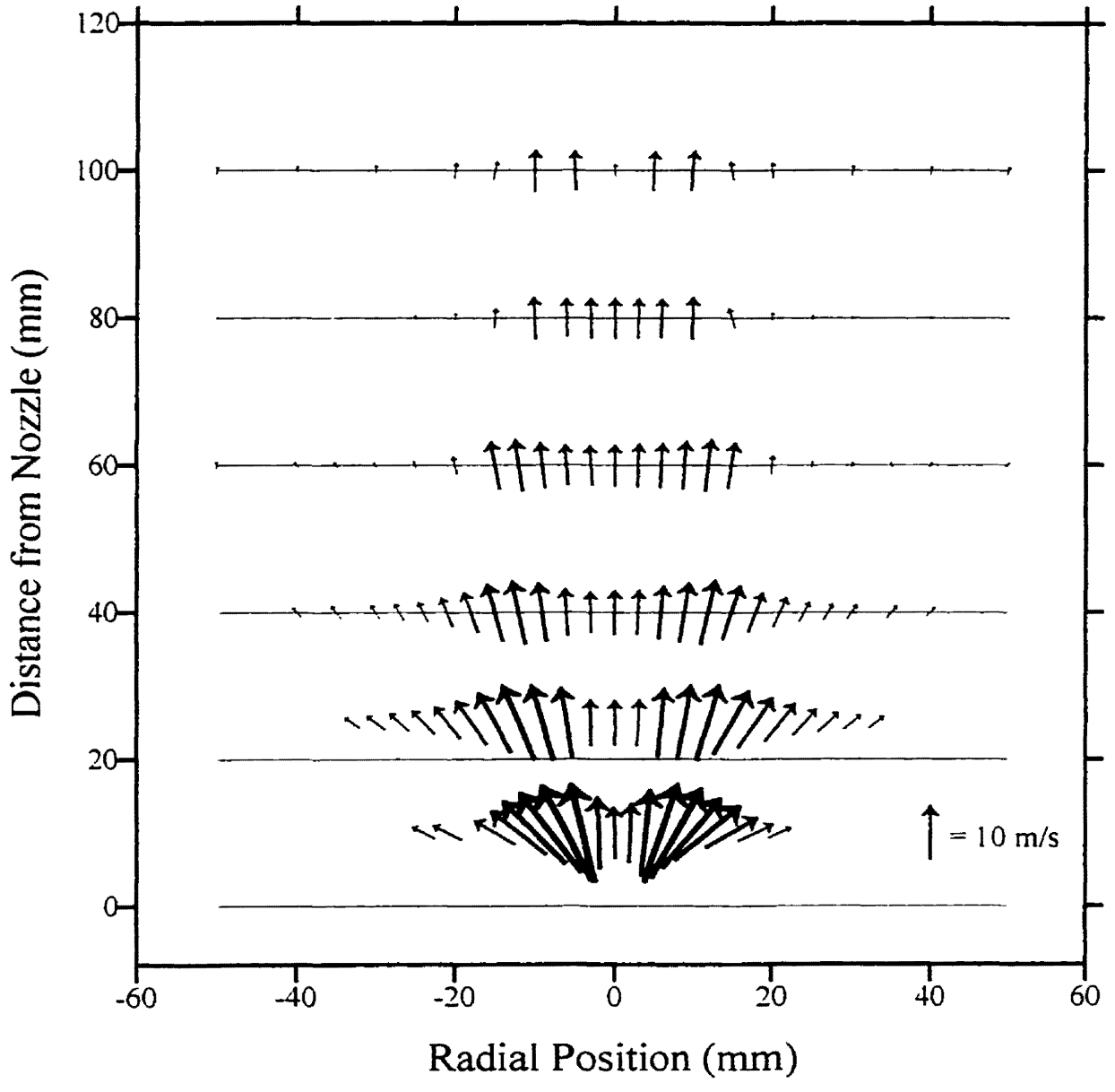


FIGURE 6.55: Vector plot of large droplet (>30μm) velocity with annular air = 2.38 *l*/s

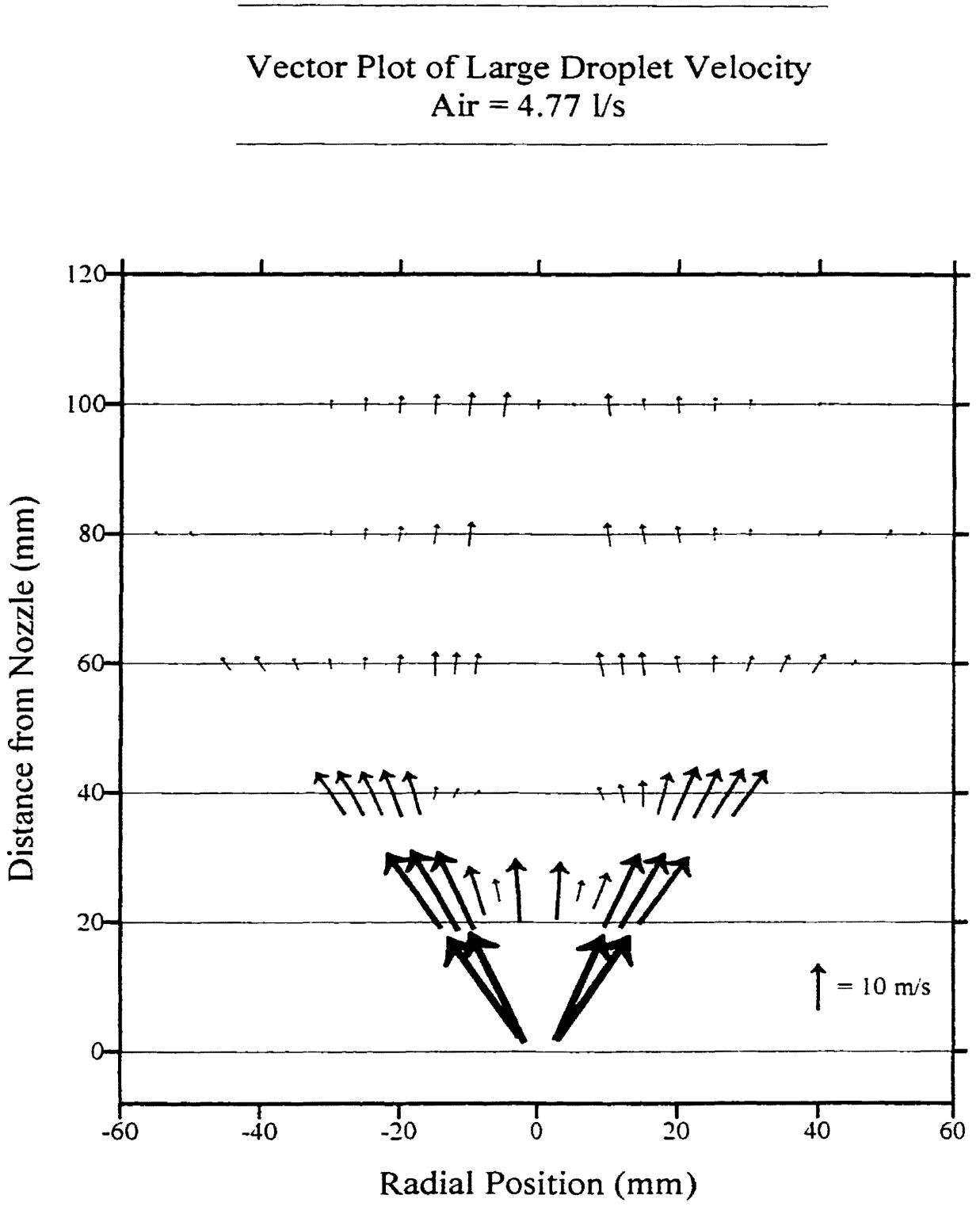


FIGURE 6.56: Vector plot of large droplet (>30μm) velocity with annular air = 4.77 *l*/s

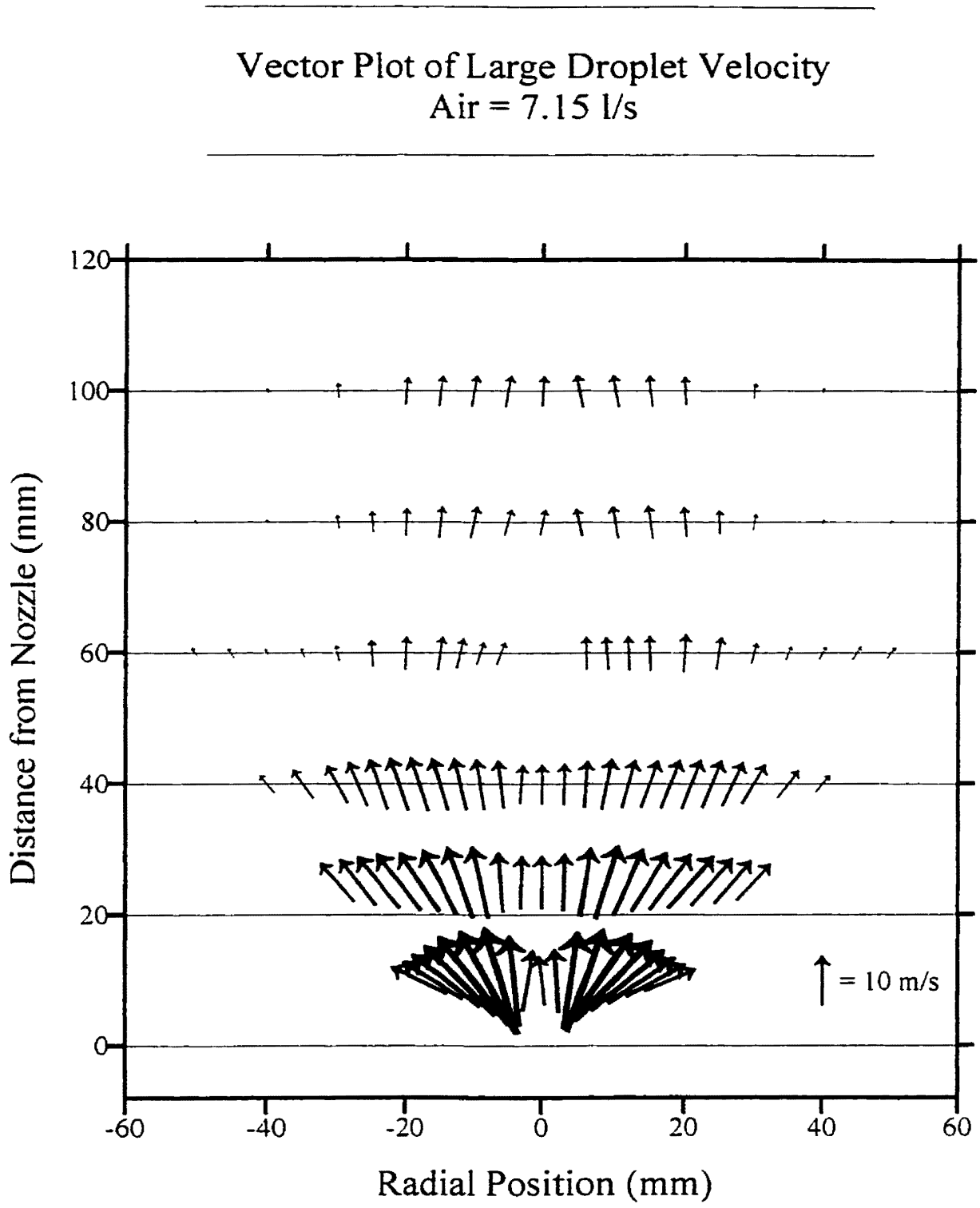


FIGURE 6.57 Vector plot of large droplet (>30μm) velocity with annular air = 7.15 *l*/s

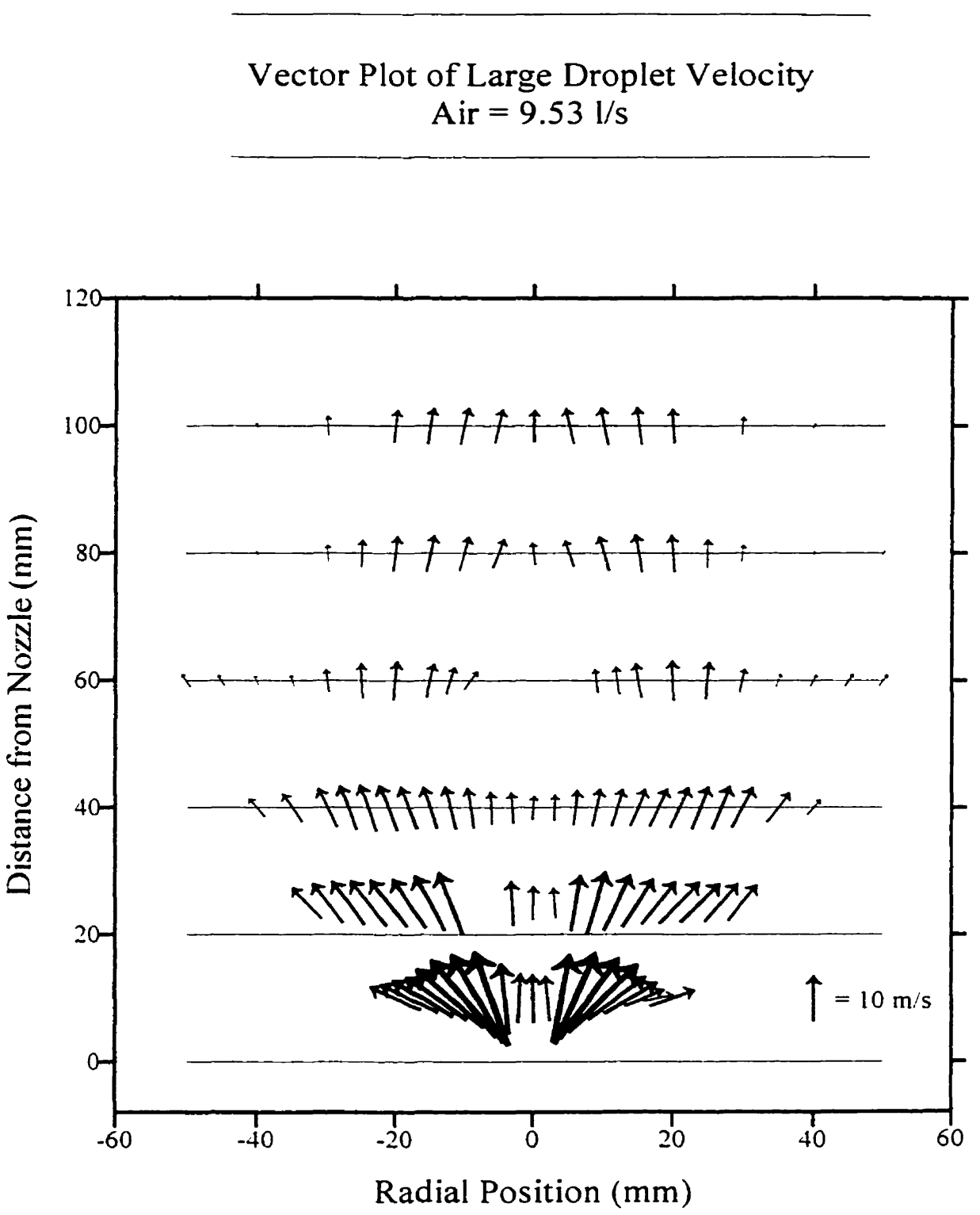


FIGURE 6.58: Vector plot of large droplet (>30μm) velocity with annular air = 9.53 *l*/s

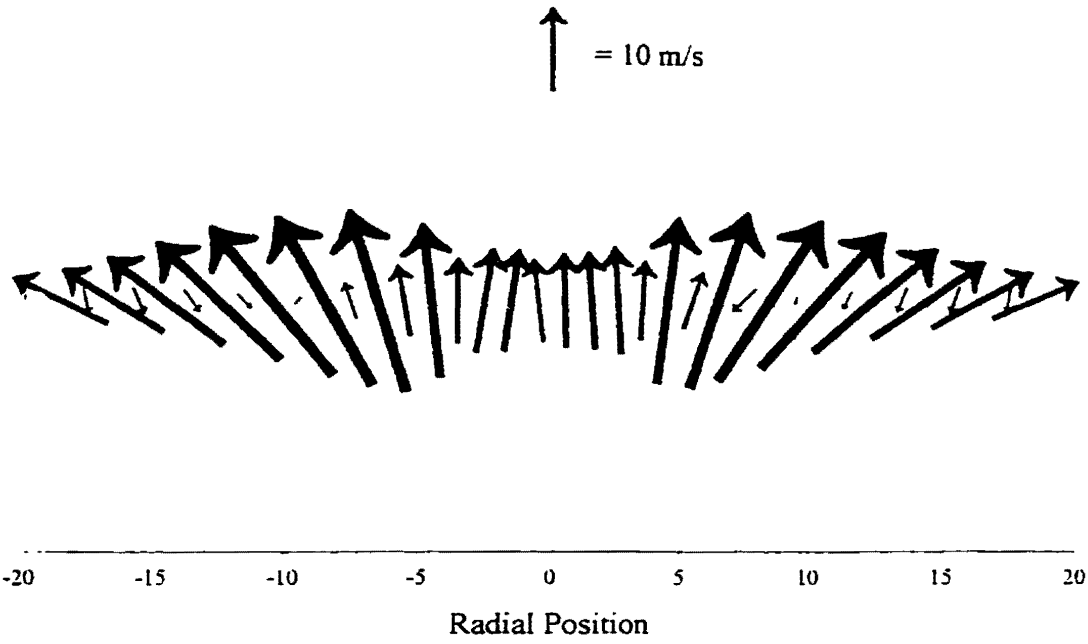


FIGURE 6.59: Vector plot of large droplet (>30μm, red) and gas-phase (blue) velocity in the z = 10mm plane with annular air flow = 7.15 *l*/s

6.5. Temperature Measurements

Temperature measurements made using a Pt/Pt-10%Rh thermocouple are presented in Figures 6.60-6.66. As discussed earlier, no attempt has been made to compensate measurements for radiation or conduction losses, or for droplet impaction. It was anticipated that examination of the raw temperature data time series would reveal droplet impacts as obvious periods of low temperature readings, but this was not the case. No droplet strikes, as judged in this way, were apparent in the data sets examined.

Examination of Figures 6.60 to 6.66 reveal that the temperature peaks correspond to the mean reaction zone locations indicated by PLIF OH fluorescence images, as discussed in Section 6.2. In the z = 25mm plane, there is a distinct centreline temperature peak for the 2.38 *l*/s annular air flow case with no reaction zone evident in this region in the PLIF image. This could be a result of a chimney effect, conveying hot products of combustion along the centreline, or an artifact due to catalytic effects, as discussed in Chapter 7.

It is apparent that increased annular air flow reduces peak temperatures in the flame in all planes measured. Peak mean temperatures measured with annular air off were nearly 2000K, while even with the lowest annular air flow rate tested, 2.38 *l*/s, the peak temperature was less than 1700K. With the highest annular air flow rate tested, the peak measured temperature was 1600K. It would appear from the figures that annular air flow reduces the width of the high temperature region in the planes within 100mm of the nozzle. This is an important consideration for compact combustion chambers such as are used in gas turbines, where it is highly desirable to keep the flame as far away from the chamber walls as possible. Beyond this distance, low frequency fluctuations of the annular air off flame made temperature measurements questionable, and are therefore not presented.

In all cases, centreline temperatures were quite high, even in the vicinity of the nozzle, where 25mm downstream, temperatures of 600-1400K were measured. There is little difference in centreline temperature distribution for the higher annular air flow rates (4.77-9.52 *l*/s), as seen in Figure 6.67. Since the inner structure of the flame with annular air off and annular air = 2.38 *l*/s are similar, it is surprising that the respective centreline temperature plots are so different. It is likely that the very high temperatures measured near the nozzle for the

air = 2.38 *l*/s case are the result of catalytic effects and do not reflect the actual temperature in this region, as will be discussed in Chapter 7.

Droplet lifetimes at these temperatures are on the order of 20 ms for a 30 μm droplet at 20m/s initial relative velocity [70], while transit times through the hot regions are on the order of 3 ms, and hence all but the smallest droplets do not completely evaporate prior to emerging from the hot region near the nozzle.

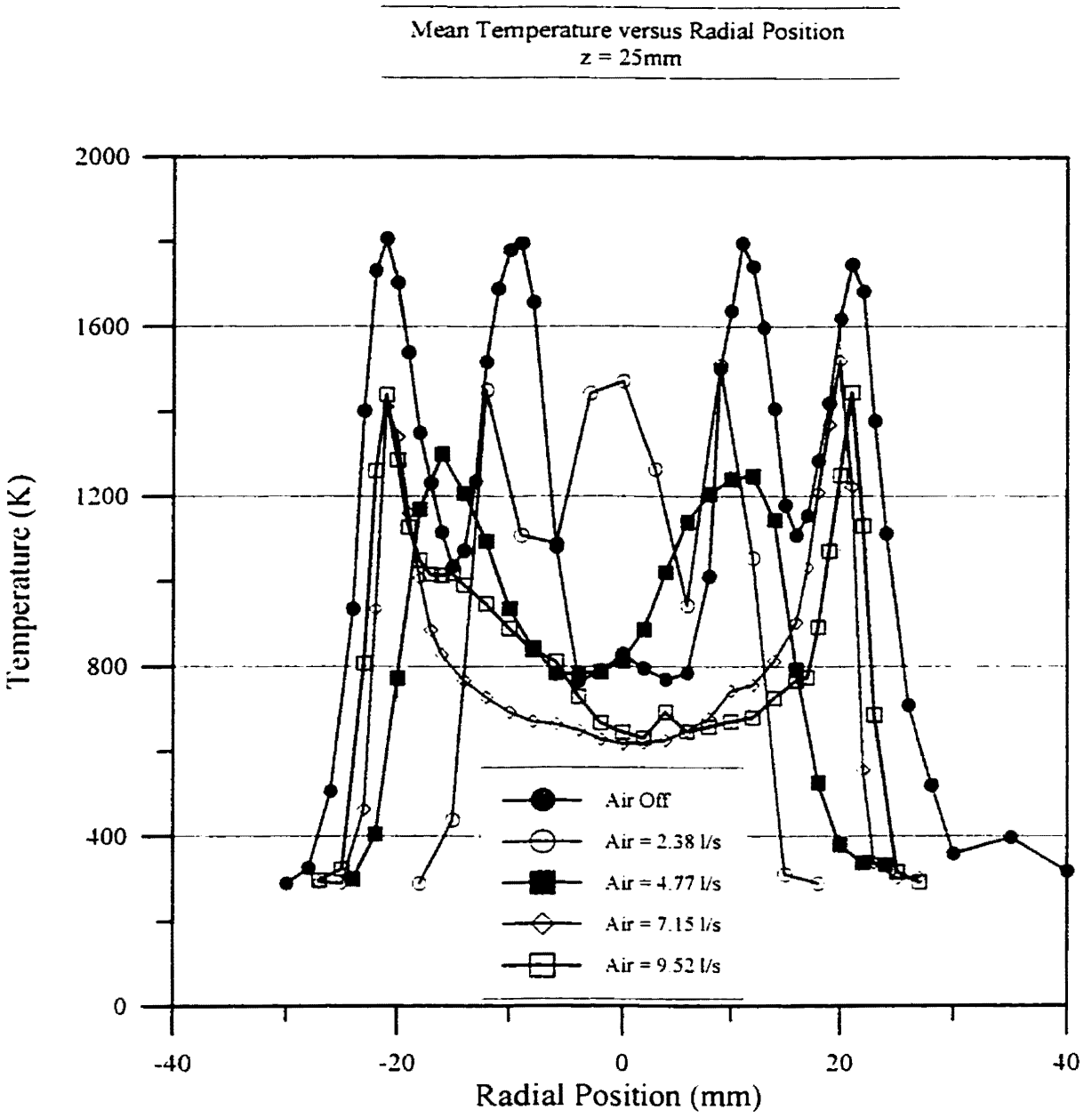


FIGURE 6.60: Temperature variation in the z = 25mm plane

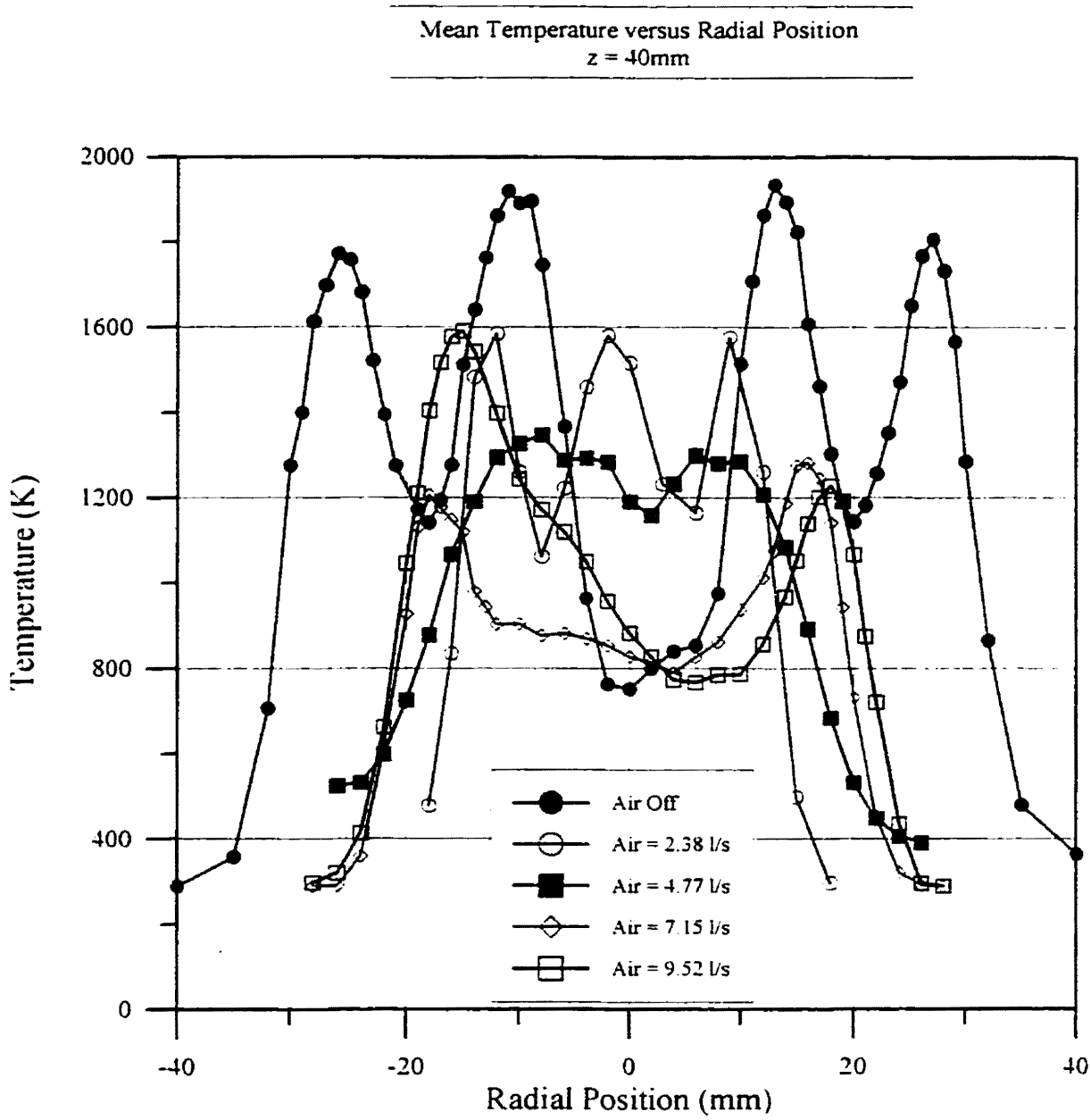


FIGURE 6.61: Temperature variation in the z = 40mm plane

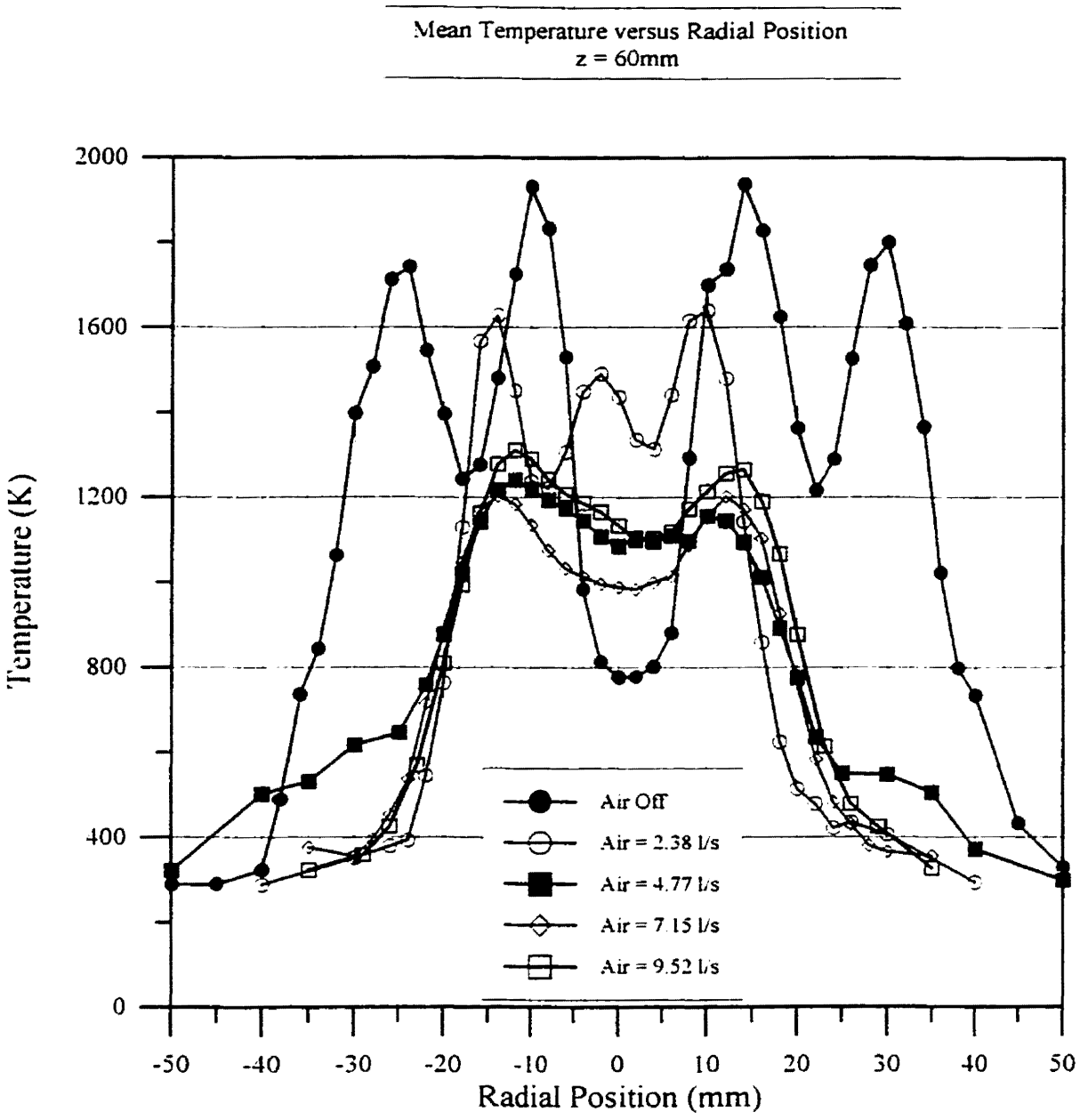


FIGURE 6.62: Temperature variation in the z = 60mm plane

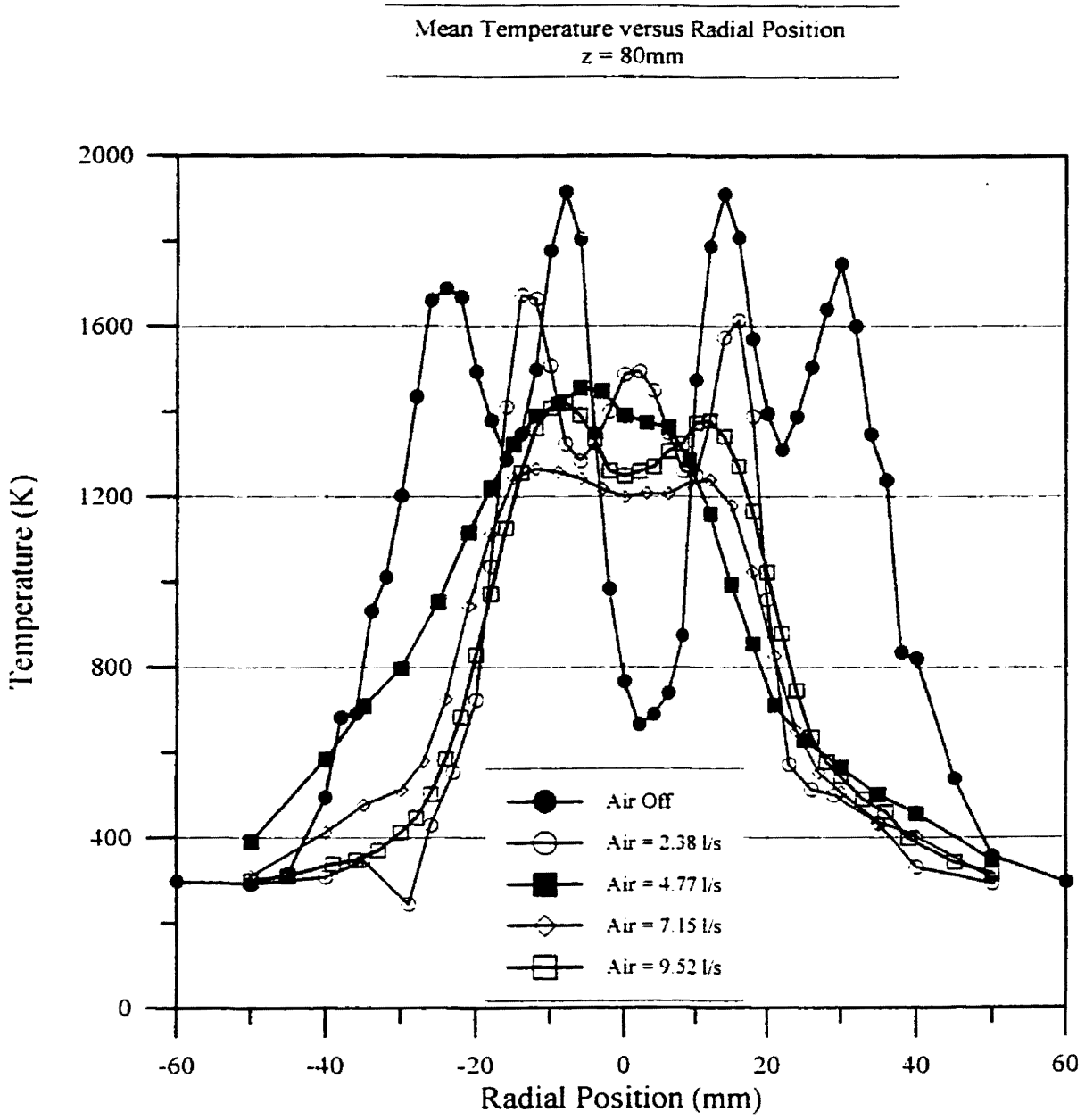


FIGURE 6.63: Temperature variation in the z = 80mm plane

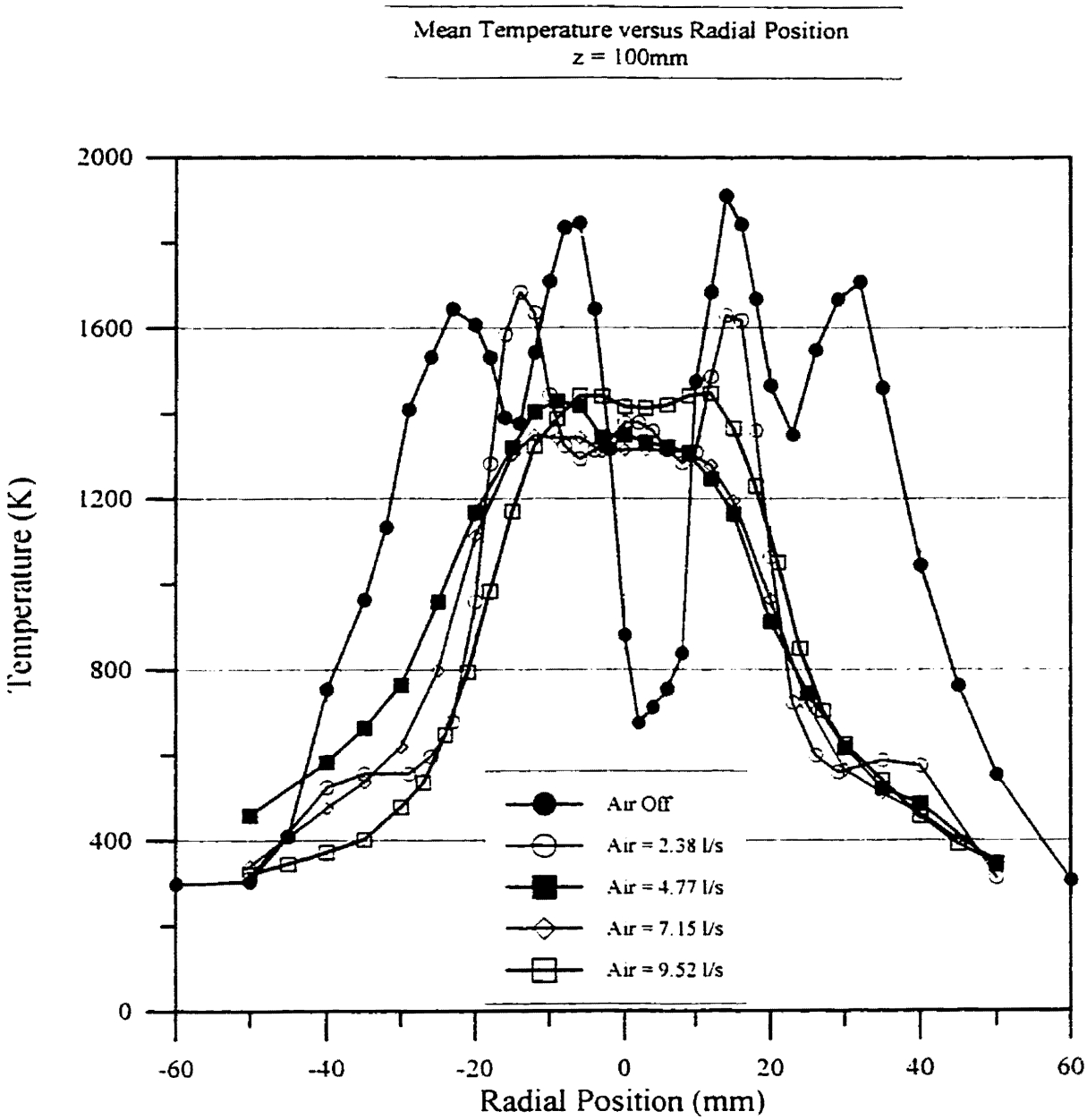


FIGURE 6.64: Temperature variation in the z = 100mm plane

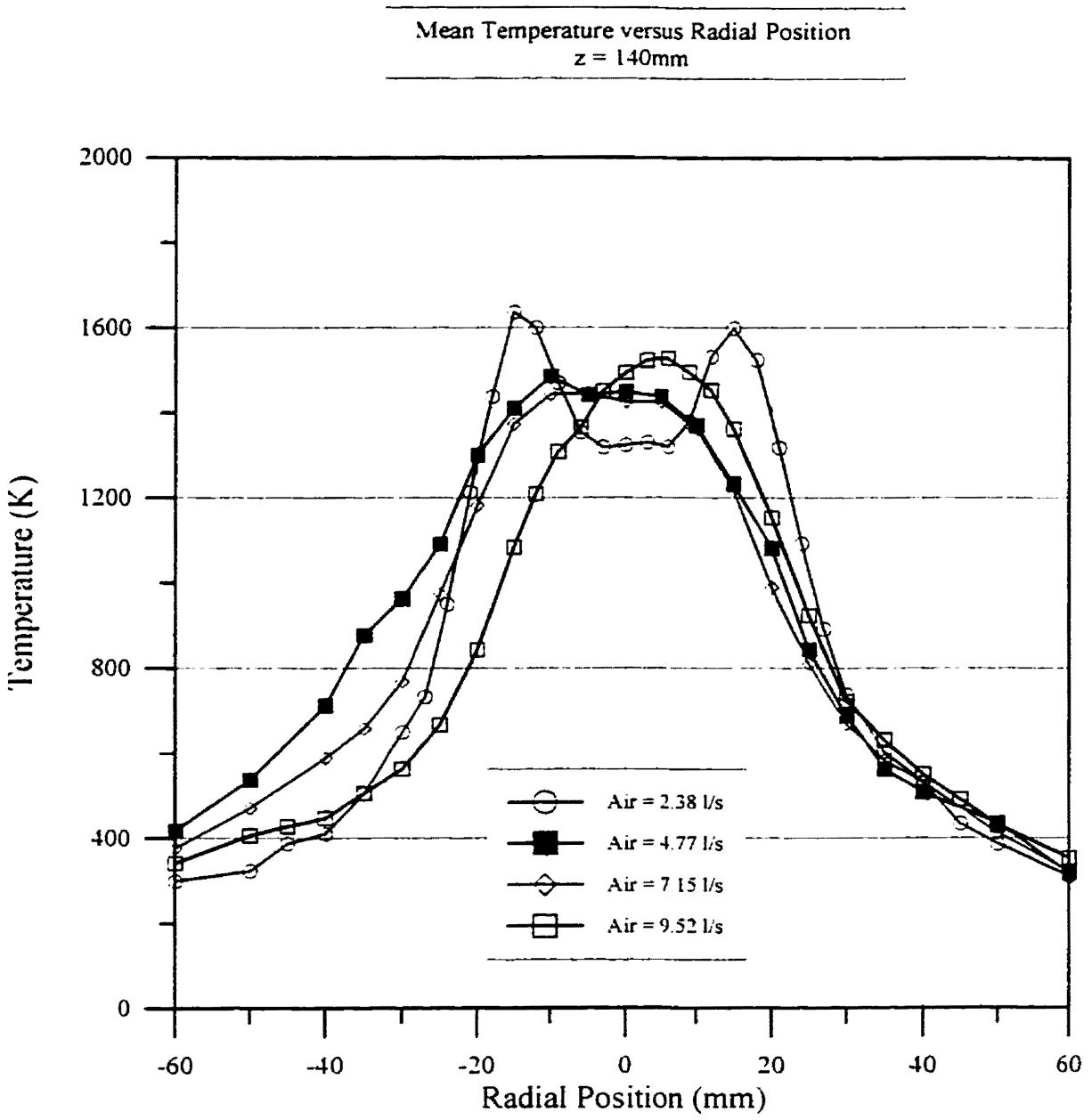


FIGURE 6.65: Temperature variation in the z = 140mm plane

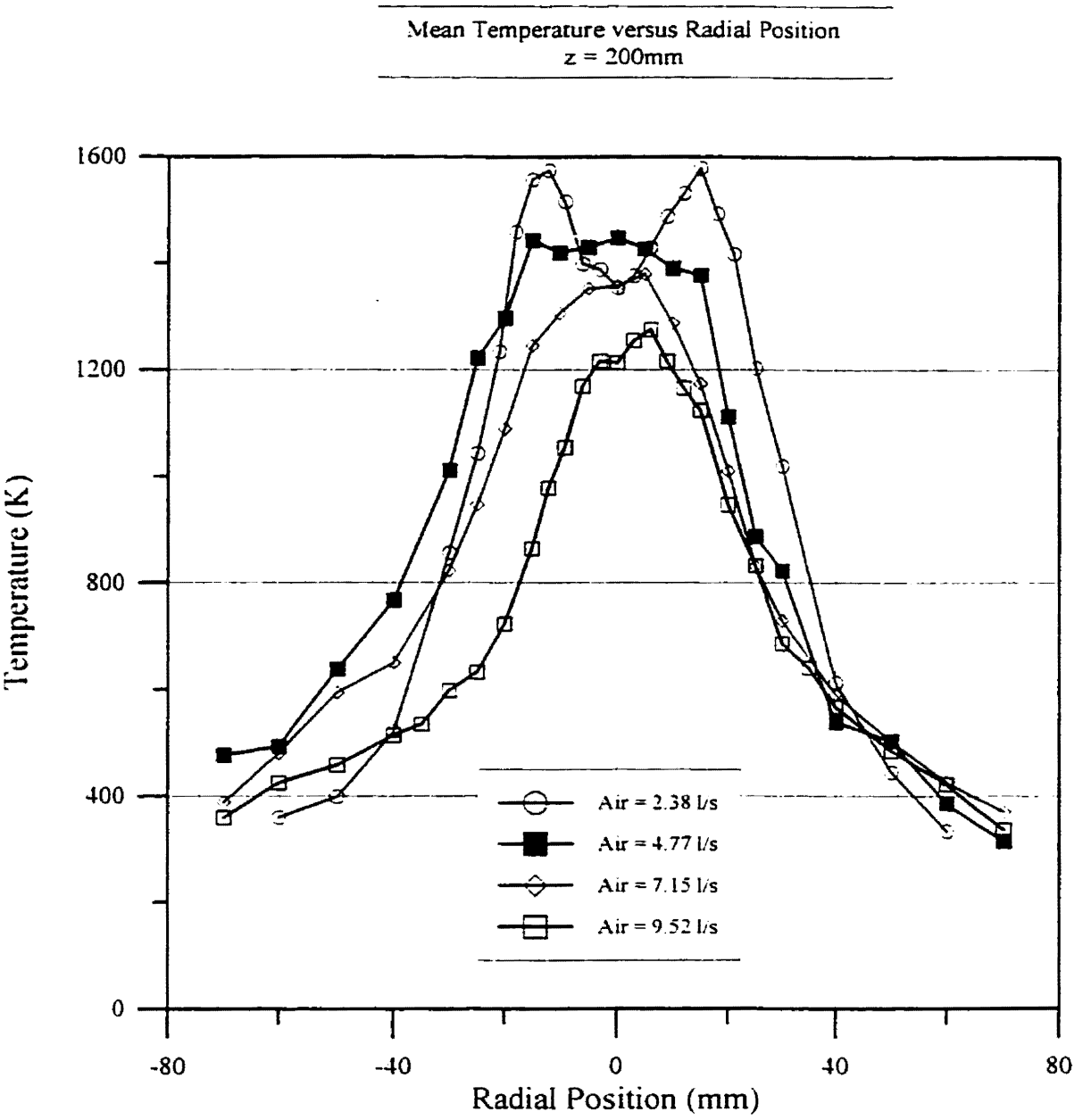


FIGURE 6.66: Temperature variation in the z = 200mm plane

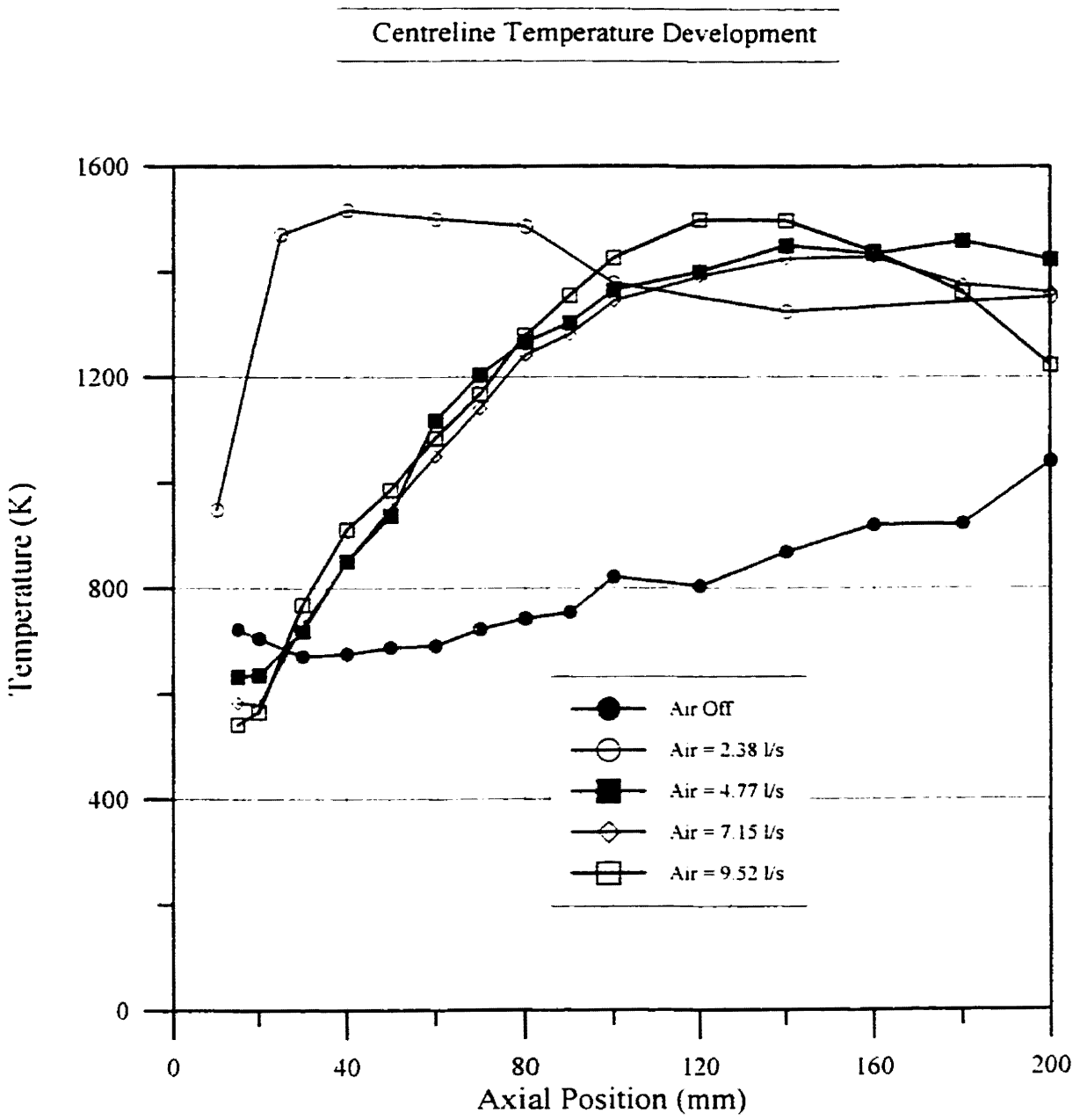


FIGURE 6.67: Centreline temperature development

6.6. Turbulence Measurements

Turbulence measurements were made using methanol fuel dyed with 3g/l of acid red #1 resulting in a droplet absorptivity of approximately $\gamma = 0.015$ /μm to enhance the visibility of seed particles as discussed in section 4.1.6. The measurements were made on centreline, with the PDI system configured to obtain one velocity component rather than two to maximize data acquisition rates. The resulting data sets were processed as discussed in Section 6.5 to include velocity data from small droplets only.

Due to the failure of the nozzle used for the previous measurement sets presented, a different nozzle was used for these measurements. Although the new nozzle was also a Delavan 0.75-60°A pressure-swirl nozzle, it was found to differ slightly from the one used in the previous sections of this work, and hence the turbulence measurements made using this new nozzle are treated independently. Figure 6.68 presents the droplet size distribution for the new and old nozzles in the z = 25mm plane, with annular air off. It is apparent that there is very little difference between the mean droplet size distribution issued from these nozzles. Figure 6.69, presents the mean droplet velocity distribution for the new and old nozzles. As can be seen, there is some difference in centreline velocity distribution between the two nozzles, although the velocity distribution off-axis is nearly identical. Visually, there is no apparent difference in flame structure for all conditions tested between the new and old nozzles.

Addition of dye to the fuel resulted in no apparent change to the structure of the flame, as would be expected since the dye loading is light (~3 g/*l*). The luminosity of the flame increased substantially due to increased soot formation, which turned out to be fortuitous, since dying the fuel allowed the photomultiplier gain to be set sufficiently high that soot particles could be detected, and hence the flame was self-seeding. Since soot particles are small and non-spherical, the validation rate was quite low (~10-15%), but overall data rates were quite high. It should be noted that light scattering by soot particles is by reflection, and the PDI system was configured in refraction mode, so size measurements of the soot were in error. However, essentially all the soot diameter measurements were in the first diameter bin (0.5μm) whether the system was configured in refraction or reflection mode, hence the soot particles

were sufficiently small to accurately follow the flow.

Figure 6.70 presents a comparison of centreline gas-phase mean velocity for the burning and non-burning methanol spray with an annular air flow rate of 4.77*l/s*. As can be seen, the velocities are radically different, particularly in the region near the nozzle. For the non-burning case, a recirculation zone is evident, extending to approximately 45mm downstream of the nozzle. Beyond the recirculation zone, the velocity increases rapidly until reaching a steady value near 4 m/s approximately 100mm downstream of the nozzle, and slowly decaying with increasing distance from the nozzle. In the case of the burning spray, no negative velocity, indicating no recirculation, is noted beyond approximately 5mm from the nozzle. In this region, velocity increases rapidly at a rate of approximately 1.8(m/s)/mm, reaching a maximum near 9m/s 10mm downstream of the nozzle. The velocity then decays to approximately 5m/s 75mm downstream of the nozzle, before increasing to about 5.8m/s. It is interesting to note that the velocity curves are parallel beyond 80mm downstream of the nozzle, with the burning case having a somewhat higher velocity than the non-burning case, suggesting that the flow in the far field is dominated by the annular air jet rather than combustion.

Figure 6.71 shows the centreline mean axial velocity development for all air flow rates tested under burning conditions. It is interesting to note that for all air flow rates tested, there is no evidence of a recirculation zone, except for the case where the annular air flow rate was 7.15 *l/s*. It is surprising that the velocity depression is smaller for the 9.52 *l*/s case than the 7.15 *l*/s case, and is likely due to the increased air entrainment possible due to the larger flame stand-off distance noted in the PLIF images, which diminishes the impact of recirculating flow, and moves the location of the velocity minimum farther downstream. There does appear to be a velocity deficit in the region near the nozzle for all cases, becoming more and more evident as annular air flow rate increases. As one would expect, the velocity far downstream of the nozzle increases with increasing annular air flow rate, and appears to reach a steady value in the manner of a round jet.

Figure 6.72 presents the centreline development of axial RMS velocities for all annular air flow rates tested. As can be seen, the magnitude of the RMS fluctuating velocity reaches

a maximum in the region near the nozzle for all cases. In the air off and 2.38 *l*/s cases, the RMS velocities are almost identical over the entire distance measured, suggesting that the annular air jet has little influence on the centreline flow at low flow rates. However, as annular air flow increases beyond this level, the RMS velocity on centreline increases in all cases, indicating that the momentum of the annular air jet penetrates to the flow core in these cases. Turbulence intensities based on local mean velocity are quite high, as shown in Figure 6.73, particularly in the region near the nozzle, since local mean velocities are low. However, the turbulence intensities quickly stabilize beyond z = 80mm, ranging from about 10% for the low annular air flow cases to about 25% for the higher flow rates.

Figure 6.74 presents the centreline development of the integral time scales, as determined from integration of the autocorrelation function. In the region near the nozzle, it is inappropriate to invoke Taylor's hypothesis to obtain an integral length scale by multiplying the time scale by the mean velocity, as the flow is highly anisotropic and of high turbulent intensity. It can be seen that increasing annular air flow rate seems to increase the integral timescale in the region beyond 50mm. Applying Taylor's hypothesis in the far field (z = 100mm) leads to integral length scales that increase with annular air flow rate, ranging from 1.7 cm to 2.4 cm for annular flow rates of 2.38*l/s* to 9.52 *l/s*. For the air off case, the flow is nearly laminar, with very low turbulent intensity (less than 10%). In this case, the integral time scale reflects the slow, non-turbulent fluctuations of the flow, rather than the turbulent timescale, leading to an artificially long timescale and turbulent Reynolds number.

Figure 6.75 presents a plot of turbulent shear stress in the z = 60mm plane. As can be seen, the shear stress is near zero on centreline, as would be expected in an axisymmetric flow. Peak absolute shear stress occurs at a radial position of approximately 12mm, corresponding to the location of maximum mean temperature and the mean position of the reaction zone. It is interesting to note that this region does not appear to correspond to a region of maximum mean velocity gradient, suggesting that combustion, rather than mean velocity gradient, is responsible for the high turbulent shear in this region.

Distance from Nozzle	Annular Air Flow Rate	Re_L $= u'L/\nu$	Re_λ $= u'\lambda/\nu$
20mm	7.15 *l*/s	264	48
60mm	7.15 *l*/s	30	16
100mm	7.15 *l*/s	102	30
140mm	7.15 *l*/s	187	41
60mm	Off	211	43
60mm	2.38 *l*/s	18	12
60mm	4.77 *l*/s	55	22
60mm	9.52 *l*/s	62	23

Table 6.3: Summary of turbulent Reynolds numbers at locations of spectra measurements

Figure 6.76 presents the axial turbulent energy spectra obtained on centreline with an annular air flow rate of 7.15*l/s* at four axial locations; z = 20, 60, 100 and 140mm. Table 6.3 presents the corresponding turbulent Reynolds numbers at these locations and flow conditions. Re_L is the turbulent Reynolds number based on u' and the integral length scale, while Re_λ is the turbulent Reynolds number based on u' and the Taylor microscale. The spectrum obtained at z = 20mm, corresponding to a location with a reverse flow at nearly 2m/s, shows quite high turbulent energy, with a steeper slope than the -5/3 typically obtained from homogeneous isotropic high Reynolds number turbulence. This would be expected since the turbulent Reynolds number Re_λ is quite low, indicating a lack of inertial sub-range and the corresponding -5/3 slope [71]. In the z = 60mm plane, the total turbulent energy has diminished somewhat, while the slope of the spectrum has increased in magnitude, suggesting that there is considerable turbulent energy production at the larger scales ongoing in this region, likely due to the energy released in the combustion process. The spectra produced at z = 100 and z = 140mm are nearly identical, even though the mean velocities differ at these locations, suggesting that some form of equilibrium has been reached between turbulent energy generation and dissipation.

Figure 6.77 presents turbulent energy spectra on centreline in the z = 60mm plane for all air flow rates tested. The total turbulent energy, represented by the area under the energy spectra curves, generally increases with increasing annular air flow rate. The exception is the air = 4.77 *l*/s case, which is likely due to the flame impingement phenomenon discussed earlier, which results in superheating the fuel spray and alters the flow field substantially. As expected from turbulent Reynolds number considerations, there is no evidence of an inertial sub-range and characteristic -5/3 slope.

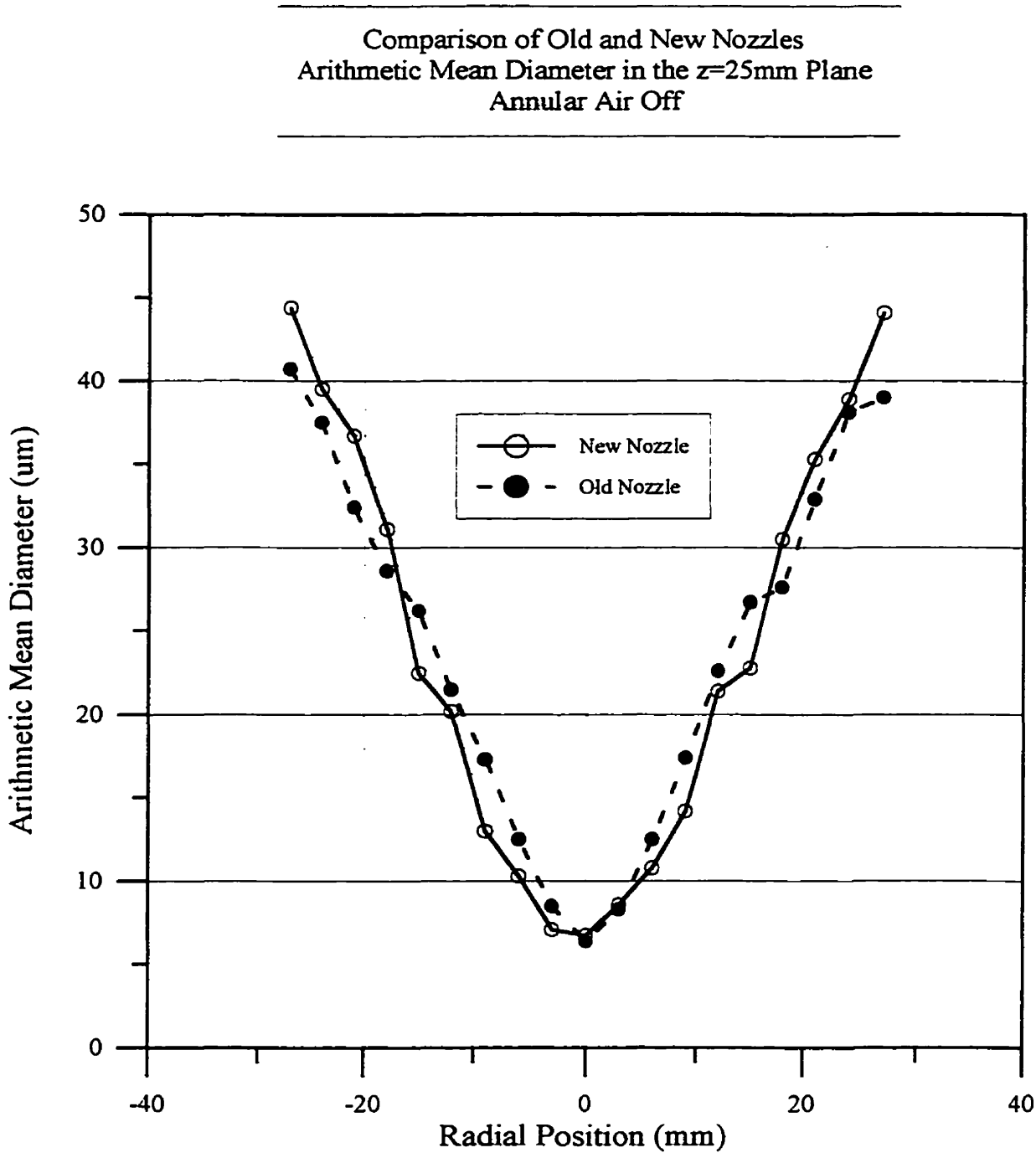


FIGURE 6.68: Comparison of arithmetic mean diameter for the old and new nozzles in the z = 25mm plane with annular air off

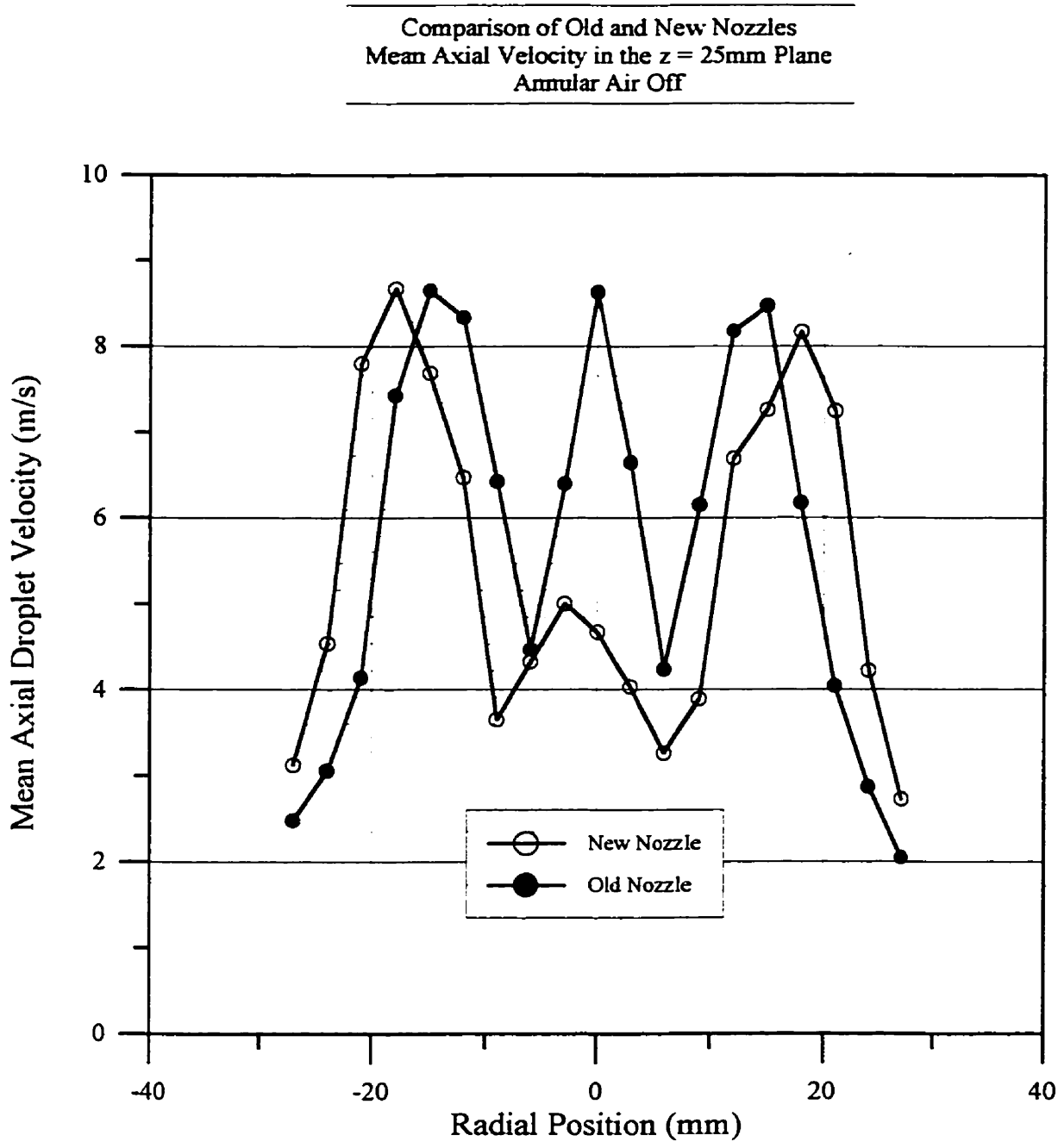


FIGURE 6.69: Comparison of mean axial droplet velocity for old and new nozzles in the z = 25mm plane with annular air off

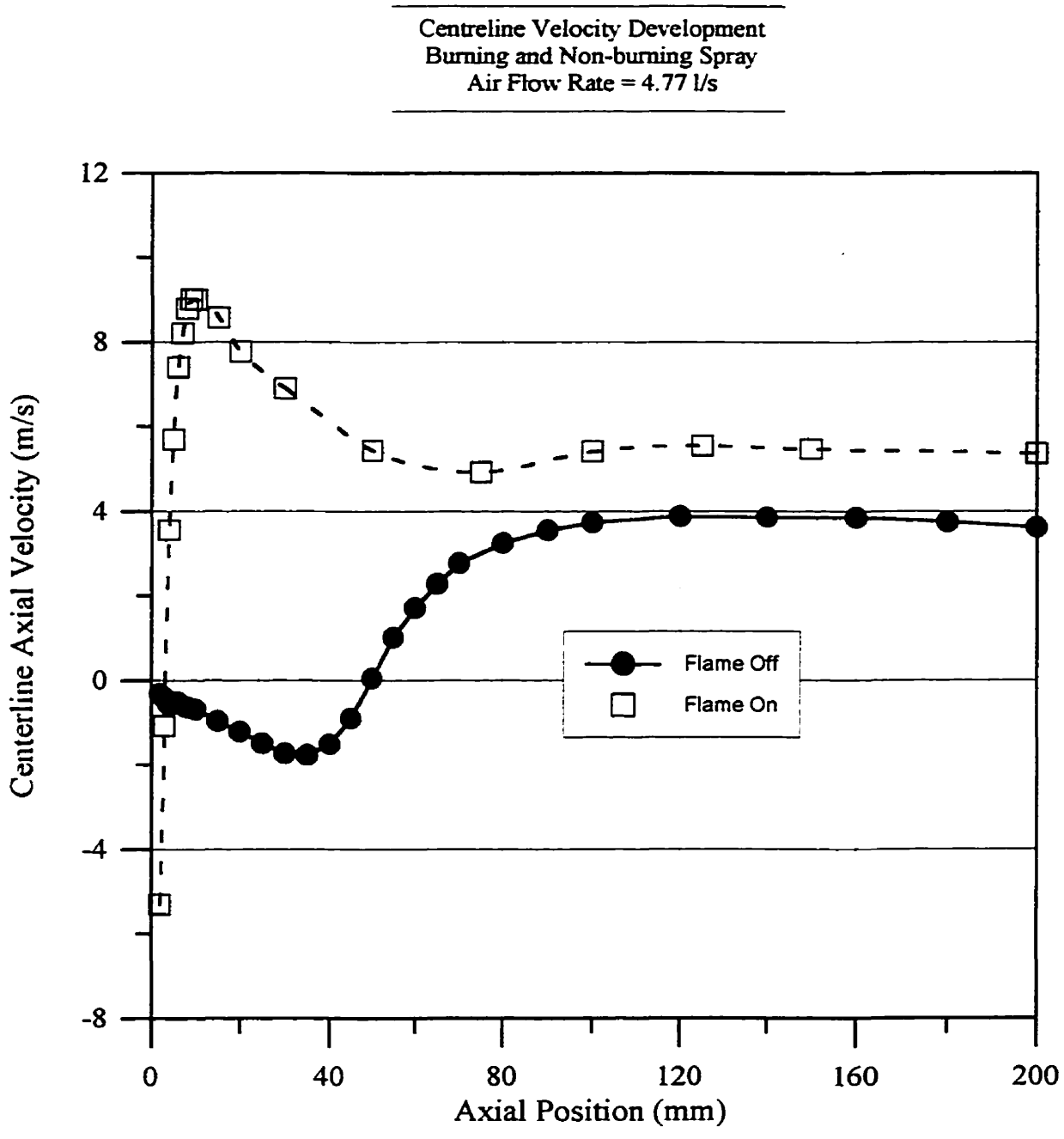


FIGURE 6.70: Centreline velocity development for the burning and non-burning spray cases with an annular air flow rate of 4.77 *l*/s

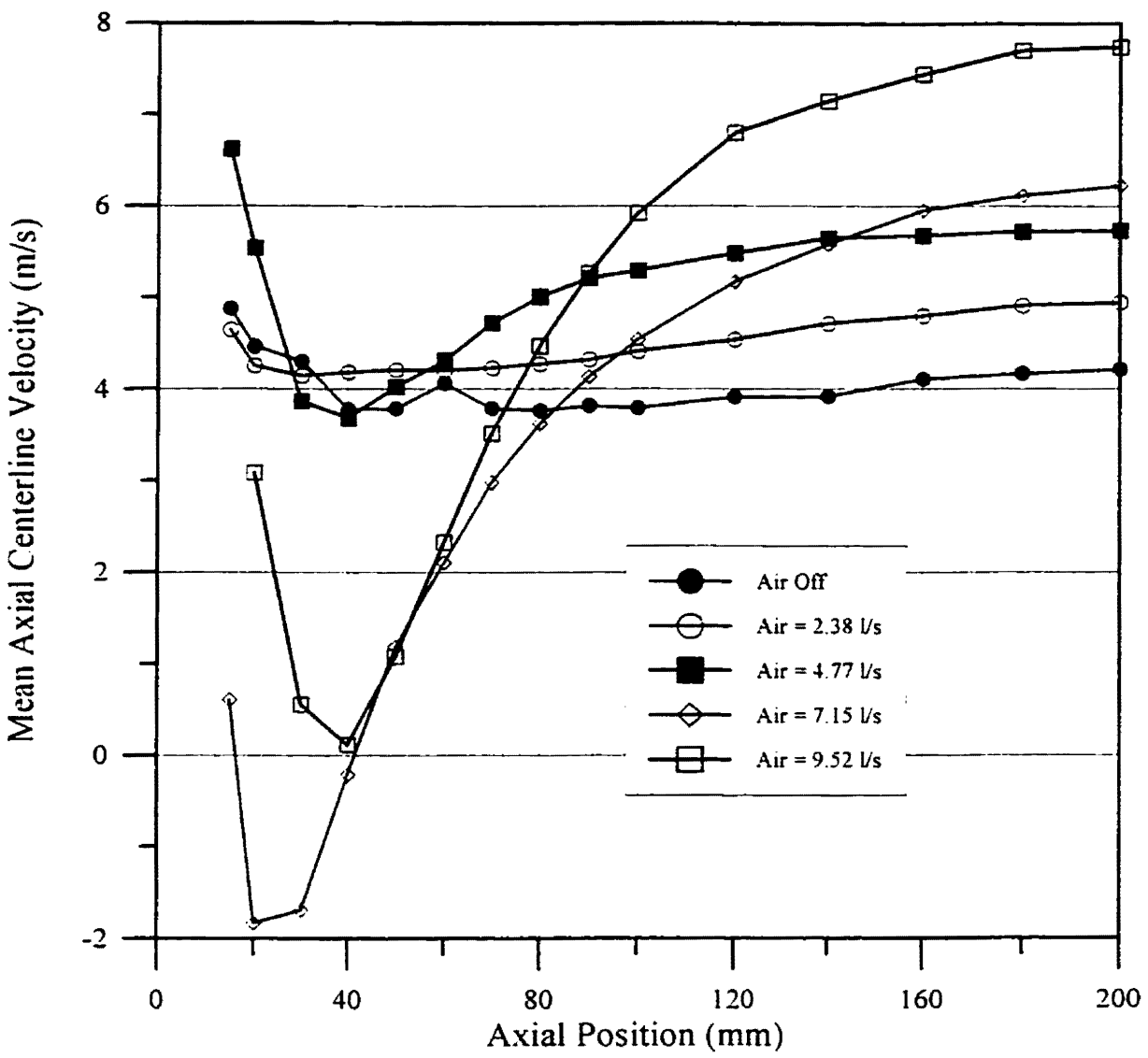


FIGURE 6.71: Mean axial centreline velocity development for all air flow rates tested

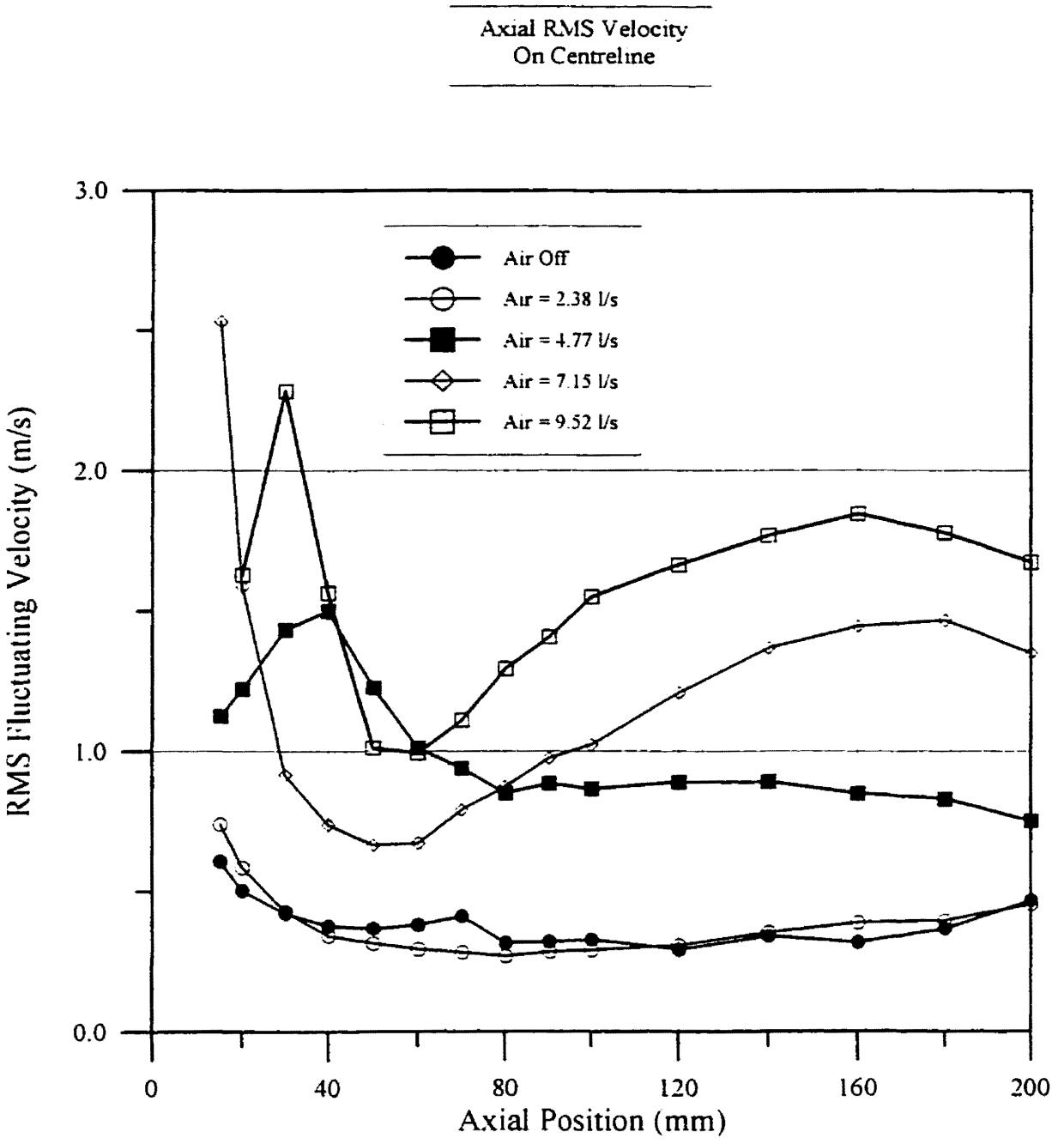


FIGURE 6.72: Centreline RMS fluctuating velocity (u') development

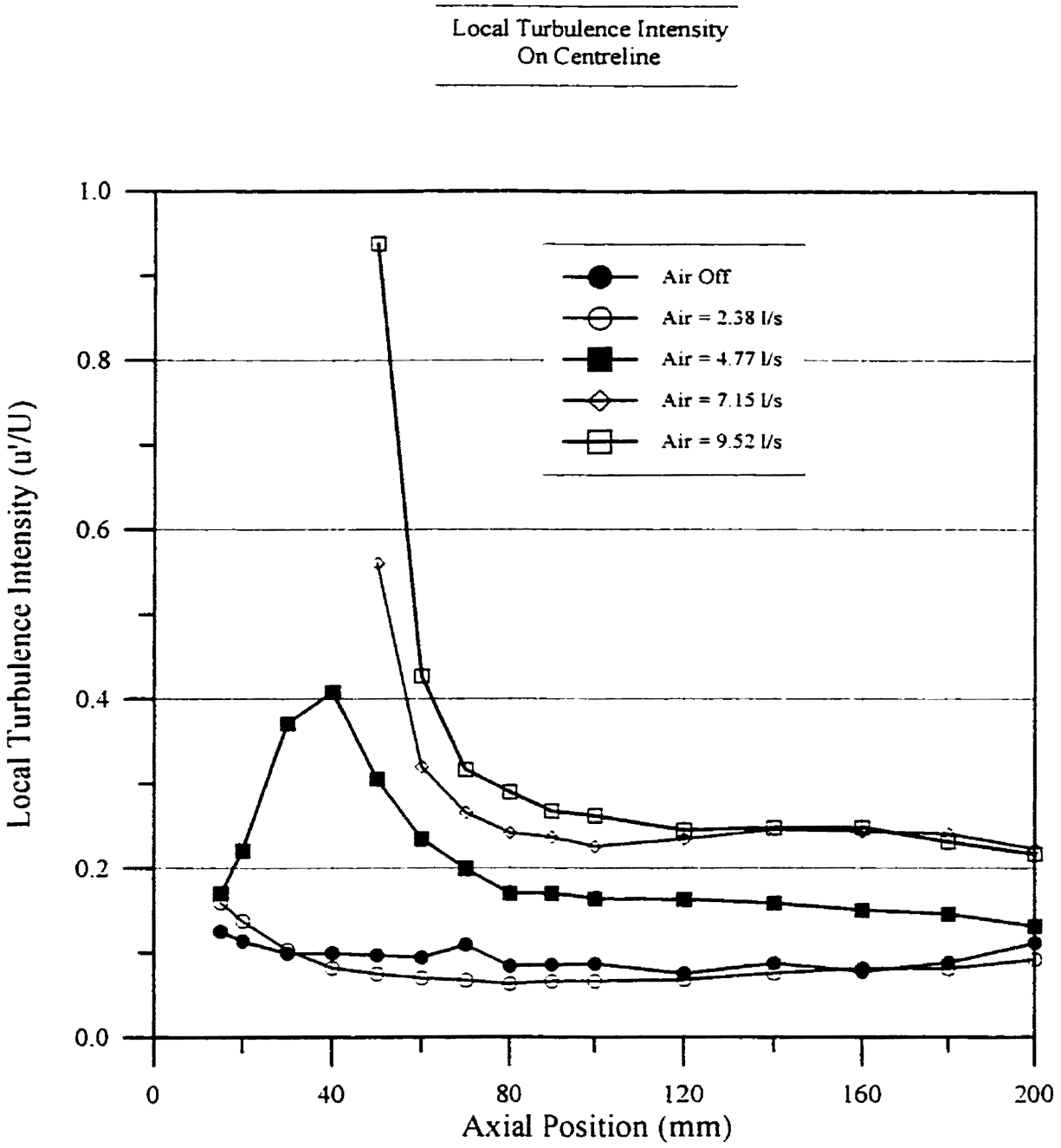


FIGURE 6.73: Centreline local turbulence intensity (u′/U)

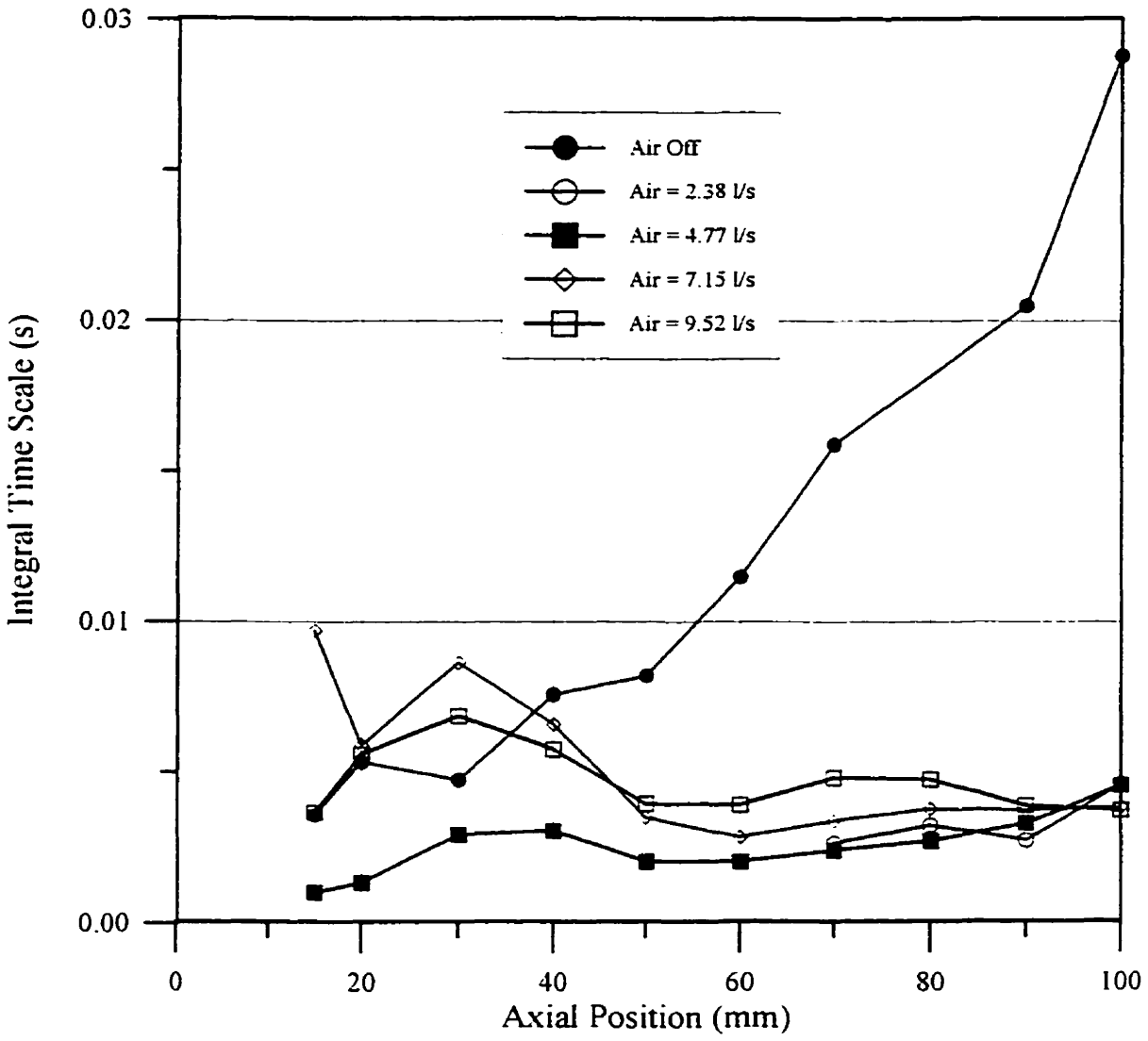


FIGURE 6.74: Centreline integral time scale development

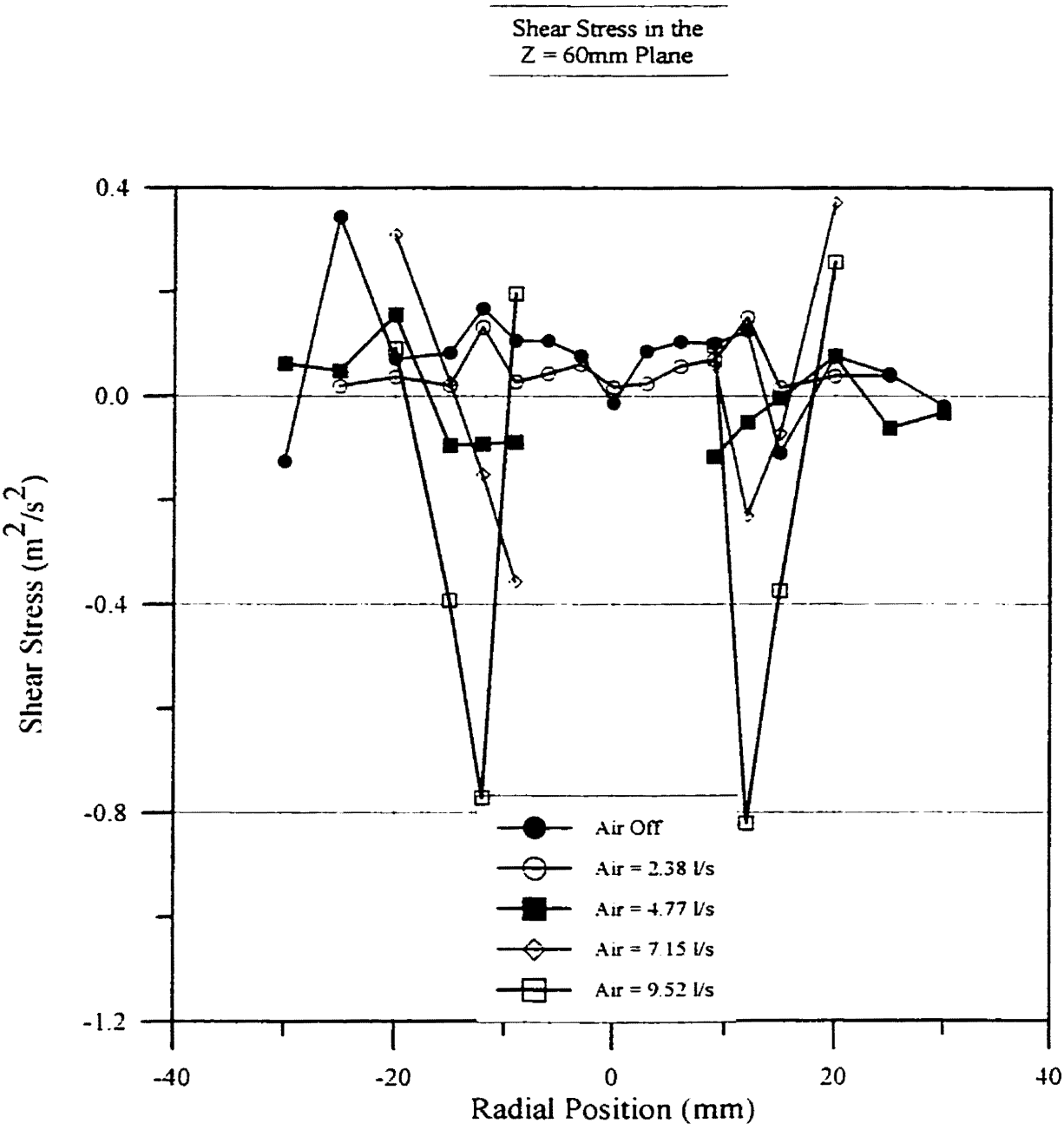


FIGURE 6.75: Shear stress in the z = 60mm plane

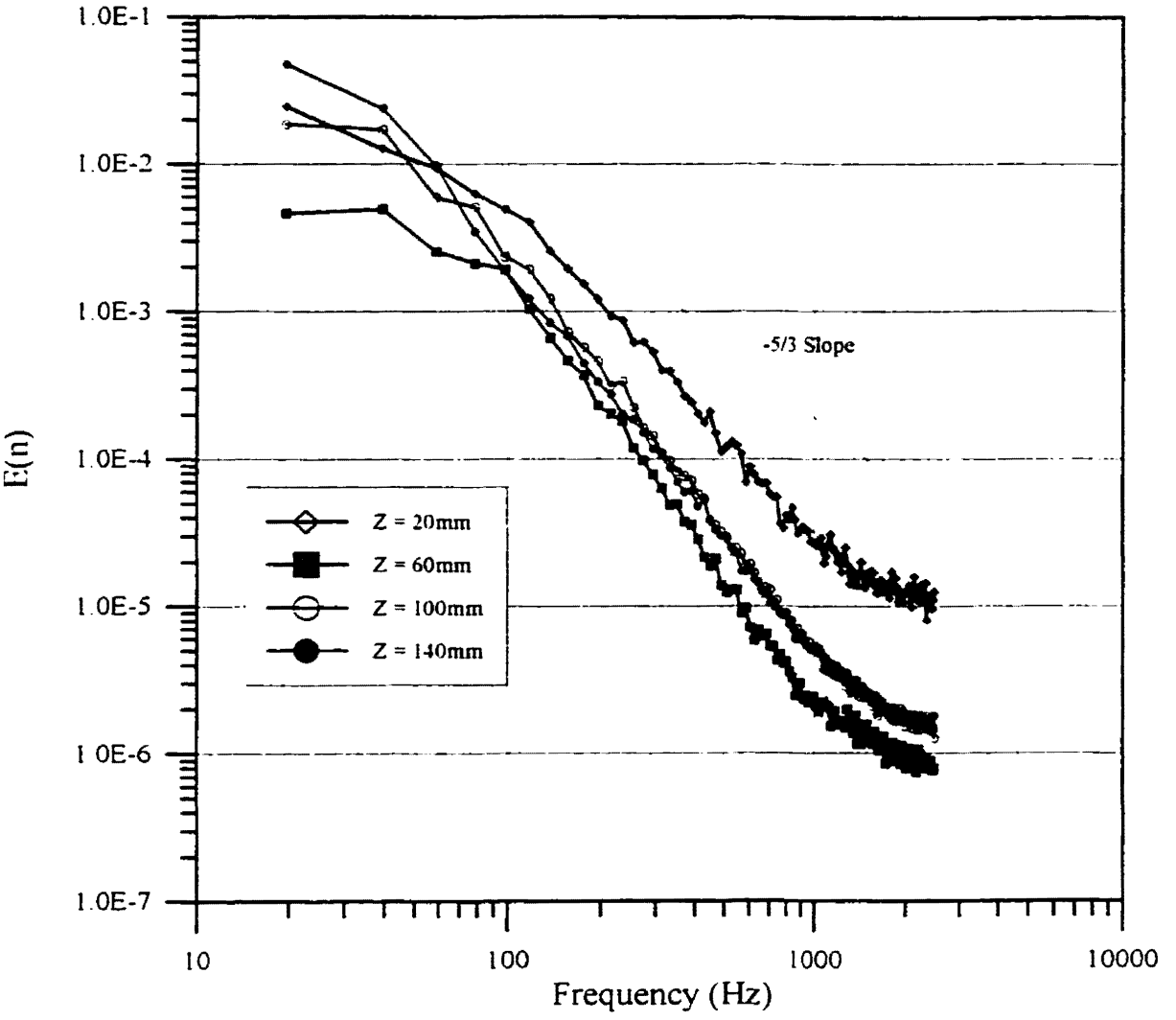


FIGURE 6.76: Turbulent centreline energy spectra development with axial distance from the nozzle, with an annular air flow rate of 7.15*l s*

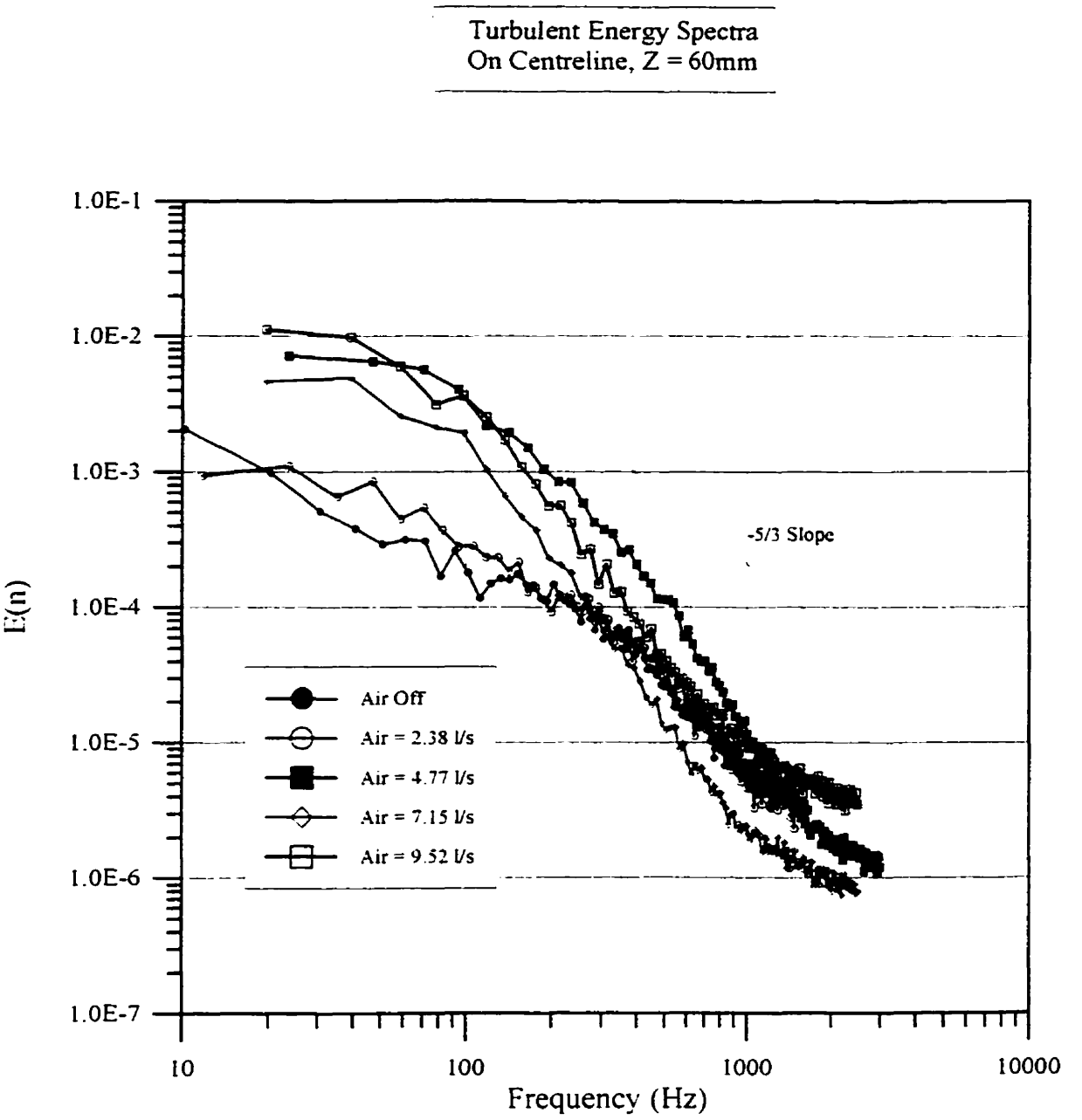


FIGURE 6.77: Turbulent energy spectra on centreline, 60mm downstream of the nozzle

6.7. SUMMARY

The photographs presented in Section 6.1 provide a good overall picture of the flame, and show a strong influence of the annular air jet on the flame structure. Overall, the length of the flame is seen to shorten considerably with increasing annular air flow rate, and the flame structure alter considerably from a two reaction zone system to a single reaction zone system. Evidence of flame impingement on the bluff body surface is seen in Figure 6.3a and b. It is also evident that some of the fuel spray escapes the flame sheath in all cases, although it appears that the annular air jet may be redirecting some of the escaping spray in a direction parallel to the flame, keeping fuel vapour in a region that may be re-entrained further downstream.

The PLIF images provided good detail on both the time-averaged and instantaneous structure of the reaction zones, and confirmed the presence of an inner and outer reaction zone system for the annular air off case. Increasing annular air flow rates produced a single reaction zone tulip-shaped structure in the region near the nozzle which appeared to become more steady with increasing annular air flow rates. Symmetry of the reaction zone in the region near the nozzle was strong, but instantaneous symmetry in the far field tended to disappear with increasing annular air flow rates, although time-averaged symmetry was still present.

Quantitative OH concentration measurements obtained from the PLIF images showed that peak time-averaged OH concentrations corresponded well with the mean temperature peaks, although a temperature peak in and of itself did not necessarily indicate a region of high OH concentration. Peak instantaneous OH concentrations were on the order of 5400 PPM, consistent with other workers' measurements in similar flames. The peak OH concentration did not appear to vary with annular air flow rate.

An attempt to produce CH fluorescence images in the spray flame was not successful due to the low signal level available, and the noisiness of the spray flame environment.

Measurements of droplet size showed that the arithmetic mean diameter increased monotonically with increasing radial position in all planes except in the z = 10mm plane, where small droplets recirculated by the annular air jet reduce the mean diameter outside the peak flux region of the spray. In the regions downstream of the nozzle, no large difference in the droplet diameter distribution with annular air flow rate is evident, except for the air = 4.77 *l*/s

case, where quite different distributions (see Figure 6.33) are evident, due to the flame impingement phenomenon discussed earlier.

Volume flux measurements were made in several planes for all annular air flow rates tested. In the regions 40mm downstream of the nozzle and further, a volume flux peak on centreline was observed for the 0 and 2.38 *l*/s air flow rate cases. This centreline peak disappeared with increasing annular air flow rate. Integration of the volume flux curves suggested that the air off case resulted in the fastest evaporation of the fuel, but this was likely due to the lack of re-entrainment velocity and settling of droplets due to gravity.

Mean velocity maps of the gas-phase flow as well as the large droplet field showed that the annular air jet produced some recirculation in the region near the nozzle, outside the spray cone. This recirculation entrained small droplets and returned them to the hot region where the flame was stabilized. Increasing annular air flow rates also produced a channeling effect in the downstream region, with both gas-phase and large droplet vectors directed towards the flow centreline, suggesting a confinement effect.

Temperature measurements made using thermocouples showed that peak mean temperature decreased with the annular air flow rate. The location of temperature peaks tended to coincide with reaction zone location except for the centreline temperature peaks, where PLIF measurements showed low OH concentrations and hence no reaction zone.

Turbulence measurements using dyed methanol fuel produced good results in many locations in the spray, even in the presence of large droplets. Mean centreline velocity plots showed the presence of centreline recirculation in only one annular air flow case, while in non-reacting annular flows, this recirculation is always present. Turbulent intensities are quite high, particularly in the region near the nozzle, where mean velocities are low or zero, while fluctuating velocities are high. Beyond $z = 80$mm, the turbulent intensities stabilize to between 10 and 25%. Integral timescales also fluctuate considerably in the region near the nozzle, but tended to stabilize in the downstream region. The integral timescales were similar for all annular air flow rates in this region, except for the air off case, as this case was nearly laminar with low turbulent intensity. Integral length scales in this region were approximately 2 cm. Turbulent energy spectra were obtained on centreline for several flow conditions, and at

several axial locations. The spectra showed a clear relationship between total turbulent energy and annular air flow rate. Due to the low turbulent Reynolds numbers associated with high viscosity flows, there was no evidence of an inertial sub-range in the spectra.

Overall, the annular air jet appears to shorten the spray flame considerably, and confine the spray by directing the flow to centreline. These attributes are desirable in space-limited combustion chambers where compact, clearly defined flames are necessary.

CHAPTER 7

EXPERIMENTAL UNCERTAINTIES

7.1. Introduction

Since one of the major objectives of this work is to demonstrate the applicability of combining PDI, PLIF and thermocouple thermometry to spray flame analysis, a major consideration is the analysis of the various uncertainties associated with each experimental technique.

Every measurement has a certain level of uncertainty and error associated with it. The error is defined as the difference between the true value of the variable measured and the exact value. The uncertainty is associated with the level of possible error of a measurement, within a specified confidence interval. Two types of errors in measurements give rise to measurement uncertainties; bias and precision errors. Bias errors are "fixed" errors which result in an offset between the mean of a set of measurements and the true mean value, while precision errors result in scatter about the actual mean value. In any measurement system, there can be many independent sources of bias and precision errors, which can often be dealt with statistically to estimate the total combined uncertainty of a given measurement set using the following:

$$S = \sqrt{\sum_{i=1}^{n} S_i^2} \qquad 7.1$$

$$B = \sqrt{\sum_{i=1}^{n} B_i^2} \qquad 7.2$$

where: S = Total precision error

S_i = Individual precision errors

B = Total bias error

B_i = Individual bias errors

The total combined uncertainty is given by:

$$\delta = \sqrt{B^2 + (tS)^2} \qquad 7.3$$

where: δ = Total measurement uncertainty

t = Student t value. For a 95% confidence interval, $t = 2$.

The measurement of time-varying quantities such as velocity involves precision errors associated with the necessarily finite sample sizes that must be taken. These precision errors in estimation of mean quantities are not only dependent on sample size, but also on the nature of the measured quantity itself. Estimation of mean velocity in a velocity field of very low turbulent intensity can be achieved with relatively few samples over a time span that is long relative to the time scales of the flow, while a highly turbulent flow would require more samples to achieve the same level of accuracy. The equation relating the precision error to sample size and measured quantity characteristics is given by Castro [41] as:

$$S = \frac{z_{\alpha/2}\,\sigma}{\sqrt{N}} \qquad 7.4$$

where: $z_{\alpha/2}$ = Standard normal variate (=1.96 for a 95% confidence interval)

σ = Standard deviation of sample set

N = Number of samples

In the case of turbulent velocity measurements, the standard deviation can be replaced by the RMS velocity fluctuation, and the precision error in mean velocity becomes:

$$\frac{S_U}{U} = \frac{z_{\alpha/2}}{\sqrt{N}} \frac{u'}{U} \qquad 7.5$$

where: U = Mean velocity

u' = RMS velocity fluctuation

The uncertainties associated with RMS velocity can be determined from:

$$\frac{S_{rms'}}{u} = \frac{z_{\alpha/2}}{\sqrt{2N}} \qquad 7.6$$

where: S_{rms} = Uncertainty in RMS

u' = RMS velocity

As will be discussed in further detail in later sections, some of the bias and precision errors associated with the experimental systems used in this work are relatively straightforward to assess. However, many of the uncertainties encountered are much more difficult to resolve, and remain unknown at present.

7.2. PDI Uncertainties

The Aerometrics Phase Doppler Particle Analyzer system consists of an optical system and a processing unit. Uncertainties associated with individual droplet size and velocity measurement are relatively easy to assess, and are related to the system hardware and processing technique. Uncertainties associated with statistical calculations such as mean diameter and volume flux are much more difficult to quantify, as are uncertainties associated with user-selected parameters such as photomultiplier voltage, threshold and filter settings.

All PDI measurements depend ultimately on the geometry of the system. The velocity measurement is dependent on the fringe spacing in the probe volume, which is in turn dependent on the beam intersection angle and laser wavelength. The laser wavelength is known to a high degree of precision, and does not contribute to instrument uncertainties. The beam

intersection angle is determined by the transmitting lens focal length and beam separation (see Equation 4.1), each of which is known and/or measurable to better than 0.5% accuracy. The constant of proportionality between phase difference and droplet diameter is given by Equation 4.7 and is dependent on the sine of the elevation and off-axis angles. The elevation angle ψ is determined by the effective detector separation, which is calibrated at the factory to a high degree of precision. The off-axis angle ϕ is determined by the physical installation of the transmitter and receiver, nominally set to 30°, with an approximate accuracy of 0.5°. The bias error induced by this level of error can be estimated from:

$$dD = \frac{d}{d\phi}\left[\frac{\delta \Delta \Phi (m-1)}{\pi m \sin\phi \sin\psi}\right]\Delta\phi \qquad 7.7$$

Solving the above for $\phi = 30°$ and $\Delta\phi = 1°$ leads to an uncertainty of approximately 1.5%.

The other term in the phase/diameter relationship is the relative index of refraction *m* between the fuel and air. Although this is known to a high degree of precision, it is a function of droplet temperature. Since the fuel droplet can be at any temperature from below ambient to its boiling point, the index of refraction is variable between these limits. For methanol, the index of refraction ranges from 1.3108 to 1.3329 over the temperature range from 10°C to near boiling at 64.5°C[72], resulting in a sizing uncertainty of approximately 4%. Recent work by Schneider and Hirleman [73] examined the effect of index of refraction gradients on particle sizing, as larger particles would not be isothermal in a combusting environment and radial gradients in temperature and hence refractive index would be present. It was concluded that, for atmospheric pressure flames, there is insufficient temperature and refractive index range to cause a significant sizing error. However, in high pressure combustion systems with fuels able to reach several hundred degrees, this effect should be addressed.

The diameter-phase relationship given in Equation 4.7, derived through the laws of geometric optics, assumes that the particles are spherical, and considerably larger than the incident light wavelength. More rigorous Mie scattering theory predicts oscillations in the phase/diameter relationship as particle size approaches the incident wavelength, increasing uncertainties in sizing for this range of particles. The lower limit of applicability of the

geometric optics relationship is the subject of some discussion in the particle sizing field. Naqwi and Durst[74],[75] performed a detailed theoretical analysis of the scattering process, and concluded that a PDI system could be configured to accurately size particles as small as 0.5μm, at the expense of overall size range. In fact, their calculations showed that a system configured to accurately size these small particles would have a maximum sizing capability of approximately 2μm! More practical sizing ranges can be achieved at the expense of low end accuracy. Rather than examining this problem from a theoretical point of view, Ceman *et al*[76] and O'Hern *et al*[77] performed a set of experiments using a vibrating orifice aerosol generator capable of accurately producing droplets as small as 3.7μm, and assessing the Aerometrics Phase Doppler Particle Analyzer's sizing ability directly. Oscillations in response were found to occur at the two commonly employed collection angles tested. Sizing errors were found to increase dramatically below 10μm, and were on the order of 60% at 5μm. The threshold for sizing errors over 10% was found to be approximately 17μm at a 30° collection angle.

Another source of uncertainty arises from the Doppler signal analysis technique. The Aerometrics Doppler signal analyzer employs a fast Fourier transform technique to determine the frequency and phase of the Doppler signal. The technique uses single bit quantization of the Doppler signal, with a user-selectable sample size and sampling frequency. In order for this technique to work well, the combination of sample size and sampling frequency must cover several full cycles of the Doppler signal. Since the spray being measured will contain a broad range of droplet velocities and hence Doppler frequencies, care must be taken to select sample size and sampling rates, as well as mixer frequencies, that result in all bursts being adequately sampled. In effect, this requires knowing the characteristics of the flow prior to obtaining measurements, and generally requires one or two iterations to determine optimum settings. Assuming that the instrument is properly configured, the expected frequency and phase RMS errors are approximately 6000 Hz and 2.5° respectively at a sampling rate of 20 MHz and sample size of 256 and a SNR of 5, as presented by Ibrahim *et al*[78]. For a typical 2 MHz burst from a 50μm droplet, this corresponds to an uncertainty of 0.3% on velocity and 1% on diameter. However, as burst frequency and particle diameter diminish, the importance of

frequency and phase uncertainties become more pronounced. In fact, with the instrument configured to cover a 1.5-75μm size range, the phase uncertainty translates to a 36% size uncertainty at 1.5μm. It is interesting to note that some workers maintain that single bit quantization as used by the Aerometrics system cannot give reliable results (Høst-Madsen and Anderson [79]). While these claims do have some merit when the system is badly configured (ie sampling rate and sample size inappropriately set for the flow being measured), there has been no practical evidence to suggest that the Aerometrics results are unreliable. It should be noted that the authors of the above-cited reference are employed by Dantec Measurement Technology A/S, which is Aerometric's direct competitor, and use 8-bit quantization in their system.

The Aerometrics system reports statistical data rather than individual particle data. Generally, the system is set to measure a fixed number of particles, then compute statistical mean diameters as well as mean and RMS velocity and volume flux. The statistical uncertainties associated with calculations of means from finite sample sizes can be determined from Equation 7.4. However, the errors associated with instrument uncertainties are difficult to quantify, since they are dependent on the actual distribution measured. As discussed above, the uncertainty of a given measurement is dependent on the particle size, increasing as size decreases. Therefore, it would be expected that a data set consisting of mostly small particles would have more uncertainty associated with its calculated means than one that is skewed more to larger particles. In addition, in any experiment, the system only validates a certain percentage of Doppler bursts, while others are rejected for a number of reasons, including low SNR, non-sphericity, and velocity and/or diameter outside pre-set bounds. Typically, the validation rate ranges between 85 and 95%, thus 5 to 15% of the droplets passing through the probe volume are not measured. If these unmeasured droplets are randomly distributed with respect to velocity and diameter, no bias in mean measurements will be induced. However, if there is a bias in rejections, then the data set itself will be biased. For example, as discussed in the previous chapter, there are locations in the flow where high relative velocity between the droplets and the gas phase may cause distortion of large droplets. These deformed droplets would cause data rejection due to non-sphericity, biasing the measurement set towards smaller

droplets. The extent of the bias induced is dependent on the size distribution itself, as well as the distribution of size of droplets rejected, an unknown entity. A similar bias towards large particles can easily result if the photomultiplier gain is set too low to detect the smaller particles, skewing the data set towards larger particles. In this case, there is no way of knowing if or how many small particles have gone undetected, and thus no way of quantifying the bias. These types of uncertainties have been acknowledged in the literature, but there does not seem to be any work reported directed at quantifying these effects. In order to estimate the importance of these effects, consider a log-normal distribution of 10000 droplets, with a geometric mean diameter of 20μm and a standard deviation of 1.65μm, as illustrated in Figure 7.1. Table 7.1 lists the statistical mean diameters calculated based on the entire distribution, as well as those calculated based on non-detection of the smallest 10% of the distribution, the largest 10%, and the smallest 5% combined with the largest 5%.

Diameter	**True (μm)**	**Largest 90% (μm)**	**Smallest 90% (μm)**	**Middle 90% (μm)**
D_{10}	22.63	24.19	19.75	21.70
D_{20}	25.49	26.71	21.19	23.26
D_{30}	28.56	29.56	22.48	24.75
D_{32}	35.86	36.18	25.30	28.03

TABLE 7.1: Effect of droplet rejection bias on mean diameters

As can be seen, non-detection of the smallest 10% of droplets leads to little error in the computed mean diameters, while non-detection of the largest 10% of droplets leads to substantial underestimation of mean diameters for this type of distribution. Obviously, the relative degree of error is distribution dependent, but significant errors may be occurring if data rejection is non-random.

Count corrections for probe volume area variation with size class, required to obtain unbiased statistical diameters according to Equation 4.9, depend on the instrument software

estimation of gain, G^2. This estimate is highly uncertain. However, the dependency of the correction factor on G, given in Equation 4.8 is not strong, and 50% errors in estimation of G lead to negligible errors in the probe area correction.

Volume flux measurements made by the system are particularly uncertain. The instrument calculates the volume flux by determining the effective probe area for each size class, then multiplies the count in each size class by the mean droplet volume in that size class, divided by the probe area and time span of acquisition. The major source of uncertainty in this calculation arises from the determination of the probe area. As discussed earlier, the width of the probe area is dependent on droplet size, droplet velocity, intensity distribution and photomultiplier gain. The Aerometrics software includes a proprietary routine to determine the probe area in each size class based on the maximum transit time of particles through the probe volume in each size class. The assumption is made that, in a size class containing many counts, the longest transit time of particles in that size class corresponds to the particle whose trajectory carried it through the centre of the probe volume, defining the probe volume width when the transit time is multiplied by the particle's velocity. In many sprays this provides an adequate result. However, in the case of sprays with a wide size distribution, each size class may only have a few particles associated with it, and the assumption that the longest transit time corresponds to a trajectory passing through the centre of the probe volume may be erroneous, leading to underestimation of probe volume area and overestimation of volume flux. In dense sprays, it is also possible (indeed likely) that some measurements would involve multiple particles passing through the probe volume. If one particle enters the probe volume before the preceding one exits, and if they are of similar size and velocity, the instrument will not reset after the first particle leaves, but will only count a single particle, with a transit time corresponding to that of the sum of the two particles, resulting in a large overprediction of probe area. It is possible to reduce the likelihood of multiple particle detection by reducing photomultiplier gain and increasing the threshold setting, but this would result in reduced detectibility of small particles. McDonell and Samuelsen[80] found that flux measurements showed a strong dependence on photomultiplier gain setting which did not show asymptotic behavior, unlike diameter measurements which tended to stabilize after photomultiplier gain

was set sufficiently high to detect the small particles. Integration of their flux data over the spray field yielded a volume flow rate more than double the injected amount, which they attributed to difficulties with the software calculation algorithm. Based on the results of McDonell and Samuelsen [80] as well as the results reported in Section 6.7, it would seem that volume flux measurements should be treated carefully, and used in qualitative fashion rather than quantitatively. It is important to note that, although both probe area corrections and absolute probe area calculations depend on determination of effective gain, it is only flux measurements that are sensitive to errors in its calculation.

7.3. Turbulent Statistics Uncertainties

Measurement of turbulent statistics in a reacting multi-phase flow is quite difficult to accomplish, for reasons outlined elsewhere in this work. In order to obtain gas-phase velocity data, it is necessary to obtain a data set of spray droplet velocity and seed particle velocity, then filter out all data associated with particles that are deemed too large to accurately follow the gas-phase flow. As discussed earlier, the cut-off diameter for particles that will follow a

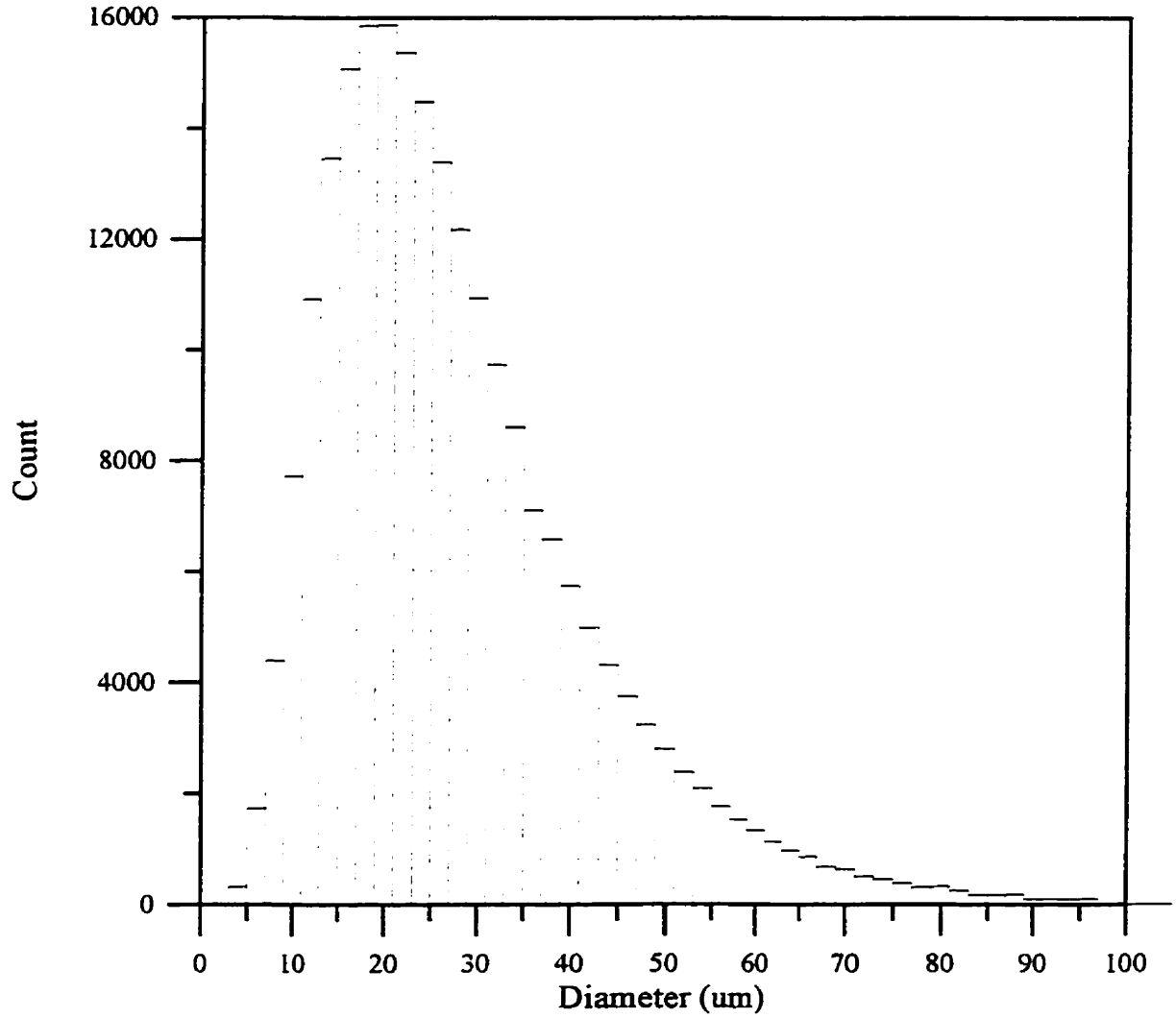


FIGURE 7.1: Log-normal distribution with $D_g = 20\mu m$, $\sigma_g = 1.65\mu m$

flow with an integral timescale on the order of 1 ms is approximately 5μm. Hence, most gas-phase velocity data presented herein is based on filtered data sets consisting of particles measured to be 5μm and smaller. It should be noted that the PDI system has an uncertainty on the order of 2μm in this size range, hence the resulting velocity data set will have velocity measurements associated with a broad distribution of particle sizes ranging from approximately 0.5 to 7μm. While all these particles will follow the gas-phase flow reasonably well, there will always be some slippage when velocity gradients are present, with larger particles exhibiting more slip than smaller ones. Hence, the degree to which the calculated mean and fluctuating velocities correspond to the actual gas-phase velocity depends on the nature of the flow (turbulent intensity, shear) as well as the size distribution of the particles in the filtered data set. For particles subjected to a linear velocity gradient of 0.5 (m/s)/mm, a 5μm particle will lag the flow by approximately 7%, while a 1μm particle would exhibit less than 1% lag [81]. Another source of uncertainty in these velocity measurements arises from the sometimes small data sets remaining after all large droplet data has been removed. In these instances, the final data set may have only a few hundred data points in a flow field of 30% turbulent intensity. In these instances, the associated mean velocity uncertainty would be on the order of 6% and the error in RMS velocity would be on the order of 13%.

Determination of mean velocity based on seed particles passing randomly through a probe volume can lead to a bias towards faster particles, if the flow is essentially uniformly seeded, as the particle flux of faster moving particles is higher than slower moving ones. One method discussed by Buchave *et al* [82] to reduce this bias is to weight the mean velocity calculation by gate time (essentially equal to travel time across the probe volume). Mean velocity calculations based on this method differed by less than 1% from those calculated using an unweighted average, and hence this method was not used.

Another source of uncertainty arising from velocity measurements based on seed particle velocity in flames results from themophoretic effects in regions of high temperature gradients. Sung *et al* [83] performed experiments and calculations for a methane/oxygen/nitrogen counterflow flame and found that deviations were in excess of 15 cm/sec in the worst case. The thermophoretic effect is strongest in regions of extremely high

temperature gradient, and would therefore only be significant near the reaction zone itself.

Finally, some uncertainties are associated with motion of the probe volume itself due to index of refraction gradients and fluctuations as the laser passes through the reaction zone. Extreme fluctuations result in the probe volume decoupling and/or moving out of the field of view of the receiving optics, resulting in loss of data. In general, the probe volume will always be in motion, and all measured velocities will include a component due to this motion. Since the motion is essentially random, mean velocity calculations would not be affected, but RMS velocities could be overestimated. This effect has been studied by Ancimer and Fraser [84], and have been found to be on the order of 3 cm/s under certain conditions. To minimize this effect, it is recommended that probe lasers intersect the flame sheet at a near-normal incidence angle. In this work, measurement of radial velocity required traversing the burner in a direction normal to the optical axis of the probe volume, and hence for many measurements, the laser crossed the flame sheet at an oblique angle, so that the flame-induced velocity bias could not be minimized. However, since most RMS velocities measured were on the order of 0.5 m/s and higher, the associated error is not large.

The uncertainty in integral timescale determination, obtained by integrating the autocorrelation function, is related to the filtered data set effective data rate. The PDI system makes a measurement each time a particle passes through the probe volume, rather than at fixed time intervals. The resulting filtered data set therefore consists of random arrival time data. In order to convert the data set to a fixed interval set compatible with the curently used software, a linear interpolation technique was employed. The resulting data set was therefore no longer based on actual velocity measurements, but on a processed set with uncertain correlation to the original. As long as the fixed interval used in generating this data set was on the same order as the mean sampling rate in the original, filtered set, errors are not expected to be large. However, in order to ensure that this criteria was met, the time interval in the final data set was often quite large, often on the order of 1ms. The resulting autocorrelation was often not well resolved, resulting in large uncertainties when integrated to obtain the integral timescales. In many cases, the calculated integral timescale was of the same order as the data interval, suggesting that the calculated integral timescale is highly uncertain. In other regions

of the flow, the integral timescale was an order of magnitude larger than the data interval, and is considered more reliable.

The uncertainty associated with the power spectrum function is given by Bendat and Piersol [85] as:

$$\frac{S_{PSF}}{E(f)} = \frac{1}{\sqrt{n_d}} \qquad 7.8$$

where: S_{PSF} = Uncertainty in power spectrum function

$E(f)$ = Power spectrum function

n_d = Number of distinct sub-records

In this work, the number of distinct sub-records was generally on the order of 40, although this varied with data set size, resulting in an uncertainty on the order of 15%.

7.4. PLIF Uncertainties

In some respects, there are few uncertainties associated with PLIF imaging of OH. If the intent is to image reaction zone location, uncertainties are limited to the physical set-up of the system and camera characteristics. If the intent is to determine quantitatively the hydroxyl radical concentration, the sources of uncertainty are many. The work reported herein uses PLIF to both image the reaction zone, and to measure the mean and peak OH concentration, and hence a detailed uncertainty assessment is warranted.

As discussed in section 4.2.1, the induced fluorescence at low excitation levels is proportional to the overlap integral between the laser linewidth and the absorption linewidth of the molecule being excited, the coefficient of spontaneous emission A, and the quench rate Q, as well as the ground state population of the molecules being excited.

The overlap integral between the laser pulse and the absorption linewidth can be determined with a reasonable degree of accuracy. The laser linewidth has been measured using an etalon as described in the laser manual[86]. The etalon used was a Lambda Physik FL-82

with a free spectral range (FSR) of 0.67 cm^{-1}, and a projection lens of 1000mm to focus the fringe pattern, which was imaged using the ICCD. The etalon was equipped with several coatings suitable for different wavelength ranges, with a minimum usable wavelength of 320 nm, higher than the 283nm nominal operating wavelength. Hence, the linewidth was measured at 320nm, as well as at the exit of the dye laser at 566nm. The linewidth was determined from the following equation:

$$\Delta v = T \cdot \frac{2\,FSR}{A} \qquad 7.9$$

where: Δv = Laser linewidth (cm^{-1})

T = FWHM width of 2nd ring of fringe pattern

A = Spacing between 1st and 3rd ring of fringe pattern

FSR = Etalon free spectral range

The measured linewidth at 320nm was found to be 0.25 cm^{-1}, very close to the manufacturer's specification of 0.18 cm^{-1} (min) and to that measured by Wong[87] using a somewhat different method. Uncertainties in this measurement are mainly due to the limited resolution of the ICCD camera used to resolve the FWHM width of the second ring. This uncertainty is estimated to be approximately 20%. However, for a typical OH measurement at 1500K, an uncertainty of 20% on laser linewidth results in a total uncertainty of only 10% for the combined linewidth overlap and spectral irradiance terms. This is not a general case, but arises because the laser line width is of the same order as the absorption line width. Hence, an overestimation of laser linewidth leads to an underestimation of the spectral irradiance, and an overestimation of the overlap integral. In cases where the laser linewidth is much larger than the absorption linewidth, the overlap integral would not significantly change with small errors in laser linewidth estimation, but the spectral irradiance term would. It should also be noted that there is a temperature dependence of the absorption lineshape due to Doppler and pressure broadening. In the range of 1000 to 2000K, the Doppler linewidth ranges from 0.20

to 0.27 cm^{-1}, and the pressure broadened linewidth ranges from 0.11 to .08 cm^{-1} and the resulting overlap integrals range from 0.84 to 0.68 $E/\Delta\nu$ respectively. Hence, any uncertainty in temperature can lead to some uncertainty in overlap integral.

Another uncertainty in the laser fluence arises from the laser itself in terms of shot to shot variation of total and point laser power. Since power measurements were made with a time-averaging instrument, and LIF images were made using a single laser pulse, it was necessary to assess the variability of the laser power on a shot to shot basis. This was performed by imaging the light scattered by the laser sheet when directed onto a smooth surface, and recording the total intensity count of all pixels in the sheet image. The variation of this total count on a shot-to-shot basis represents the variation of total sheet energy, again on a shot-to-shot basis, which was found to be approximately 10%. A similar quantification, looking at a single pixel in the sheet image, showed a 15% variation, suggesting some variability in laser light distribution across the sheet on a shot-to-shot basis.

Perhaps the most significant source of uncertainty in the estimation of OH concentration is the value used for the quenching rate, Q. The quench rate is dependent on knowledge of the concentration and collisional cross-section of each species present in the region of interest, as well as the temperature. Particularly in the reaction zone itself, a region of non-equilibrium, this is not well known at all. Some experimental measurements have been made of the quench rate in various types of flames, as well as some theoretical predictions. For methanol, the quench rate has been reported to be $(5\pm1)\times10^8$ s^{-1} at 2000K[88],[89]. As with the absorption linewidth, the quench rate is temperature dependent, hence uncertainties in temperature translate into uncertainties in quench rate. Garland and Crosley [55] summarized the state of the art as "...OH quenching can be estimated to within 30-50% in many cases...".

The spectroscopic constant for spontaneous emission A is well known and is not a major source of uncertainty. Copeland *et al* [59] reported values for the transition probabilities with uncertainties on the order of 9% for the transitions of interest in this work. Table 7.2 summarizes the uncertainties associated with the fluorescence emission.

In addition to the above uncertainties associated with fluorescence emission, there are other possible sources of error. One possible source of error involves the polarization of

fluorescence emission, resulting in non-isotropic emission. Since the exciting radiation is highly polarized, some degree of polarization is likely to be preserved on emission. Since each emitting molecule is likely to undergo many collisions before emitting, some depolarization will occur. This problem was analyzed in some detail by Doherty and Crosley[90], who concluded that significant errors in signal interpretation could result if this effect were not considered when examining spectra, but that broadband collection schemes as used in this work would not be significantly affected. Another source of error not considered in the data analysis is absorption effects resulting from excitation beam absorption through the flame, and fluorescence reabsorption prior to arrival at the collection optics. The first effect, arising from laser absorption from OH and outscattering by fuel particles as the laser sheet passes through the flame, was assessed by measuring the beam energy before and after the flame, and was found to be negligibly small. The effect of fluorescence trapping was not measured, but would be expected to be of the same order as beam absorption or somewhat larger, due to the larger Einstein coefficients for (0,0) and (1,1) fluorescence.

The other major source of uncertainty associated with fluorescence measurements is in the fluorescence detection system, the ICCD and associated optics. The uncertainties associated with the ICCD camera depend on the signal being measured. For low level signals, the uncertainty is related to photon shot noise, readout noise and dark charge buildup. Photon shot noise is related to the statistics of photon counting, described by a Poisson distribution. The readout noise is related to the ICCD electronics and the uncertainty associated in measuring the electron count of the pixel well. Dark charge build-up is related to the slow accumulation of electrons in the pixel well in the absence of incident signal, which can be minimized by cooling the ICCD. The total noise of the ICCD measurement is given by [62]:

$$N_T = \left[N_R^2 + N_D^2 + N_{ph}^2 \right]^{1/2} \qquad \textbf{7.10}$$

where: N_T = Total signal noise

N_R = Readout noise of the ICCD

N_D = Dark charge noise of the ICCD

N_{ph} = Photon shot noise associated with the signal

The total readout noise N_R of the ICCD is typically around 10 electrons, or, at a gain setting of 1 counts per photoelectron, 10 counts. The dark charge build-up during a typical 100ms exposure, with the ICCD cooled to -35°C is approximately 1 electron, or 1 count at the above gain setting. The typical incoming signal produces a peak count reading on the order of 3000 counts, and the associated shot noise is the square root of the signal, or 55 counts. Hence, for the typically high signal levels encountered in this work, the predominant source of uncertainty of the above is shot noise, at approximately 2%, or an SNR of 50. The corresponding OH concentration at this signal level in the configuration used in this work was approximately 5400PPM. The lowest OH concentration measurable with reasonable accuracy would be approximately 15 PPM, with a shot noise limited SNR of around 3.

Perhaps the most significant source of error associated with the fluorescence detection system with respect to quantifying peak OH concentrations as presented in this work arises from the 12% pixel to pixel non-uniformity arising from the image intensifier. There is a 12% variation in output signal for a uniform input signal. Since the system was calibrated on the basis of a single proportionality constant between incident photon flux and pixel intensity count for all pixels, no attempt was made to calibrate each individual pixel. Hence, any photon count derived from a given pixel has a 12% uncertainty associated with it. In addition, the technique employed to calibrate the system used the sum of intensity count over a few pixels to determine the above-mentioned proportionality constant, and hence the uncertainty associated with this count would introduce a bias error estimated at around 5%.

It should be noted that many other possible sources of error have been removed by the technique employed to calibrate the system. For example, bias errors associated with the power meter used to measure laser energy, which can be large, are eliminated since the same instrument is used for Rayleigh calibration and LIF imaging. Geometric errors as well as optical and quantum efficiency uncertainties are also eliminated in the same fashion, as the same geometric and optical set-up is used for calibration and OH imaging. The only optical factor not calibrated out in this fashion is the interference filter efficiency at the various

fluorescence wavelengths, and these are supplied by the manufacturer to a high degree of certainty.

Combining all the above errors, the uncertainty associated with OH concentration at a given point is on the order of 40%, quite a high level of uncertainty. Although the accuracy of the concentration measurements can be improved by more precise experimental techniques for calibration, linewidth measurements etcetera, a major source of error is uncertainty associated with the quench rate.

Parameter	**Uncertainty**	**Remarks**
Laser Power Variation in Sheet	15%	As measured
Laser Power Measurement	10%	Per power meter specs
Laser Linewidth	20%	Limited by camera resolution
Overlap Integral	10%	Dependent on laser linewidth
Quench Rate	20-30%	Major uncertainty
Einstein A coefficient	9%	As measured by Copeland *et al* [59]
Pixel to pixel variability	12%	Manufacturer's spec.
Shot noise (typical signal)	2%	Low for strong signals
Calibration bias error	5%	Estimated

TABLE 7.2: Summary of fluorescence measurement uncertainties

7.5. Temperature Measurement Uncertainties

Uncertainties associated with thermocouple measurements have been quite well documented, as outlined in [91]. However, methods of quantifying and minimizing these uncertainties are less well developed. The uncertainties associated with thermocouple measurements can be divided into two broad categories: time-response uncertainties and thermal uncertainties. Time response uncertainties are associated with the thermal response time of the thermocouple junction to changes in medium temperature, while thermal uncertainties are associated with heat loss/gain effects such as radiation and conduction losses from the thermocouple junction, as well as catalytic effects on the thermocouple surface. In measurements of mean temperature, as presented in this work, the second class of uncertainty is dominant. The response of a thermocouple immersed in a flow field can be modeled by considering a heat balance on the thermocouple junction. The resulting equation is:

$$A_b h_b (T_g - T) + 2\pi r^2 k_w \frac{dT_w}{dx}\Big|_{x=0} - \sigma \epsilon A_b (T^4 - T_{surr}^4) + q_{cat} = m_b C_b \frac{dT}{dt} \qquad 7.11$$

where:

A_b = Surface area of thermocouple junction

h_b = Effective convection coefficient at junction

T_g = Actual gas temperature

T = Thermocouple junction temperature

r = Radius of thermocouple wire

k_w = Thermocouple wire thermal conductivity

T_w = Thermocouple wire temperature

x = Distance from junction ($x = 0$ is junction)

σ = Stefan-Boltzmann constant

ϵ = Junction emissivity

T_{surr} = Surroundings temperature

q_{cat} = Heat addition due to catalysis

m_b = Junction mass

C_b = Junction specific heat

The first term in the above equation describes the rate of heat transfer to the thermocouple junction from the flow field by convection. The second term describes the rate of heat conduction into or out of the junction by conduction along the lead wires. The third term describes heat loss from the junction to the surroundings by radiation. The time-dependent term on the right hand side describes the time response of the junction. For steady state mean temperature measurements, this term is taken as zero. In order to compensate a measurement for conduction and radiation losses, many terms must be known. The convection coefficient, dependent on local fluid properties, velocity, and shape and dimensions of the junction, can be estimated using correlations. Temperature gradients along the leadwires, which must be evaluated to assess conduction losses, depend on local flow conditions as well as convection coefficients, and are difficult to assess. Radiation measurements depend on knowledge of temperatures of all participants' temperatures and relative importance. In some cases, such as lean combustion of non-sooting fuels, radiation can be considered as radiant exchange between the thermocouple junction and the far surroundings, neglecting exchange between hot gases. However, in other flames where particulate loadings are high, or where hot gases may be participating, these losses are extremely difficult to quantify. Attya and Whitelaw[92] estimated that the radiation correction is less than 5% for an 80μm thermocouple wire where the burning mode of the spray flame was primarily a diffusion flame. Uncertainties and errors associated with fuel droplet strikes on the thermocouple junction itself, or on the lead wires near the junction, do not appear to have been quantified. Conduction losses can be minimized by using long leadwires, and orienting the thermocouple in the flow to minimize temperature gradients in the vicinity of the junction.

Although the effect is not well quantified, catalytic effects involving reactions at the thermocouple surface can produce large errors. Bare platinum thermocouples are particularly susceptible, since platinum is a particularly effective catalyst for a large number of reactions. Pita and Nina[93] investigated the catalytic effect in a premixed propane/air flame, as well as in a 20°C hydrogen/air non-reacting flow, and concluded that substantial errors associated with catalytic effects are present in radical-rich flame zones. The magnitude of the error was not quantified, depending strongly on local composition. It was also found that, within the

ranges tested, the effect was independent of thermocouple size and local flow velocity.

In this work, severe catalytic action was initiated upon shut-down after operating with an annular air flow rate of 4.77 *l/s*, a condition which caused heating of the bluff body due to flame impingement. On shut-down, methanol left in the nozzle vaporized and emerged from the nozzle as a vapour jet which caused sufficient catalytic action on contact with the thermocouple that it was seen to glow. Turning on the fuel spray and directing it at the thermocouple enhanced this reaction, and caused a temperature reading over 1600K. This phenomenon is illustrated in Figure 7.2. hence, in this case, the error induced by the catalytic effect is on the order of 1300K when the fuel spray is at 300K, or 430%! It should be noted that an attempt to induce this catalytic reaction using a type K (Ni-Cr/Ni-Al) thermocouple was unsuccessful, even though nickel is itself a good catalyst. Although there was no evidence of catalytic effects of this degree in the reacting flow, measurements made in regions of high fuel vapour concentration and in reaction zones must be considered suspect. Measurements made in post-combustion regions are likely free of catalytic effects.

In this work, mean temperature measurements have primarily been reported, and these are not strongly affected by thermocouple time constant issues. Uncertainties associated with mean temperature measurements are largely associated with statistical uncertainties, as well as instrument and data acquisition errors. The configuration used in this work involved amplifying the thermocouple output using a custom-made, 400x amplifier, resulting in an output signal ranging from approximately 0 to 7.2V over a temperature range of 300 to 2000K. This signal was fed to an analog to digital converter board, configured for a range of 0 to 10V, and 12 bit digitization, resulting in a resolution of 2.44mV/count. Since the output of a type S thermocouple changes by approximately 0.01mV/K (4.2mV/K at 400x amplification), the temperature resolution of the acquisition system is approximately 0.5K. RMS uncertainty when measuring a steady signal is better than 1K. The bias error at 373K was also better than 1K. The calibration curve used for a type S thermocouple has a stated accuracy of ±0.5K over the thermocouple range, but actual conformity of the thermocouple to this curve depends on thermocouple quality and purity.

Typical measurement sets consisted of 2048 measurements obtained at a 250 Hz

sampling rate. The statistical uncertainty associated with a sample set of this size is less than 0.5% for a 1500K mean temperature measurement with an RMS of 100K. It should be noted that RMS temperatures measured are likely to be low due to the slow thermal response of the thermocouple relative to the fluctuating timescales of the flow.

It would appear that uncertainties associated with conduction and radiation losses dominate uncertainties in temperature measurements in regions of the flow where catalytic effects and droplet strikes are unlikely, and are on the order of 5%, while in regions where catalytic effects and/or droplet strikes are likely, uncertainties are much higher, and unquantified.

Uncertainty	Value	Remarks
Analog to Digital Conversion	0.5K	12 bit digitization
Bias error	0.5%	Estimated
Radiation loss	5%	Attya and Whitelaw [94]
Conduction Losses	Small	Long leads, proper alignment
Catalytic Errors	Unquantified	Can be large
Statistical Uncertainties	<1%	Large sample, small σ
Estimated Total Uncertainty (excluding catalytic effect)	7%	

Table 7.3: Summary of temperature measurement uncertainties

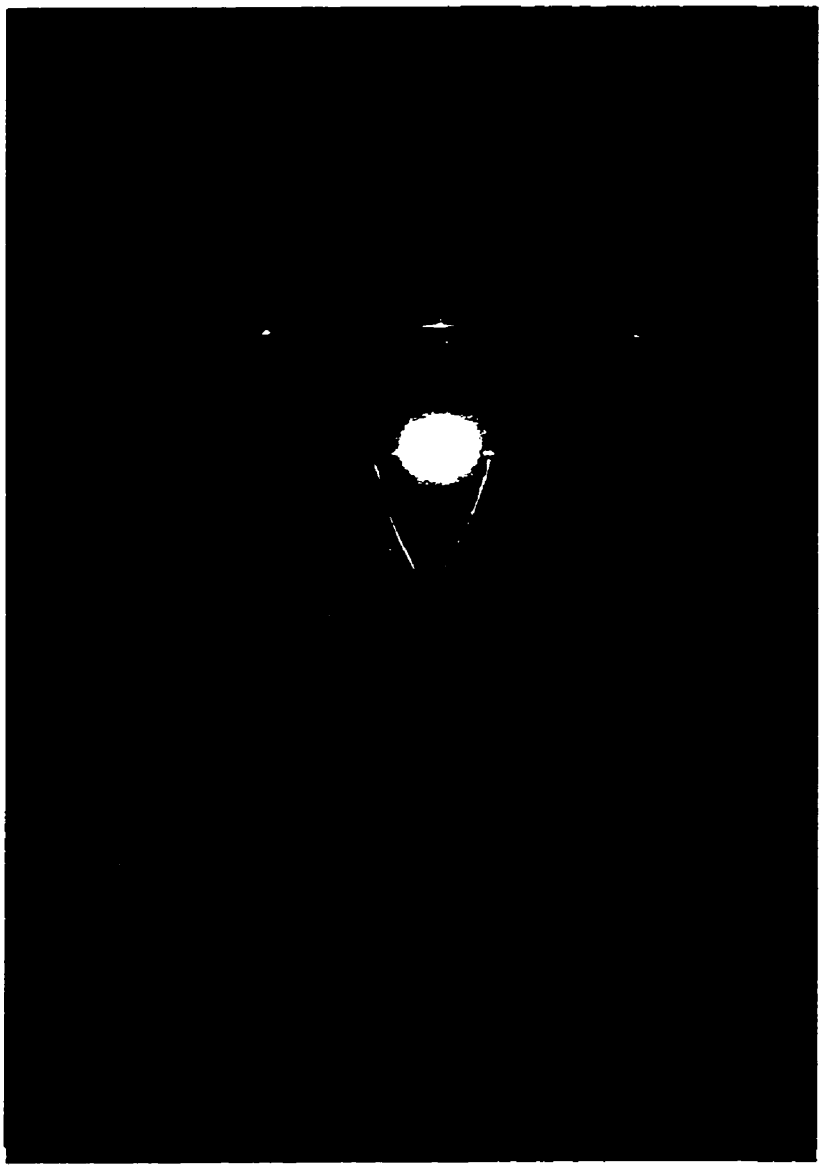


FIGURE 7.2: Catalytic surface combustion on thermocouple

CHAPTER 8

CONCLUSIONS AND RECOMMENDATIONS

This work has combined phase Doppler interferometry, planar laser-induced fluorescence and thermocouple thermometry to effectively investigate the interaction of an annular jet with a spray flame.

Phase Doppler interferometry allows determination of droplet size and velocity at any point in the flow field non-intrusively, and with little interference from the flame itself. Post-processing of resulting data sets allows extraction of gas-phase velocities. Doping the liquid fuel with very small quantities of a dye that is strongly absorbing at the probe laser wavelengths increases the sensitivity of the phase Doppler system to small seed particles significantly, allowing determination of integral time scales and turbulent energy spectra of gas-phase flows in many regions of the spray flame, information that has been difficult or impossible to obtain previously.

Planar laser-induced fluorescence imaging provides an excellent tool to image reaction zone location and structure on an instantaneous as well as time-averaged basis in the spray flame. The excitation/detection scheme used allows easy discrimination of OH fluorescence, even in the presence of strong Mie scattering of the excitation laser from fuel droplets. Uncertainties associated with quenching rates, as well as pixel to pixel sensitivity variations, limit the accuracy of OH concentration measurements to approximately 40%. Although the CH fluorescence imaging scheme employed in this work successfully imaged CH in a bunsen burner flame, it was not successful in imaging CH in the spray flame, largely due to interference from fuel droplet Mie scattering and low CH concentration levels.

Thermocouple temperature measurements were successfully obtained over much of the spray flame field, with little evidence of data contamination due to fuel droplet impingement on the thermocouple wire. Possible catalytic effects raised questions about the accuracy of temperature measurements in fuel rich regions as well as in reaction zones.

The combination of these instrument systems provided complementary information about the spray flame, and is a highly effective set of research tools.

The effect of an annular air jet on the spray flame is highly pronounced. Overall flame structure changes radically from the air off case, becoming much shorter, and structured with a single reaction zone instead of the double reaction zone structure in the no air case. Overall flame length is reduced by more than 50% with annular air on, and peak temperatures in the flame are reduced substantially. Turbulent intensities are very high with annular air on, and the turbulent structure is highly anisotropic. The fuel distribution pattern is strongly affected by the annular air jet, which helps entrain small droplets in the flame stabilization region near the nozzle, and helps direct droplets to the flame centreline in the far field.

Experimentally, future work should refine the dyed spray method of enhancing visibility of seed particles, with investigation of different dyes and seeding methods being a priority, in order to maximize data rates to enable better turbulent analysis, which has not yet been done in spray flames. Alternate schemes for imaging CH in dirty environments should also be investigated. With respect to the annular air jet burner, the next stage in the investigation should be to examine the burner performance in an enclosed combustion chamber, a more practical configuration than the upward-firing torch set-up used in this work.

CHAPTER 9

REFERENCES

1. Chigier, N.: " *An Assessment of Spray Technology*" Atomization and Sprays Vol. 3 No. 4 1993, pp. 365-371

2. Chigier, N.A., Beér, J.M.: "*The Flow Region Near the Nozzle in Double Concentric Jets*" J. of Basic Engineering, Dec. 1964, pp. 797-804

3. Davies, T.W., Beér, J.M.: "*Flow in the Wake of Bluff Body Flame Stabilizers*" 13th Symp. (Int'l) on Combustion, 1971, pp. 631-638

4. Durâo, D.F.G., Whitelaw, J.H.: "*Velocity Characteristics in the Near Wake of a Disk*" J. of Fluid Mechanics V.85 Pt 2 1978, pp.369-385

5. Taylor, A.M.K.P., Whitelaw, J.H.: "*Velocity Characteristics in the Turbulent Near Wakes of Confined Axi-Symmetric Bluff Bodies*" J. of Fluid Mechanics V.139 1984, pp.391-416

6. Pope, S.B., Whitelaw, J.H.: "*The Calculation of Near-Wake Flows*" J. Fluid Mechanics V73 part 1 1976, pp. 9-32

7. Li, X., Tankin, R.S.: " *A Study of Cold and Combusting Flow Around Bluff Body Combustors*" Combustion Science and Technology V.52 1987, pp. 173-206

8. Li, X., Tankin, R.S.: "*Spray Behaviour in Annular Air Streams*" Combustion Science and Technology V.64 1989, pp. 141-165

9. McDonnell, V.G., Samuelsen, G.S.: "*Structure of Vaporizing Pressure Atomized Sprays*" Atomization and Sprays V.3 No.3 1993, pp.321-364

10. McDonnell, V.G., Adachi, M., Samuelsen, G.S.: "*Structure of Reacting and Non-Reacting, Non-Swirling, Air Assisted Sprays, Part 1: Gas Phase Properties*" Atomization and Sprays V.3 No. 4 1993, pp. 389-410

11. McDonnell, V.G., Adachi, M., Samuelsen, G.S.: "*Structure of Reacting and Non-Reacting, Non-Swirling, Air Assisted Sprays, Part 2: Drop Behaviour*" Atomization and Sprays V.3 No. 4 1993, pp. 411-436

12. McDonnell, V.G., Adachi, M., Samuelsen, G.S.: "*Structure of Reacting and Non-Reacting Swirling, Air-Assisted Sprays*" Comb. Sci. and Tech. V.82, 1992, pp.

225-248

13. Friedman, J.A., Renksizbulut, M.: "*Interaction of an annular air jet with a Non-evaporating Liquid Spray*" Part. Part. Syst. Charact. Vol. 11, 1994, pp. 442-452

14. Saumweber, C., Friedman, J.A., Renksizbulut, M.: "*Simultaneous Droplet Size and Gas-phase Turbulence Measurements in a Spray Flow Using Phase Doppler Interferometry*" Part. Part. Syst. Charact. Vol. 14, 1997, pp.233-242

15. Hardalupas, Y., Liu, C.H., Whitelaw, J.H.: "*Experiments with Disk Stabilized Kerosene-Fuelled Flames*" Combust. Sci. and Tech. V.97 1994, pp. 157-191

16. Allen, M.G., Hanson, R.K.: " *Digital Imaging of Species Concentration Fields in Spray Flames*" 21st Symposium (Int'l) on Combustion 1986, pp. 1755-1762

17. Allen, M.G., McManus, K.R., Sonnenfroh, D.M., Paul, P.H.: "*Planar Laser-induced Fluorescence Imaging Measurements of OH and Hydrocarbon Fuel Fragments in High Pressure Spray Flame Combustion*" Applied Optics V.34 N.27 1995, pp. 6287-6300

18. Goix, P.J., Edwards, C.F., Cessou, A., Dunsky, C.M., Stepkowski, D.: "*Structure of a Methanol / Air Coaxial Reacting Spray Near the Stabilization Region*" Combustion and Flame 98 1994, pp. 205-219

19. Stepkowski, D., Cessou, A., Goix, P.: "*Flame Stabilization and OH Fluorescence Mapping of the Combustion Structures in the Near Field of a Spray Jet*" Combustion and Flame 99 1994, pp. 516-522

20. Humphries, W. Vincent, J.H.: "*Near Wake Properties of Axisymmetric Bluff Body Flows*" Appl. Sci. Res. Vol. 32, 1976, pp. 649-669

21. Lefebvre, A.H.: "*Atomization and Sprays*" Hemisphere Publishing Co., New York, 1989

22. Fraser, R.P., Eisenklam, P.: "*Research in to the Performance of Atomizers for Liquids*" Imp. Coll. Chem. Eng. Soc. J., Vol. 7, 1953, pp. 52-68

23. Hinze, J.O.: "*Fundamentals of the Hydrodynamic Mechanism of Splitting in Dispersion Processes*" J. of the AIChE, Vol. 1, No. 3, 1955, pp. 289-295

24. Bearman, P.W., Morel, T.: "*Effect of Free Stream Turbulence on the Flow Around Bluff Bodies*" Progress in Aerospace Sciences Vol. 20, 1983, pp. 97-123

25. Warnica, D.: "*Aerodynamic Drag of Droplets in Turbulent Flow Fields*" PhD Thesis, University of Waterloo, 1992

26. Omielan, W.: "*The Effects of Turbulent Spatial Scale and Intensity on the Aerodynamic Drag of Droplets*" MASc Thesis, University of Waterloo, 1994

27. Hinds, W.: " *Aerosol Technology*" John Wiley and Sons, New York, 1982

28. Westbrook, C.K., Dryer, F.L.: " *A Comprehensive Mechanism for Methanol Oxidation*" Combustion Science and Technology Vol. 20, 1979, pp. 125-140

29. Olikara, C.,Borman, G.L.: " *A Computer Program for Calculating Properties of Equilibrium Combustion Products with Some Applications to I.C. Engines*" SAE paper 750468, 1975

30. Chigier, N., McGreath, C.G., Makepeace, R.W.: "*Dynamics of Droplets in Burning and Isothermal Kerosene Sprays*" Combustion and Flame *23*, 1974, pp. 11-16

31. Chigier, N.: " *Energy, Combustion and Environment*" McGraw Hill, 1981

32. Dodge, L.G.: " *Comparison of Performance of Drop-Sizing Instruments*" Applied Optics Vol. 26 No. 7, 1987, pp. 1328-1341

33. Meyer, P., Chigier, N.: " *Dropsize Measurements Using a Malvern 2200 Particle Sizer*" Atomisation and Spray Technology Vol. 2 No. 4, 1986, pp. 261-298

34. Cormack, A.M.: " *Representation of a Function by Its Line Integrals, with Some Radiological Applications*" Journal of Applied Physics, Vol. 34, No. 9, 1963, pp. 2722-2727

35. Hammond Jr., D.C.: "*Deconvolution Technique for Line of Sight Optical Scattering Measurements in Axisymmetric Sprays*" Applied Optics Vol. 20 No. 3, 1981, pp. 493-499

36. Durst , F., Zare, M: "Laser Doppler Measurements in Two-Phase Flows" Proc. Of the Laser Doppler Anemometry Symposium, 1974, Hemisphere, Washington, D.C., 1977, pp. 403-429

37. Dodge, L.G., Rhodes, D.J., Reitz, R.D.: " *Drop-size Measurement Techniques for Sprays: Comparison of Malvern Laser-Diffraction and Aerometrics Phase/Doppler*" Applied Optics Vol. 26, No. 11, 1987, pp. 2144-2154

38. Cossali, E., Hardalupas, Y.: " *Comparison Between Laser Diffraction and Phase Doppler Velocimeter Techniques in High Turbidity, Small Diameter Sprays*" Experiments in Fluids, Vol. 13, 1992, pp. 414-422

51. Daily, J.W.: "*Laser-Induced Fluorescence Spectroscopy in Flames*" Prog. Energy Combust. Sci. Vol. 23, pp. 133-199

52. Eckbreth, A.C.: "*Laser Diagnostics for Combustion Temperature And Species 2nd Ed.*" Overseas Publishers Association, Amsterdam, the Netherlands, 1996

53. Melles Griot, "Spectral Data-313FS10-50-01 Interference Filter" Melles Griot, Ottawa, Ontario, 1995

54. Allen, M.G., McManus, K.R., Sonnenfroh, D.M., Paul, P.H.: "*Planar Laser-induced Fluorescence Imaging Measurements of OH and Hydrocarbon Fuel Fragments in High Pressure Spray-Flame Combustion*" Applied Optics, Vol. 34 No. 27, 1995, pp. 6287-6300

55. Garland, N.L., Crosley, D.R.: "*On the Collisional Quenching of Electronically Excited OH, NH and CH in Flames*" 21st Symp. (Int'l) on Combustion 1986, the Combustion Institute, 1986, pp. 1693-1702

56. Tsujishita, M., Hirano, A.: "*Two-dimensional Quenching Lifetime Measurements of OH:$A^2\Sigma(v'=1)$ and NO: $A^2\Sigma(v'=0)$ in Atmospheric Pressure Flames*" Applied Physics B Vol. 62, 1996, pp. 255-262

57. Dieke, G.H., Crosswhite, H.M.: "*The Ultraviolet Bands of OH Fundamental Data*" J. Quant. Spectrosc. Radiat. Transfer Vol. 2, 1962, pp. 97-199

58. Allen, M.G., Howe, R.D., Hanson, R.K.: "*Digital Imaging of Reaction Zones in Hydrocarbon-Air Flames Using Planar Laser-induced Fluorescence of CH and C_2*" Optics Letters Vol. 11 No. 3, 1986, pp. 126-128

59. Copeland, R.A., Jeffries, J.B., Crosley, D.R.: "*Transition Probabilities of OH $A^2\Sigma - X^2\Pi$ Bands with $v' = 0$ and $v'' = 0$ to 4*" Chemical Physics Letters Vol. 138 No. 5, 1987, pp.425-430

60. Atkins, P.W.: "*Physical Chemistry 2nd Edition*" Oxford University Press, 1982

61. Bernath, P.F., Brazier, C.R., Olsen, T., Hailey, R., Fernando, W.T.M.L., Woods, C., Hardwick, J.L.: " *Spectroscopy of the CH Free Radical*" J. of Molecular Spectroscopy Vol. 147, 1991, pp. 16-26

62. Princeton Instruments: "*High Performance Digital CCD Cameras*", Princeton Instruments Inc., Trenton, N.J., 1994

63. Luque, J. , Crosley, D.R.: " *Absolute CH Concentrations in Low-Pressure Flames Measured with Laser-Induced Fluorescence*" Applied Physics B Vol. 63, 1996, pp. 91-98

64. Born, M., Wolf, E.: "*Principles of Optics*" Pergamon Press Ltd., Oxford, 1980

65. Bilger, R.W.: "*Reaction Zone Structure in Turbulent Diffusion Flames*" Joint Int'l Conference Australia/New Zealand and Japanese Sections, The Combustion Institute, 1989

66. Keyes, D.E., Smooke, M.D.: "*Numerical Solution of 2-D Axisymmetric Laminar Diffusion Flames*" Comb. Sci. And Technology V. 67, 1989, pp. 85-122

67. Drake, M.C., Pitz, R.W., Lapp, M., Fenimore, C.P., Lucht, R.P., Sweeney, D.W., Laurendeau, N.M.: "*Measurements of Superequilibrium Hydroxyl Concentrations in Turbulent Non-Premixed Flames Using Saturated Fluorescence*" 20th Symposium (Int'l) on Combustion, The Combustion Institute, 1984, pp. 327-336

68. Noyce, J.R., Sheppard, G.W., Yamba, D.: "*Measurements of Mixing and Species Concentrations Within a Gas Turbine Type Combustor*" Combustion Science and Technology, Vol. 25, 1981

69. Smooke, M.D., Xu, Y., Zurn, R.M., Lin, P., Frank, J.H., Long, M.B.: "*Computational and Experimental Study of OH and CH radicals in Axisymmetric Laminar Diffusion Flames*" 24th Symposium (Int'l) on Combustion, The Combustion Institute, 1992, pp. 813-822

70. Renksizbulut, M., Bussmann, M., Li, X.: "*A Droplet Vaporization Model for Spray Calculations*" Part. Part. Syst. Charact. Vol. 9, 1992, pp.59-65

71. Hinze, J.O.: "*Turbulence 2nd Edition*" McGraw Hill, New York, 1987

72. Dean, J.A.: "*Lange 's Handbook of Chemistry 14th Edition*" McGraw Hill, 1992

73. Schneider, M, Hirleman, E.D.: "*Influence of Internal Refractive Index Gradients on Size Measurements of Spherically Symmetric Particles by Phase Doppler Anemometry*" Applied Optics, Vol. 33 No. 12, 1994, pp. 2379-2388

74. Naqwi, A.A., Durst, F.: "*Light Scattering Applied to LDA and PDA Measurements Part 1: Theory and Numerical Treatments*" Part. Part. Syst. Charact. Vol. 8, 1991, pp. 245-258

75. Naqwi, A.A., Durst, F.: "*Light Scattering Applied to LDA and PDA Measurements Part 2: Computational Results and Discussion*" Part. Part. Syst. Charact. Vol. 9, 1992, pp. 66-80

76. Ceman, D.L., O'Hern, T.J., Rader, D.J.: "*Phase Doppler Droplet Sizing-Scattering Angle Effects*" ASME Fluids Engineering Division FED V.95, ASME, 1990, pp. 61-63

77. O'Hern, T.J., Rader, D.J., Ceman, D.L.: "*Droplet Sizing Calibration of the Phase Doppler Particle Analyzer*" Proceedings of the ASME Fluid Measurements and Instrumentation Forum, San Diego, 1989

78. Ibrahim, K.M., Wertheimer, G.D., Bachalo, W.D.: "*Signal Processing Considerations for Low Signal to Noise Ratio Laser Doppler and Phase Doppler Signals*" 4th International Conference on Laser Anemometry, Cleveland, 1991

79. Høst-Madsen, A., Andersen, K: "*Lower Bounds for Estimation of Frequency and Phase of Doppler Signals*" Meas. Sci. Technol. Vol. 6, 1995, pp.637-652

80. McDonell, V.G., Samuelsen, S.: "*Sensitivity Assessment of a Phase Doppler Interferometer to User-Controlled Settings*" Liquid Particle Size Measuring Techniques: 2nd Volume, ASTM STP 1083, 1990, pp. 170-189

81. Weckman, E.J.: "*Lecture Notes: Experimental Methods in Fluid Mechanics and Heat Transfer Module 5: Laser Doppler Anemometry*" University of Waterloo, 1993

82. Buchhave, P., George, W.K. Jr., Lumley, J.L.: "*The Measurement of Turbulence with the Laser-Doppler Anemometer*" Ann. Rev. Fluid Mech. Vol. 11, 1979, pp.443-503

83. Sung, C.J., Law, C.K., Axelbaum, R.L.: "*Thermophoretic Effects on Seeding Particles in LDV Measurements of Flames*" Combust. Sci. And Tech. Vol. 99, 1994, pp. 119-132

84. Ancimer, R.J., Fraser, R.A.: "*Flame-Induced Laser-Doppler Velocimetery Velocity Bias*" Meas. Sci. Technol. Vol. 5, 1994, pp. 83-92

85. Bendat, J.S., Piersol, A.G.: "*Random Data*" John Wiley and Sons, Toronto, 1986

86. Lumonics, Inc.: "*Spectrummaster Pulsed Dye Lasers*" Lumonics Inc.,Ottawa, 1994

87. Wong, R.: "*Laser Induced Fluorescence Spectroscopy Applied to an Atmospheric Pressure Flame*" MASc Thesis, University of Waterloo, 1991

88. Allen, M.G., McManus, K.R., Sonnenfroh, D.M., Paul, P.H.: "*Planar Laser-induced Fluorescence Imaging Measurements of OH and Hydrocarbon Fuel Fragments in High Pressure Spray Flame Combustion*" Applied Optics Vol. 34 No. 27, 1995, pp. 6287-6300

89. Paul, P.H.: "*A Model for Temperature Dependent Collisional Quenching of OH* $A^2\Sigma^+$" J. Quant. Spectrosc. Radiat. Transfer Vol. 51 No. 3, 1994, pp. 511-524

90. Doherty, P.M., Crosley, D.R.: "*Polarization of Laser-Induced Fluorescence in OH in an Atmospheric Pressure Flame*" Applied Optics *23*, 1984, pp. 713-721

91. Baker, H.D., Ryder, E.A., Baker, N.H.: "*Temperature Measurement in Engineering*" Omega Engineering Ltd., Stamford, CT, 1975

92. Attya, A.M., Whitelaw, J.H.: "*Velocity, Temperature and Species Concentration in Unconfined Kerosine Spray Flames*" ASME paper No. 81-WA/HT-47, 1981

93. Pita, G.P.A., Nina, M.N.R.: "*Errors Induced by Catalytic Effects in Premixed Flame Temperature Measurements*" Int'l Congress on Instrumentation in Aerospace Simulation Facilities, IEEE Publication 89CH2762-3, 1989

APPENDIX 1

ICCD CAMERA CALIBRATION AND OH CONCENTRATION CALCULATION

The ICCD camera was calibrated using a Rayleigh scattering method described in Chapter 4. In order to apply this method, the Rayleigh scattering cross section for air at the calibration wavelength must be computed, which requires a knowledge of the index of refraction of air. The Cauchy dispersion formula [64] produces results with 0.1-0.2% deviation from experiment in the ultraviolet, and is the basis for the index of refraction calculation:

$$n_i - 1 = A_1\left(1 + \frac{B_1}{\lambda^2}\right) \qquad \text{A-1}$$

where: n_i = Index of refraction

$A_1 = 28.79 \times 10^{-5}$ for air [64]

$B_1 = 5.67 \times 10^{-15}$ for air [64]

λ = Wavelength (312×10^{-9} m)

Substitution of the above values into Equation A-1 leads to:

$$n_i - 1 = 3.0467 \times 10^{-4}$$

Once the index of refraction of air is known, the Rayleigh scattering cross-section can be computed from the following, which is valid for small solid collection angles, when the laser polarization and the observation angle are at 90° [64]:

$$\sigma_{Ray} = \frac{\pi^2 (n_i^2 - 1)^2}{\lambda^4 N_A^2} \frac{3}{3 - 4\rho} \qquad \text{A-2}$$

where: σ_{Ray} = Rayleigh scattering cross section (cm^2/sr)

n_i = Index of refraction as calculated above

λ = Wavelength in cm (3.12×10^{-5} cm)

N_A = Number density of air molecules (2.47×10^{19} /cm^3 at 1 atm, 20°C)

ρ = Laser depolarization factor (0.03 assumed)

Substitution of the above values into Equation A-2 leads to the following:

$$\sigma_{Ray} = 6.605 \times 10^{-27} \text{ cm}^2/\text{sr}$$

The intensity of Rayleigh scattered light from a small irradiated volume can be given by:

$$E_{Ray} = \left(n E_i\right)\left(N_A \sigma_{Ray} \Omega\right)\left(L\right) \qquad \textbf{A.3}$$

where: E_{Ray} = Rayleigh scattered energy

E_i = Incident laser energy (0.0028 J/pulse)

n = Number of laser pulses during exposure (50)

N_A = Number density of air molecules (2.47×10^{19} /cm^3)

σ_{Ray} = Rayleigh scattering cross-section (6.605×10^{-27} cm^2/sr)

Ω = Collection solid angle (sr- see below)

L = Length of imaged volume (0.0122 cm)

It should be noted that the above equation results from eliminating the laser cross-section area A from Equation 4.56. The solid collection angle is defined by the effective collection lens diameter at the aperture selected, and the distance from the imaged volume to the front lens, and is given by:

$$\Omega = \frac{\pi D^2}{4 r^2} \qquad \textbf{A.4}$$

where: D = Effective collection lens diameter (23mm at f/4.5)

r = Distance from imaged volume to lens (623mm)

The collection solid angle under these conditions is:

$$\Omega = 0.00107 \text{ sr}$$

Hence, the Rayleigh scattered energy under these conditions is:

$$E_{Ray} = 2.98 \times 10^{-13} \text{ J}$$

To convert the scattered power to the number of photons collected over the exposure time, it is necessary to divide by Planck's constant and the scattered light frequency as follows:

$$n_{pp} = \frac{E_{Ray}}{h\,\nu} \qquad \textbf{A-4}$$

where: n_{pp} = Number of photons collected at lens

h = Planck's constant (6.63×10^{-34} J-s)

$\nu = 9.62 \times 10^{14}$ Hz

Substitution of the scattered power into Equation A-4 leads to:

$$n_{pp} = 467{,}200 \text{ photons}$$

In order to obtain a calibration factor for the ICCD camera, the individual pixel intensity counts from a stack of pixels covering the entire height of the laser beam are summed up. This sum of intensity counts corresponds to the collection of n_{pp} photons Rayleigh scattered from a volume of air LA cm^3, as defined in the above equations. Since the laser was firing into room air, which has some particulate suspended in it, some scattered light arrives at the lens due to Mie scattering from dust, thus contaminating the signal. In addition, there is a 12% pixel to pixel response variation across the ICCD, thus making the assessment of intensity count difficult. In order to reduce the uncertainty, summation of

intensity counts were performed at 100 locations along the imaged laser beam, and the lowest sums assumed to be due to pure Rayleigh scattering. In fact, it was generally obvious when a pixel imaged light scattered from dust, as an unusually high intensity count would be present in marked contrast to its neighbors. Using this method, the intensity count associated with the arrival of 467,200 photons at the lens resulted in an intensity count of approximately 160,000. The calibration factor corresponding to this count is therefore 0.342 counts/photon. It should be noted that this calibration factor, obtained with the camera gain set at 8.0 and the lens set at f/4.5, would have to be adjusted for use with different gain and/or lens settings, using the data presented in Figures 4.16 and 4.17.

One major advantage of this calibration method is that lens efficiencies and the quantum efficiency of the ICCD are included in the calibration factor, and need not be evaluated explicitly. However, if it were desired to use the camera to image fluorescence at a frequency other than the one used in the above calculation, recalibration at the new frequency would be required.

A1.2 OH CONCENTRATION CALCULATIONS

In order to obtain the OH concentration from a PLIF image, it is necessary to convert the pixel intensity output into the appropriate incident photon count, using the calibration factor obtained above, adjusted for aperture and gain setting as appropriate. This photon count can then be converted into a concentration measurement as outlined below.

From Equation 4.43, the number of photons incident on the lens for a particular pixel is given by:

$$n_{pp} = \left(\frac{B_{10}}{c} \right) \left[\frac{1}{h_L} \int_0^{\infty} E(\nu)\, g(\nu)\, d\nu \right] (f_w f_J n_0)(A_p)(F_y) \left(\frac{\Omega}{4\pi} \right) \qquad \textbf{4.43}$$

where: n_{pp} = Number of photons incident on a pixel

B_{10} = Coefficient for stimulated absorption (6.95×10^{23} cm^3/J-s^2)

h_L = Laser sheet height (7.0 cm)

$E(\nu)$, $g(\nu)$ = Laser and absorption lineshapes

F_y = Fluorescence yield

f_v, f_J = Boltzmann fractions

n_0 = Number density of fluorescing species (OH)

A_p = Area imaged by pixel (2.86×10^{-4} cm^2)

Ω = Collection solid angle (5.75×10^{-4} sr D = 23mm, r = 850mm)

The terms in square brackets represent the overlap integral between the laser lineshape and the absorption lineshape. For the conditions used in this work, at a mean temperature of 1500K and laser pulse energy of 2.8 mJ/pulse with a linewidth of 0.2 cm^{-1}, the resulting spectral irradiance is approximately 0.75 x E/$\Delta\nu$, or 2.8×10^{-13} J-s. The overlap integral was evaluated from Equations 4.46-4.54 using MathCAD 6.0. Some care must be taken in evaluating the overlap integral numerically, since the functions being integrated are essentially non-zero over a very narrow band. The step size used by the numerical integrator will be much larger than the non-zero function width, resulting in erroneous values, unless the limits of integration are suitably defined.

The fluorescence yield, F_y, is given by Equation 4.42 as:

$$F_y = \frac{T_{11} A_{11} + T_{00} \frac{V}{Q_0} A_{00}}{Q_1 + V} \qquad \textbf{4.42}$$

where:

F_y = Fluorescence yield

T_{00}, T_{11} = Filter transmision at (0,0) and (1,1) wavelengths (0.11 and 0.17 respectively)

A_{00}, A_{11} = Einstein coefficients for (0,0) and (1,1) transitions (1.44×10^6 and 8.38×10^5 /s respectively)

V = Vibrational transfer rate (1.12×10^9 /s)

Q_0, Q_1 = Quench rates from v``=0 and v``=1 (6.6 x 10^8 /s for both at 1500K)

Substitution of the above values in to Equation 4.42 leads to:

$$F_y = 2.22 \times 10^{-4}$$

The ground state Boltzmann fractions f_v and f_J can be found using Equations 4.47 and 4.48 The vibrational Boltzmann fraction is given by:

$$f_v(T) = \exp\left(-\frac{v\,h\,c\,\omega_v}{k\,T}\right)\left[1 - \exp\left(-\frac{h\,c\,\omega_v}{k\,T}\right)\right] \qquad \textbf{4.44}$$

$$f_J(T) = \frac{h\,c\,B_v}{k\,T}(2J + 1)\exp\left(-\frac{B_v J(J+1)\,h\,c}{k\,T}\right) \qquad \textbf{4.45}$$

where: J = Rotational quantum number ($Q_1(6)$ transition, N = 6, J = 6-1/2)

v = Vibrational quantum number *(v = 0)*

h = Planck's constant (6.63 x 10^{-34} J-s)

c = Speed of light (3 x 10^{10} cm/s)

B_v = Rotational constant (18.513 cm^{-1})

ω_v = Vibrational constant (3569.59 cm^{-1})

k = Boltzmann constant (1.38 x 10^{-23} J/K)

T = Temperature (1500K assumed)

Substitution of the above leads to the following Boltzmann fractions:

$$f_{J=6.5} = 0.105$$

$$f_v = 0.968$$

A typical PLIF single shot image, obtained under the above conditions, shows a peak pixel intensity of approximately 3,000 equivalent counts after background subtraction and compensation for gain setting as well as sheet intensity at the location of the reading. Using the calibration factor obtained in Section A.1, this corresponds to N_{pp} = 8,770 photons. Substitution of this value into Equation 4.43 and solving for n_0 leads to:

$$n_0 = 2.6 \times 10^{16} /cm^3$$

To convert the number density n_0 to a concentration, it is necessary to divide by the total number density at the local temperature, obtained from:

$$n_t = 2.47 \cdot 10^{19} \cdot \frac{T_0}{T}$$

where: n_t = Total number density at atmospheric pressure ($1/cm^3$)

T_0 = Reference temperature (293 K)

T = Actual temperature (K)

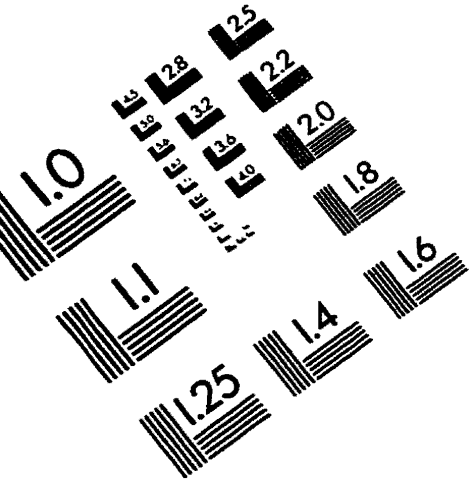
Assuming a local temperature of 1500K leads to a total OH concentration of:

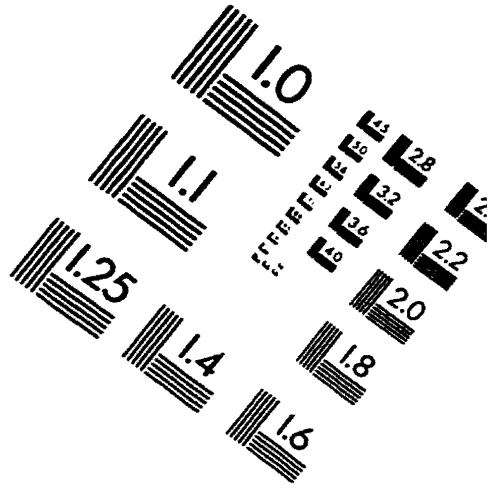
[OH] = .0053, or 5300 PPM

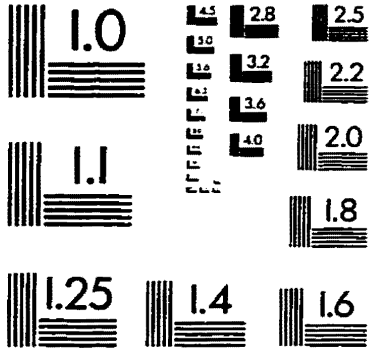
This value should be adjusted to allow for local variation in laser sheet intensity, by refering to Figure 4.18.

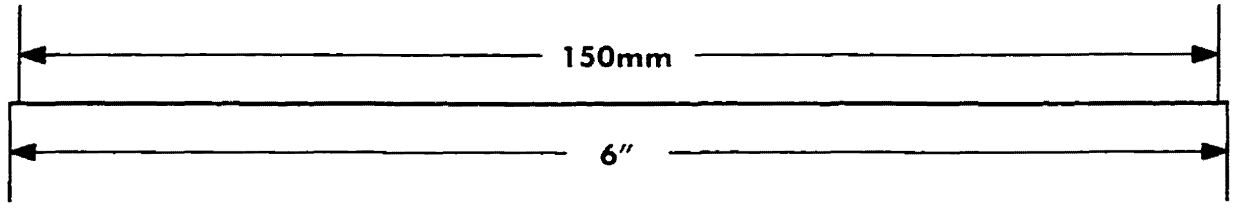
Determination of the local instantaneous OH concentration depends to a large degree on knowledge of the local temperature. The quench rate, Boltzmann fraction and laser lineshape/absorption lineshape overlap integral all have some temperature dependency.

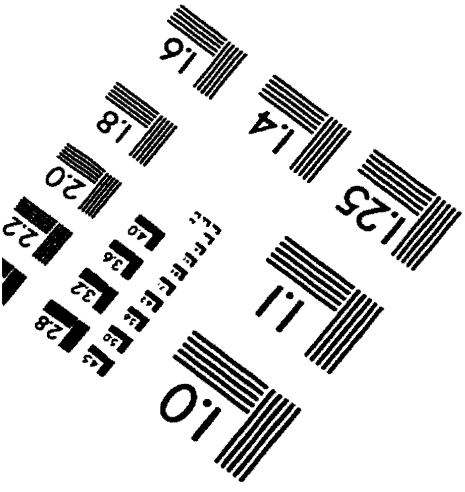
IMAGE EVALUATION TEST TARGET (QA-3)

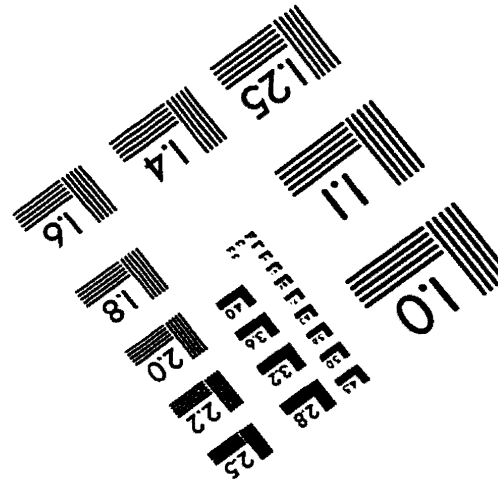












APPLIED IMAGE, Inc
1653 East Main Street
Rochester, NY 14609 USA
Phone: 716/482-0300
Fax: 716/288-5989

© 1993, Applied Image, Inc., All Rights Reserved